INTRODUCTION

The development of reinforced plastics requires broad knowledge and interdisciplinary approaches. The great variety of these materials results in diversity of specialization and poor communication among scientists and engineers working in different sectors. Consequently, often the experience acquired in one area does not benefit others even though it could be of great value to them.

This series of annual symposia has been organized to promote exchange of ideas and knowledge among those working on polymer composites in industry or in academia. For us it is a pleasure organizing these meetings. We are proud to assemble together, on a common ground, the specialists and experts from different sectors of polymer composites.

The symposium "Composites-'87" of November 5 and 6 will be the seventh in a series on "Polymer Composites" and the eighteenth organized and sponsored by the Industrial Materials Research Institute of the National Research Council of Canada. The remaining symposia are part of the two other series on "Mathematical Modeling of Plastics Processing and Properties", and on "Polymer Blends".

Proceedings of these symposia have been published in the technical journals of the Society of Plastics Engineers: "Modeling" and "Polyblends" in Polymer Engineering and Science and "Composites" in Polymer Composites (viz. 3, No. 4 of 1982; 5, Nos. 1 and 4 of 1984; 6, No. 4 of 1985; 7, No. 5 of 1986). The proceedings of this meeting will also be published in the latter journal. In addition, the entire symposium will be recorded and the tapes stored in the Institute library for two years, available to anyone interested in the subject. These meetings provide a source of the most recent information and an open forum for discussion and consultation. They facilitate contacts between the academic and commercial competences and improve understanding, mutual respect and cooperation among the participants.

As organizers of "Composites-'87", we welcome you with thanks for participating. Furthermore, we shall be grateful for any suggestions on further improvements to the content and format of these meetings.

T. Vu-Khanh and L.A. Utracki, Organizers
NRCC/IMRI, 75 De Mortagne, Boucherville, Qué., J4B 6Y4
(514) 641-2280 - Telex 055-61622

Conseil national
de recherches Canada

National Research
Council Canada

Institut de génie
des matériaux

Industrial Materials
Research Institute

75, De Mortagne, Boucherville, Qué., Canada J4B 6Y4
(514) 641-2280

Référence File

IMRI SYMPOSIUM SERIES
"COMPOSITES-'87", NOVEMBER 5-6, 1987
Co-Chairmen: T. Vu-Khanh and L.A. Utracki

PRELIMINARY PROGRAM
November 5th, 1987

08:00 Registration

08:30 Introduction

08:35 1. A.W.-L. Chen, A. Miyase, P.H. Geil and S.S. Wang, "ANELASTIC DEFORMATION AND FAILURE OF A THERMOPLASTIC MATRIX FIBER COMPOSITE AT ELEVATED TEMPERATURE", National Center for Composite Material Research, Univ. Illinois, Chicago, Illinois.

09:30 2. P. Labossière and K.W. Neale, "A GENERAL STRENGTH THEORY FOR ORTHOTROPIC FIBRE-REINFORCED COMPOSITE LAMINAE", Faculty of Applied Science, Univ. Sherbrooke, Sherbrooke, Québec.

10:00 **Pause**

10:20 G.L. BATA, "WELCOMING REMARKS"

10:30 3. C. Poon, R.F. Scott and S. Lee "TOUGHENED RESIN TESTING OF NEW GENERATION CARBON FIBER/EPOXY SYSTEMS", NRCC/NAE, Ottawa, Ontario

11:00 4. D.R. Moore and R.S. Prediger, "A STUDY OF LOW ENERGY IMPACT OF CONTINUOUS CARBON FIBRE REINFORCED COMPOSITES", I.C.I. Chemicals and Polymers group, Middlesbrough, Cleveland, England.

11:30 5. S.V. Hoa, J. Daoust, B.L. Du and T. Vu-Khanh*, "INTERLAMINAR STRESSES IN TAPERED LAMINATES", Dept. Mech. Eng., Concordia Univ., Montréal and * NRCC/IMRI, Boucherville, Québec.

12:00 **Lunch**

13:30 6. D.S. Matsumoto, S.K. Gifford and M. Vallance, "A NOVEL METHOD FOR THE MEASUREMENT OF MODE II DELAMINATION IN AEROSPACE COMPOSITES", General Electric Company, Schenectady, New York.

14:00 7. C. Roy and M. El Ghorba, "MONITORING PROGRESSION OF MODE II DELAMINATION DURING FATIGUE LOADING THROUGH ACOUSTIC EMISSION IN LAMINATED GLASS FIBER EPOXY COMPOSITE", Dept. Mech. Eng., Univ. Sherbrooke, Sherbrooke, Québec.

14:30 **Pause**

8. Paper no. 8 by J.C. Seferis is withdrawn.

15:00 9. P. McConnell, "CANADAIR'S EXPERIENCE IN DEVELOPING AIRCRAFT COMPOSITE STRUCTURES", Canadair Limited, St-Laurent, Québec.

15:30 10. M. Munro, "MANUFACTURING OF FIBRE COMPOSITE COMPONENTS BY FILAMENT WINDING",Dept. Mech. Eng., Univ. Ottawa, Ottawa, Ont.

November 6th, 1987

08:30 11. J.L. White, W. Szydlowski, J. Kim and K. Min, "SIMULATION OF FLOW IN INTERNAL MIXERS AND TWIN SCREW EXTRUDERS", Center for Polymer Engineering, Univ. Akron, Akron, Ohio.

09:00 12. A. Rochette, L. Choplin, P.A. Tanguy, "RHEOLOGY OF MICA-FILLED POLYPROPYLENE AS INFLUENCED BY COUPLING AGENTS", CERSIM, Univ. Laval, Québec, Qué.

09:30 13. T. Malik, P.J. Carreau and M. Grmela, "MECHANICAL AND RHEOLOGICAL PROPERTIES OF CARBON BLACK FILLED POLYETHYLENES", Dept. Chem. Eng., Ecole Polytechnique, Montréal, Québec.

10:00 **Pause**

10:30 14. E. Trujillo, C. Richard and H.P. Schreiber, "PROCESSING SEQUENCE AND THE PROPERTIES OF VINYL COMPOUNDS", Dept. Chem. Eng., Ecole Polytechnique, Montréal, Québec.

11:00 15. K.C. Cole, D. Noël and J.-J. Hechler, "APPLICATION OF DIFFUSE REFLECTANCE FT-IR TO FIBER-REINFORCED COMPOSITES", NRCC/IMRI, Boucherville, Québec.

11:30 16. D.A. Scola, "HIGH TEMPERATURE POLYIMIDES, CHEMISTRY AND PROPERTIES", United Technologies Research Center, East Hartford, CT.

12:00 **Lunch**

13:30 17. C.B. Saunders, L. W. Dickson, A. Singh, A. Carmichael and V.J. Lopata, "RADIATION-CURABLE CARBON FIBER PREPREG COMPOSITES", Atomic Energy of Canada, Pinawa, Manitoba.

14:00 18. T. Masuda and L. Li, "LONG-TIME MECHANICAL RELAXATION IN PARTICLE-POLYMER BLEND SYSTEMS", Kyoto Univ., Kyoto, Japan.

14:30 **Pause**

15:00 19. J. Denault and T. Vu-Khanh "ROLE OF MORPHOLOGY AND COUPLING AGENT IN FRACTURE PERFORMANCE OF GLASS-FILLED POLYPROPYLENE"' NRCC/IMRI, Boucherville, Québec.

15:30 20. R.G. Raj, B.V. Kokta, D. Maldas and C. Deneault, "USE OF WOOD FIBERS IN THERMOPLASTIC COMPOSITES: VI. ISOCYANATE AS A BONDING AGENT FOR POLYETHYLENE - WOOD FIBER COMPOSITES", UQTR, Trois-Rivières, Québec.

16:00 21. S. Polizzi, N. Stribeck, H.G. Zachmann and R. Bordeianu*, "STRUCTURE AND PROPERTIES OF OIL EXTENDED STYRENE BUTADIENE BLOCK COPOLYMERS", Inst. Techn. Makromol. Chemie, Univ. Hamburg, Hamburg, FRG, *Chem. Res. Inst. Icechim, Bucharest, Romania.

ANELASTIC DEFORMATION AND FRACTURE OF A THERMOPLASTIC-MATRIX FIBER COMPOSITE AT ELEVATED TEMPERATURE

by

A.W.-L. Chen, A. Miyase, P.H. Geil and S.S. Wang
National Center for Composite Materials Research
College of Engineering
University of Illinois at Urbana-Champaign
Urbana, Illinois, U.S.A

Presented at the 8th annual NRCC/IMRI symposium "Composites-'87",
November 5 and 6, 1987, Boucherville, Que., Canada

PART I MATRIX BEHAVIOR

1. INTRODUCTION

Recent introduction and development of new types of thermoplastics has brought the resurgence of interest in their application as a matrix material for high performance structural composites. These thermoplastics possess not only excellent chemical resistance but very good high temperature stability; therefore, elevated temperature applications of the composites are considered. However, thermoplastics show time dependent deformation behavior even at room temperature. With increase in temperature, the deformation behavior becomes more pronounced. Thus, it is obvious that good understanding of the time dependent deformations of both the matrix and the composites, including viscoelastic and viscoplastic deformations at elevated temperatures, become very important issues.

A promising family of thermoplastics are semicrystalline polymers with various amounts of crystallinity (1,2). Typical examples are PEEK (Polyether ether ketone), PPS (Polyphenylene-sulphide) and J1 polymer. The coexistence of crystalline and amorphous phases in semicrystalline polymers, however, brings highly complex problems. Mechanically, the phases behave differently and interact with each other. In addition, the introduction of fibers adds further complexities to the problem in the case of composites. The existence of fibers causes not only mechanical interactions with the matrix but morphological changes in the polymers (2,3).

At present, applications of thermoplastic matrix composites for structural purposes are not yet widely spread; however, thermoplastic matrix composites possess many potential advantages over thermoset matrix composites. These include: longer shelf life and less scrap resulting in lower fabrication costs, and better damage tolerance because of higher interlaminar fracture toughness (4-7).

J1 polymer is a semicrystalline polyamide produced by DuPont. Its structural characterization and time-temperature dependent mechanical properties are described in this paper. As part of a continuing study on thermoplastic matrix composites, the structure and transverse properties, including the viscoelastic behavior, of AS4/J1 polymer unidirectional composites are described in an accompanying paper (8).

2. MATERIALS, SPECIMEN PREPARATION AND EXPERIMENTS

2.1 Materials

Based on similarity of fiber diffraction patterns (9,10) J1 polymer is believed to be the homopolymer poly (bis 4-4' decyclohexylmethane) n - dodecanediamide

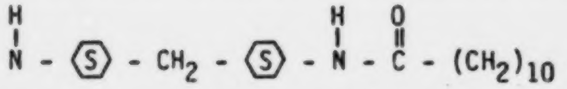

$\overset{H}{\overset{|}{N}} - \langle S \rangle - CH_2 - \langle S \rangle - \overset{H}{\overset{|}{N}} - \overset{O}{\overset{\|}{C}} - (CH_2)_{10} - \overset{O}{\overset{\|}{C}} - .$ It has a density close to one, a melting point of ca 290°C and a T_g near 145°C (11). Injection molded samples and extruded films were supplied by DuPont. Compression molded films were prepared from dried pellets by molding at 315°C, 1200 psi and cooled under various conditions.

2.2 Thermal Analysis

Differential Scanning Calorimetry (DSC) measurements were made using DuPont equipment with a heating rate of 20°C/min. The extruded film, as-received, and compression molded samples were studied.

2.3 Wide Angle X-ray Diffraction (WAXD)

WAXD scans in reflection and/or transmission were obtained using Philips or Rigaku diffractometers, at room and elevated temperature, using Cu K_α radiation.

2.4 Electron Microscopy

Transmission (TEM) and scanning electron microscopy samples were prepared by standard techniques in our laboratory (9).

2.5 Fourier Transform Infrared (FTIR)

FTIR studies, as a function of temperature, were conducted on dried extruded film on a Nicolet 7000 IR spectrometer. 100 scans were added for each spectrum.

2.6 Dynamic Mechanical Spectroscopy

G', G" and tan δ of various samples were measured on a Rheometric System IV Dynamic Mechanical Spectrometer at about 1 Hz, 5°C temperature increments, in the torsion rectangular mode.

2.7 Tensile Stress-Strain Properties

Standard ASTM D638 samples, 0.1 inch thick, were examined at various temperatures in an MTS servo hydraulic testing machine at a strain rate of 0.5 min^{-1}. Mini-dumbbell shaped samples of the compression molded films, cooled at different rates, were tested at 0.06 min^{-1} strain rate.

2.8 Viscoelastic Creep Properties

The ASTM D638 shaped samples were also used for creep. An MTS, under load control, was used with a 1" gauge length LVDT extensiometer. A constant load below σ_y, where σ_y is the yield stress of J1 at a particular temperature, was used at each temperature. Creep strain was recorded up to 17 min.

3. RESULTS AND DISCUSSION

Extended discussion of the results presented here are included in ref. 9 and will be published.

3.1 Structural Characterization

3.1.1 Morphology

J1 polymer cast from solution consists of well formed spherulites composed of radial arrays of fibrils (lamellae?) When crystallized from the melt, as in the samples used here, only poorly formed spherulites and/or randomly arranged fibrils are seen.

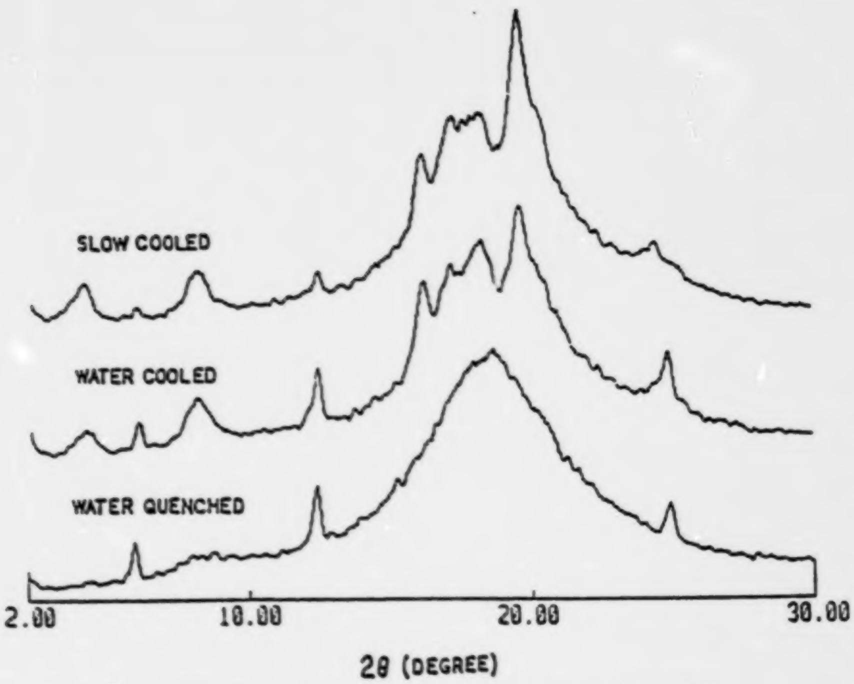

Figure 1. WAXD scans of compression molded neat resin samples cooled at different rates (reflection).

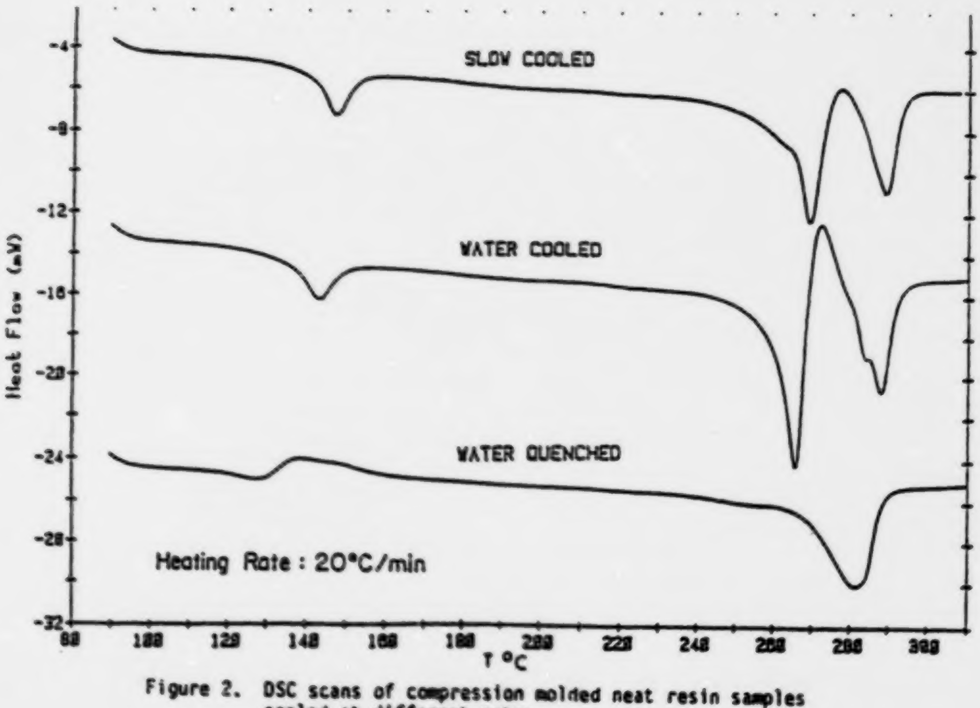

Figure 2. DSC scans of compression molded neat resin samples cooled at different rates.

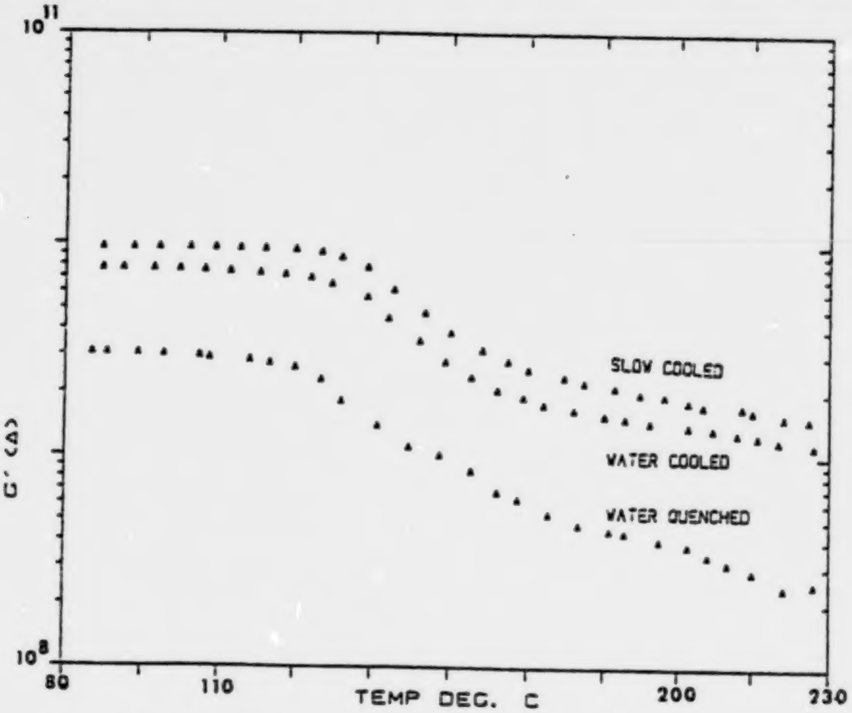

Figure 3. Storage modulus of compression molded samples cooled at different rates.

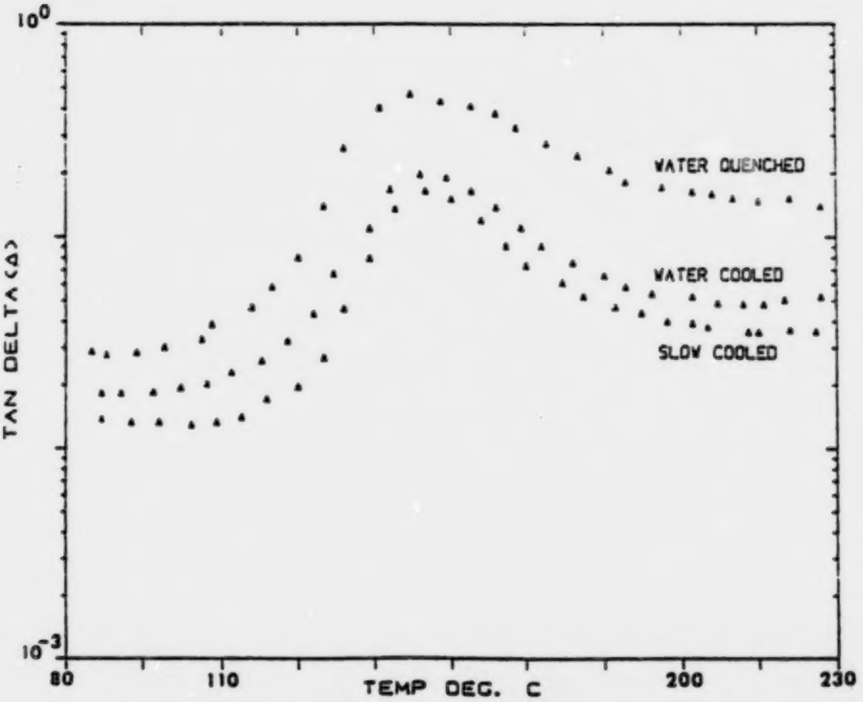

Figure 4. Tan δ of compression molded samples cooled at different rates.

3.1.2 WAXD

Figure 1 shows WAXD scans of compression molded samples cooled at 3 rates; the slow and water cooled samples were cooled in the press whereas the water quenched sample was directly immersed in room temperature water. The sharp peaks at 6, 12 and 24°, 2θ, have been shown to be due to an additive. The spacings on flat plate photographs of drawn J1 agree with those reported by Barton (10); the spacings here do not, indicating that the unit cell in the melt crystallized samples differs from that in a drawn sample. In particular the molecular axis repeat is slightly shorter (43.6 A here vs. 45 A for Barton). The hko reflections, 15-23°, 2θ, also differ.

The water quenched sample is "completely amorphous". Using its scan as a model and drawing in an appropriate line separating the crystalline and amorphous scattering, the crystallinities of the other two samples shown are 19.9% (slow cooled) and 18.2% (water cooled) respectively; i.e. they are relatively close and low compared, for instance, to PEEK or polyethylene.

Annealing of a crystalline sample at 200°C for up to 20 hours showed no obvious change in the WAXD pattern.

3.1.3 Thermal Analysis

Figure 2 shows DSC traces of the same 3 samples. DSC scans of the extruded samples were similar to those of the water quenched sample in showing only a single melting peak (~ 280°C), as well as having an exothermic peak in the vicinity of 140°C; this peak is attributed to crystallization of the amorphous polymer, the resulting crystals melting as a single peak at 280°C.

The double melting peak in the samples cooled in the press can be attributed to a melting - recrystallization - remelting phenomenon. The endothermic peaks at ~ 140° could be due to 1. a difference in heating and cooling rates (T_g overshoot), 2. disruption of the H-bonded network in the amorphous regions (12), permitting segmental molecular motion and/or 3. a crystal-liquid crystal transition. Our results suggest none of these explanations are appropriate. In particular: on successive heating and cooling runs, both at a constant, given rate, the peak near 140° is seen, with opposite sign, in both types of runs; FTIR measurements of free and H-bonded NH show a gradual change with increasing temperature; and WAXD studies at elevated temperature show no significant change in this temperature region. For convenience T_g has been taken as the temperature of the endothermic peak, i.e. 140°C; the presence of the peak makes its determination by DSC difficult. The double melting peak also makes crystallinity determinations by DSC difficult.

3.2 Mechanical Characterization

3.2.1 Dynamic Mechanical Spectra

G' and tan δ, as a function of temperature, are shown for the 3 compression molded samples in Figures 3 and 4. As

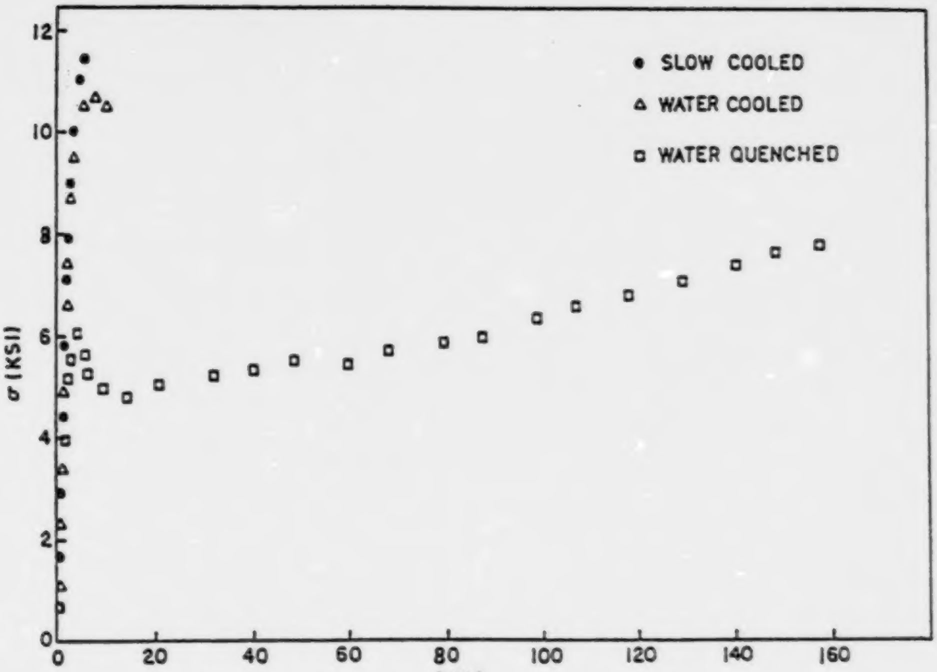

Figure 5. Tensile stress-strain curves of compression molded neat resin samples cooled at different rates.

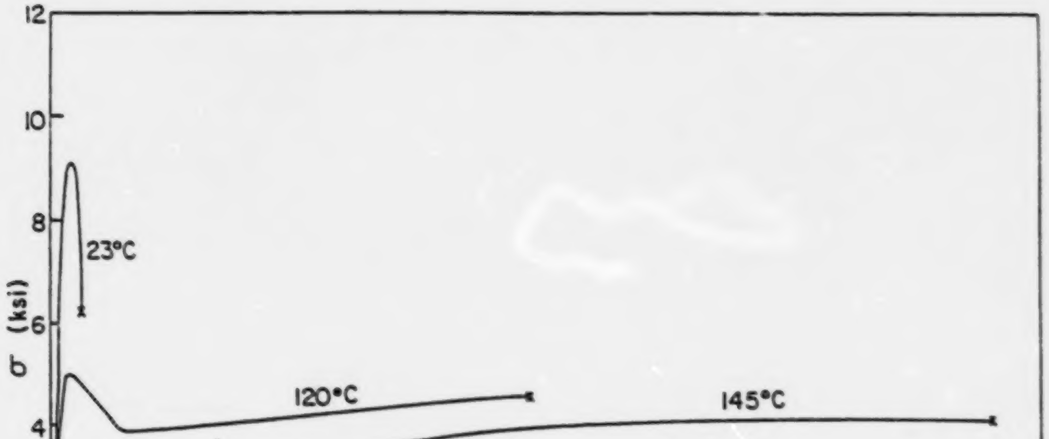

Figure 6. Tensile stress-strain curves at neat resin samples (injection molded) at different temperatures.

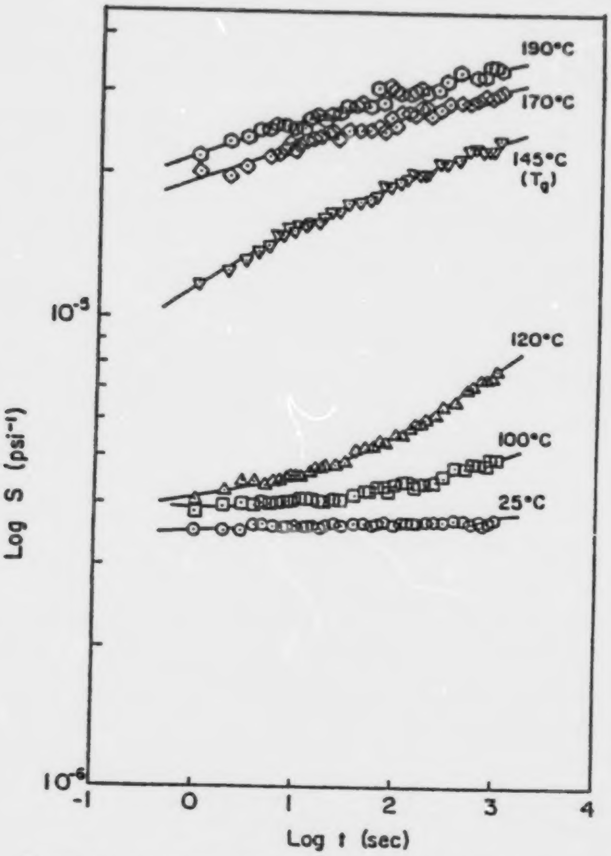

Figure 7. Creep compliance data of J1-polymer neat resin at various temperatures.

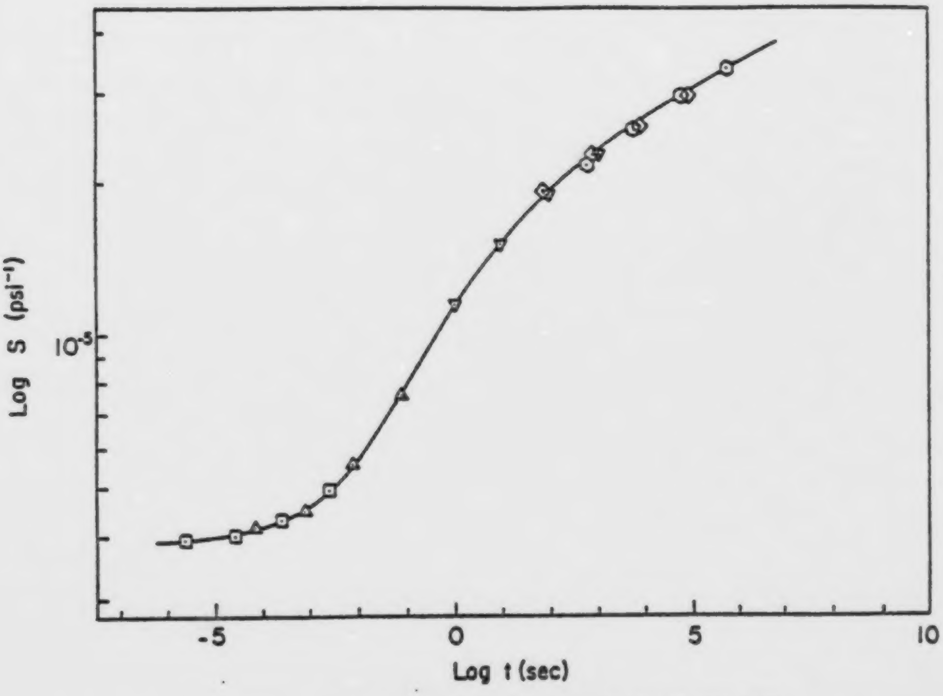

Figure 8. Master curve for creep compliance of J1-polymer neat resin at reference temperature T = 145°C.

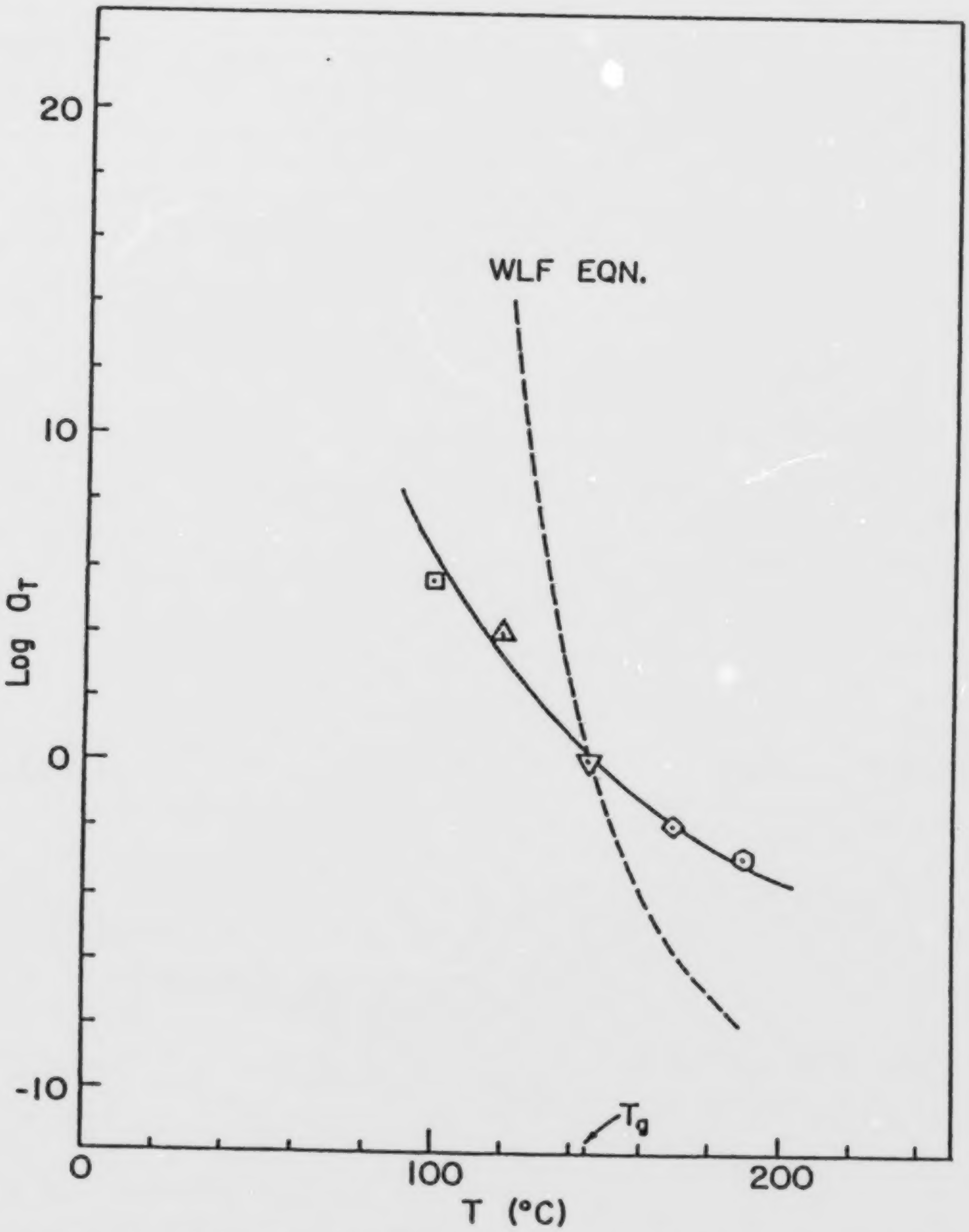

Figure 9. Shift factors for construction of master curve of J1-polymer neat resin with reference temperature T = 145°C.

expected G' is largest for the most crystalline samples, over the entire temperature range. The presence of the crystals is seen to result in a relatively constant modulus above T_g, G' for the water quenched samples dropping considerably more rapidly. G" has a peak, of nearly identical height in all 3 samples, at a T_g of ca 150°C. The relative heights of the corresponding tan δ (G"/G') peaks are as expected, i.e. the water quenched sample is the highest. The corresponding data for the injection molded sample was similar.

3.2.2 Tensile Data

The stress-strain curves for the 3 types of samples are shown in Figure 5. Whereas the crystalline samples are essentially brittle at room temperature, the amorphous sample is seen to be remarkably ductile. Micrographs of the fracture surfaces show that all 3 samples failed in a locally ductile manner. The modul of the samples are ca. 343,500 psi for both crystalline samples and 227,000 psi for the amorphous sample.

3.2.2 Plastic Deformation Zone

The plastic deformation zone was examined by several electron microscope sample preparation techniques (9). A large craze field is observed surrounding an advancing crack.

3.3 Effect of Temperature on Properties

3.3.1 Tensile Data

The stress-strain curves for injection molded samples drawn at various temperatures are shown in Figure 6. Clearly, as the draw temperature is increased, the yield stress and modulus decrease, while the elongation increases. A plot of the modulus vs. temperature shows a significant drop in the region between 100 and 140°C, centered at about 120°C.

3.3.2 Viscoelastic Creep

The creep compliance curves for injection molded J1 are shown in Figure 7. HorizontaL shifting alone is sufficient to produce a master curve (Figure 8). The shift factors (Figure 9), however, do not obey the WLF equation (13), probably as a result of the crystallinity of the sample.

4. CONCLUSIONS

(1) J1 is a low crystallinity polymer, the crystallinity and properties of which can be affected by processing conditions.

(2) The unit cell in the melt-crystallized samples is different than that found in fibers.

(3) The thermal behavior of crystalline samples in the vicinity of T_g (ca 145°C) (the reversible endo-exo peak behavior found on heating-cooling) cannot yet be explained. A double melting peak (T_m = 290°C) is attributed to melting-recrystallization-remelting.

(4) The crystalline samples fail brittlely (locally ductile) in tension at room temperature whereas an amorphous sample failed in a ductile manner. The modulii of the crystalline samples are some 50% greater than that of the amorphous sample.

(5) As a function of increasing draw temperature the modulus and yield stress decrease, while the elongation increases.

(6) Creep data can be superposed to form a master curve by horizontal shift alone; the shift factors do not obey the WLF equation.

(7) G' increases slightly with increasing crystallinity below T_g whereas G''_{max} is nearly constant and tan δ_{max} at T_g decreases. The T_g peak in G" is at about 150°.

5. ACKNOWLEDGEMENTS

This research was supported by the National Science Foundation through the Polymer Program of the Division of Material Research and the DuPont Company.

6. REFERENCES

1. J. D. Muzzy and A. O. Kays, Polym. Comp., 5, 169 (1984).
2. A. Lustiger, SAMPE J., 20, Sept/Oct, 13 (1984).
3. Y. Lee and R. S. Porter, Polym. Eng. Sci., 25, 633 (1986).
4. J. T. Hoggatt, 5th National SAMPE Technical Conference, Materials and Processes for the 70's, Cost Effectiveness and Reliability, 91 (1973).
5. C. C. Martin Ma, J. E. O'Connor and A. Y. Lou, 29th National SAMPE Symposium, Technology Vector, 29, 753 (1984).
6. J. T. Hartness, 14th National SAMPE Technical Conference, Materials and Process Advances, 14, 26 (1982).
7. K. B. Su, Proceeding of 5th International Conference on Composite Materials, W. C. Harrigan Jr., J. Strife and A. K. Dhingra eds., TMS-AIME, Warrendale, PA, 1985, pp. 995-1006.
8. A. Miyase, S. S. Wang, A. Chen and P. H. Geil (this meeting).
9. A. Chen, Ph.D. thesis, University of Illinois (1987).
10. R. Barton, Am. Phys. Soc. meeting New York, March 1987.
11. I. Y. Chang, Comp. Sci. Tech., 24, 1985, pp. 61-79.
12. G. A. Gordon, J. Polym. Sci., A2, 1693 (1971).
13. J. D. Ferry, "Viscoelastic Properties of Polymers", J. Wiley and Sons, Inc., New York (1980).

PART II UNIDIRECTIONAL COMPOSITE LAMINATE

1.INTRODUCTION

In an accompanying paper [1], the structural characterization and time-temperature dependent mechanical properties of the semi-crystalline thermoplastic matrix resin, J1 polyamide, produced by DuPont, are described. In this paper, a part of a major continuing study on thermoplastic matrix composites, the structure and properties, including viscoelastic behavior, of the AS4/J1-polymer unidirectional composite at elevated temperatures are described.

2.MATERIAL, SPECIMEN PREPARATION AND EXPERIMENTS

2.1 Material

The AS4/J1-polymer composite was supplied by DuPont in the form of prepreg and unidirectional laminates. The unidirectional prepreg tapes made by the DuPont melt impregnation process were used to fabricate composite plates. The plates were made using a 6 inch x 6 inch steel mold at 300°C curing temperature, under 1200 psi pressure. After consolidation, the whole molding assembly was cooled down to room temperature under pressure.

2.2 Thermal Analysis

Differential scanning calorimetry (DSC) measurements were made using DuPont 990DSC with 1090 Thermal Analyzer. Approximately 5mg of the prepreg and 10mg of the 4-ply composite were used. The nominal heating rate employed was 20°C/min.

2.3 Wide Angle X-Ray Diffraction (WAXD)

WAXD scans in a transmission mode were obtained using a Rigaku D-Max diffractometer with appropriate counting and recording equipment. Specimens were 4-ply AS4/J1-polymer composites in an as-received condition.

2.4 Dynamic-Mechanical Property Measurements

Dynamic-mechanical properties were measured using a Rheometric System IV at a frequency of 1 Hz. and at a temperature increment of 5°C/min. under a torsional mode. Specimens of approximately 2.5 inch x 0.5 inch rectangular shape were made from the 8-ply composite with fibers in the transverse direction.

2.5 Viscoelastic Creep Experiment

Viscoelastic creep experiments were run at 25°C, 100°C, 120°C, 145°C, 170°C and 190°C in the inplane transverse direction. Straight sided coupon specimens with one-inch in width and six-inch in length were cut out of 16-ply plates. In order to prevent damage of the composite specimen in the grips, aluminum tabs were adhesively bonded using a high temperature film adhesive. Creep experiments were carried out using a servo-hydraulic testing machine under load control mode. Creep

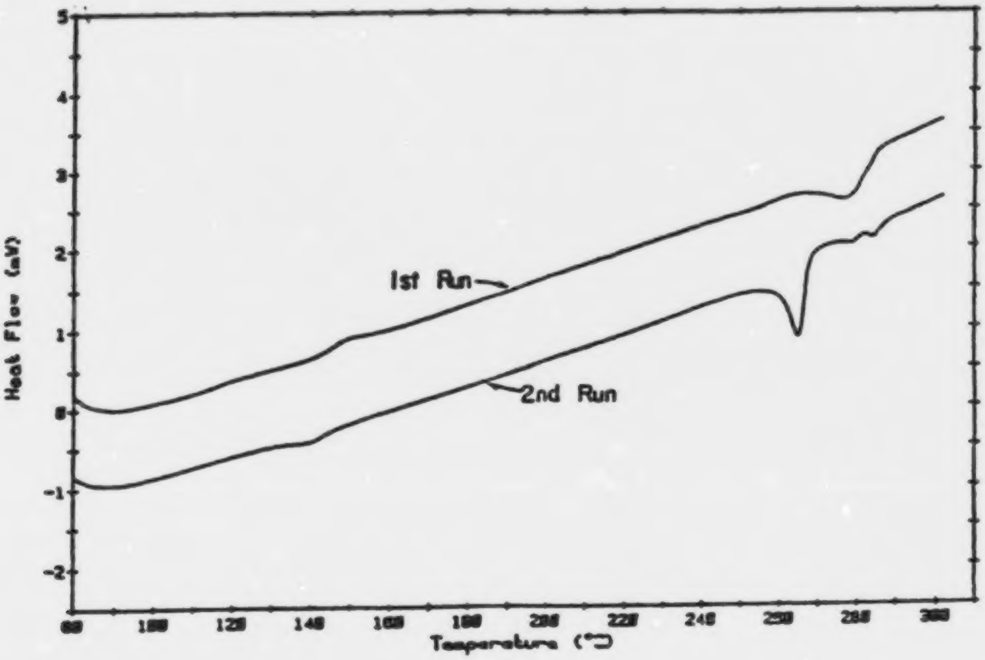

Fig. 1. DSC scan of unidirectional AS4/J1 polymer composite prepreg.

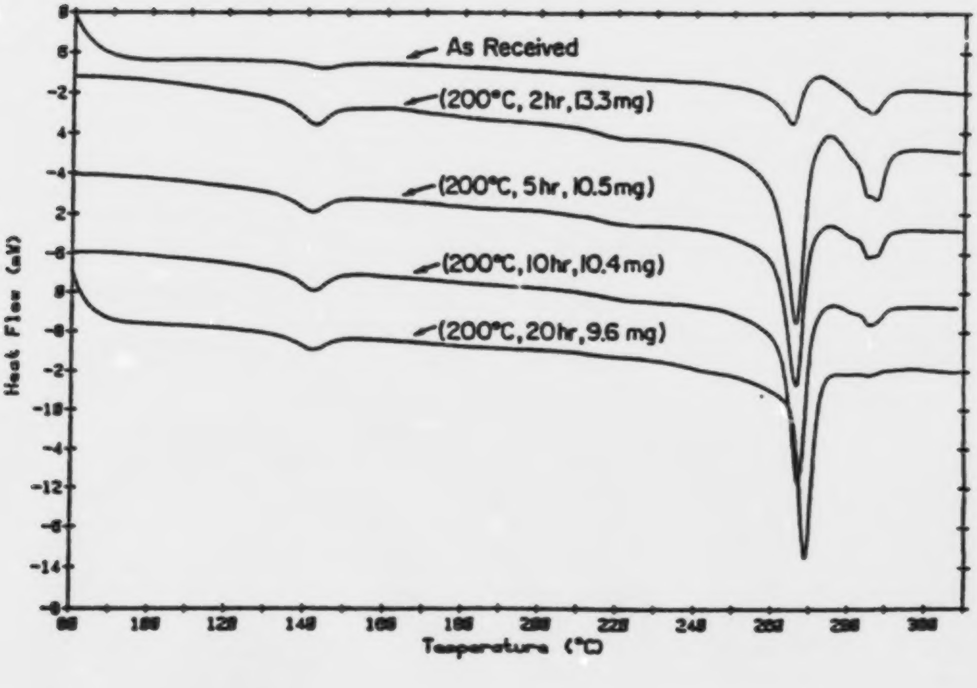

Fig. 2. Effects of annealing on DSC scan of a 4 ply unidirectional AS4/J1 polymer composite laminate.

strain measurements were made by a LVDT extensometer with 1.5-inch gage length. Thermoelastic properties were measured first by conducting tensile tests at various temperature levels. In the viscoelastic creep experiments, specimens were loaded to different, predetermined stress levels based on the tensile tests within 0.75 seconds to avoid failure during loading. Elapsed time and displacement data were printed out in appropriately selected time intervals, and then analyzed and reduced to time vs. compliance plot.

3 RESULTS AND DISCUSSION

3.1 Structural characterization

The J1-polymer thermoplastic resin used as a composite matrix material is a polycarbonamide (PACM-n). The structural characterization of the neat resin, which is described in Part I of the study [1], indicates the semicrystalline nature of the polymer. This was also demonstrated in the AS4/J1-polymer composite from a DSC scan (Fig. 1) taken from the composite prepreg. The results show that T_g of the prepreg is about 145°C and T_m about 280°C, which are in good agreement with T_g and T_m of the resin [1]. During the second run, after immediate fast cooling of the sample in air, double melting peaks were observed. This may be attributed to a melting-recrystallization-remelting process in the relatively slow cooled composite, according to the previous study on the neat resin behavior [1].

Annealing of slow cooled material above T_g ,in this case 200°C, provides an additional evidence of this recrystallization behavior. A series of DSC scans of the samples annealed at 200°C at various periods of time is shown in Fig. 2. With increasing annealing time, the melting behavior was altered significantly but no change was observed for the T_g. The annealing process seems to perfect the original crystal and to allow no further recrystallization followed by remelting. It may also be noted that the matrix in the prepreg behaves like a quenched sample in the melting temperature range. On the other hand, the matrix in the composite laminate shows a similar melting behavior as a slow cooled sample [1].

3.2 Crystallinity Measurements from WAXD

For semicrystalline monolithic polymers, the degree of crystallinity is one of the most important indices determining the chemical and mechanical properties. Preliminary X-ray diffraction results [2] taken under a reflection mode indicated the difficulties in differentiating crystalline peaks from the diffraction pattern of the graphite fiber. The WAXD scan under a transmission mode, with the length of the beam normal to and the scan direction parallel to the fibers, allows to separate the diffraction pattern of the graphite fibers from the diffraction profile of the matrix material [3,4]. The WAXD scan

3 K

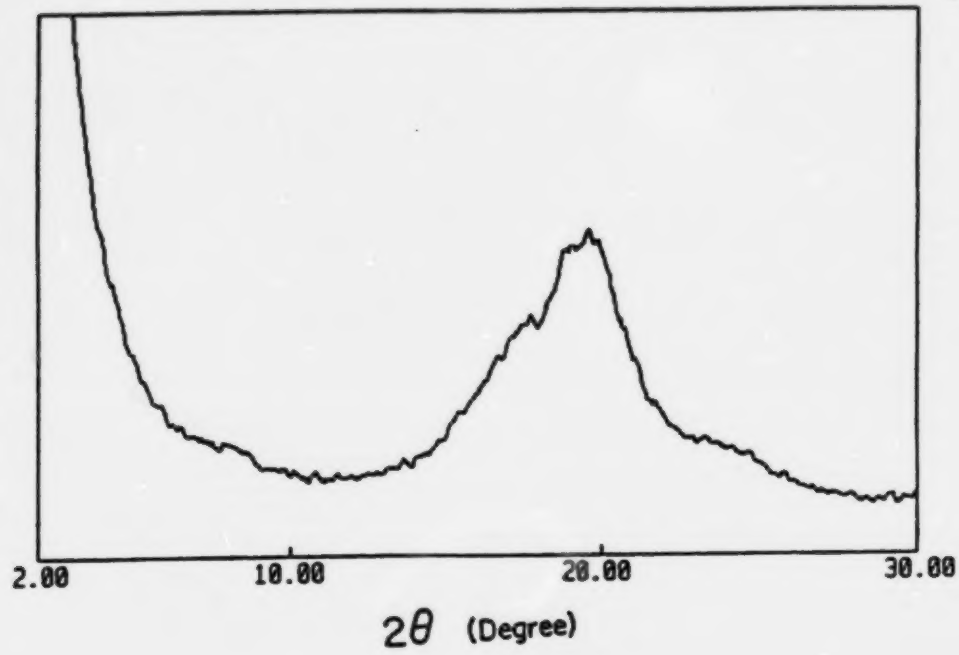

Fig. 3. WAXD scan of a 4 ply unidirectional AS4/J1 polymer composite laminate under transmission mode.

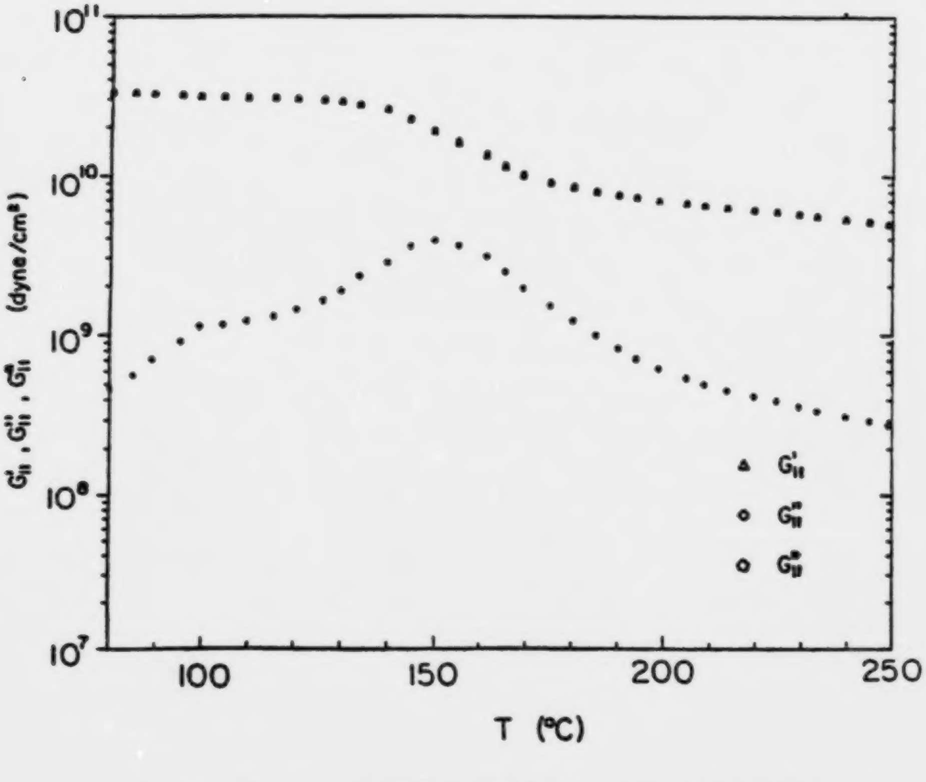

Fig. 4. Dynamic mechanical properties in transverse direction of a 8 ply unidirectional AS4/J1 polymer composite laminate.

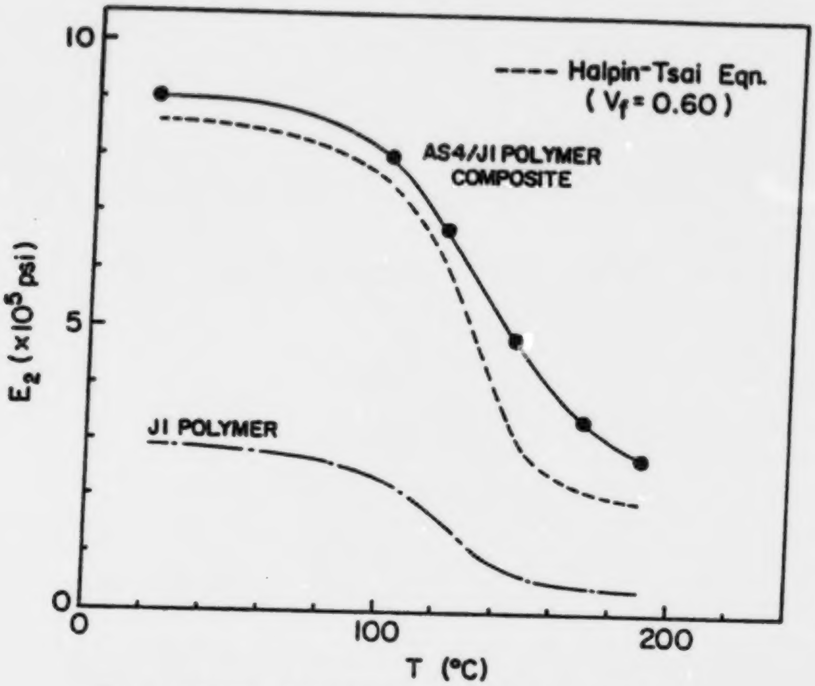

Fig. 5. Effects of temperature on transverse elastic modulus of AS4/J1 polymer composite, together with elastic modulus of neat J1 polymer resin and Halpin-Tsai prediction.

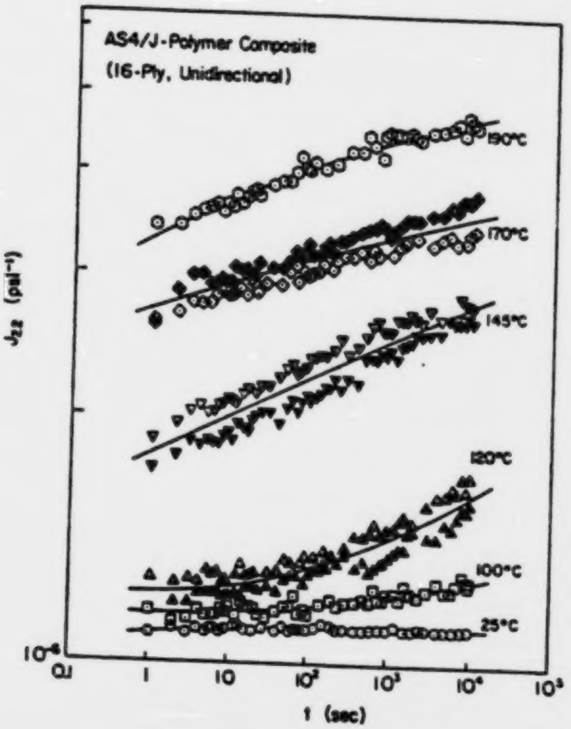

Fig. 6. Transverse viscoelastic creep compliance data of AS4/J1 polymer composite at various temperatures.

taken under these conditions is shown in Fig. 3. Drawing in an amorphous background peak of similar shape to the peak in the water-quenched neat resin [1], crystallinity of the matrix was calculated to be approximately 16%. The relatively poor crystalline peak resolution in the scan in Fig. 3 may be result from the small crystal size, low degree of perfection, instrumentation effects and/or crystal orientation in a transcrystalline layer induced by nucleation around the graphite fibers. The latter is known to occur in PEEK/graphite composites [3-6].

3.3 Dynamic-Mechanical Properties Measurement Results

Dynamic-mechanical properties measurements on the unidirectional composite in the transverse direction are shown in Fig. 4. As expected, the storage modulus (G') dropped significantly and the loss modulus (G'') reached a peak around 145°C. This is because, in the transverse direction, resin properties are generally recognized to dominate the composite properties.

3.4 Thermoelastic Properties

Variation of the transverse elastic modulus of the unidirectional composite with the temperature is shown in Fig. 5. The effect of temperature on the thermoelastic properties of neat J1-polymer is also shown for comparison. The transverse modulus of the composite retains its room temperature value up to approximately 100°C. Approaching to 145°C, the value of E_2 decreases very sharply, and above this temperature, the stiffness reduction levels off. This behavior of the thermoplastic composite agrees with that of the matrix neat resin. Using the Halpin-Tsai equation with elastic modulus values of the fibers and matrix and the fiber volume fraction of 0.60, predicted results are also shown in the figure. The thermoelastic modulus reduction due to the increase of temperature agrees with experimental results very closely up to 120°C. However, above this temperature the discrepancies between them seem to increase. This may result from morphological differences between the bulk J1-polymer and the polymer in the fiber composite.

3.5 Viscoelastic Creep Behavior

Stress levels used for creep compliance measurements in the transverse direction were kept below 2/3 of yield stress based on the 0.1% offset stress definition for all temperatures. The compliance curves obtained for various temperatures are plotted in Fig. 6. At the room temperature almost no compliance change was observed. With the increase in temperature, the compliance change with time increased sharply. Above 145°C, the glass transition temperature of the J1-polymer, the compliance increase gradually leveled off. Using the well known time-temperature superposition concept, construction of a master curve for T=145°C was attempted. In this study, only horizontal

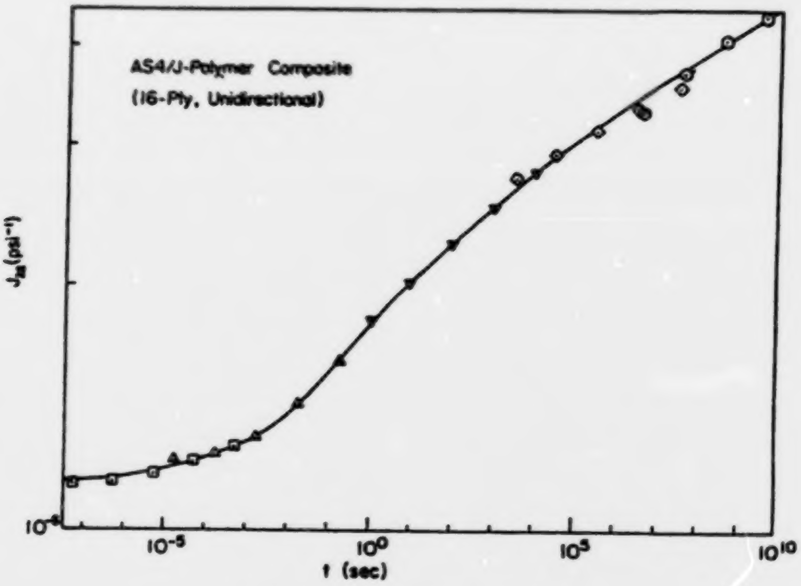

Fig. 7. Master curve for transverse viscoelastic creep compliance of AS4/J1 polymer composite at reference temperature T=145°C.

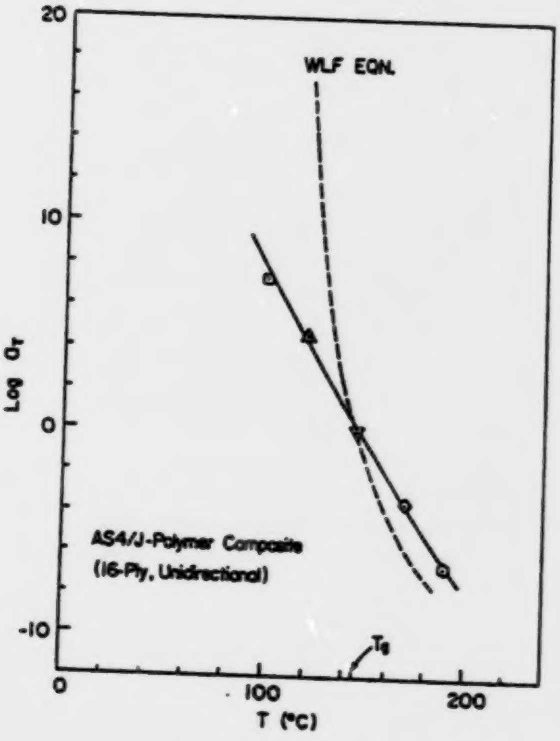

Fig. 8. Shift factors for construction of master transverse viscoelastic creep compliance curve of AS4/J1 polymer composite at reference temperature T=145°C

shifts were made, because the variation of density of the composite with temperature is considered to be very small. And the master curve is shown in Fig. 7. The master curve obtained was very smooth over the entire time range except for a very small disturbance in the very long-time region. The shift factor for constructing the master curve is also given in Fig. 8 for comparison with that based on the well known WLF equation. The agreement between them was found to be good in spite of the fact that the equation was originally developed for amorphous polymers. This result was surprising because the matrix material, i.e. the J1-polymer, is a semicrystalline polymer. In many cases, it is recognized that master curves can not be constructed in general for semicrystalline polymers except ones with very low crystallinity without using both horizontal and vertical shifts [7-9]. In addition, the composite contains graphite fibers approximately 60% by volume. To understand this phenomena fully further experimental and analytical investigations are in progress.

4 CONCLUSIONS

Based on the experimental results obtained in this study, the following conclusions can be reached:

(1) The morphology and the structure, i.e. the degree of order, of the semicrystalline thermoplastic matrix in a composite can be greatly affected by processing variables.
(2) Crystallinity of the matrix in the AS4/J1-polymer composite was found to be approximately 16% from the WAXD scan under a transmission mode.
(3) Dynamic mechanical properties along the transverse direction are highly time and temperature dependent. Creep compliance measurements also indicate the same nature.
(4) Transverse thermoelastic properties of the thermoplastic matrix composite are significantly different from those of the neat resin.
(5) The master curve of the transverse creep compliance of the semicrystalline AS4/J1-polymer thermoplastic matrix composite can be obtained using time temperature superposition.
(6) The shift factor obtained for this composite is in agreement with predictions by the well-known WLF equation.

5 ACKNOWLEDGEMENT

This research was supported by the Office of Naval Research, National Science Foundation through the Polymer Program of the division of Material Research, and the DuPont Company.

6 REFERENCES

[1] A. Chen, A. Miyase, P.H. Geil and S.S. Wang, (this meeting).

[2] A. Chen, Ph.D. thesis, University of Illinois (1987)

[3] D.J. Blundell, J.M. Chalmers, M.W. Mackenzie and W.F.Gaskin, SAMPE Quarterly, 6, (4), 22, (1985).

[4] M.R. James and D.P. Anderson, "Advances in X-Ray Analysis, Vol. 29", C.S. Barrett, J.B. Cohen, J. Faber Jr., R. Jenkins, D.E. Leyden, J.C. Russ and P.K. Predecki eds., Plenum, N.Y., 291, (1986).

[5] J.A. Peacock, B. Fife, E. Nield and C.Y. Barlow, "Composite Interface", H. Ishida and J.L. Koenig eds., Elsevier, N.Y., 143, (1986).

[6] Y. Lee and R.S. Porter, Polym. Eng. Sci., 26, (9), 633, (1986).

[7] K. Nagamatsu, T. Takemura, T. Yoshitomi and T. Takemoto J. Polym. Sci., 33, 515, (1958).

[8] R.W. Pen, J. Polym. Sci., Part 2, 4, 545, (1966).

[9] A. Crugnola, M. Pegorano and F. Danusso, J. Polym. Sci., Part A2, 6, 1705, (1968).

A GENERAL STRENGTH THEORY FOR ORTHOTROPIC FIBER-REINFORCED COMPOSITE LAMINAE

by

P. Labossière and K.W. Neale*
Ecole de génie
Université de Moncton
Moncton, New Brunswick, Canada

*Faculté des sciences appliquées
Université de Sherbrooke
Sherbrooke, Québec, Canada

Presented at the 8th annual NRCC/IMRI symposium "Composites-'87",
November 5 and 6, 1987, Boucherville, Que., Canada

ABSTRACT

Thin, orthotropic fibre-reinforced composite laminae under plane stress loading conditions are considered. The essential conditions that must be satisfied in developing phenomenological strength criteria for such materials are first established. A new, parametric failure criterion is then presented. It is shown that this entirely general formulation encompasses all previously proposed failure theories (e.g. tensor polynomial criterion) for orthotropic laminae. Examples of application and the inherent advantages and drawbacks of the proposed parametric approach are discussed.

In the past, the formulation of strength criteria for composite materials has closely paralleled the development of yield criteria in metal plasticity. The parametric approach advocated here for the failure of composite materials was inspired by a general formulation recently proposed by Budiansky (1) for the plastic yielding of sheet metals.

1. INTRODUCTION

Because of their favourable strength-to-weight characteristics, advanced fibre-reinforced composite materials are steadily being selected over traditional materials in the fabrication of structural components. In many applications, these elements consist of thin laminae reinforced either unidirectionally or bi-directionally, and assembled together to form a laminate. These components are generally subjected to bending and in-plane loadings, and are therefore usually analyzed on the assumption of plane stress conditions.

To characterize the strength properties of a particular lamina, strength or failure theories are employed. Analytical methods (e.g. classical lamination theory) can be used in conjunction with these failure criteria to determine the overall strength properties of a laminate. Among the many failure criteria that have been proposed for unidirectional and bi-directional composite laminae, the maximum stress and maximum strain theories are still the most widely used in practice (2). This is mainly because they are the easiest to apply. Also, simple hypotheses concerning failure modes can be associated with the failure parameters in these theories. Among researchers, however, the tensor polynomial theory of Tsai and Wu (3) has received the widest attention. This is due to the mathematical generality of the tensorial formulation, which can be manipulated according to well-established rules. Moreover, as shown by Wu (4), this theory encompasses every failure criterion previously proposed for fibre-reinforced laminae.

Although the tensor polynomial equation can be expanded to any degree, the quadratic form has been the most popular choice so far. In plane stress, this leads to an ellipsoid-shaped failure surface in the $\sigma_1 - \sigma_2 - \tau_{12}$ stress space. Here, σ_1 and σ_2 are the normal stresses in the plane (1-2 directions) of the lamina and τ_{12} is the shear stress. For unidirectional or bi-directional composites σ_1 and σ_2 are referred to the material axes (fibre directions), with σ_1 in the fibre direction for the unidirectional case. For both of these cases, the failure envelope is symmetrical about the shear plane $\tau_{12} = 0$. This envelope can be defined by six strength parameters, five of which are calculated from uniaxial and shear tests on a lamina. The remaining constant, referred to as the interaction parameter, describes the orientation and length of the major and minor axes of the ellipsoid. It is usually calculated from the results of a biaxial test. Unfortunately, its value depends on the particular biaxial test selected (see, for example, ref. (5)) and different failure envelopes can be obtained when different tests are employed. This suggests that an ellipsoid may not always provide the best analytical representation of the experimental failure envelope for a fibre-reinforced lamina.

In order to improve the correlation between experimental data and theoretical failure surfaces, some authors have suggested including cubic terms in the tensor polynomial theory (e.g. Tennyson et al., ref. (6)). However, the gain in accuracy obtained is accompanied by the significant complexity of determining many additional strength parameters in the failure equation. In plane stress, five interaction parameters must be found with the cubic form, instead of one with the quadratic theory. Despite this drawback, this approach has nevertheless been actively pursued in recent years.

As the tensor polynomial theory is tending to become prohibitively complicated and difficult to handle with the inclusion of terms of higher degree, it is perhaps worthwhile to attempt the general formulation of failure criteria from an alternative point of view. It is the purpose of this study to suggest a new approach, inspired from recent work done in the field of metal plasticity. We shall focus on the failure of unidirectional or bi-directional laminae. These materials are orthotropic, with the material (fibre) axes as the axes of orthotropy (1-2 directions). The general ideas presented, however, can readily be extended to more general anisotropic materials.

The essential conditions that must be satisfied in developing a strength criterion for orthotropic laminae will first be identified. Then, the general form of a new plastic yield criterion recently proposed by Budiansky (1) for transversely-isotropic sheet materials will be discussed. An extension of the basic ideas put forward by Budiansky will then be proposed to describe failure of orthotropic, fibre-reinforced laminae. Finally, an example of application of this approach will be presented.

2. ESSENTIAL CHARACTERISTICS OF A FAILURE CRITERION FOR FIBRE-REINFORCED COMPOSITES

We consider fibre-reinforced orthotropic laminae which are subject to various combinations of in-plane tensile, compressive, and shear loadings. For these laminae, the orientation of the loading axes with respect to the axes of orthotropy must be taken into account. From the usual transformation rules, any set of applied stresses can be transformed into components σ_1 , σ_2 , τ_{12} with respect to the material axes. The failure criterion can thus, without loss of generality, be written in terms of the stresses σ_1 , σ_2 , and τ_{12} and be represented graphically in this three-dimensional stress space. To ensure that the ultimate strength for any stress combination is finite, the failure surface must be closed.

Symmetries of the material properties will introduce certain symmetries in the failure envelope. Consider, for example, an isotropic material. Its uniaxial tensile and compressive strengths must be identical in all directions. When we have equal strengths in uniaxial tension and compression, the failure surfaces must be symmetric with respect to the planes $(\sigma_p + \sigma_q)$ and $(\sigma_p - \sigma_q)$, where p and q are the principal directions of stress.

With unidirectional or bi-directional fibre-reinforced laminae, the tensile strengths in the two directions of orthotropy are not normally the same. Furthermore, the compressive strengths in these directions are not necessarily equal. This rules out the possibility of symmetry with respect to the plane $\sigma_1 = \sigma_2$ or the planes $\sigma_1 = 0$ and $\sigma_2 = 0$. This becomes obvious when one considers pure shear loadings on a lamina with material axes oriented at $\theta = 45°$ or $\theta = -45°$ with respect to the applied loads. For such loadings the shear strengths will generally differ. Similarly, by considering equal biaxial tension or compression, where the corresponding strengths P and P' generally differ, we see that no inherent symmetry with respect to the plane $(\sigma_1 - \sigma_2)$ is possible. For a material transversely isotropic with respect to the 1-direction, all the usual symmetries for isotropic materials no longer exist. This leads to the conclusion that there are no inherent symmetries of the failure envelope relative to the σ_1 and σ_2 planes.

An orthotropic lamina under pure shear with respect to its principal directions must have the same strength whether the shear is positive or negative. Also, such a lamina with material axes oriented at an angle $+\theta$ or $-\theta$ with respect to an applied shear stress will exhibit the same ultimate strength. That is, identical failure stresses are found with respect to the material axes, except for the sign of the shear stress. This implies that the failure surface must be symmetrical with respect to the plane $\tau_{12} = 0$. This is the only symmetry inherent to such materials, and it must be reflected in any proposed failure equation.

It is generally desirable that the parameters of a failure criterion be expressed in terms of easily measurable strength characteristics, such as tensile strengths X, Y (along the material axes); compressive strengths X', Y'; shear strength S ; and equal biaxial tensile and compressive strengths P and P'. Of all these values, the tensile strengths X, Y along the material directions are the easiest to measure experimentally. For that reason, most existing failure criteria are expressed in terms of the strengths X, Y, X', Y', and S . However, it should be pointed out that this is not an absolute requirement, and it may sometimes be more convenient to use other strength characteristics.

The number of complete experimental failure envelopes published in the literature is rather limited. However, from the results published by Wu (4) for graphite-epoxy, or by Suhling et al. (7) for paperboard, one might be led to assume as a first approximation that projections of the failure envelopes in the $\sigma_1 - \sigma_2$ plane maintain the same overall shape for different levels of constant shear stress τ_{12} . This observation could be retained as an hypothesis for some materials and eventually be integrated in the failure criterion. Although it has never been explicitly specified in the development of existing failure criteria, this characteristic is implicit in all existing quadratic failure criteria.

In summary, any plane stress failure criterion for orthotropic laminae can be written in terms of the stress components σ_1 , σ_2 and τ_{12} with respect to the axes (1-2) of orthotropy. It should not include in general any inherent symmetry except for symmetry of the failure surface about the plane $\tau_{12} = 0$. The parameters of the criterion could be calculated from any combination of experiments, and not necessarily from uniaxial or compressive tests in the material directions. Finally, if the shapes of the projections of the failure envelope in the $\sigma_1 - \sigma_2$ plane at different levels of constant shear stress τ_{12} are similar, this observation should be incorporated in the proposed failure theory.

3. BUDIANSKY'S YIELD CRITERION FOR PLANE-ISOTROPIC SHEET MATERIALS

Historically, the formulation of failure theories for composite materials has closely paralleled the development of yield criteria for the plastic response of ductile metals. Although these phenomena are clearly unrelated, it has been observed that failure surfaces for fibre-reinforced materials often bear close resemblances to the surfaces which describe the plastic yielding of anisotropic metals. Accordingly, most of the existing failure theories for composite materials have originated from previously proposed models of ductile plastic flow. Hill's (8) yield criterion for anisotropic metals, for example, was one of the

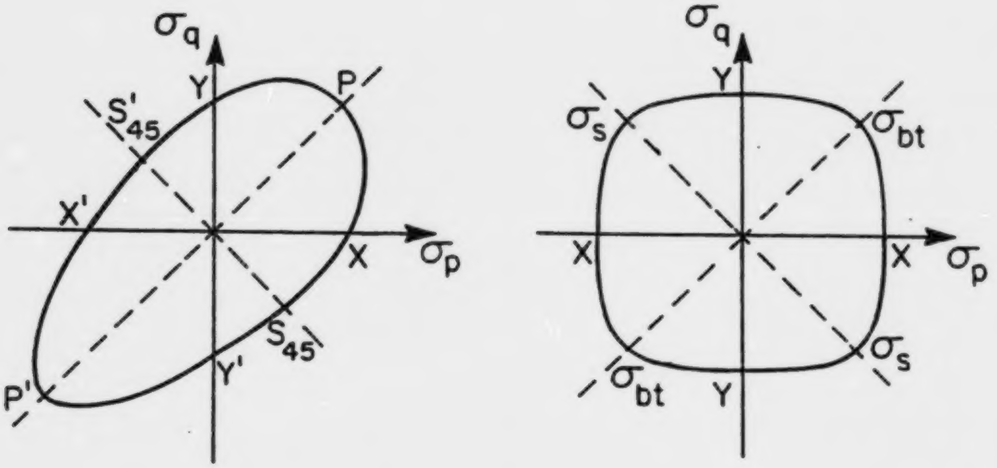
σq
Y
P
S'45
X'
X
σp
S45
Y'
P'
σq
Y
σs
σbt
X
X
σp
σs
σbt
Y

Fig. 1 Isotropic failure criteria.

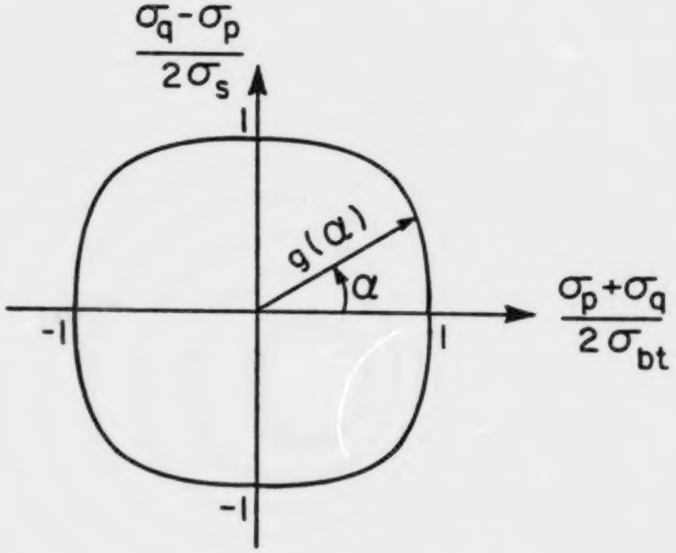
(σq-σp)/2σs
1
g(α)
α
(σp+σq)/2σbt
-1
1
-1

Fig. 2 Budiansky's failure criterion

first plasticity theories to be adopted as a failure criterion for composites. Here, recent advances in sheet metal plasticity will serve as a basis for the formulation of general failure criteria for fibre-reinforced composite laminae. Our approach is inspired by a recent contribution of Budiansky (1), which we shall first briefly review.

In the area of sheet metal forming, the effects of anisotropy are often important. Some sheets are transversely isotropic, with their plane of isotropy in the plane of the sheet metal. Moreover, these elements are limited to plane stress conditions. This has motivated the development of various yield criteria especially applicable to these materials and loading conditions. Hill's yield criterion, originally written for anisotropic materials, is often used by reducing the appropriate parameters to the transversely isotropic case. Another criteria subsequently proposed by Hill (9) has also been employed. More recently, a general yield criterion for transversely-isotropic sheet metals under in-plane loads was introduced by Budiansky (1). Budiansky shows that all previously proposed criteria for such materials are special cases of his generalized yield function.

Assuming the sheet metal to be isotropic in its plane and submitted only to in-plane stresses, Budiansky's formulation can, in all generality, be written in terms of the two principal stresses in the plane σ_p and σ_q. A general yield locus in the stress space $\sigma_p - \sigma_q$ is shown in Figure 1. This yield function must be symmetric with respect to the axis P - P' oriented at 45° with the axis σ_p. The particular case of equal strengths in tension and in compression causes further symmetry of the failure envelope with respect to an axis oriented at -45° ($S_{45} - S'_{45}$) with respect to σ_p. The 45° and -45° axes of symmetry intercept the failure surface at the points of yield under biaxial stress σ_b and under pure shear σ_S, respectively. This allowed Budiansky to postulate that any failure condition can be described parametrically in the following polar coordinate form:

$$x \equiv \frac{\sigma_p + \sigma_q}{2\,\sigma_b} = g(\beta)\cos\beta$$

$$y \equiv \frac{\sigma_p + s_q}{2\,\sigma_S} = g(\beta)\sin\beta \qquad (1)$$

This yield locus is shown schematically in Figure 2.

In Equations (1), the failure criterion $g = g(\beta)$ is a function of the angle β. Budiansky showed that all yield criteria previously proposed for isotropic materials are special cases of Equation (1). Moreover, this new parametric form can accomodate any shape of failure envelope, making it theoretically possible to describe given experimental data with any desired degree of accuracy. For example, an experimental yield locus could conceivably be fitted with suitable expressions of the form

$$g(\beta) = \sum^{n} a_n \cos(2n\beta) \qquad (2)$$

where the a_n are constants. With such a representation, a sufficient number of terms could be included to achieve an accurate curve fit. Alternatively, different portions of the failure envelope could be fitted with different types of equations.

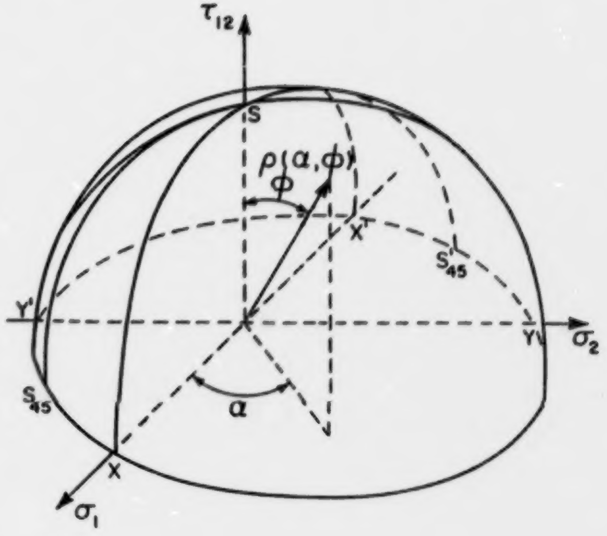
τ_{12}
S
$\rho(\alpha,\phi)$
ϕ
X'
S_{45}
Y'
Y
σ_2
S_{45}
α
X
σ_1

Fig. 3 Parametric failure envelope for fibre-reinforced materials.

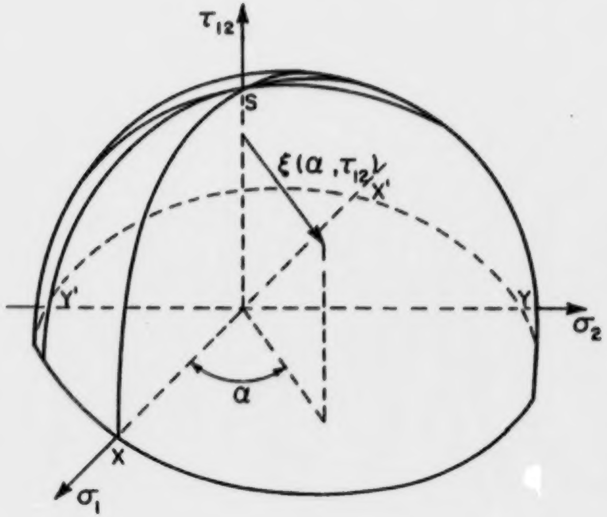
τ_{12}
S
$\xi(\alpha, \tau_{12})$
X'
Y'
Y
σ_2
α
X
σ_1

Fig. 4 Parametric failure envelope in cylindrical coordinates.

4. A GENERAL FAILURE CRITERION FOR ORTHOTROPIC LAMINAE

In the same way that Hill's yield criterion has been adapted to describe the strength characteristics of fibre-reinforced materials, we shall extend Budiansky's yield criterion and formulate an analogous failure theory for orthotropic laminae. As established previously, the failure envelope must satisfy the following conditions: it must first be a closed surface in the three-dimensional stress space $\sigma_1 - \sigma_2 - \tau_{12}$, and secondly, be symmetrical with respect to the plane $\tau_{12} = 0$. A general failure surface satisfying these conditions is depicted in Figure 3. Only the upper half is shown since a mirror image gives the form of the failure envelope for negative values of τ_{12}.

The position of any point on this failure surface can be identified in the spherical coordinate system as follows:

$$\begin{aligned} \sigma_1 &= \rho(\alpha,\phi) \cos \alpha \sin \phi \\ \sigma_2 &= \rho(\alpha,\phi) \sin \alpha \sin \phi \\ \tau_{12} &= \rho(\alpha,\phi) \cos \phi \end{aligned} \qquad (3)$$

Here $\rho(\alpha,\phi)$ is the magnitude of the radius vector from the origin of the system of axes to the failure point for a given stress combination, the angle α locates the relative position of this vector with respect to the axes σ_1 and σ_2, and ϕ indicates its angular position relative to the τ_{12}-axis. These parameters can be defined separately as functions of the stress values σ_1, σ_2 and τ_{12} at failure. The value of angle α is given by

$$\alpha = \text{arc tan} \left(\frac{\sigma_2}{\sigma_1}\right) \qquad (0 < \alpha < 2\pi) \qquad (4)$$

The angular position of the failure point from the τ_{12}-axis is given by

$$\phi = \cos^{-1}\left[1 + \frac{\sigma_1^2 + \sigma_2^2}{\tau_{12}^2}\right]^{-\frac{1}{2}} \quad (0 < \phi < \pi) \tag{5}$$

Since the angles α and ϕ are sufficient to identify the position of any stress vector $(\sigma_1, \sigma_2, \tau_{12})$, the modulus of that vector is a function of α and ϕ, i.e., $\rho = \rho(\alpha,\phi)$. Its length from the origin to the failure point is

$$\rho(\alpha,\phi) = (\sigma_1^2 + \sigma_2^2 + \tau_{12}^2)^{\frac{1}{2}} \tag{6}$$

This value must be positive for any angle α and ϕ. Geometric consistency and symmetry with respect to the plane $\tau_{12} = 0$ also requires that the following equalities be satisfied for all points:

$$\begin{aligned} \rho(\alpha,\phi) &= \rho(\alpha + 180^\circ, -\phi) \\ \rho(\alpha,\phi) &= \rho(\alpha, \ 180^\circ \ -\phi) \end{aligned} \tag{7}$$

Equations (3) are a natural extension of Budiansky's yield function and can be considered as general failure equations for orthotropic laminae in plane stress. This new parametric failure criterion given by $\rho = \rho(\alpha,\phi)$ is always a closed surface when appropriate functions of the angles α and ϕ are chosen. Once a function $\rho = (\alpha,\phi)$ is found to represent the failure surface, it can be used with the classical stress transformation equations to predict the failure conditions for stress combinations defined with respect to any system of reference axes.

5. GENERALITY OF THE PARAMETRIC FAILURE CRITERION

It has already been demonstrated by Wu (4) that the tensor polynomial criterion encompasses all failure criteria previously suggested for fibre-reinforced laminae. It will now be shown that the tensor polynomial criterion is itself a special case of Equations (3) when plane stress conditions are assumed. Recall that the tensor polynomial equation, in the standard reduced notation for stresses, is

$$F_i\sigma_i + F_{ij}\sigma_i\sigma_j + F_{ijk}\sigma_i\sigma_j\sigma_k + \ldots = 1 \qquad (8)$$

where the F_i, F_{ij}, etc. are strength constants.

Substituting in Equation (8) the values σ_1 and σ_2 and τ_{12} ($= \sigma_6$) from Equation (3), we find that

$$\sum_{k=1}^{n} \rho^k(\alpha,\phi)\, f_k(\alpha,\phi) = 1 \qquad (9)$$

where n is the degree of the tensor polynomial expression. The coefficients F_i, F_{ij}, etc. are incorporated implicitly in the various functions $f_k(\alpha,\phi)$. To clarify this, consider the quadratic tensor polynomial, or Tsai-Wu criterion, written as follows:

$$F_1\sigma_1 + F_2\sigma_2 + F_{11}\sigma_1^2 + F_{22}\sigma_2^2 + F_{66}\tau_{12}^2 + 2F_{12}\sigma_1\sigma_2 = 1 \qquad (10)$$

Substituting Equations (3) in the above expression gives

$$\rho(\alpha,\phi)\, f_1(\alpha,\phi) + \rho^2(\alpha,\phi)\, f_2(\alpha,\phi) = 1 \qquad (11)$$

where

$$f_1(\alpha,\phi) = F_1 \cos\alpha \sin\phi + F_2 \sin\alpha \sin\phi$$

$$f_2(\alpha,\phi) = F_{11} \cos^2\alpha \sin^2\phi + F_{22} \sin^2\alpha \sin^2\phi$$

$$+ F_{66} \cos^2\phi + 2F_{12} \cos\alpha \sin\alpha \sin^2\phi$$

In this case, the failure function is given by the positive root of

$$\rho(\alpha,\phi) = \frac{-f_1(\alpha,\phi) \pm [f_1^2(\alpha,\phi) + 4 f_2(\alpha,\phi)]^{\frac{1}{2}}}{2 f_2(\alpha,\phi)} \tag{12}$$

In the same way, the cubic tensor polynomial used by Tennyson et al. (6) can be written as

$$\rho(\alpha,\phi)\, f_1(\alpha,\phi) + \rho^2(\alpha,\phi)\, f_2(\alpha,\phi) + \rho^3(\alpha,\phi)\, f_3(\alpha,\phi) = 1 \tag{13}$$

where $f_1(\alpha,\phi)$ and $f_2(\alpha,\phi)$ are the same as above, and

$$\begin{aligned} f_3(\alpha,\phi) = {} & 3F_{112} \cos^2\alpha \sin\alpha \sin^3\phi + 3F_{221} \sin^2\alpha \cos\alpha \sin^3\phi \\ & + 3F_{166} \cos\alpha \sin\phi \cos^2\phi + 3F_{266} \sin\alpha \sin\phi \cos^2\phi \end{aligned} \tag{14}$$

In principle, it is possible to express any degree of the tensor polynomial expression in the parametric form $\rho(\alpha,\phi)$. For the two above examples, the functions $\rho = \rho(\alpha,\phi)$ are more complicated to write than the original tensor polynomial equations. For polynomials of degree higher than the quadratic tensor polynomial, the expression $\rho = \rho(\alpha,\phi)$ may be unwieldly and unlikely to be obtainable in explicit form. Nevertheless, these examples do demonstrate the generality of the parametric function $\rho = \rho(\alpha,\phi)$ and show the equivalence of the parametric and tensor polynomial approaches. It can be easily shown that Budiansky's representation (1) is a special case of the parametric form (3).

A single parametric strength equation valid for all fibre-reinforced laminae has not yet been developed and, as a result, a particular failure equation must be invented for each material. This is a disadvantage in comparison with Hill-type and tensor polynomial theories in which the strength parameters are defined directly from specific experimental results such as uniaxial strengths in the axes of symmetry.

However, with the above existing theories the failure envelopes have the same overall shape. For instance, all quadratic tensor polynomials are ellipsoids. It is perhaps unrealistic to expect that a single equation can be found to represent all possible failure envelopes for a wide variety of fibre-reinforced laminae. Such an equation would certainly be useful, and it is to a certain extent an interesting feature of the tensor polynomial theory. Although this aspect has not been investigated in detail here, there is reason to believe that such a general equation, should it indeed exist, might be easier to obtain in parametric form than with a tensorial equation. The reason for this conjecture is that any parametric equation can be constructed from a series of closed trigonometric functions. This technique is more likely to generate more universally applicable general failure surfaces than the higher-degree tensor polynomials, which do not necessarily describe closed surfaces.

As an example of a general parametric form consider the following series representation:

$$\rho(\alpha,\phi) = \sum_m \sum_n B_{mn}[\sin (2n - 1)\alpha]\,[1 + \sin (2m - 1)\phi] \qquad (15)$$

This form satisfies all of the requirements specified previously for orthotropic laminae. This trigonometric function can theoretically describe any failure surface which is symmetric about the plane $\rho(\alpha,90°)$ or $\tau_{12} = 0$. However, a large number of terms may sometimes be required to describe the real failure surface in question. Other functions requiring less terms may be written. These questions should be more closely scrutinized in future attempts to improve the usefulness of the parametric approach for the description of failure surfaces.

6. ALTERNATIVE FORMS OF THE PARAMETRIC FAILURE CRITERION

The parametric failure criterion presented in the previous section was written directly in stress space using spherical coordinates. However, depending on the available experimental data, it may be more convenient to use other representations or coordinate systems. For example, it might be preferable to represent the failure envelope in a non-dimensional form, for example, in the system of axes $\sigma_1/X - \sigma_2/Y - \tau_{12}/S$, as follows:

$$\begin{aligned} \sigma_1/X &= \rho'(\alpha',\phi') \cos \alpha' \sin \phi' \\ \sigma_2/Y &= \rho'(\alpha',\phi') \sin \alpha' \sin \phi' \\ \tau_{12}/S &= \rho'(\alpha',\phi') \cos \phi' \end{aligned} \tag{16}$$

The parameters α', ϕ', and $\rho'(\alpha',\phi')$ are similar to α, ϕ, and $\rho(\alpha,\phi)$ in the total stress space.

Some authors have published experimental failure surfaces by giving their projections in the $\sigma_1 - \sigma_2$ plane for different values of the shear stress τ_{12} (e.g. Rowlands et al. (5)). Often the overall shapes of these projections are similar for the different values of τ_{12}. In such cases, it is more convenient to write the failure criterion in terms of cylindrical, rather than spherical, coordinates. This is illustrated in Figure 4, where the failure envelope is described parametrically in cylindrical coordinates as

$$\begin{aligned} \sigma_1 &= \xi(\alpha,\tau_{12}) \cos \alpha \\ \sigma_2 &= \xi(\alpha,\tau_{12}) \sin \alpha \end{aligned} \tag{17}$$

For the case of similar $\sigma_1 - \sigma_2$ projections for various levels of τ_{12}, we can write

$$\begin{aligned} \sigma_1 &= \psi(\alpha) \cos \alpha \, \Gamma(\tau_{12}) \\ \sigma_2 &= \psi(\alpha) \sin \alpha \, \Gamma(\tau_{12}) \end{aligned} \tag{18}$$

In Equation (17), the parameter $\xi(\alpha,\tau_{12})$ is the magnitude of the vector going from the τ_{12}-axis to the failure point, in the plane of the shear stress τ_{12}. The angle α still indicates the orientation with respect to the σ_1-axis. In terms of the stresses σ_1 and σ_2, the parameters α and $\xi(\alpha,\tau_{12})$ are

$$\begin{aligned} \alpha &= \tan^{-1} (\sigma_2/\sigma_1) \qquad (0 < \alpha < 2\pi) \\ \xi(\alpha,\tau_{12}) &= [\sigma_1^2 + \sigma_2^2]^{\frac{1}{2}} \end{aligned} \tag{19}$$

The function $\xi(\alpha,\tau_{12})$ or, alternatively $\psi(\alpha)$ and $\Gamma(\tau_{12})$, have to be determined to provide the best possible representation of the available experimental data.

All spherical and cylindrical coordinate expressions above are equivalent representations of the same failure surface and they are consequently related to each other mathematically. In the next section, we shall illustrate how these expressions can be used to describe experimental data.

7. EXAMPLES OF APPLICATION OF THE PARAMETRIC FAILURE CRITERION

The validity of a proposed strength criterion can only be judged from the point of view of its ability to accurately predict material failure under any loading condition. With a parametric criterion of the form $\rho = \rho(\alpha,\phi)$, many functions of the angles α and ϕ can be written, and the one providing the best correlation has to be selected. In this section, a best-fit technique which minimizes the error between

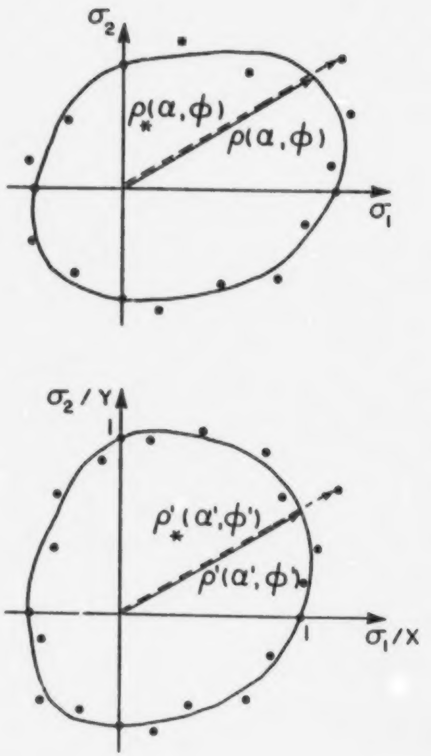

Fig. 5 Experimental theoretical correlation.

TABLE 1 - Biaxial Strength Data for Graphite-Epoxy Fabric (10)

(all units: 10^3 psi)

σ_1	σ_2	τ_{12}	σ_1	σ_2	τ_{12}	σ_1	σ_2	τ_{12}
70.6	0.0	0.0	-73.3	0.0	0.0	29.1	58.1	0.0
66.4	0.0	0.0	0.0	-51.4	0.0	0.0	43.1	16.8
59.0	0.0	0.0	0.0	-82.3	0.0	35.1	0.0	17.5
65.0	0.0	0.0	0.0	-57.3	0.0	33.6	0.0	18.4
66.9	0.0	0.0	0.0	-68.1	0.0	45.6	46.9	15.4
66.6	0.0	0.0	0.0	-76.3	0.0	45.8	47.0	15.5
0.0	69.7	0.0	0.0	0.0	17.5	27.2	73.2	6.1
0.0	71.7	0.0	0.0	0.0	16.6	29.6	59.3	0.0
0.0	71.8	0.0	0.0	0.0	17.1	29.5	59.0	0.0
0.0	65.4	0.0	0.0	0.0	17.5	27.9	55.8	0.0
0.0	71.5	0.0	0.0	0.0	-17.6	58.8	29.4	0.0
0.0	70.0	0.0	0.0	0.0	-17.6	57.5	28.8	0.0
-65.3	0.0	0.0	0.0	0.0	-17.2	45.4	46.6	15.3
-42.5	0.0	0.0	0.0	0.0	-16.7	-26.8	57.5	0.0
-58.5	0.0	0.0	57.3	28.6	0.0	-	-	-
-67.5	0.0	0.0	58.2	29.1	0.0	-	-	-

$X = 65.8 \times 10^3$ psi
$X' = 66.2 \times 10^3$ psi
$Y = 70.0 \times 10^3$ psi
$Y' = 67.1 \times 10^3$ psi
$S = 17.2 \times 10^3$ psi

experimental data and the criterion is employed. The method is illustrated in Figure 5 where, as a matter of convenience, only the plane $\tau_{12} = 0$ is shown. For a lamina loaded proportionally from the origin to the failure point, the total error between the experimental data and the parametric curve is defined as

$$E_t = \sum_{n=1}^{N} \left(\rho_{*n}(\alpha,\phi) - \rho_n(\alpha,\phi)\right)^2 \qquad \text{in real stress space}$$

$$E_t = \sum_{n=1}^{N} \left(\rho'_{*n}(\alpha',\phi') - \rho'_n(\alpha',\phi')\right)^2 \qquad \text{in normalized stress space} \tag{20}$$

where N is the total number of experimental points, $\rho_n(\alpha,\phi)$ or $\rho'_n(\alpha',\phi')$ is the predicted failure strength for the n^{th} loading path as calculated from the proposed criterion, and $\rho_{*n}(\alpha,\phi)$ or $\rho'_{*n}(\alpha',\phi')$ is the radial distance from the origin of the system of axes to the n^{th} failure point.

To illustrate the parametric approach advocated here, we shall examine the experimental data reported by Tennyson and Wharram (10) for an orthotropic graphite-epoxy composite. The lamina is identified as a NARMCO Rigidite 5208-WT300, a plain weave fabric (over 1, under 1) of UCC Thornel 300 graphite fibres impregnated with Narmco 5208 epoxy resin. Tension and compression tests were performed on flat coupons, while torsion and other biaxial tests were performed on tubular specimens. The experimentally-determined failure data are listed in Table 1, which also contains the measured strengths in simple tension, compression, and shear in the principal material directions. These results show very good consistency for all loading paths, except for a small amount of scatter for the uniaxial compressive strengths.

TABLE 2 - Normalized Strength Data for Graphite-Epoxy Fabric

σ_1/X	σ_2/Y	τ_{12}/S	α' (°)	ϕ' (°)	$\rho'(\alpha',\phi')$
1.073	0.0	0.0	0.0	90.0	1.073
1.009	0.0	0.0	0.0	90.0	1.009
0.897	0.0	0.0	0.0	90.0	0.897
0.988	0.0	0.0	0.0	90.0	0.988
1.017	0.0	0.0	0.0	90.0	1.017
1.012	0.0	0.0	0.0	90.0	1.012
0.0	0.996	0.0	90.0	90.0	0.996
0.0	1.024	0.0	90.0	90.0	1.024
0.0	1.026	0.0	90.0	90.0	1.026
0.0	0.934	0.0	90.0	90.0	0.934
0.0	1.021	0.0	90.0	90.0	1.021
0.0	1.000	0.0	90.0	90.0	1.000
-0.992	0.0	0.0	0.0	-90.0	0.992
-0.646	0.0	0.0	0.0	-90.0	0.646
-0.889	0.0	0.0	0.0	-90.0	0.889
-1.026	0.0	0.0	0.0	-90.0	1.026
-1.114	0.0	0.0	0.0	-90.0	1.114
0.0	-0.734	0.0	90.0	-90.0	0.734
0.0	-1.176	0.0	90.0	-90.0	1.176
0.0	-0.819	0.0	90.0	-90.0	0.819
0.0	-0.973	0.0	90.0	-90.0	0.973
0.0	-1.090	0.0	90.0	-90.0	1.090
0.0	0.0	1.017	all	0.0	1.017
0.0	0.0	0.965	all	0.0	0.965
0.0	0.0	0.994	all	0.0	0.994
0.0	0.0	1.017	all	0.0	1.017
0.0	0.0	-1.023	all	0.0	1.023
0.0	0.0	-1.023	all	0.0	1.023
0.0	0.0	-1.000	all	0.0	1.000
0.0	0.0	-0.971	all	0.0	0.971

TABLE 2 - Normalized Strength Data for Graphite-Epoxy Fabric (cont'd)

σ_1/X	σ_2/Y	τ_{12}/S	α' (°)	ϕ' (°)	$\rho'(\alpha',\phi')$
0.871	0.409	0.0	25.154	90.0	0.962
0.884	0.416	0.0	25.201	90.0	0.977
0.442	0.830	0.0	61.963	90.0	0.940
0.0	0.616	0.977	90.0	32.231	1.155
0.533	0.0	1.017	0.0	27.659	1.148
0.511	0.0	1.070	0.0	25.528	1.186
0.693	0.670	0.895	44.033	47.123	1.315
0.696	0.671	0.901	43.952	47.017	1.322
0.413	1.046	0.355	68.454	72.481	1.179
0.450	0.847	0.0	62.019	90.0	0.959
0.448	0.843	0.0	62.012	90.0	0.955
0.424	0.797	0.0	61.987	90.0	0.903
0.984	0.420	0.0	25.164	90.0	0.988
0.874	0.411	0.0	25.185	90.0	0.966
0.690	0.666	0.890	43.986	47.137	1.308
-0.407	0.821	0.0	116.369	90.0	0.916

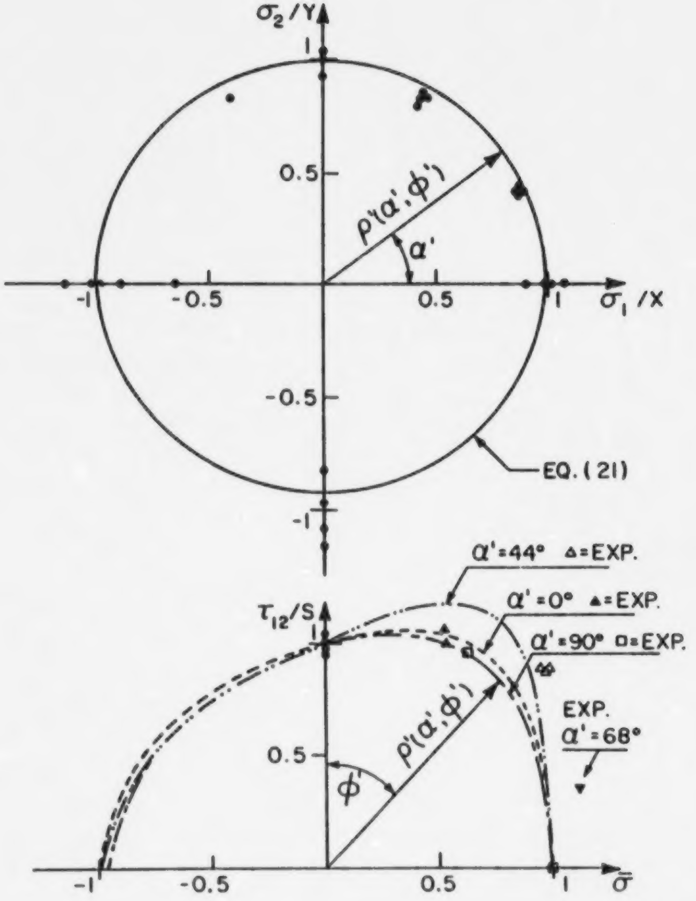

Fig. 6 Biaxial stresses in graphite epoxy fabric.

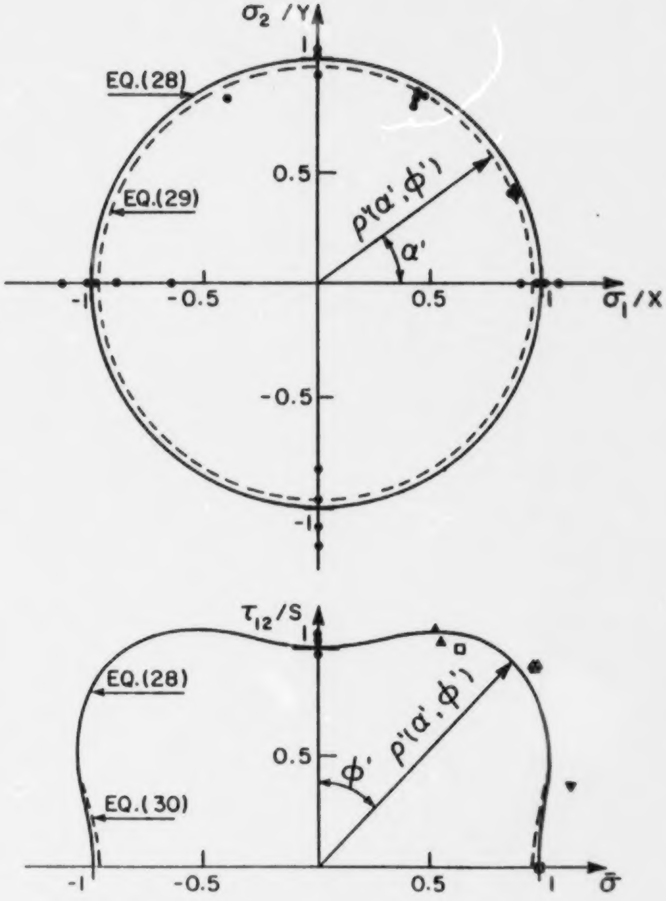

Fig. 7 First parametric solution.

It can be observed that the strengths in tension and compression in the two material axes of symmetry are almost identical. This suggests the use of the parametric failure criterion in the normalized space σ_1/X - σ_2/Y - τ_{12}/S. The experimental results used here, as expressed in this normalized system of axes, are listed in Table 2. Also given in this table are the angles α' and ϕ', and the radial distance $\rho'(\alpha',\phi')$ from the origin of the system of axes to the measured failure point.

The failure equation proposed by Tennyson and Wharram for this material was the cubic tensor polynomial. In the plane $\tau_{12} = 0$, the quadratic form was found to be the best representation and the constants F_{12}, F_{122}, F_{112} were set equal to zero. The values of the remaining constants F_{166} and F_{266} were determined from the failure data for tubular specimens submitted to internal pressure. The failure equation obtained was

$$\begin{aligned} &9.183\times10^{-8}\sigma_1 - 6.174\times10^{-7}\sigma_2 + 2.296\times10^{-10}\sigma_1^{\,2} \\ &+ 2.129\times10^{-10}\sigma_2^{\,2} + 3.380\times10^{-9}\tau_{12}^{\,2} + 3(-1.097\times10^{-14})\,\sigma_1\tau_{12}^{\,2} \\ &+ 3(-8.845\times10^{-15})\,\sigma_2\tau_{12}^{\,2} = 1 \end{aligned} \tag{21}$$

This equation is an ellipse in any plane τ_{12} = constant. The location of the ellipse's centre varies with the level of shear stress τ_{12}, but all these ellipses have their principal axes in the directions of σ_1 and σ_2 since there are no interaction terms involving the product $\sigma_1\sigma_2$.

The normalized data of Table 2 and the failure equation (21) are shown in Figure 6, in the plane $\tau_{12}/S = 0$. Here the failure surface is circular but is slightly off centre from the origin. Slices of the failure envelope at various angles α' are also shown in the plane τ_{12}/S - $\bar{\sigma}$ where

$$\bar{\sigma} = [(\frac{\sigma_1}{X})^2 + (\frac{\sigma_2}{Y})^2]^{\frac{1}{2}}$$

The failure equation (21) slightly overestimates the lamina strength in the plane $\tau_{12} = 0$ and underestimates it everywhere else. However, it gives a fairly accurate representation of the experimental results for most points. The main difficulty encountered with Equation (21) is the determination of the theoretical strength value for a given ratio of the stresses σ_1- σ_2- τ_{12}, which must be found solving for the roots of the cubic equation. This process could be simplified by using a parametric failure equation.

We shall now attempt to write the failure equation for this material in the form

$$\xi'(\alpha',\tau_{12}/S) = \psi'(\alpha')\ \Gamma'(\tau_{12}/S) \qquad (22)$$

This form uses cylindrical coordinates in the normalized stress space, and indicates that the shape of the failure surface will remain centred about the origin in all the planes τ_{12}/S , with its size controlled by the function $\Gamma' = \Gamma'(\tau_{12}/S)$. In the plane $\tau_{12}/S = 0$, the following equality must be satisfied

$$\Gamma'(\tau_{12}/S) = \Gamma'(0) = 1 \qquad (23)$$

Since the failure strengths in tension and compression in the material directions all appear to be identical, a possible function $\psi'(\alpha')$ can be taken as

$$\psi'(\alpha') = 1.0 \qquad (24)$$

This is a circle in the plane $\tau_{12}/S = 0$ and it provides an accurate description of the experimental data in this plane. Above this plane,

TABLE 3 - Average Data for $\tau_{12} \neq 0$

$\rho'_*(\alpha',\phi')$	α' (°)	ϕ' (°)	ρ'_{avg}	α'_{avg}	$k(\alpha')$	$k_{avg}(\alpha')$
1.148	0	27.659	1.167	0	0.360	0.419
1.186	0	25.528			0.478	
1.322	43.952	47.017			0.646	
1.308	43.986	47.137	1.315	44	0.618	0.632
1.315	44.033	47.123			0.632	
1.179	68.454	72.481	1.179	68.45	0.624	0.624
1.155	0	32.231	1.155	90	0.344	0.344

the function $\Gamma' = \Gamma'(\tau_{12}/S)$ will control the area of this circle in different planes to reproduce as accurately as possible the failure data listed in Table 3. Therefore, at any level of shear stress τ_{12}, it is assumed that the failure function is a circle centered on the τ_{12} axis which can then be written as

$$\Gamma'(\tau_{12}/S) = \xi'(\alpha',\tau_{12}/S)/\psi'(\alpha') = \text{constant} \qquad (25)$$

With $\Gamma = \Gamma'(\tau_{12}/S)$ constant for a constant shear τ_{12}, the following equality can be substituted in Equation (22)

$$\Gamma'(\tau_{12}/S) = \Gamma'(\phi') \qquad (26)$$

In Figure 6 we see that for any value of α' and ϕ' that does not lie on the plane $\tau_{12}/S = 0$ or on the axis τ_{12}, the experimental radius $\rho_*'(\alpha',\phi')$ is always greater than unity. For that reason, the following function $\Gamma' = \Gamma'(\phi')$ is suggested

$$\Gamma'(\phi') = 1 + G(\sin\phi' \cos\phi')^2 \qquad (27)$$

It satisfies the conditions $\Gamma'(0°) = \Gamma'(90°) = 1$ and $G > 0$ is a parameter to be determined. Minimizing the error obtained with Equation (21), the best value of the constant G, for the available data, is $G = 1.17$. The failure equation is then

$$\rho'(\alpha',\phi') = 1 + 1.17\,(\cos\phi' \sin\phi')^2 \qquad (28)$$

This is shown in Figure 7 and compared with experimental data. In the plane $\tau_{12}/S = 0$, the failure surface still overestimates slightly the strength at most of the points, except on the axes. Above that plane, Equation (28) produces a "crown-shaped" failure surface that is identical for any plane at an angle α'. It can be observed that this shape tends to follow more closely the experimental results above the plane

$\tau_{12} = 0$. Since no data are available for negative values of ϕ', the comparisons between the tensor polynomial criterion and the parametric form Equation (28) in this region cannot really be made.

Since many points are available on $\tau_{12}/S = 0$ and since they seem to define a circular area, a slight improvement of the theoretical-experimental correlation could be obtained here by taking the function $\psi'(\alpha')$ as

$$\psi'(\alpha') = 0.96845 \tag{29}$$

This is the average radius from the origin of the system of axes to the experimental failure points on this plane. Accordingly, the entire strength surface can be rewritten as follows:

$$\rho'(\alpha',\phi') = 1.00125 \cos^2\phi' + 0.96845 \sin^2\phi' + G \sin^2\phi' \cos^2\phi' \tag{30}$$

where now a value G =1.24 is found to minimize the error with the experimental data. This equation is also reproduced in Figure 7. A significant improvement over Equation (28) has been obtained in the plane $\tau_{12}/S = 0$, but the error has slightly increased for the points above this plane.

In the previous solution, it was assumed that the failure envelope would be circular in each plane τ_{12}/S = constant, and centred on the τ_{12}/S-axis. It was thus easier to write a failure equation in cylindrical coordinates. The resulting failure envelope differed considerably from the one obtained with the cubic tensor polynomial theory. In both cases, the available experimental data are described equally as well, although the portions of the failure surface where no experimental points were measured are represented differ considerably. To demonstrate the flexibility of the parametric approach, an alternate failure envelope will now be written for the same experimental data.

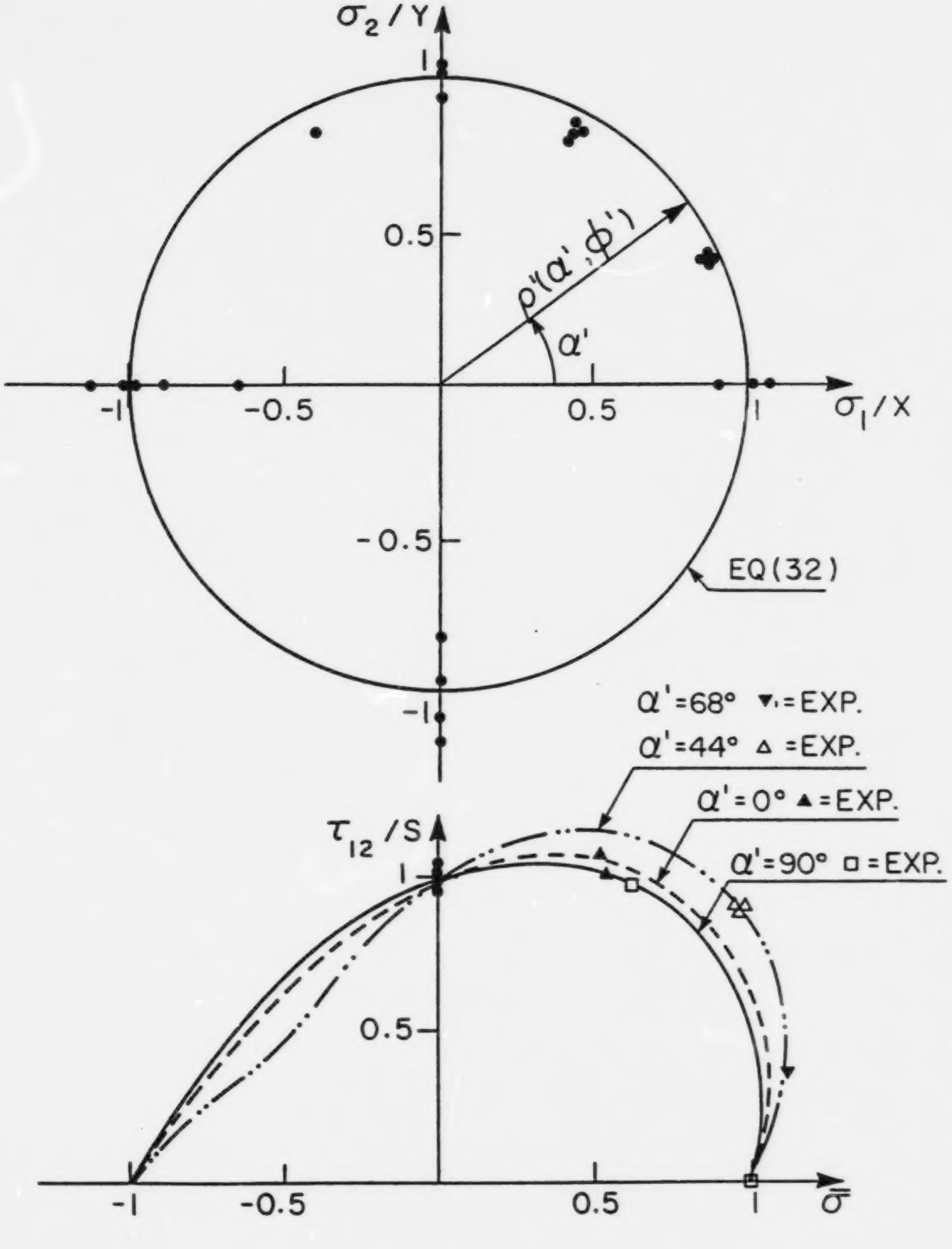

Fig. 8 Second parametric solution.

Let it now be assumed that the failure equation has the form given by Equation (16) in spherical coordinates. As for the previous solution, the normalized system of axes will be used. Also, the following equalities must be satisfied:

$$\rho'(\alpha',90^\circ) = 1$$
$$\rho'(\alpha', 0^\circ) = 1 \qquad (31)$$

For any value of α' and ϕ' outside the plane $\tau_{12}/S = 0$, or on the axis τ_{12}/S, the experimental radius $\rho'_*(\alpha',\phi')$ is always greater than unity. The following function $\rho'(\alpha',\phi')$ is advanced

$$\rho'(\alpha',\phi') = 1 + k(\alpha') \sin\phi' \left|\cos\phi'\right| \qquad (32)$$

which satisfies the conditions (31). This equation differs from (28) as it is no longer symmetrical with respect to the angle ϕ'. The absolute value of $\cos\phi'$ ensures symmetry of the failure envelope with respect to the plane $\tau_{12}/S = 0$ but will introduce discontinuity in the slope of the failure surface at the midplane.

The experimental data to be used with Equation (32) are summarized in Table 3. All data fall on the planes $\alpha' = 0^\circ$, $\alpha' = 44^\circ$, $\alpha' = 68^\circ$, $\alpha' = 90^\circ$. The value of the function $k(\alpha')$ to fit each point is also given in this table. The experimental values of the function $k(\alpha')$, which consist of the averages of the four points on each α'-plane listed in Table 2, are shown in Figure 8.

A function $k = k(\alpha')$ now has to be written. If a single equation is written for the entire surface, it has to satisfy the conditions (7). In view of Equation (32), this leads to the following restraint

$$k(\alpha') = - k(\alpha' + 180^\circ) \qquad (33)$$

Accordingly, a function can be written as a series of sines and cosines, such as

$$k(\alpha') = \sum_m b_m \sin^{2m-1}\alpha' + \sum_n a_n \cos^{2n-1}\alpha' + \sum_s c_s \sin^p\alpha' \cos^q\alpha' \qquad (34)$$

where the sum of $p+q$ must be an odd integer. Since four points must be fitted, four terms of this equation must be retained. A first solution can be obtained with

$$k(\alpha') \equiv k_1(\alpha') = a_1 \cos\alpha' + b_1 \sin\alpha' + a_2 \cos\alpha'^2 + c_1 \cos\alpha' \sin^2\alpha' \qquad (35)$$

Substituting the average values from Table 2 gives

$$k(\alpha') = 0.419 \cos\alpha' + 0.344 \sin\alpha' - 0.322 \cos^2\alpha' + 0.598 \cos\alpha' \sin^2\alpha' \qquad (36)$$

Alternatively, the function $k = k(\alpha')$ could be given by

$$k(\alpha') \equiv k_2(\alpha') = a_1 \cos\alpha' + b_1 \sin\alpha' + a_2 \cos^3\alpha' + a_3 \cos^5\alpha' \qquad (37)$$

After substitution of the experimental data we get the following function

$$k(\alpha') = k_2(\alpha') = 0.967 \cos\alpha' + 0.344 \sin\alpha' + 1.097 \cos^3\alpha' + 0.549 \cos^5\alpha' \qquad (38)$$

It is difficult to decide which of the functions $k_1(\alpha')$ or $k_2(\alpha')$ would give the best result when substituted back into (32) since both of them include the average experimental points listed in Table 2. However, since the function $k(\alpha') = k_2(\alpha')$ is more regular, it might be expected to produce better results.

A quantitative assessment of the error (20) can be measured for the parametric criteria and compared with the cubic tensor polynomial. Both criteria produce approximately the same total error, and it is difficult to claim for this example that one gives a decidedly more accurate representation than the other. More experimental data would be useful to assess their respective accuracies in portions of the failure envelope where data are missing. However, it is important to recognize that the calculation of theoretical failure values is much simpler with the parametric approach than with the cubic tensor polynomial. Moreover, for the example treated here, the cubic tensor polynomial requires seven independent parameters, whereas the parametric form (Equation (28)) uses only four parameters (X, Y, G, and G). This is definite advantage of the parametric failure criterion. Finally, in the event that experimental data were made available in other regions of the failure surface and discovered not to correspond to the proposed analytical function, one could immediately be rewritten with another more appropriate parametric function as was shown through the two different parametric solutions for the above example. In contrast with the tensor polynomial formulation new values for the strength parameters F_{ij} and F_{ijk} would be required, and this involves a relatively complicated procedure, as mentioned earlier.

8. CONCLUSION

In recent years, many failure criteria have been proposed for composite materials. Among these, the tensor polynomial theory has received the most attention. It is attractive because it encompasses every criterion proposed previously, it is a single continuous function, and the rules of transformation for tensors render it applicable in any reference system. The quadratic form of the tensor polynomial expansion is the most widely used, but it does not always provide an accurate representation of failure data for composites. The cubic expansion requires a greater number of parameters and does not always describe a closed surface. Furthermore, determining the failure stresses for a given loading path entails the sometimes cumbersome task of solving for the roots of a cubic equation.

In view of the ongoing discussions concerning the merits of the tensor polynomial theory, it seemed timely to explore a new approach for predicting failure of fibre-reinforced laminae. Ideas recently brought forward by Budiansky for predicting plastic yielding in sheet materials were adapted here to describe the strength of orthotropic laminae. It was suggested that a general parametric representation of the failure surface be explored.

The following characteristics of the parametric approach were established. First, it was shown that the tensor polynomial theory was a special case of the proposed parametric criterion, and that all existing criteria could be written in parametric form. Second, the failure surface can always be made to be closed if appropriate functions are selected, thus eliminating the need for additional conditions to ensure closure. Third, it is possible to describe failure surfaces of irregular shapes without resorting to a large number of parameters. This can be achieved through the use of higher-order equations, the use of non-integer exponents, or by fitting different portions of the failure surface with different equations. The inherent advantage of the parametric approach is its flexibility. Finally, in applying the parametric criterion it is a straightforward matter to determine the failure strength for any proportional loading path, in contrast to the involved methods usually required with the higher-order forms of the tensor polynomial theory.

A single parametric function, universally applicable to all fibre-reinforced laminae, has not yet been postulated. A new equation $\rho = \rho(\alpha,\phi)$ has to be devised for each material, depending on the available experimental data. When only the uniaxial strengths in the axes of material symmetry are known, there are no grounds for rejecting the existing theories (e.g. the quadratic tensor polynomial equation) in favour of the parametric approach because all experimental data are well reproduced with these theories. However, if additional available results cannot be reconciled with the quadratic form, the expansion of the expansion of the tensor polynomial equation to include cubic terms may not always be the best solution. A parametric approach can be a useful alternative.

Finally, the question of developing a general parametric equation for all fibre-reinforced laminae was not investigated in detail here. It was shown, however, that a series of trigonometric functions does describe all failure surfaces satisfying the conditions of Section 2. Additional investigations should be pursued in this regard.

ACKNOWLEDGEMENTS

This work was supported in part by the Natural Sciences and Engineering Research Council of Canada (NSERC) and le Gouvernement du Québec (Programme FCAR).

REFERENCES

1. B. Budiansky, "Mechanics of Material Behavior," p. 15, Elsevier Science, Amsterdam (1984).
2. Soni, R.S., J. Reinf. Plast. Comp. 1 34 (1983).
3. Tsai, S.W. and Wu, E.M., J. Comp. Mater. 5 58 (1971).
4. Wu, E.M., "Composite Materials, Vol. 2: Mechanics of Composite Materials," Academic Press, New York (1974).
5. Rowlands, R.E., Gunderson, D.E., Suhling, J.C. and Johnson, M.W., J. Strain Anal. 20 121 (1985).
6. Tennyson, R.C., MacDonald, D. and Nanayaro, A.P., J. Comp. Mater. 12 63 (1978).
7. Suhling, J.C., Rowlands, R.E., Johnson, M.W. and Gunderson, D.E., Exp. Mech. 25 75 (1985).
8. Hill, R., "The Mathematical Theory of Plasticity," p. 318, Oxford University Press, London (1950).
9. Hil, R., Math. Proc. Camb. Phil. Soc. 85 179 (1979).
10. Tennyson, R.C. and Wharram, G.E., NASA Contractor Rep. #172547 (1985).

Toughened Resin Testing of New Generation Carbon Fiber/Epoxy Systems

C. Poon, R.F. Scott and S. Lee

National Aeronautical Establishment
National Research Council of Canada
Ottawa, Ontario K1A 0R6

ABSTRACT

Four commercially available carbon fiber/prepreg systems have been processed and subjected to NASA's proposed standard tests for toughened resins (NASA Ref. Publication 1092). One prepreg system was Narmco Corporation's Rigidite T300/5208 which was included as a baseline while the other three systems employed Hercules' IM6 fiber in new generation resin systems. Descriptions of the tests, including open-hole tension and compression, compression after impact, double cantilever beam and edge delamination tension, as well as results are presented.

INTRODUCTION

The extensive application of composites in aircraft structures has brought significant benefits in weight savings. However, commonly used epoxy resin systems, such as Narmco 5208 and Hercules 3501, are brittle. This brittleness of the matrix has produced several undesirable characteristics. It is well known that conventional carbon/epoxy composites are notch sensitive; tensile strength reductions of 50% are typical for coupons containing a fastener hole (1). Test data also indicate that impact damage, even though barely visible, may degrade laminate compressive strength seriously. Matrix-dominated failure modes such as delamination and matrix cracking may occur at relatively low stress levels. These factors have caused severe limitations in design strain allowables in order to ensure safe applications of composites. For a typical untoughened resin carbon/epoxy, Narmco T300/5208, design allowable strains are 4,500 μm/m for tension and 4,000 μm/m for compression (2). Design studies (3) have predicted that weight savings as compared to an aluminium baseline for upper wing surfaces constructed with composites would increase from 26% to 38% if the design allowable strains could be increased from the current levels to 6,000 μm/m. Similar weight savings would be expected for lower wing surfaces which are typically designed by tension loading.

Within the last several years, improvements have been made in the constituents of carbon/epoxy composites. Toughened resins that demonstrate improved resistance against delamination and impact as well as high strain fibers that possess better strength

TABLE 1 – TOUGHENED RESIN CHARACTERIZATION PROGRAM

PART A: LAMINATE MECHANICAL PROPERTIES

- LONGITUDINAL TENSION TEST
- TRANSVERSE TENSION TEST
- LONGITUDINAL COMPRESSION TEST
- TRANSVERSE COMPRESSION TEST
- ±45° TENSILE IN-PLANE SHEAR TEST

PART B: HOT-WET COMPRESSIVE PROPERTIES

- COMPRESSION TEST AT 93 ± 3°C ON PRECONDITIONED SPECIMENS

PART C: TOUGHENED RESIN CHARACTERIZATION

- OPEN-HOLE TENSION TEST
- OPEN-HOLE COMPRESSION TEST
- COMPRESSION AFTER IMPACT TEST
- DOUBLE CANTILEVER BEAM TEST
- EDGE DELAMINATION TENSION TEST

TABLE 2 – UNIDIRECTIONAL LAMINA TENSILE AND IN-PLANE SHEAR PROPERTIES OF FOUR MATERIAL SYSTEMS

	Longitudinal (0°)			Transverse (90°)			±45° Shear		
Test Method	ASTM D3039-76			ASTM D3039-76			ASTM D3518-76		
Properties	At 1% Strain	Ultimate		At 1% Strain	Ultimate		At 0.5% Strain	Ultimate	
	E_1^T GPa (C.V.)	X_1^T GPa (C.V.)	ϵ_1^T %	E_2^T GPa (C.V.)	X_2^T MPa (C.V.)	ϵ_2^T %	G_{12} GPa (C.V.)	τ_{12} MPa (C.V.)	γ_{12} %
T300/5208	144.8 (2.1)	1.35 (6.9)	0.93	9.4 (2.2)	47.6 (11.3)	0.51	4.8 (4.7)	94.5 (1.5)	6.83
IM6/5245C	173.1 (1.9)	2.61 (3.7)	1.50	8.5 (8.7)	60.0 (11.0)	0.72	5.5 (6.1)	117.9 (9.4)	10.1
IM6/1806	155.9 (3.9)	1.85 (5.2)	1.19	7.9 (5.0)	40.7 (10.0)	0.51	4.1 (8.6)	91.0 (17.5)	8.85
IM6/F584	175.9 (3.5)	2.56 (5.6)	1.45	8.8 (5.7)	47.6 (17.0)	0.55	5.5 (6.2)	122.0 (3.5)	9.90

C.V. = Coefficient of Variation

TABLE 3 – UNIDIRECTIONAL LAMINA COMPRESSIVE PROPERTIES OF FOUR MATERIAL SYSTEMS

	Longitudinal (0°)			Transverse (90°)		
Test Method	ASTM 3410-75			Northrop		
	Ultimate			Ultimate		
Properties	E_1^C GPa (C.V.)	X_1^C GPa (C.V.)	ϵ_1^C %	E_2^C GPa (C.V.)	X_2^C MPa (C.V.)	ϵ_1^C %
T300/5208	141.3 (2.5)	1.18 (4.2)	0.88	8.97 (6.4)	199.3 (8.6)	2.2
IM6/5245C	141.7 (2.4)	1.28 (5.3)	0.96	7.04 (4.7)	220.0 (3.7)	3.1
IM6/1806	138.9 (7.4)	1.18 (6.2)	0.90	5.86 (20.78)	199.3 (8.4)	3.5
IM6/F584	146.2 (3.6)	1.34 (3.2)	0.99	8.28 (4.7)	232.4 (5.2)	3.0

C.V. = Coefficient of Variation

TABLE 4 – HOT-WET COMPRESSIVE STRENGTH

MATERIAL SYSTEM	STRENGTH, MPa*
T300/5208	559
IM6/5245C	559
IM6/1806	414
IM6/F584	548

DATA REPRESENT AVERAGE OF FIVE TESTS. SPECIMENS PRE-SOAKED IN WATER BATH AT 65°C FOR 4 WEEKS AND TESTED AT 93 ± 3°C.

and modulus characteristics have been produced. As a result of these improvements, it is hopeful that some of these currently available high strain/toughened resin composites would achieve the goal of meeting the higher requirements in design strain allowables and consequently would offer substantially more weight savings. Several promising systems suitable for primary structural applications have been identified in a recent survey (4). Before these new systems can be adopted for structural applications, characterization tests must be performed to obtain information on material performance and properties which are essential factors in a material selection process.

The Structures and Materials Laboratory, NAE / NRC, in collaboration with the Canadian aircraft industry, has investigated three commercially available high strain/toughened resin systems in a characterization program. This program consists of three main parts as indicated in Table 1. Mechanical properties and hot/wet properties, as listed under items A and B of Table 1, have been determined and the experimental methods and results are described elsewhere (5). However, for the sake of completeness, these properties are presented in Tables 2 to 4. Characterization results from five toughened resin tests outlined in part (c) of Table 1 are presented in this paper. The proposed NASA test methods (6) have been adopted in this program. Except for the open-hole tension test which determines the notched tensile strength, the other four tests emphasize the characterization of matrix-dominated failure modes.

SPECIMEN PREPARATION

The three high strain / toughened resin composites evaluated were Narmco IM6/5245C, Hexcel IM6/F584 and American Cyanamid IM6/1806. A conventional carbon/epoxy system, Narmco T300/5208, was tested as a baseline material. All materials were procured in the form of unidirectional prepreg tapes. These tapes were cut into plies with the desired fiber orientations and dimensions. Then they were laid up by hand according to desired stacking sequences and vacuum-bag cured by autoclave processes to form laminated panels. The curing processes recommended by the prepreg manufacturers were closely followed. After curing, all panels were subjected to ultrasonic C-scan inspection to ensure that the panels were free of significant defects.

Specimens were cut from the panels using a diamond-impregnated abrasive cutting wheel and then finished to the final dimensions by milling. In cases where a high degree of precision is required such as the loaded ends of the open-hole compression specimens and the compression-after-impact specimens, a grinding operation was used to ensure that the loading edges were straight and parallel to within .013 mm. For the open-hole tension specimens and the open-hole compression specimens, holes were prepared by first drilling the hole undersize and then enlarging them to the required diameters with solid carbide two flute end mills. Composite laminates were clamped between two plexiglass plates during hole preparation to prevent surface damage from occurring. The squared-off end tabs for the edge delamination specimens and the metal hinges of the double cantilever beam

TABLE 5 – SPECIMEN GEOMETRY FOR THE TOUGHENED RESIN TESTS

Test	Specimen Dimension mm	Ply Orientation	Required Data	Test Replicates
Compression after Impact	127.0 by 254	$[45/0/-45/90]_{6S}$	Strength Strain	3
Edge Delamination Tension Test	38.1 by 254 Tabbed	$[+35/-35/0/90]_{2S}$	Interlaminar Fracture Toughness	5
Open-hole Tension	38.1 by 254 6.35 diam. hole	$[45/0/-45/90]_{6S}$	Strength Strain	3
Open-hole Compression	127.0 by 254 25.4 diam. hole	$[45/0/-45/90]_{6S}$	Strength Strain	3
Double Cantilever Beam	38.1 by 228	$[0]_{24T}$	Interlaminar Fracture Toughness	5

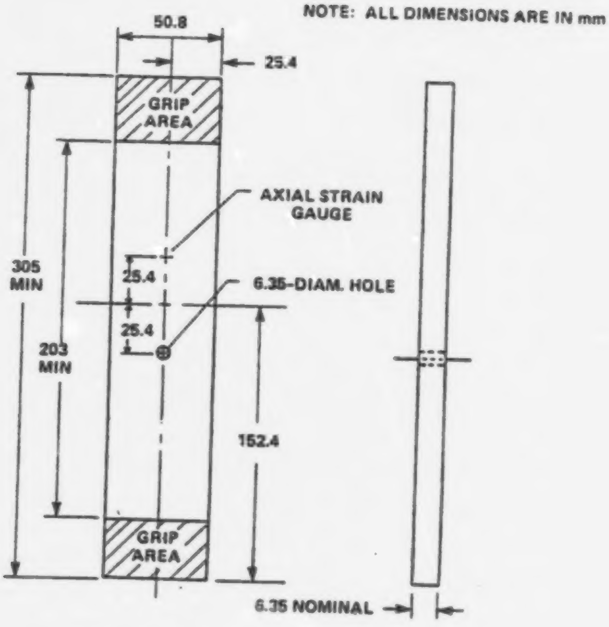
NOTE: ALL DIMENSIONS ARE IN mm
50.8
25.4
GRIP AREA
AXIAL STRAIN GAUGE
305 MIN
25.4
6.35-DIAM. HOLE
25.4
203 MIN
152.4
GRIP AREA
6.35 NOMINAL

FIG. 1: OPEN-HOLE TENSIÓN TEST SPECIMEN

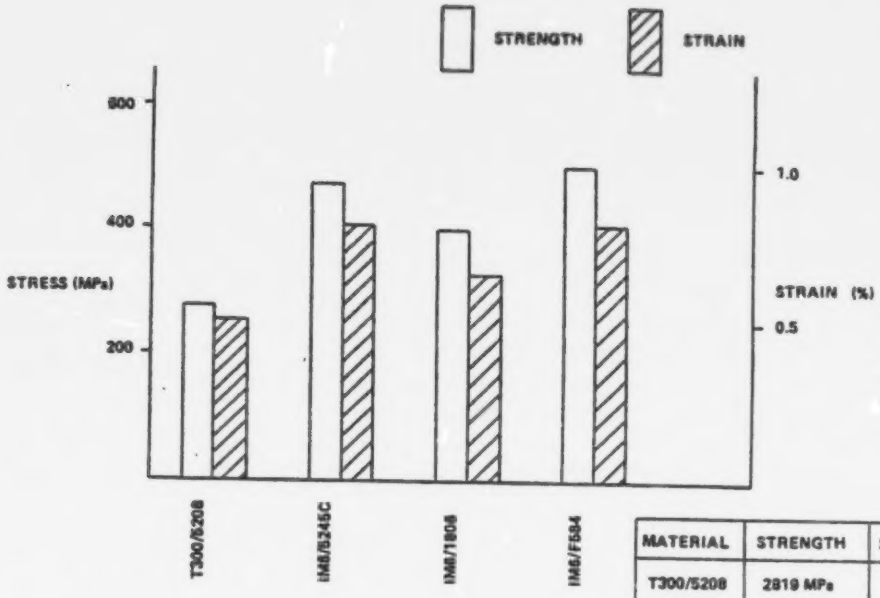

MATERIAL	STRENGTH	STRAIN
T300/5208	2819 MPa	0.52
IM6/5245C	482.0 MPa	0.81
IM6/1806	399.5 MPa	0.65
IM6/F584	492.8 MPa	0.80

OPEN-HOLE TENSION

FIG. 2: OPEN-HOLE TENSILE STRENGTH AND STRAIN

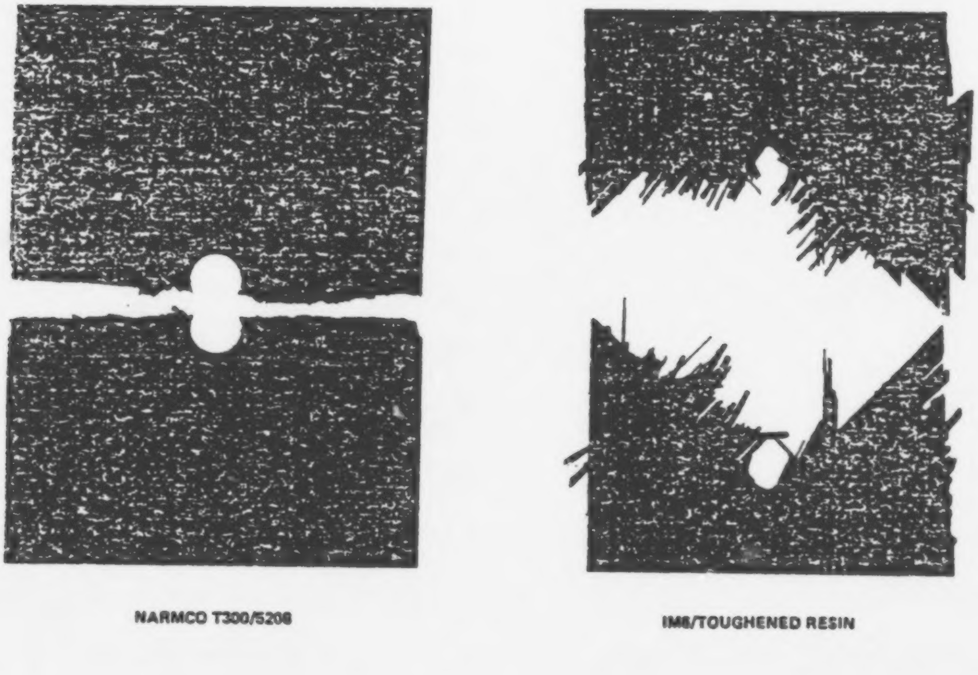

NARMCO T300/5208

IM6/TOUGHENED RESIN

FIG. 3: TYPICAL FAILED SPECIMENS FROM OPEN-HOLE TENSION TEST

specimens were installed by adhesive bonding using HYSOL EA 9320 adhesive. The dimensions of the finished specimens were measured and recorded. A summary of specimen configurations for the five toughened resin tests is presented in Table 5.

OPEN-HOLE TENSION TEST

This test was conducted to determine the notched tensile strength of the composites investigated. Coupons containing an open hole of 6.35 mm were loaded statically to failure at a loading rate of 89 KN/min. Each coupon had one axial strain gauge mounted at the location shown in Figure 1 to measure the far-field strains in the coupon.

A comparison of the tensile strength and the tensile strain-to-failure for the four material systems is presented in Figure 2. The data presented represent an average of three tests. As shown in Figure 2, the notched tensile properties of the toughened resin systems are significantly higher than those of the baseline system.

A typical failed coupon fabricated with IM6/toughened resin composite is shown in Figure 3 along with a failed coupon fabricated with the baseline material for comparison. [illegible]s noted that the fracture occurred in a relatively " clean " and brittle manner across the specimen at the notched section for the baseline specimens. Fracture originated at the edge of the hole and propagated perpendicular to the loading direction until complete separation of the laminate occurred. For the toughened resin material systems, the fracture was rather "explosive" as it

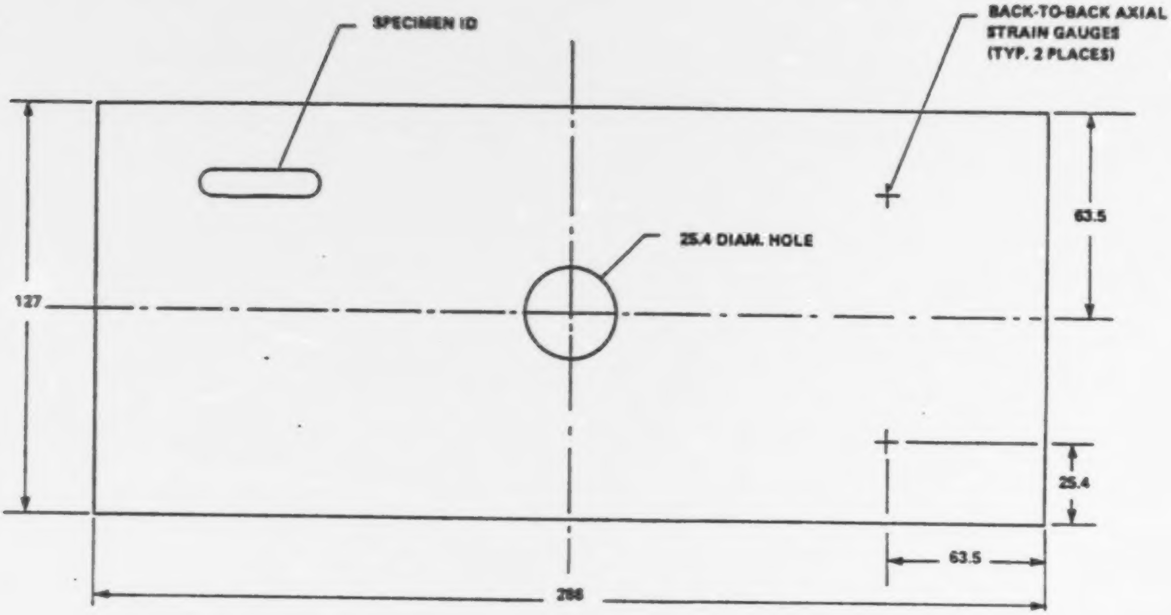
SPECIMEN ID
BACK-TO-BACK AXIAL STRAIN GAUGES (TYP. 2 PLACES)
25.4 DIAM. HOLE
127
63.5
25.4
63.5
288

FIG. 4: INPLANE OPEN-HOLE COMPRESSION TEST SPECIMEN. DIMENSIONS ARE IN mm

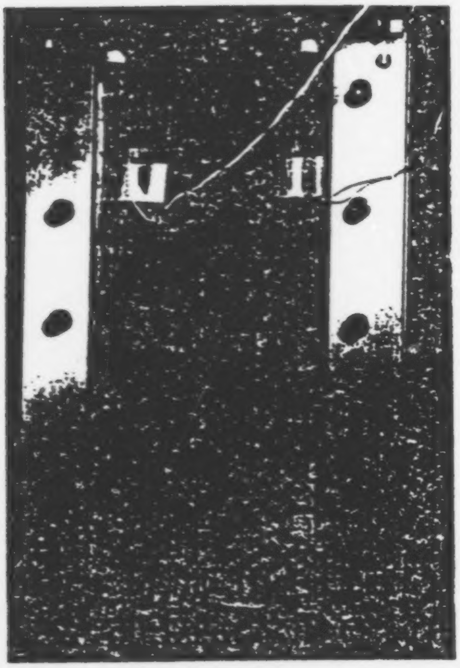

FIG. 5: TEST FIXTURE FOR OPEN-HOLE COMPRESSION TEST

was associated with loud noises shortly before and at separation and damaged areas were generally larger than those of the baseline system. As indicated in Figure 3, the most notable damage occurred in the 45 deg. plies where delamination took place and fibers were pulled out and broken at 45 deg. to the loading direction.

The increase in strengths and strains at failure for the IM6/toughened resin composites appears to result from superior fiber property translation within the more ductile resin matrix. Based on the data presented, a static tensile design strain allowable of 6,000 μm/m could be attained for these advanced composites.

OPEN-HOLE COMPRESSION TEST

This test was performed to determine the compressive behaviour of laminates containing an open hole with a diameter of 25.4 mm under in-plane loading. Specimens were loaded to failure under stroke controll at a displacement rate of 1.27 mm/min. There were two pairs of axial strain gauges mounted back-to-back on each specimen at the locations indicated in Figure 4. These strain gauges were used to measure the far-field strains and to indicate, if any, the presence of global buckling in the specimen tested. A special compression test fixture, as indicated in Figure 5, was used to provide simple support to the specimen along its long edges oriented parallel to the loading direction and to provide clamping support to the short edges (loaded edges) in order to suppress end brooming. The side supports on the long

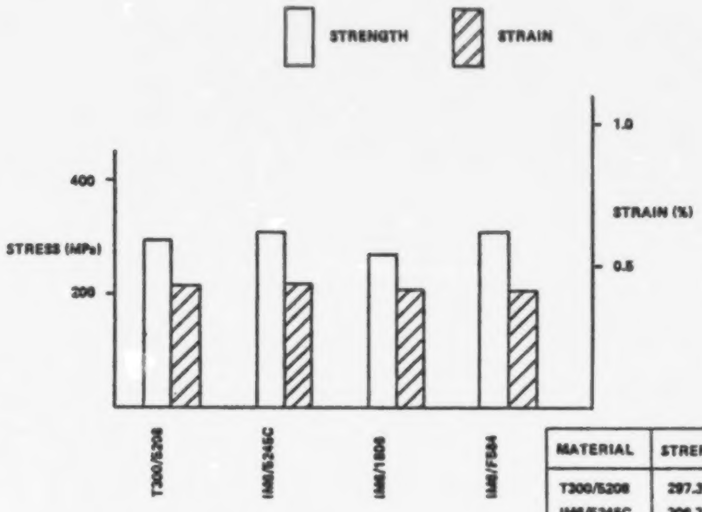

MATERIAL	STRENGTH	STRAIN
T300/5208	297.3 MPa	4358.5
IM6/5245C	306.7 MPa	4479.0
IM6/1806	270.9 MPa	4258.5
IM6/F584	300.9 MPa	4288.0

OPEN-HOLE COMPRESSION

FIG. 6: OPEN-HOLE COMPRESSIVE STRENGTH AND STRAIN

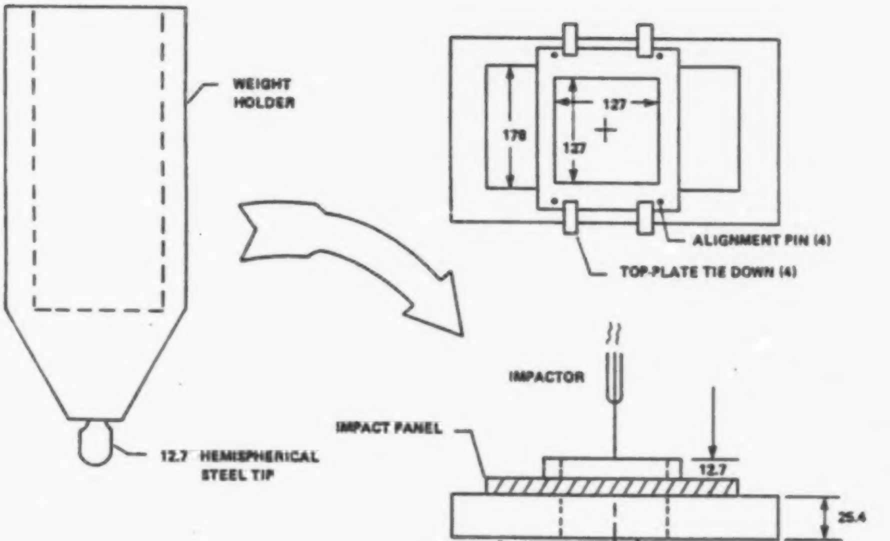
WEIGHT HOLDER
12.7 HEMISPHERICAL STEEL TIP
127
178
127
ALIGNMENT PIN (4)
TOP-PLATE TIE DOWN (4)
IMPACTOR
IMPACT PANEL
12.7
25.4
STEEL BASE PLATE
127 BY 127 SQUARE CUTOUT (THROUGH THICKNESS)

FIG. 7: IMPACT TEST APPARATUS. DIMENSIONS ARE IN mm.

edges were installed with a snug fit against a sheet of teflon material attached along the specimen edge such that the specimen can slide in the loading direction and sufficient clearance was provided between each side of the specimen and the side supports to prevent any transverse load from developing due to poisson deformation being restrained during the compression test.

The test results are presented in Figure 6. The strengths were computed based on the full width of the specimens. The strain-to-failure was the average of the measurements obtained from the four strain gauges on each specimen. The data presented in Figure 6 represent an average of three tests. Test results indicate that the toughened resins and high strain fibers have no significant beneficial effect on the compressive failure strains and strengths.

The failure mode for all the material systems appears to be the same; fiber kinking and delamination initiates at the edge of the hole, and then spreads as a local buckling band towards the specimen edges as the load increases. The absence of global buckling has been confirmed by the back-to-back strain gauge readings recorded during the test.

IMPACT CHARACTERIZATION

Impact tests were conducted using an instrumented drop-weight impact machine to demonstrate the resistance of the four material systems to low velocity impact. Specimens were ultrasonically inspected by C-scan techniques before the test. A steel fixture, shown in Figure 7, was used to support the

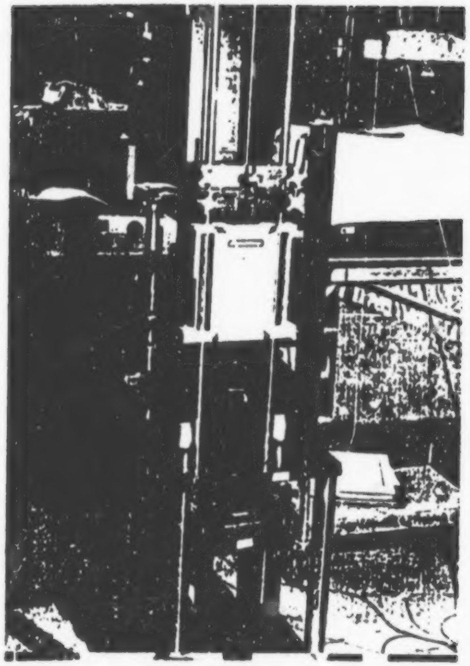

FIG. 8: TYPICAL SET-UP FOR IMPACT TEST

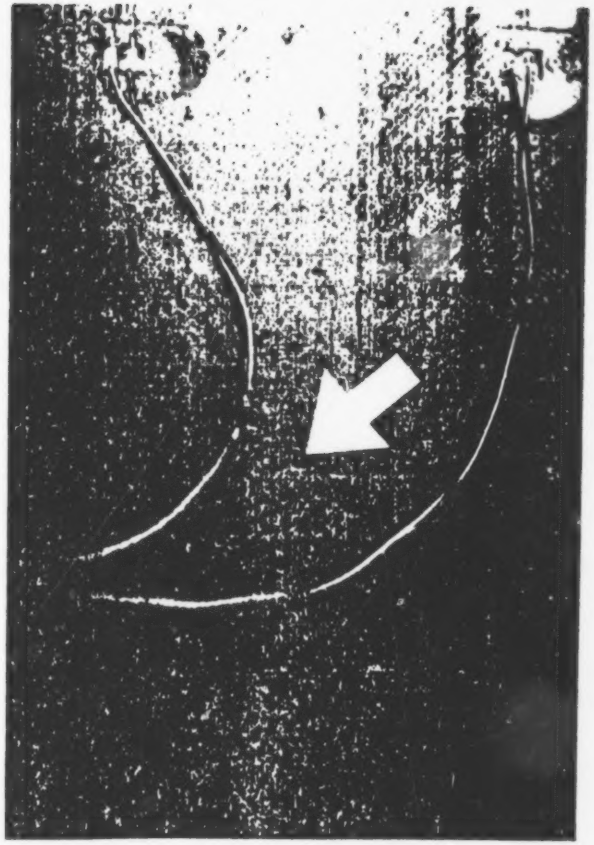

FIG. 9: TYPICAL IMPACTED SURFACE OF IM6/TOUGHENED RESIN SYSTEM

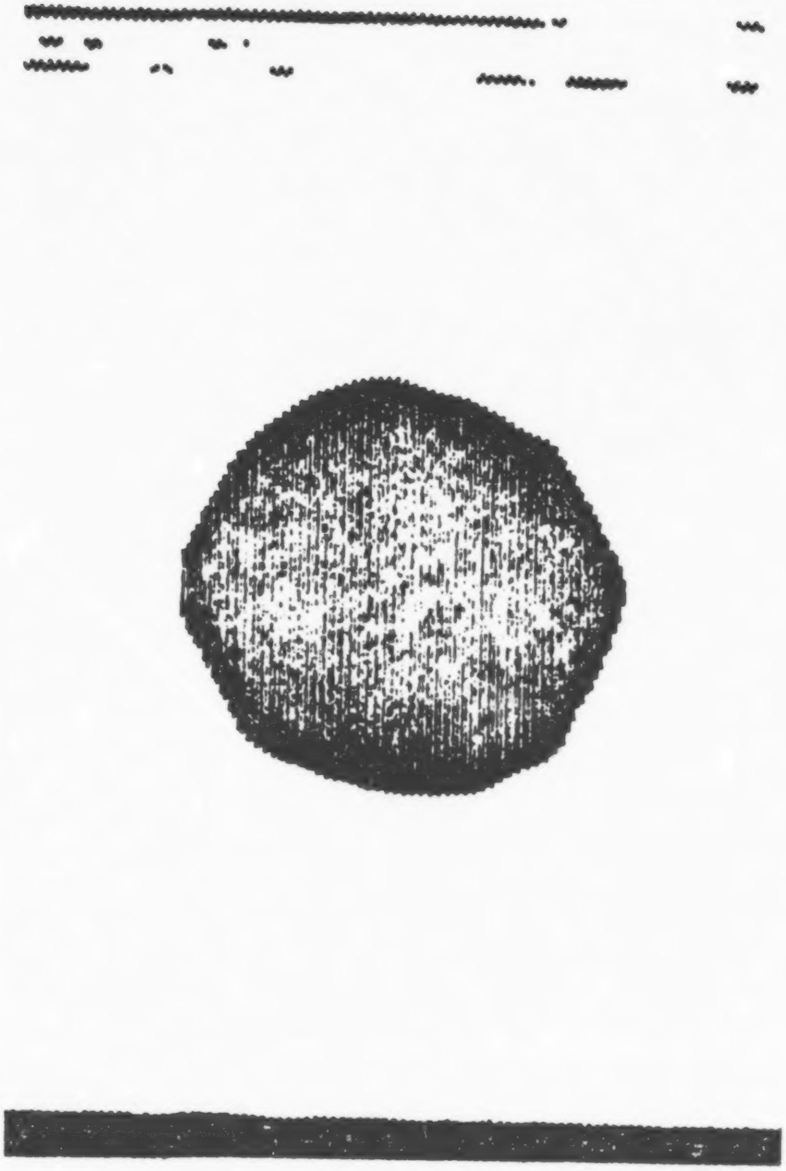

FIG. 10: TYPICAL C-SCAN RECORD OF IMPACT DAMAGE IN IM6/TOUGHENED RESIN SYSTEM

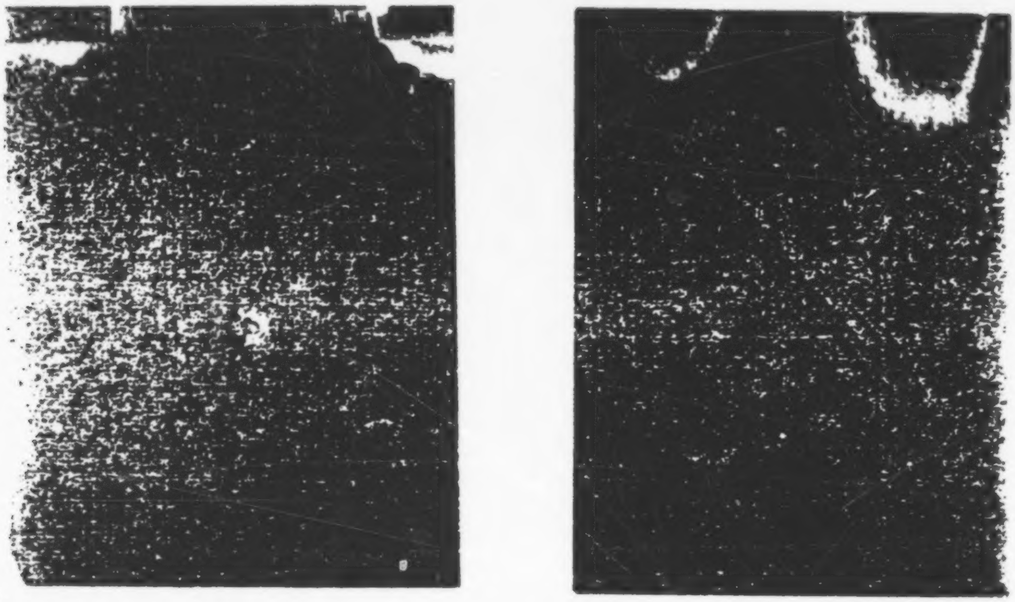

IMPACTED SURFACE

BACK SURFACE

FIG. 11: TYPICAL IMPACT DAMAGE IN NARMCO T300/5208

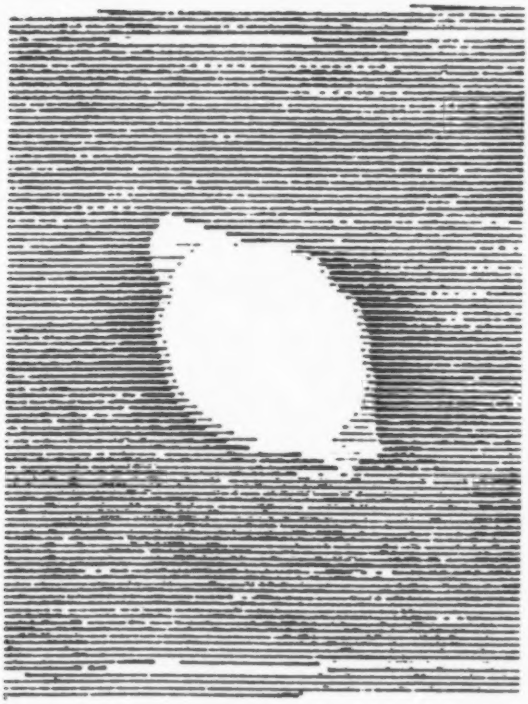

FIG. 12: TYPICAL C-SCAN RECORD OF IMPACT DAMAGE IN NARMCO T300/5208

laminate by clamping it between two plates with each plate containing a 12.7 cm by 12.7 cm central opening. Alignment pins were provided to ensure that the specimen was struck in the center by an instrumented tup with a 12.7 mm diameter hemispherical steel tip. A typical set-up for an impact test is shown in Figure 8. All specimens were subjected to impact with an energy level of 2.8 KJ. The velocity of the falling tup just prior to contact with the specimen was 3 m/sec. A pawl and rachet mechanism was used to catch the rebounding tup to prevent secondary impacts. Specimens were visually and ultrasonically inspected by C-scan techniques after the impact test to determine the extent of the damage.

Figure 9 shows a typical impacted surface of IM6/toughened resin composites. It can be seen that the impact damage is only barely visible. There was no back-surface damage in any of the toughened resin composites tested. Figure 10 shows the corresponding C-scan record. It can be seen that the internal damage is much more extensive than that shown in the impacted surface.

Figure 11 shows the impacted surface and the back surface of a typical baseline specimen. It is quite obvious that the specimen sustains crushing damage in the impacted surface and substantial delamination of the outer plies in the back surface as a result of the impact. The corresponding C-scan record is provided in Figure 12. Measurements of the impact-damaged areas based on C-scan records were not attempted because it was felt that the extent of internal damage could not be determined

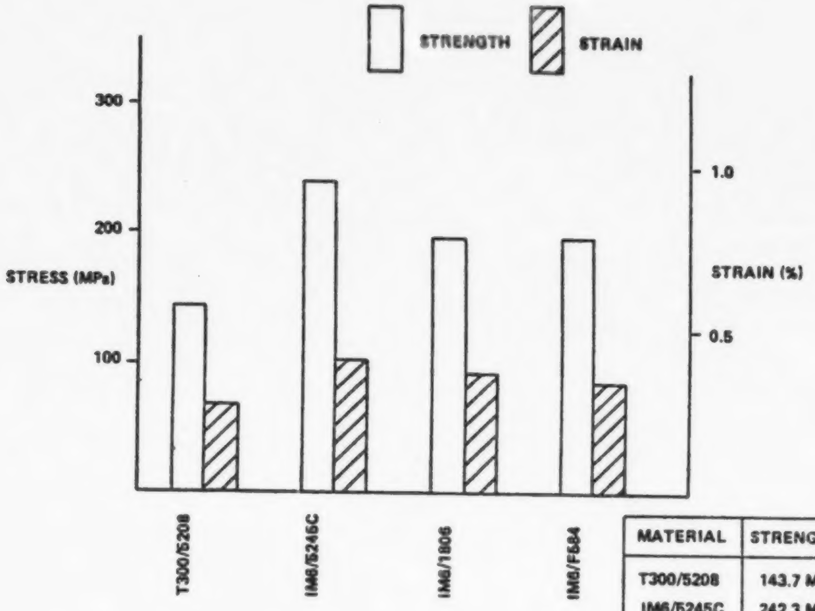

MATERIAL	STRENGTH	STRAIN
T300/5208	143.7 MPa	2730
IM6/5245C	242.3 MPa	4057
IM6/1806	198.2 MPa	3897
IM6/F584	198.3 MPa	3530

COMPRESSION AFTER IMPACT

FIG. 13: COMPRESSION AFTER IMPACT STRENGTH AND STRAIN

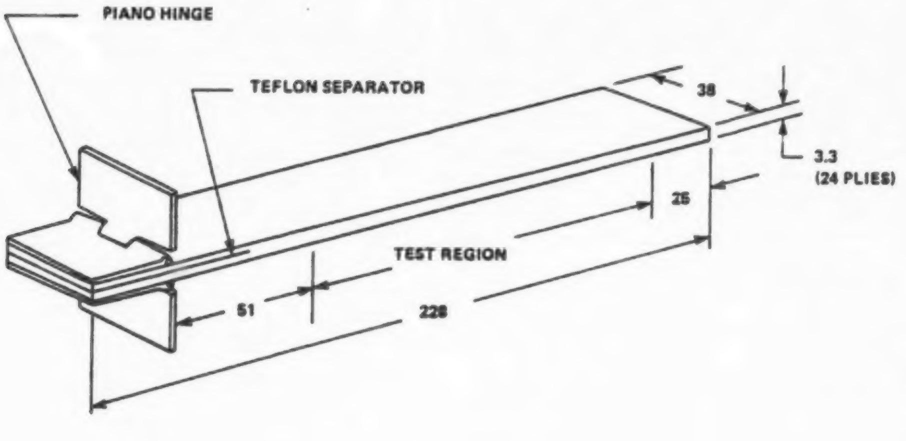
PIANO HINGE
TEFLON SEPARATOR
38
3.3
(24 PLIES)
25
TEST REGION
51
228

FIG. 14: HINGED DOUBLE CANTILEVER BEAM (HDCB) SPECIMEN.
DIMENSIONS ARE IN mm.

accurately in this manner.

COMPRESSION-AFTER-IMPACT TEST

The residual strength of the impact-damaged specimens was evaluated by a compression test. This test serves to rank the toughness of the composites according to their resistance against impact damage. The procedure used in the open-hole compression test was applied here. Specimens were remachined to 127 mm in width so that they could be placed in the test fixture used in the open-hole compression test.

A comparison of residual compressive strengths and strains at failure for the four material systems is presented in Figure 13. The data presented represent an average of three tests. All three IM6/toughened resin composites show substantial improvements relative to the baseline system. The higher residual properties clearly indicate the improved resistance to low velocity impact of these advanced composites. However, test results indicate that the design strain allowable of 6,000 μ m/m could not be attained. Therefore the residual compressive performance of these toughened composites has to be improved in order to meet this goal.

DOUBLE CANTILEVER BEAM TEST

The Mode I interlaminar fracture toughness of the four material systems was determined by this test. A double cantilever beam specimen, illustrated in Figure 14, was used to characterize the behaviour of delamination as a result of interlaminar tensile

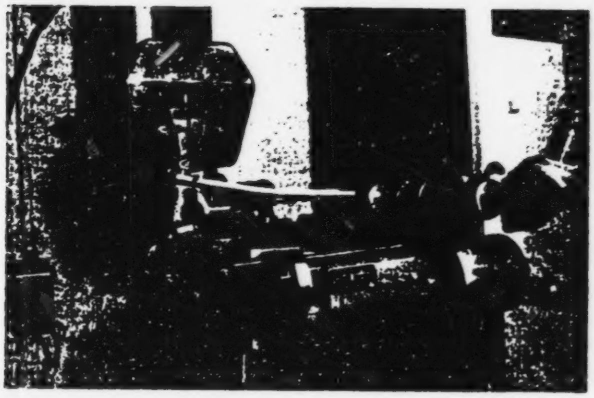

FIG. 15: TYPICAL SET-UP FOR DOUBLE CANTILEVER BEAM TEST

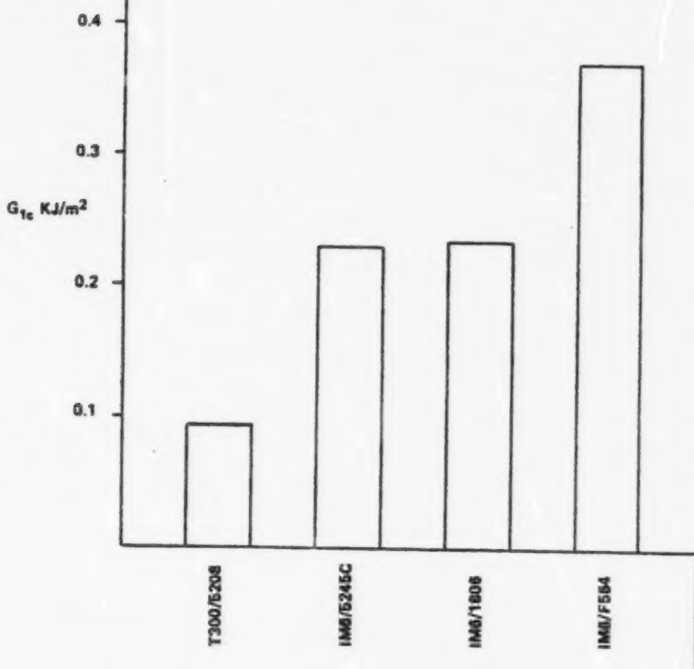

MATERIAL	G_{1c}
T300/5208	0.093
IM6/5245C	0.228
IM6/1806	0.229
IM6/F584	0.372

FIG. 16: G_{1c} DETERMINED BY DOUBLE CANTILEVER BEAM TEST

or peel stresses. A typical test set-up is shown in Figure 15. Specimens were subjected to monotonically increasing tensile load under displacement control at a rate of 10 mm/sec. Two low power travelling microscopes were used to measure crack growth on both edges of the specimen. A chart recorder was used to obtain load versus displacement plots. The specimen was loaded until the crack length reached 50.8 mm. The machine was stopped and the crack tip on both edges of the specimen was marked to allow crack length to be measured more accurately at a later stage. The load versus displacement plot was marked so that this point in the test could be identified. The machine was then restarted and the procedure was repeated for crack lengths of approximately 76.2 mm, 101.6 mm, 127 mm and 152.4 mm. The crack tip was extended beyond the final stop point before terminating the test.

The fracture toughness was calculated by the direct beam equation method (6). The equation used is provided in the following:

$$G_{Ic} = \frac{P\delta}{2ab} \left(\frac{3a - 4a_o}{a - a_o} \right) \qquad (1)$$

where G_{Ic} = fracture toughness; P = load; a = average crack length; b = width of beam; δ = deflection of double cantilever beam; and a_o = constant evaluated by the method of least squares. A computer program was developed to calculate the fracture toughness.

The fracture toughness values of the four material systems evaluated are presented in Figure 16 where each value represents

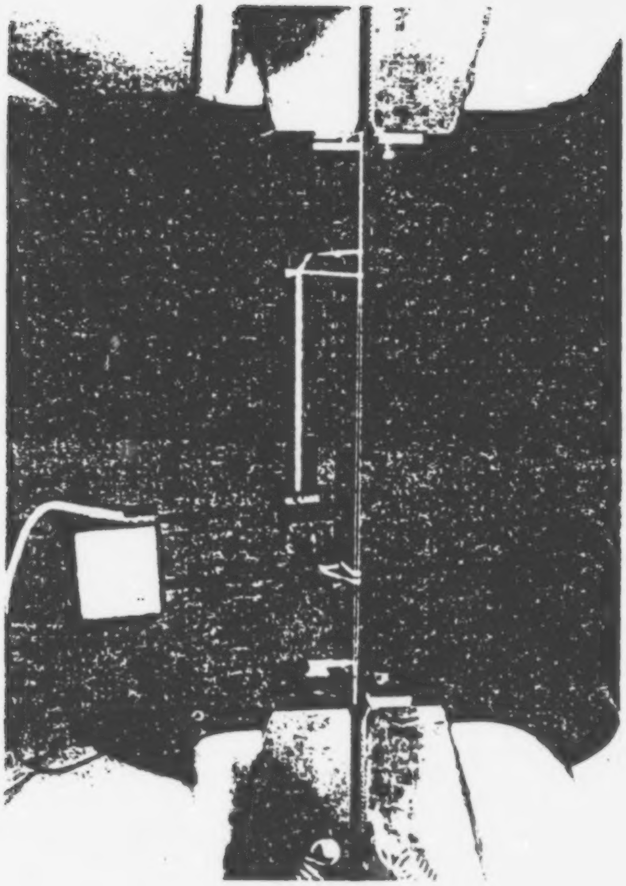

FIG. 17: TYPICAL SET-UP FOR EDGE DELAMINATION TEST

an average of five tests. The values of the toughened resin systems are 2.5 to 4 times higher than the value of the baseline system.

Macroscopic observations of the surface morphology of the delaminated areas indicated that substantially more fiber bridging occurred in the toughened resin composites than in the baseline material. Since fiber bridging has been known to increase the measured fracture toughness (7), the higher values obtained for the toughened systems should be treated with caution as the fracture mode involves both resin delamination and fiber fracture.

EDGE DELAMINATION TENSION TEST

This simple test was used to determine the mixed-mode interlaminar fracture toughness of the four material systems investigated. While the double cantilever beam specimen delaminates in Mode I, the edge delamination specimen delaminates in a mixture of Mode I (interlaminar tension or peel) and Mode II (interlaminar shear) under tensile loading. The percentages of Mode I fracture and Mode II fracture depend on the lay-up of the laminate tested. For the lay-up adopted in this test (see Table 5), the Mode I and Mode II components of the fracture toughness were determined by a finite element analysis (8) to be 90 % and 10 % respectively.

A typical test set-up is shown in Figure 17. An extensometer with an extender arm to provide a gauge length of 101.6 mm was mounted in the center of the specimen. An X-Y recorder was used

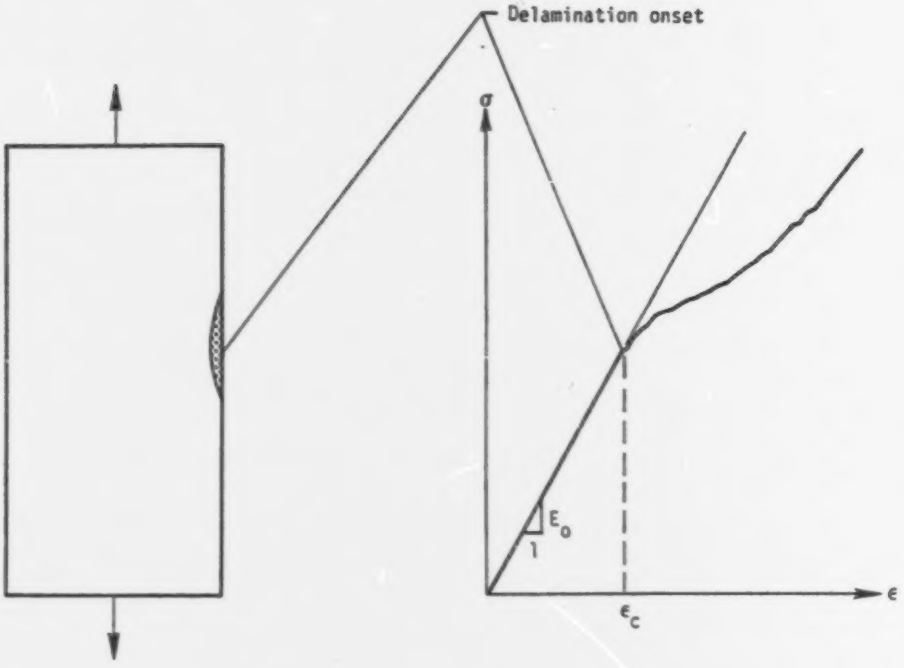
Delamination onset
σ
E_0
1
ϵ_c
ε

FIG. 18: SCHEMATICAL LOAD-STRAIN CURVE FOR DETERMINING G_c

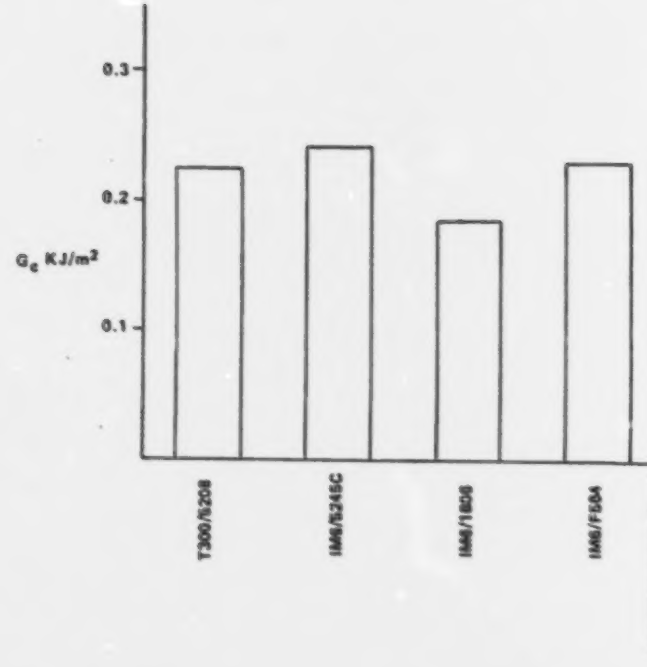

MATERIAL	G_c
T300/5208	0.227
IM6/5245C	0.245
IM6/1806	0.185
IM6/F584	0.234

FIG. 19: G_c DETERMINED BY EDGE DELAMINATION TENSION TEST

to provide a real-time analog display of the output of the extensometer and the load signals. Specimens were loaded in tension under stroke control at a rate of .00254 mm/sec. The loading was continued until visible detection of edge delamination and corresponding deviation in the load-deflection plot occurred. This point, which indicates the strain level at the onset of delamination, was noted on the load-deflection curve as illustrated in Figure 18. The loading was continued until the specimen fractured into two pieces. The strain level at fracture was recorded.

The mixed-mode interlaminar fracture was calculated by using an equation derived from laminated plate theory and simple rule of mixture for stiffness loss due to delamination (8). This equation is given in the following:

$$G_c = \frac{\epsilon_c^2 t}{2} (E_{LAM} - E^*) \tag{2}$$

where E_{LAM} is the modulus of the specimen calculated from laminated plate theory; E^* is the modulus of partially delaminated laminate; ϵ_c is the critical strain at the onset of delamination; and t is the specimen thickness.

The fracture toughness of the four material systems is presented in Figure 19. Each value represents an average of five tests. Based on the results presented, the IM6/toughened resin material systems do not appear to be tougher than the baseline system. This may be explained by the unusually high average of 227 J/m^2 obtained for Narmco T300/5208 in this test as compared

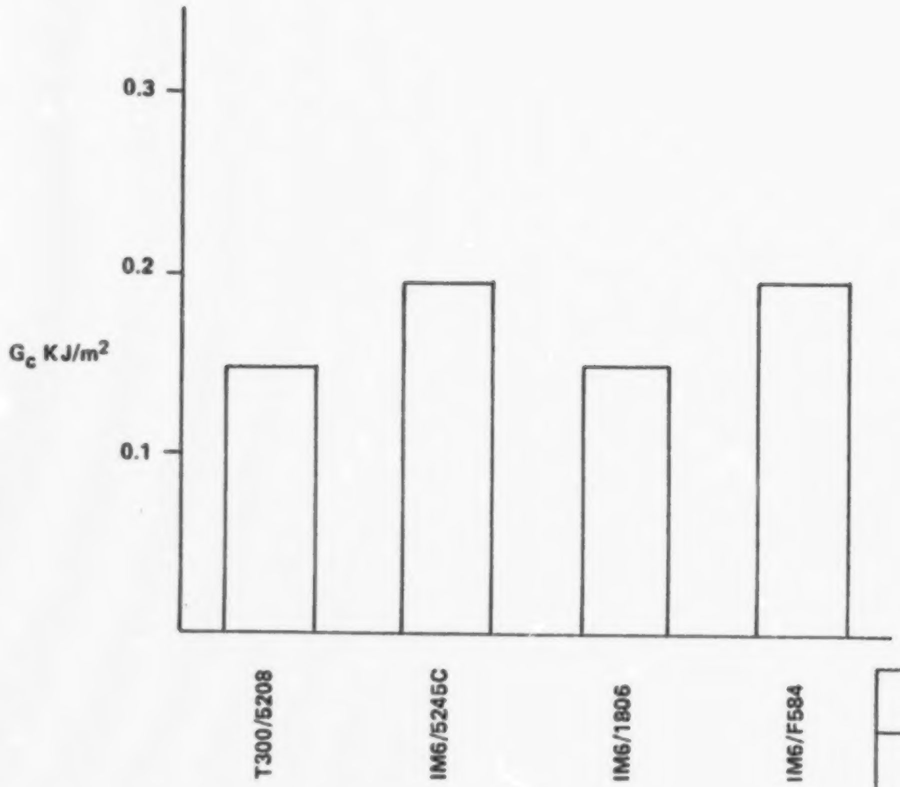

MATERIAL	G_c
T300/5208	0.146
IM6/5245C	0.196
IM6/1806	0.147
IM6/F584	0.193

FIG. 20: G_c DERIVED BY USING E_o INSTEAD OF E_{LAM}

to a reported value of 137 J/m^2 (9). An examination of the calculated modulus, E_{LAM}, for T300/5208 indicated that it is 9.3% higher than the measured modulus, E_o, determined from the linear portion of the load-deflection curve. Using E_o instead of E_{LAM} in calculating the fracture toughness, a value of 146 J/m^2 was obtained for T300/5208. This value is in better agreement with the reported value. The calculation of interlaminar fracture toughness for the IM6/toughened resin systems was repeated by using E_o instead of E_{LAM}. The results are presented in Figure 20. Based on these results, two of the three IM6/toughened resin systems were shown to have significantly higher fracture toughness than the baseline system.

The toughness of matrix resins is known to influence the onset of edge delamination and the growth of delamination under monotonically increasing tensile loads or cyclic loads in a laminated composite (9). The effect of toughness on delamination growth is not treated in the present test. However, this effect has been observed during the application of tensile loads to the specimens. For the baseline material with brittle resin, the onset of delamination was immediately followed by a sudden rapid growth which extended the delamination to the full length of the specimen. For the composites with toughened resins, delamination was observed to initiate within the gauge length when the critical strain level was reached and then it propagated in a stable manner along the edges of the specimen. The delamination reached the full length of the specimen at a much higher strain level than that at which it started. Based on this observation, it may be concluded that the IM6/toughened resin material systems have better resistance to delamination growth than the baseline system.

CONCLUSIONS

Five toughened resin tests have been performed according to procedures proposed by NASA to characterize three commercially available IM6/toughened resin systems and to compare their performance and properties with those of a conventional carbon/epoxy system, Narmco T300/5208. Conclusions based on the results obtained are provided below.

(1) Notched tensile properties of the IM6/toughened resin systems were determined by the open hole tension test to be significantly better than those of the baseline system.

(2) Results from the open hole compression test indicated that the IM6/toughened resin systems demonstrated no improvement over the baseline system in notched compressive properties.

(3) Resistance against low-velocity impact was significantly improved for the IM6/toughened resin systems relative to the baseline system as measured by the higher residual compressive strengths.

(4) IM6/toughened resin systems demonstrated improved resistance against delamination in Mode I fracture as indicated by higher values of interlaminar fracture toughness obtained by the double cantilever beam test. However, due to the presence of fiber bridging, these higher values might not be representative of matrix performance as the fracture involved fiber breakages

which tend to elevate the results.

(5) The edge delamination tension test was found to be simple but very effective in screening the toughened resins from brittle systems by evaluating the mixed-mode interlaminar fracture toughness at the onset of delamination. Two of the three toughened resin systems tested, Narmco IM6/5245C and Hexcel IM6/F584, were found to have higher fracture toughness than the baseline system while Cyanamid IM6/1806 was found to have similar fracture toughness. All three toughened systems were observed to resist delamination growth better than the baseline system.

ACKNOWLEDGMENT

This work has been supported financially by the Department of Nation Defence of Canada under Technical Program TP26B/DREP and ADM(MAT)/CRAD. The financial assistance is most gratefully appreciated. The authors would like to acknowledge the technical support of Mr. R. Gould, Mr. W.K. Ubbink and Mr. P. Gaudert in performing the experimental part of this program.

REFERENCES

1. S.P. Garbo and J.M. Ogonowski, AIAA Publ. 79-0800, (1979).
2. C.F. Griffin and J.C. Ekvall, J. Aircr., 19, 8 (1982).
3. C.F. Griffin, " Feul Containment and Damage Tolerance in Large Composite Primary Aircraft Structures". NASA CR 166083, National Aeronautics and Space Administration, (1983).
4. A. Lee, "A Material Selection Review for the PILP Contract on Development of Advanced Composite Materials Technology", Canadair Memorandum No. MCM-000-118, Canadair Ltd., Montreal, Quebec, (1984).
5. S.K. Lee, R.F. Scott, P.C. Gaudert, W.H. Ubbink and C. Poon, "Characterization and Toughened Resin Testing of New Generation Carbon Fiber/Epoxy Systems", presented at 26th Conf. Metall., Winnipeg, Manitoba, (1987).
6. NASA RP 1092 "Standard Tests for Toughened Resin Composites", NASA Langley Research Center, Hampton, Virginia, (1983).
7. L.F. Vosteen, N.J. Johnston and L.A. Teichman, "Tough Composite Materials", Ch. 1, NASA Langley Research Center, Hampton, Virginia, (1984).
8. T.K. O'Brien, "Effects of Defects in Composite Materials", Am. Soc. Test. Mater. Spec. Tech. Publ 836, American Society for Testing and Materials, Philadelphia, (1984).
9. T.K. O'Brien, "Delamination and Debonding of Materials", Am. Soc. Test. Mater. Spec. Tech. Publ. 876, American Society for Testing and Materials, Philadelphia, (1985).

A STUDY OF LOW ENERGY IMPACT OF CONTINUOUS CARBON FIBRE REINFORCED COMPOSITES

by

D.R. Moore and R.S. Prediger
ICI PLC
International Materials Centre
Wilton, Middlesbrough, England

Presented at the 8th annual NRCC/IMRI symposium "Composites-'87",
November 5 and 6, 1987, Boucherville, Que., Canada

A STUDY OF LOW ENERGY IMPACT OF CONTINUOUS CARBON FIBRE REINFORCED COMPOSTIES

D R MOORE, R S PREDIGER

ABSTRACT

Low energy instrumented falling weight impact test have been used to study the failure mechanisms in various multi-angle laminates of continuous carbon fibre reinforced composites. C-scans of impacted specimens were conducted in order to monitor an area for delamiantion damage. Photography of the tension surface during impact enabled the onset of tension surface cracking to be detected.

These techniques were employed for composites based on thermoplastic (PEEK) and thermoset (epoxy system 934) matrix materials. In addition, a range of ply numbers (8 to 40) were used in preparation of the multi-angle laminates.

Tension surface splitting can be shown to be the first failure mechanism during impact. Initiation of a tension crack occurs at a lower absorbed impact energy than that for the onset of delamination damage.

A STUDY OF LOW ENERGY IMPACT OF CONTINUOUS CARBON FIBRE COMPOSITES

D R MOORE, R S PREDIGER

1 INTRODUCTION

Impact events are known to be potential causes of damage in composite materials; in turn, damage can seriously impair the engineering properties of a composite structure. Consequently, the more information that can be obtained from an impact evaluation, the more certain can be the ultimate performance of a material. Impact tests feature strongly in the study of composite systems, from compression after impact studies (1) to various instrumented impact evaluations (eg 2, 3, 4, 5).

Impact tests can generate many types of failure event including interlaminar fracture (delamiantion), intralaminar fracture (between fibre cracking) and translaminar fracture (breaking of fibres). Dependent an the laminate lay-up, choice of fibre, or matrix type, then the energy absorbed in impact can be a complicated combination of energies for these various fracture events. (6)

The particular question that we wish to discuss in this paper is what fracture processes can be interpreted in instrumented falling weight impact tests. In addition, since through-thickness events are less likely in service, we especially address the interpretation of low energy instrumented falling weight impact.

Many practical lay-ups for continuous carbon fibre composites will be based on multi angle laminates. Such systems are known to delaminate under impact loading. Therefore, a specific issue relates to whether the monitoring of force deflection signals during impact can be interpreted in terms of delamination damage. The larger the number of plies in a multi angle laminate, the greater the opportunity for delamination damage. This occurs because shear stress, the root cause of delamination, rises with increasing thickness. Therefore, this study accommodates laminate thickness as a variant in the samples for study.

Other fracture mechanisms are also known to occur during impact. Consequently, it is useful to be able to monitor and identify these various events. To this end, photography, in association with the monitoring of the impact force-time signal, is used in order to clarify such issues (4).

Finally, since fracture toughness depends strongly on the components in the composite, particularly the matrix, then the material subjects of this work accommodate both thermoplastic and thermoset composite systems.

2 MATERIALS AND EXPERIMENTATION

2.1 MATERIALS

Two continuous 61% by volume carbon fibre composite materials are the subjects of the work; one based on a thermoplastic matrix, the other on a thermoset material. The selection of the composites is aimed at providing a broad base of subject materials, as opposed to attempting a rigorous comparison of materials.

The thermoplastic composite is AS4/PEEK which comprises Hercules AS4 carbon fibres and a poly ether ether ketone matrix. The thermosetting composite is T-300/934 which comprises Toray T-300 carbon fibres and an epoxy formulation. The AS4/PEEK composite is ICI's APC-2 material; the T-300/934 is a Fiberite material with 934 being a Fiberite epoxy formulation. Both materials were consolidated according to manufacturer's recommendations. Multi-angle laminates were prepared according to the following scheme:-

(i) AS4/PEEK $[\pm 45]_{ns}$
where n= 2, 4 and 10 (ie 8, 16 and 40 plies)

(ii) AS4/PEEK $[-45/0/+45/90]_{ns}$
where n= 2 and 5 (ie 16 and 40 plies)

(iii) T-300/934 $[\pm 45]_{ns}$
where n= 2, 4, 5 and 10 (ie 8, 16, 20 and 40 plies)

2.2 INSTRUMENTED FALLING WEIGHT IMPACT EQUIPMENT

Impact testing was conducted on a falling weight impact apparatus with instrumentation. A piezoelectric transducer (Kistler cell) was attached to the falling impactor enabling a force-time signal to be monitored during impact. The transducer was connected to a charge amplifier which in turn was connected to a digital storage oscilloscope (Gould 4035) in order to collect and display any force time signal resulting from an impact event. This force-time signal could then be passed to a dedicated computer (hewlett-Packard 9816) for further analysis of the signal. This enabled the force-time signal to be converted to a force-displacement signal and also an energy-displacement signal. If the impactor reduced velocity during impact, then appropriate velocity corrections were incorporated into the software of the dedicated computer. Further details of these techniques have been published elsewhere (7, 8, 9).

Typical resonance frequency of the impact equipment is about 9 KHz; the smallest electrical filter contained in the electrical circuity was a low-pass filter of 180 KHz in the charge amplifier unit. Therefore, filtering of the impact response was negligible.

The falling weight impact equipment was a special low energy capacity site (10 Joules maximum input energy) and is illustrated in reference (7). It is constructed in such a way as to provide fine resolution (within 0.01 Joules) of input energy in a range (0.5 to 10) Joules. This is achieved by altering either the impactor mass or the drop height. Drop height was always set to be well in excess of the specimen deflection in order to avoid the need for gravity corrections in the calculation of absorbed specimen energy
(10).

All impact tests were of a low energy type. This meant that the magnitude of input energy was always less than that required for the impactor to penetrate through a specimen. Consequently, it was always necessary to catch the impactor subsequent to a first impact and prior to a second strike. Despite the absence of a 'through the thicknesss' impact event, the magnitude of the input energy was varied for all samples in order to achieve different amounts of impact damage including no detectable damage.

The geometry of the test was set by testing plaque specimens (mostly 75 mm x 75 mm) mounted on a circular support (diameter 40 mm) and impacted with a hemispherical impactor (diameter 10 mm). Impact test speeds were in the range about (1-2) m/sec, which was an insufficient range for changes due to viscoelastic effects to be a concern. (11)

2.3 DAMAGE DETECTION DURING AND SUBSEQUENT TO IMPACT

All impact specimens were intact subsequent to impact testing. They were ultrasonically C-scanned in order to reveal the projected area of impact damage. This damaged area was then measured using a Hewlett-Packard digitising slab connected to a Hewlett-Packard 9845B computer. Ultrasonic C-scan damage areas were considered significant for areas greater than 4 mm^2. The type of damage generated through the thickness of a specimen has been previously identified as a mixture of mechanisms including a dominance from delamination (5).

Damage detection during the impact event was achieved by photography of the tension surface. In order to assist photographic contrast the black specimens were painted white (4).

3 ANALYSIS OF EXPERIMENTAL RESULTS

The two continuous carbon fibre composites available as multi angle laminates with varying ply numbers represented a total of 9 samples for impact testing. For each sample, some 6 to 10 specimens were subjected to photographed low energy impact with subsequent damage analysis. The scheme of testing and analysis was similar for each sample. Therefore, the results for one sample (T-300/934, $[\pm 45]_{2S}$) will be presented in detail; the results for all samples can then be discussed in Section 4.

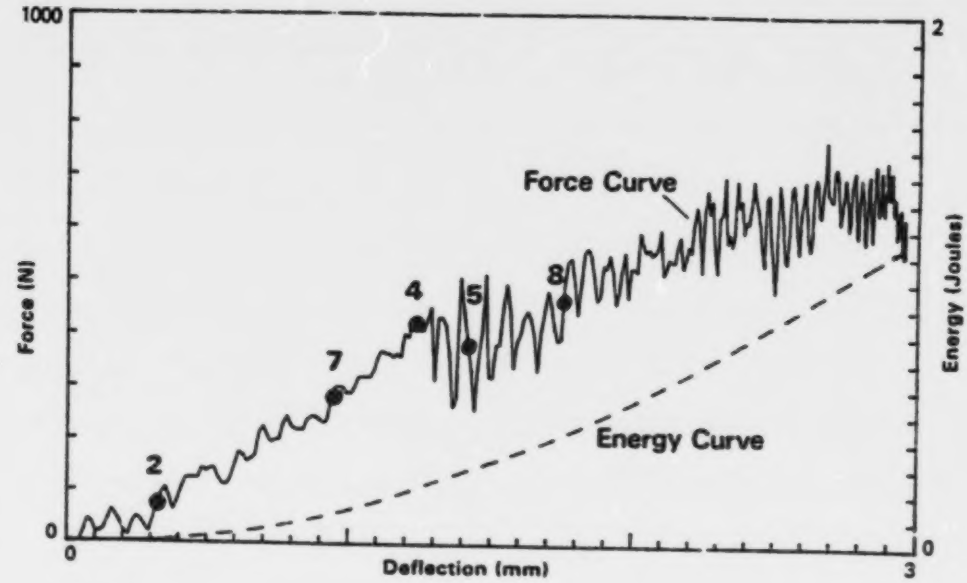

(● - Locations of photographed impact)

Figure 1 Typical Force Deflection, Energy-Deflection Plot showing points at which photographs were taken for $[\pm 45]_{s}$, T-300/934.

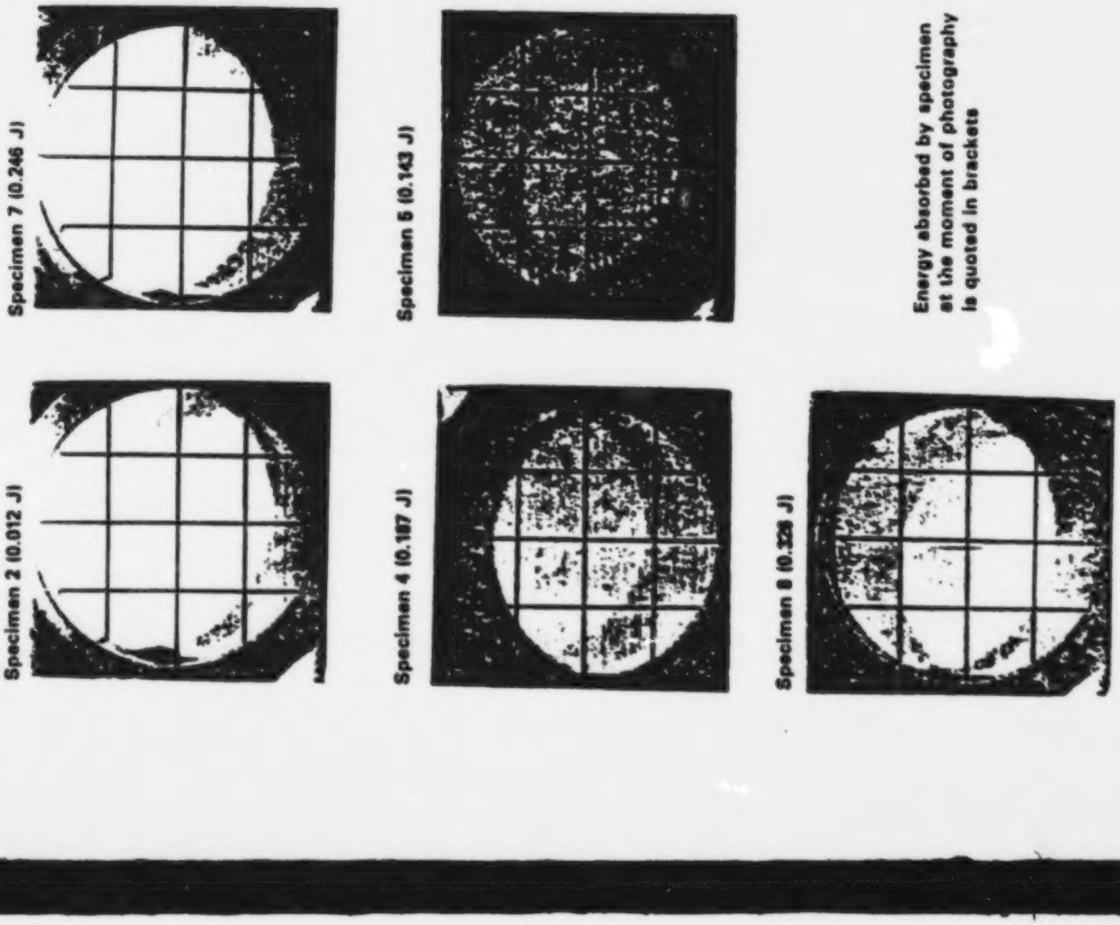
Specimen 7 (0.246 J)

Specimen 5 (0.143 J)

Energy absorbed by specimen at the moment of photography is quoted in brackets

Specimen 2 (0.012 J)

Specimen 4 (0.187 J)

Specimen 8 (0.326 J)

Figure 2 Photographs showing tension surfaces of impacted specimens, 2, 7, 4, 5 and 8 for $[\pm 45]_{s}$, T-300/934

8 specimens of T-300/934 composite for angle-ply laminate $[\pm 45]_{2S}$ were impacted with input energies in the range (0.5 to 3.2) Joules. It was only possible to take one photograph per specimen during the impact event. A typical force-deflection curve and energy-deflection curve is illustrated in Figure 1. The particular conditions for this test involved an input energy (mass x height x acceleration due to gravity) of 1.13 Joules. In terms of the force-deflection curve, the response of the specimen seems to be in two parts. For deflections up to 1.3 mm (for a specimen of thickness 1.3 mm) the response is approximately linear elastic. This region relates to absorbed specimen energy up to 0.24 Joules. At larger specimen deflections, there are considerable oscillations of the force-deflection curve. All 8 specimens exhibited this type of behaviour. Consequently, it is possibe to mark onto Figure 1 the approximate locations along this typical force-deflection characteristic where photography of the tension surface occured. It must be remembered, however, that each photograph related to a unique specimen. Five points are marked onto Figure 1 (numbered inorder of increasing deflection 2, 7, 4, 5 and 8; these numbers being specimen numbers)

Figure 2 illustrates the tension surface photograph for these particular specimens. Specimens 2, 7 and 4 show no damage of the tension surface, whilst specimens 5 and 8 show a tension surface crack (length 6.0 mm and 9.3 mm, respectively). It is therefore apparent that the start of the large force oscillation on the force-deflection curve coincides with the onset of a tension surface crack. This point will be subsequently identified as the crack initiation peak on the force-deflection curve.

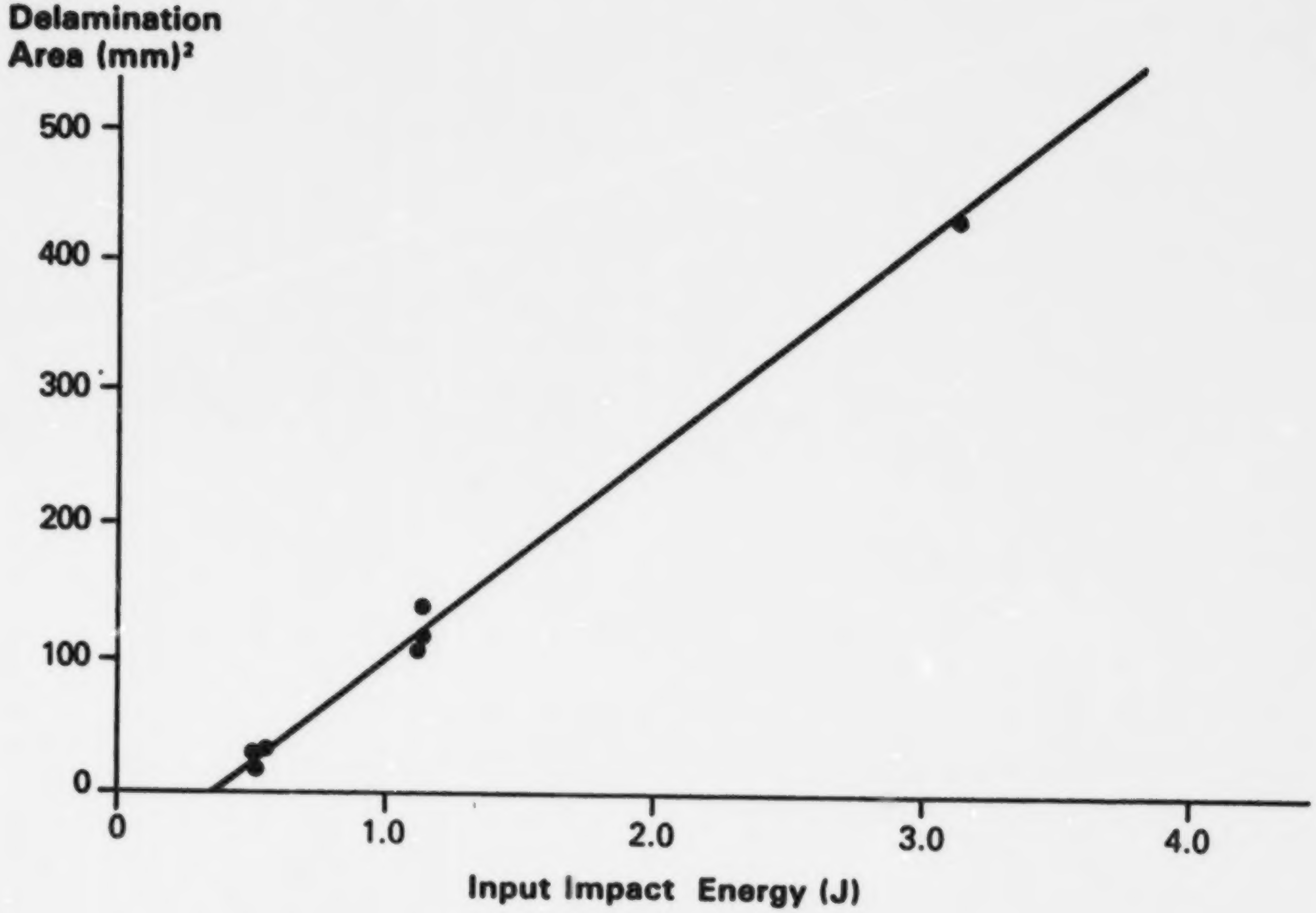

Figure 3 Delamination Area v Impact Energy Plot for $[\pm 45]_{2s}$ Laminate of T-300/934

[Estimated energy to delaminate = 0.35 Joules (±0.1)]

Analysis of all eight force-deflection curves in terms of the energy absorbed by a specimen at the point of crack initiation provides a mean value of 0.23 Joules with a standard deviation of 0.014 Joules. It appears that this tension cracking mechanism occurs with some consistency.

All eight specimens were C-scanned after impact and all revealed some C-scan damage. Figure 3 presents a graph of the area of C-scan damage versus input impact energy where a straight line can be fitted to the data. On the assumption that this C-scan damage is mainly delamination, then it can be argued that the input energy commensurate with zero C-scan damage is a good approximation to the energy required to create delaminations. In this case, a value of 0.35 Joules is obtained.

The quality of general fit of a straight line to these plots of C-scan damage area versus input energy is patchy. Consequently, the certainty involved in using this method for determining the initiation energy for delamination cannot be claimed to be high. In this particular instance, it seems to work well, in other cases it is less good.

For the case of $[\underline{+}45]_{2S}$ laminates of T-300/934, it can be noted that the initiation energy for delamination (0.35 Joules) is considerably larger than the tension splitting initiation energy (0.23 Joules). This increases confidence in the identification of tension splitting as the first failure process during impact, at least for this specific laminate.

Attempting to associate or identify some feature on the force-deflection curves at the energy level commensurate with initiation of delamination is also varied. Occasionally, there would appear to be some minimum in the smoothed force-deflection curve; yet on other occasions there is an absence of any obvious feature. Considerable care is therefore recommended in the identification of the onset of delamination by inspection of a force-deflection curve. This will be further commented on when all results are being discussed.

4 DISCUSSION OF EXPERIMENTAL RESULTS

The methodology in analysing the results was discussed in Section 3; it is now possible to summarise the results for all the samples. This will be presented in two parts. First, an indication of the force-deflection curves for the three different laminate systems discussed in Section 2.1, together with an indication of where, along these force-deflection curves, evidence from photographed impact was collected. Second, a quantitative summary of the impact energies required to achieve cracking and delamination damage.

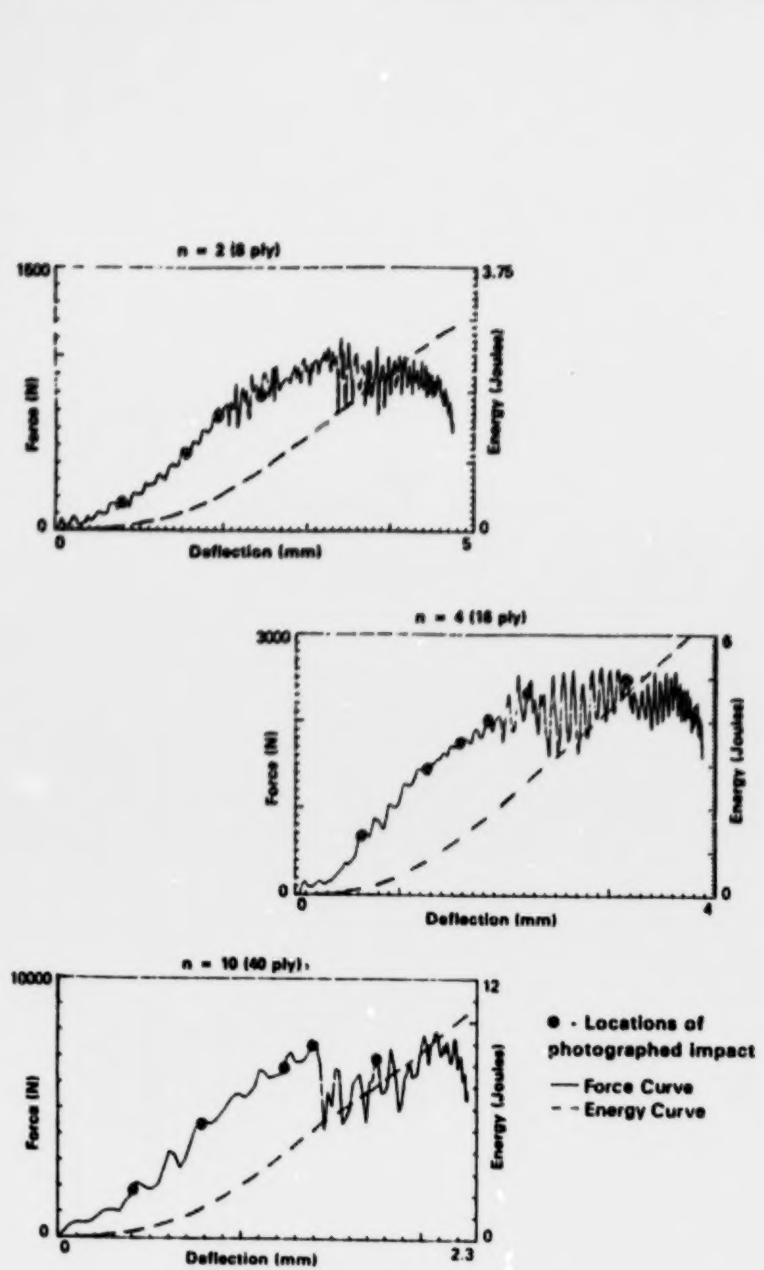

Figure 4 Force-Deflection, Energy-Deflection Curves for $[\pm 45]_{ns}$ Laminates of AS4/PEEK

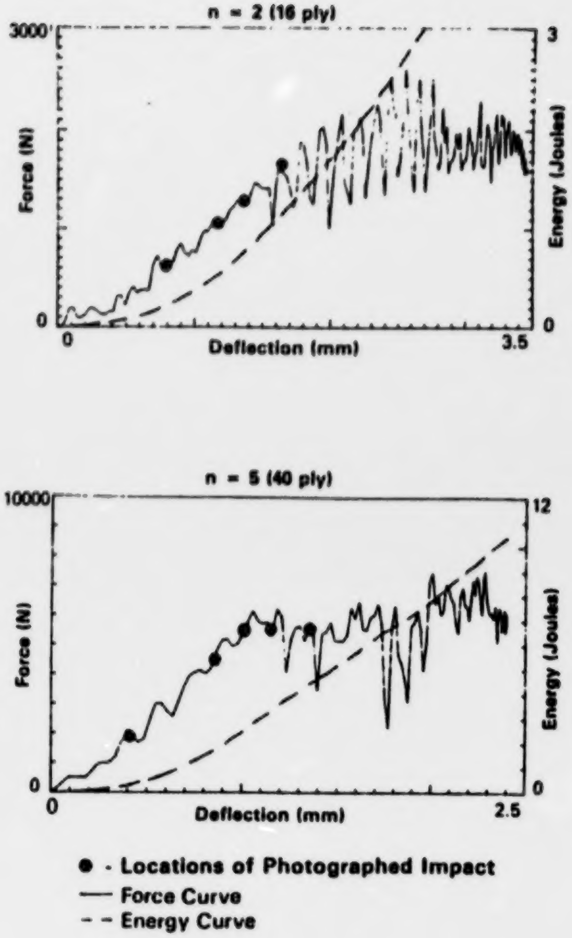

Figure 5 Force-Deflection, Energy-Deflection Curves for $[-45/0/+45/90]_{ns}$ Laminates of AS4/PEEK

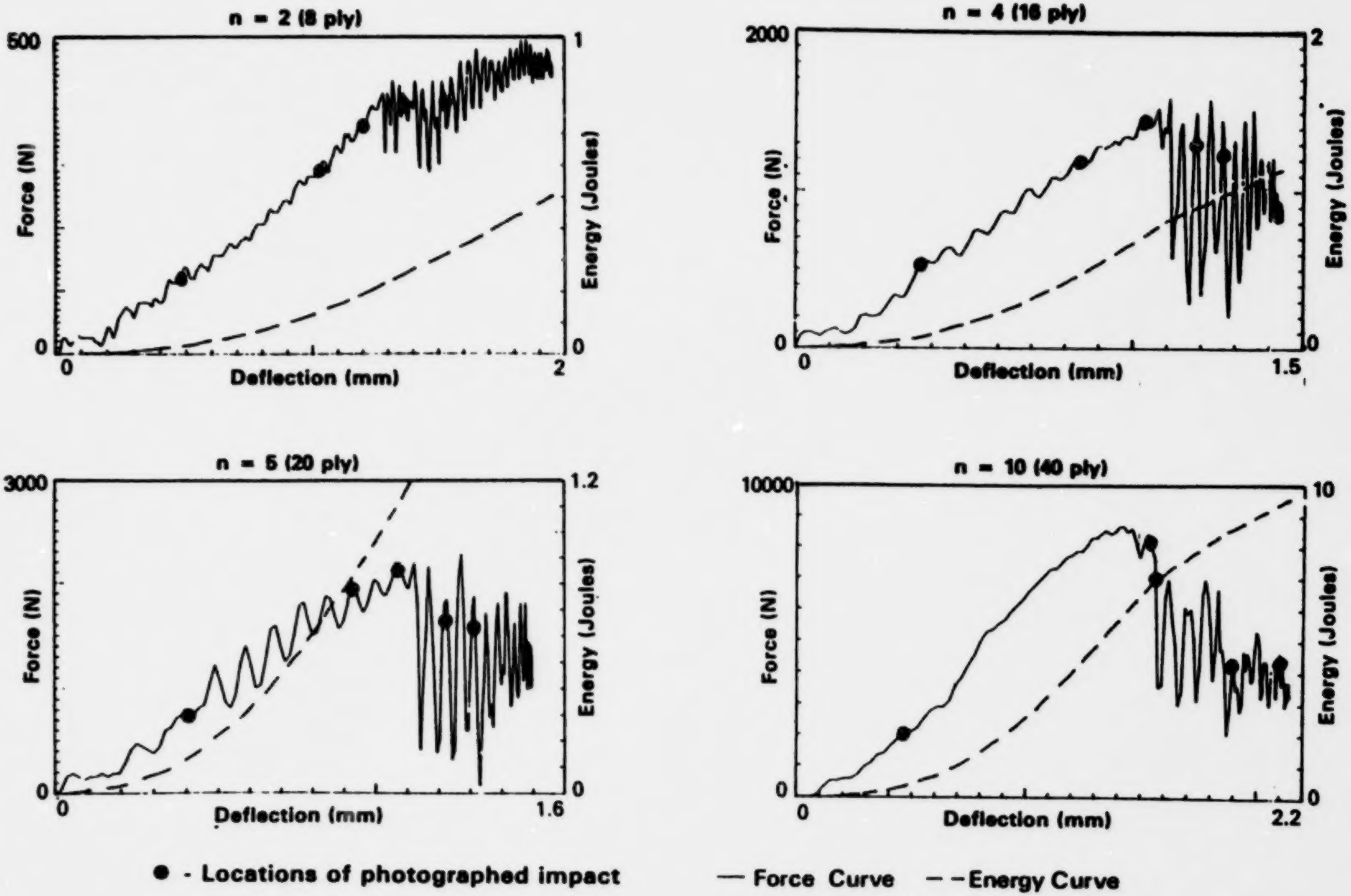

Figure 6 A selection of Force-Deflection, Energy-Deflection Curves for $[\pm45]_{ns}$ Laminates of T-300/934

4/15

	ABSORBED ENERGY AT CRACK INITIATION (JOULES)	APPROX. ENERGY FOR INITIATION OF DELAMINATION (JOULES)	APPROX. SAMPLE THICKNESS (MM)
$[\pm 45]_{2S}$	0.56 (0.11)	0.7	1.0
$[\pm 45]_{4S}$	1.4 (0.4)	1.7	1.5
$[\pm 45]_{10S}$	4.6 (0.4)	5.4	5.0
$[-45/0/+45/90]_{2S}$	0.93 (0.14)	NO ESTIMATE POSSIBLE	1.5
$[-45/0/+45/90]_{5S}$	3.5 (0.15)	4.0	5.0

TABLE 1 SUMMARY OF LOW ENERGY IMPACT RESULTS FOR AS4/PEEK LAMINATES

	ABSORBED ENERGY AT CRACK INITIATION JOULES	APPROX. ENERGY FOR INITIATION OF DELAMINATION (JOULES)	APPROX. SAMPLE THICKNESS (MM)
$[\pm 45]_{2S}$	0.23 (0.014)	0.35	1.2
$[\pm 45]_{4S}$	0.78 (0.07)	0.4	2.5
$[\pm 45]_{5S}$	1.2 (0.11)	1.2	3.0
$[\pm 45]_{10S}$	6.0 (0.79)	NO ESTIMATE POSSIBLE	6.1

TABLE 2 SUMMARY OF LOW ENERGY IMPACT RESULTS FOR T-300/934 LAMINATES

Figure 4 illustrates typical low energy impact curves for $[\underline{+}45]_{ns}$ laminates based on AS4/PEEK; the three figures relate to the three sets of ply sequences (n= 2, 5 and 10). The locations of some of the key photographed impacts are also included in Figure 5. The onset of higher frequency oscillations in the force-deflection curve can readily be associated with tension surface cracking. This observation was independent of the number of plies in the laminate.

Figure 5 illustrates similar results for the two $[-45/0/+45/90]_{ns}$ laminates. A similar conclusion was made, in that the onset of higher frequency oscillations in the force-deflection curve, corresponded to tension surface cracking.

Figure 6 illustrates the corresponding impact curves for $[\underline{+}45]_{ns}$ laminates of T-300/934. A similar conclusion emerged, namely the onset of higher frequency oscillations (and also the principal peak) in the force deflection characteristic corresponded with tension surface cracking.

Identification of the energy absorbed by the specimens in order to achieve tension surface cracking could readily be achieved. These data, together with an estimate of energy to initiate delamination damage (according to section 3) are summarised in table 1 for the two types of laminates based on AS4/PEEK and in table 2 for the laminates of T-300/934. Several comments can be made with reference to these tables:-

(i) It is evident from both tables 1 and 2 that the energy for crack initiation is less than that for initiation of delamination damage. The sole anomalous result is for the $[\pm 45]_{4S}$ laminate of T-300/934, although this might relate to the difficulty in using this method for determining the onset of delamination damage. It is therefore apparent that the first failure event in impact is tension surface splitting and that delamination processes occur at larger absorbed energies.

(ii) The results for the $[\pm 45]_{ns}$ laminates show that the energies to initiate cracks in the tension surface and to initiate delamination damage relates to the fracture toughness of the matrix material. These energies are higher for AS4/PEEK than T-300/934 at equivalent thickness where it would be expected that a critical strain energy release rate for PEEK based composites is larger than that for composites based on 934 (12,13). This implies that these low energy impact procedures have sufficient resolution to quantitatively resolve composites based on different matrix systems.

(iii) The energy corresponding to that for the onset of delamination damage could not be correlated with an obvious feature on the force-deflection impact curves. Therefore, it would seem that impact tests alone are not sufficient to detect delamination damage.

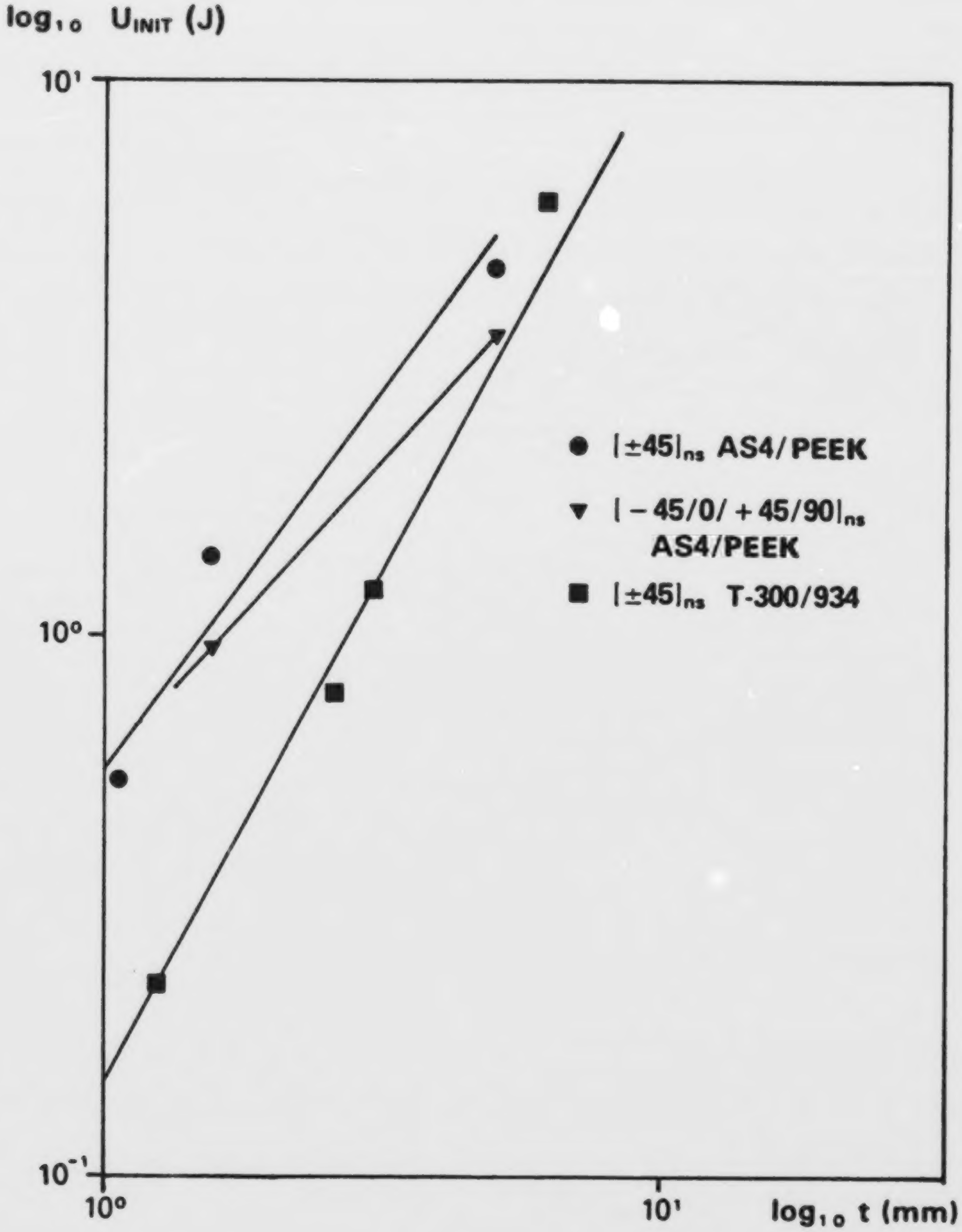

Figure 7

Energy to initiate tension surface cracks as a function of laminate thickness for AS4/PEEK and T-300/934

(iv) As the laminate thickness increases, so the energy to initiate tension surface cracks becomes similar to the apparent energy to initiate delamination damage. For example, for laminates with 40 plies, these energies are similar in magnitude. This has implications for tests such as compression after impact, particularly since it is apparent that the matrix in the composite also influences the energy threshold for the introduction of damage.

(v) The relationship between specimen thickness and energy to initiate tension surface cracks is plotted in Figure 7, from the data in tables 1 and 2. Using double logarithmic axes, the results can be fitted to a power law relationship. This graph highlights the difference in energy to initiate cracks at a particular laminate thickness in terms of matrix type and lay-up geometry. For example, less energy initiates a tension surface crack in $[-45/0/+45/90]_{ns}$ compared with $[\pm 45]_{2ns}$. It seems likely that the presence of the 0 or 90 fibres encourages the formation of intralaminar cracks.

5 CONCLUSIONS

The first failure event observed via a force-deflection curve in an instumented falling weight impact test on a plate type specimen is tension surface splitting. This would seem to be independent of the ply numbers for multi-angle laminates based on thermoplastic (PEEK) and thermoset (Epoxy system 934) matrix materials in continuous carbon fibre composites.

Delamination damage is also known to occur with impact of these laminates but could not be associated with a special feature in the force-deflection curve.

The energy to initiate delamination damage is generally larger than that required to initiate a tension surface split for the test geometry selected in this work.

6 ACKNOWLEDGEMENT

The authors acknowledge the help of colleagues in Fiberite for the preparation of the T-300/934 laminates and the APC-2 laminates.

7 REFERENCES

1 Leach D C, Moore D R, 'Toughness of Aromatic Polymer Composites Reinforced with Carbon Fibres' Composites Sci & Tech, 23 (1985) p131-161.

2 Rhodes M D, Williams J G, Starnes J H, 'Low Velocity Impact Damage in Graphite Fiber Reinforced Epoxy Laminates' Proc SPI RP/CI Conf, New Orleans 1979.

3 Byers B A, 'Behaviour of Damaged Graphite/Epoxy Laminates Under Compression Loading' NASA Contractor Report CR-159293, August 1980.

4 Moore D R, Prediger R S, 'Photographed Impact of Continuous Fibre Composites' Winter Composites Symposium, Seattle Dec 1985, T B P, A C S J 1988.

5 Nixon J A, Phillips M G, Moore D R, Prediger R S, 'A Study of the Development of Impact Damage in Cross-Ply CF/PEEK Laminates, Using Acoustic Emission. T B P, Comp. Sci & Technology 1987.

6 Crick R A, Leach D C, Moore D R, 'Interpretation of Toughness in Aromatic Polymer Composites Using a Fracture Mechanics Approach' SAMPE Journal, Dec 1986.

7 Gutteridge P A, Hooley C J, Moore D R, Turner S, Williams M J, 'A Versatile System of Impact Tests and Data'. Kunststoffe 72, 9, p543 1982.

8 Jones D P, Leach D C, Moore D R, 'On the Application of Instrumented Falling Weight Impact Testing to the Toughness of Thermoplastics'. Plast & Rub. Proc & Appl. 6, 1986 pp 67-79.

9 Johnson A E, Moore D R, Prediger R S, Reed P E, Turner S, 'The Falling Weight Impact Test Applied to Some Glass Fibre Reinforced Nylons. Part 1, Appraisal of Method'. 21 (1986) 3153-3161.

10 Johnson A, Sims G, Private communication. NPL, Teddington, England.

11 Johnson A E, Moore D R, Prediger R S, Reed P E, Turner S, 'The Falling Weight Impact Test Applied to Some Glass Fibre Reinforced Nylons. Part 2 Some Results and Interpretations'. J Mat Sci 1987.

12 Curtis D C, Leach D C, Tamblin D R, 'The Delamination Behaviour of Aromatic Polymer Composite APC-2'. ASTM Symposium on Toughened Composites, Houston, Texas March 1985.

13 Fiberite data sheet, Fiberite, Winona.

INTERLAMINAR STRESSES IN TAPERED LAMINATES

by

S.V. Hoa, J. Daoust, B.L. Du and T. Vu-Khanh*
Department of Mechanical Engineering
Concordia University
Montreal, Que., Canada, H3G 1M8

*National Research Council of Canada
Industrial Materials Research Institute
Boucherville, Que., Canada, J4B 6Y4

Presented at the 8th annual NRCC/IMRI symposium "Composites-'87",
November 5 and 6, 1987, Boucherville, Que., Canada

1. Abstract:

Tapered laminates of unidirectional layers of glass/epoxy and graphite/epoxy are investigated. These laminates have thickness variation along their length. This was accomplished by having layers dropped-off near mid-length of the laminate. Stress and strain variations were obtained using three dimensional finite element models. Calculated values using finite element method compare well with experimental results on the point of first delamination. This agreement allows determination of a suitable finite element mesh for subsequent model for other tapered laminates with fiber orientations other than unidirectional.

a)

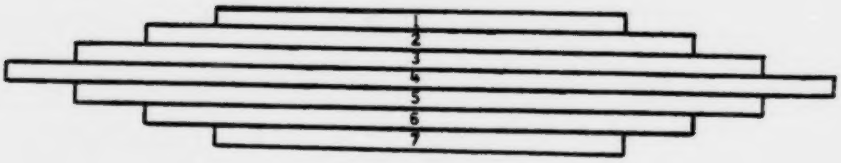

b)

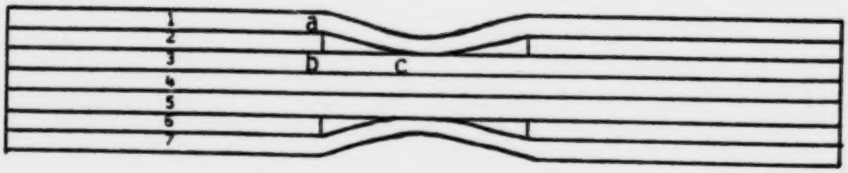
1
2
3
4
5
6
7
a
b
c

Figure 1: Two possible kinds of layer drop-offs

2. Introduction:

Due to their light weight, high strength and good fatigue resistance, composites have found many applications in the transportation industry. For some applications, laminates with variation in thickness (tapered) are desirable. One such application is the composite flywheel [1] where thickness of the flywheel decreases in the outward direction. This decrease is to take into account the variation of the centrifugal force in the radial direction. Another application is the helicopter yoke. This yoke is usually made of glass/epoxy. The yoke is tapered with thinner section at mid-length and thicker sections at two ends. The thinner mid-section allows flexibility for the yoke to accommodate flapping.

In the above applications, thickness variation is obtained by terminating some laminate layers part way in the laminate. Such part way layer termination is called layer drop-off. There can be two kinds of drop-offs as shown in figure 1. Figure 1a shows the case of external drop-off. In this figure, only layer 4 has no drop-off whereas other layers are dropped-off at two ends resulting in shorter lengths. Analysis of this kind of drop-off using finite element method was attempted by Wu and Webber [2], [3]. Figure 1b shows the case of internal drop-off. In this figure, layers 3, 4 and 5 have full length. Layers 2 and 6 are dropped-off within the laminate. Layers 1 and 7 also have full length, but are curved at the middle section of the laminate. At mid-length, layer 1 bonds with layer 3 and layer 7 bonds with layer 5. Depending on the flow of the resin and fabricating conditions, wedge ABC (figure 1) formed by the drop may or may not be filled with resin.

Figures 1a and 1b only show the schematic of the most simple tapering arrangement. Laminates used in actual applications contain many more layers and many more drop-offs. Wedges such as ABC can be short or long depending on fabrication process.

Obviously stress concentrations occur in the vicinity of wedges such as ABC. Interlaminar stresses no doubt exist. The stress, strain distributions and magnitudes of those values depend on fiber orientation, location of the drop-off, shape of wedge ABC, type of material and also loading conditions. Such a complicated structure requires the finite element method for solution. In addition, three dimensional elements are essential due to the three dimensional nature of the stress. However, it is known that finite element results for interlaminar stresses depend on the finite element mesh size [4], it is therefore necessary as a first step to determine the finite element mesh. Also, as typical of any stress determination in a defect region in composite laminates, a large number of elements is required [4]. Such a large number of three dimensional elements cannot be handled in a single run with existing computers and therefore sub-modeling will be necessary (figure 11).

In this paper, the most simple form of tapered laminates will be presented. Laminates containing unidirectional layers with internal drop-offs were studied. These laminates were fabricated and examined under microscope so that corresponding finite element models can be made. Experimental results were compared with finite element results to determine the workability of the finite element mesh.

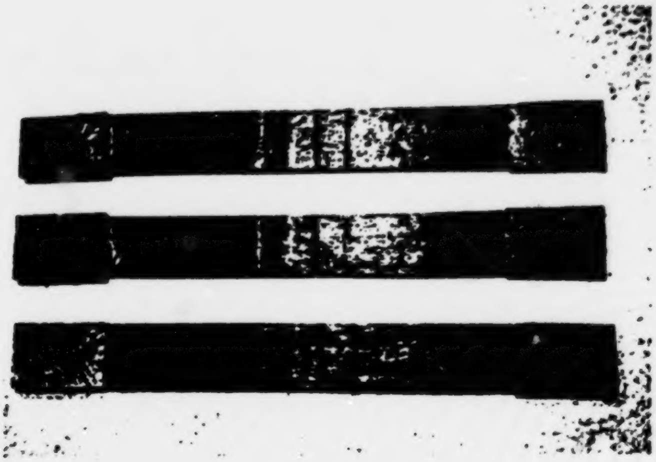

FIGURE 2: Photograph of graphite/epoxy tapered specimen

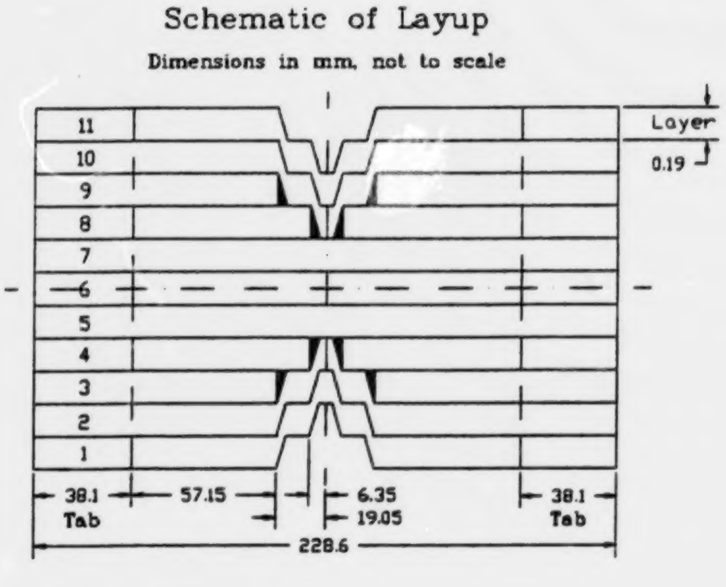
Schematic of Layup
Dimensions in mm, not to scale
11
10
9
8
7
6
5
4
3
2
1
Layer
0.19
38.1
Tab
57.15
6.35
19.05
38.1
Tab
228.6

FIGURE 3: Schematic of layup

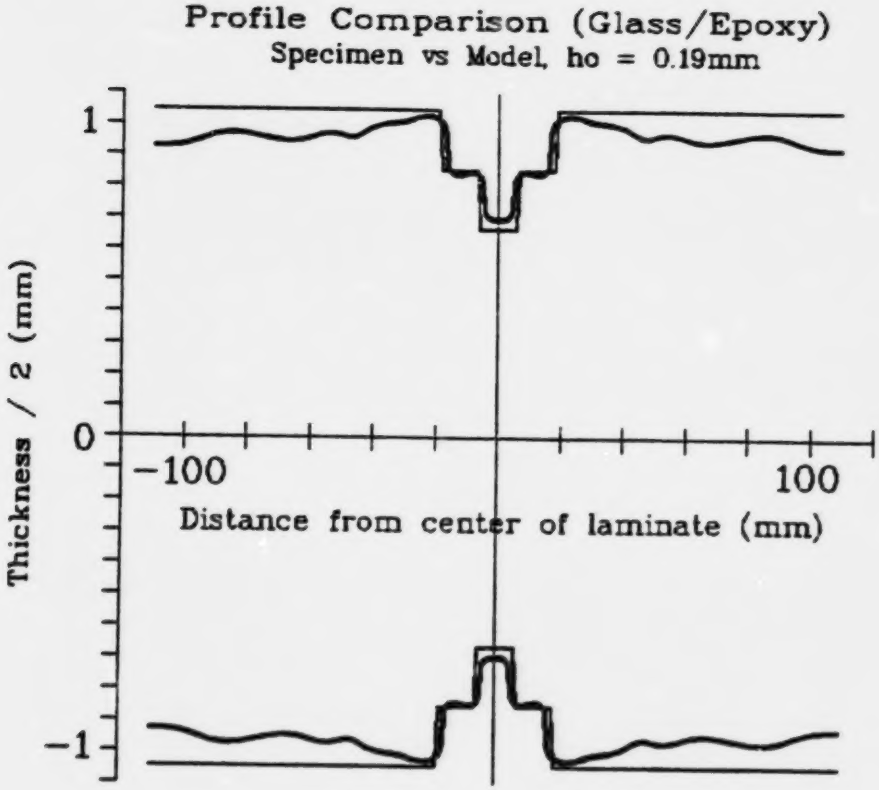

FIGURE 4: Profile comparison (glass/epoxy)

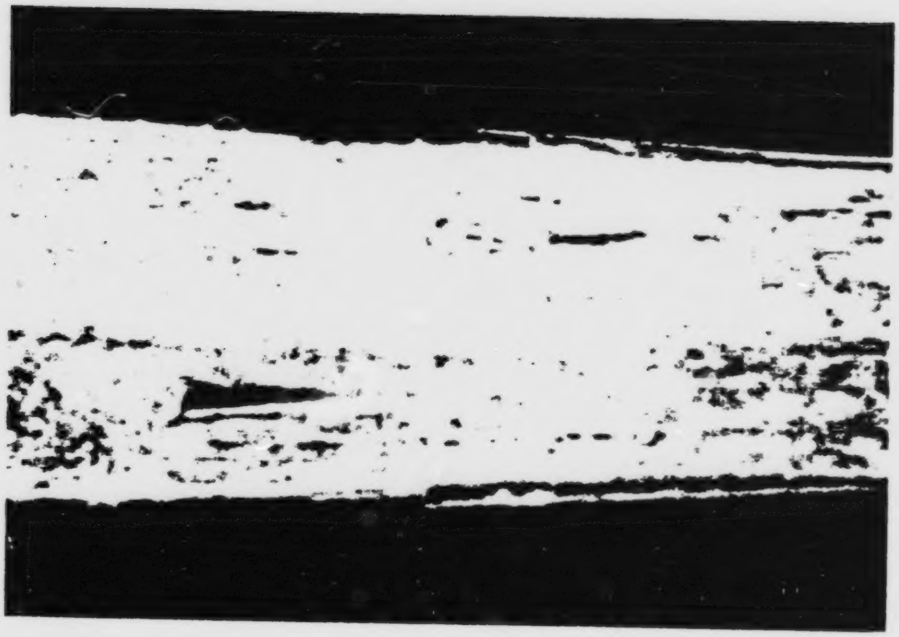

Figure 5: Photograph of graphite/epoxy drop-off regions

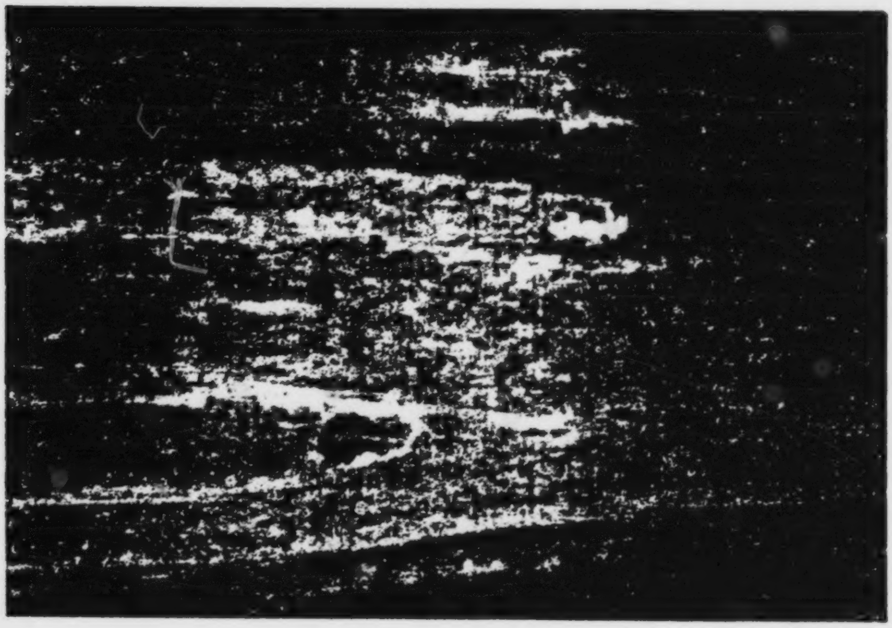

Figure 6: Photograph of glass/epoxy drop-off regions

3. Experiments:

In order to have a reasonable amount of tapering, two drop-offs were used in the laminate. A special mold was made to accommodate the change in thickness. Plates of 305 x 102 mm can be made from this mold. Tapered plates of graphite/ epoxy and glass/epoxy were made. Three samples for each material of 25.4 x t x 228.6 mm were cut from the plates for testing. Typical photographs of tapered laminate specimens are shown in figure 2. These specimens contain eleven (11) layers (see figure 3). Layers 5, 6, and 7 are straight and unaltered. They have a gage length of 152.4 mm. Layers 4 and 8 are dropped-off at the center with a missing length of 12.7 mm. Layers 3 and 9 are dropped-off further with a missing length of 38.1 mm. Note that in figure 3, the z dimension is magnified which results in a false appearance of layers being squeezed at the drop-off.

Figure 4 shows the actual profile of the edge of a specimen and that of the model used for finite element. The actual profile is shown by a curved line whereas in the finite element model the profile is discretized into steps. This discretization is an approximation and its workability will be determined when finite element results and experimental results are compared.

Figures 5 and 6 show the appearance of wedges like ABC in figure 1b for graphite/epoxy and glass/epoxy samples respectively. Some wedges are filled with resin and some are not. Most wedges in graphite/epoxy samples are dry and most wedges in glass/epoxy are filled with resin. It was discovered subsequently that because the graphite/epoxy prepregs were too old (more than two years) they did not produce good samples. Only experimental results from the glass/epoxy samples will be compared with finite element results. An ultrasonic C scan of the glass/epoxy sample

FIGURE 7: Ultrasonic C scan of glass/epoxy sample

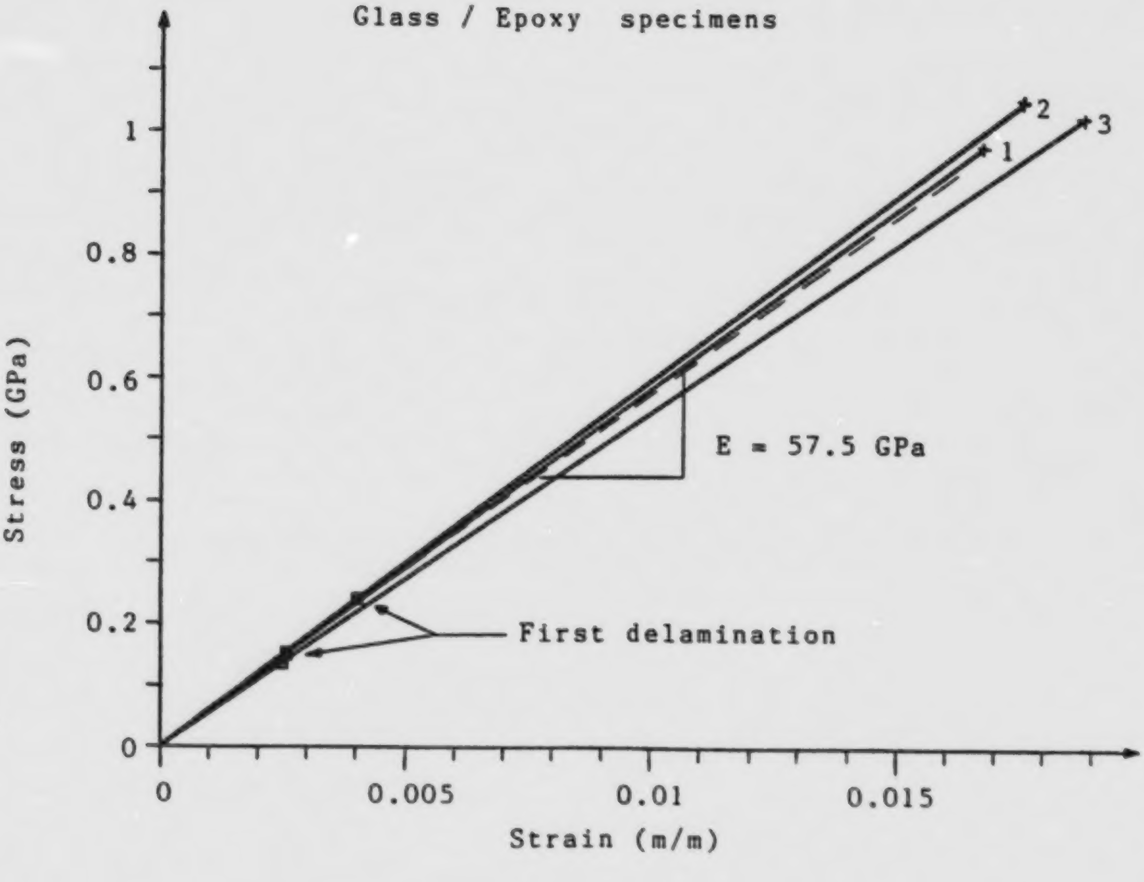

FIGURE 8: Stress-strain curves for glass/epoxy specimens

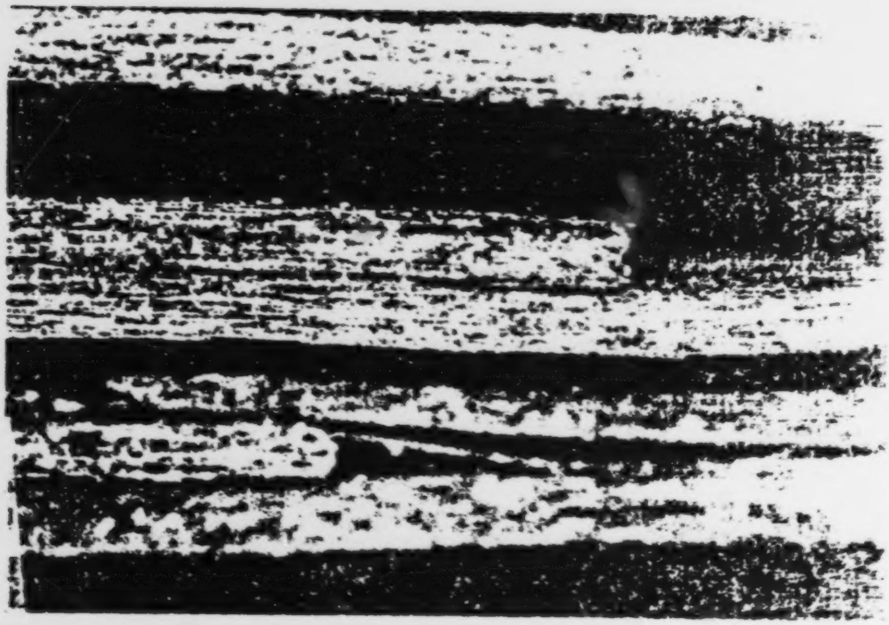

Figure 9: Photograph of ruptured graphite/epoxy drop-off regions

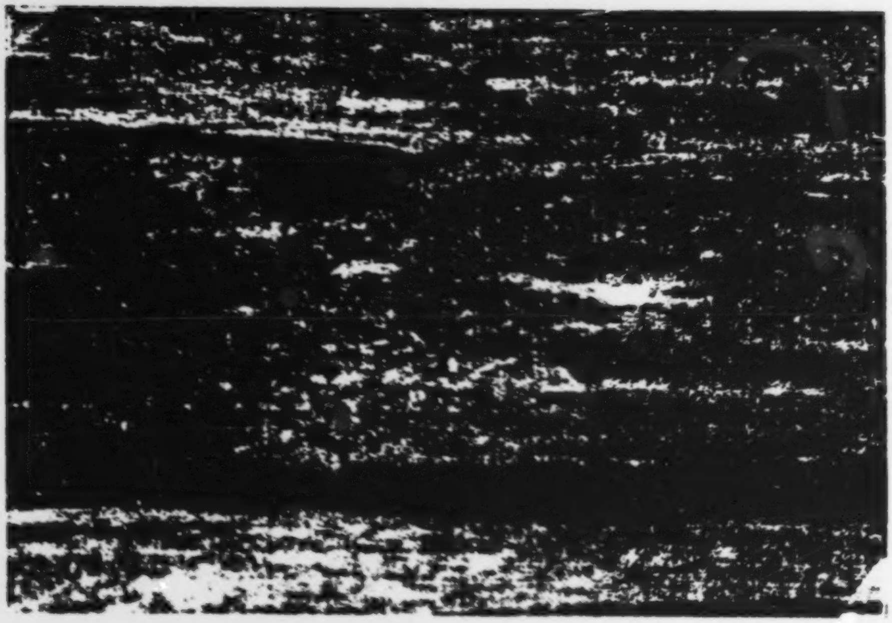

Figure 10: Photograph of ruptured glass/epoxy drop-off regions

(figure 7) indicates that only locations near the drop-off show defects, whereas other areas show no defect.

Tapered laminate coupons were tested under tension on an MTS testing machine at a rate of 5mm/minute. The strain was measured at the thinnest section using an extensometer. Stress-strain curves for the glass/epoxy samples are shown in figure 8. Stresses were calculated based on the smallest cross section at the center of the laminate. During loading, there was a loud and clear "plink" at intermediate loads. These are indicated with a square sign in the curves of figure 8. Two samples (1 & 2) were taken out after this acoustic emission event and their edges examined in the microscope. It was found that delamination has taken place along the trailing end of the wedge. Stress corresponding to this delamination was subsequently used for comparison with finite element results. It was noted that even after the acoustic emission event occurred, the load-strain curve remained straight and there was no change in slope. This can be attributed to the tensile test done along fiber direction where properties are fiber dominated.

The results from the three samples are fairly consistent giving an average modulus of E = 57.5 GPa, STD = 2.2 GPa and strength of σ_u = 1.02 GPa, STD = 0.03 GPa. The average modulus is larger than that of scotchply 1002 (38.6 GPa [5]) and the strength is comparable to that of scotchply 1002 (1.062 GPa [5]).

All sample fractured along the longitudinal direction. Figures 9 and 10 show the edge view of fractured graphite/epoxy and glass/epoxy samples respectively. Delamination occurred along the trailing edge of the wedge and spread out to both sides of the dropped-off layer. In the case of glass/epoxy samples, other layers remain intact.

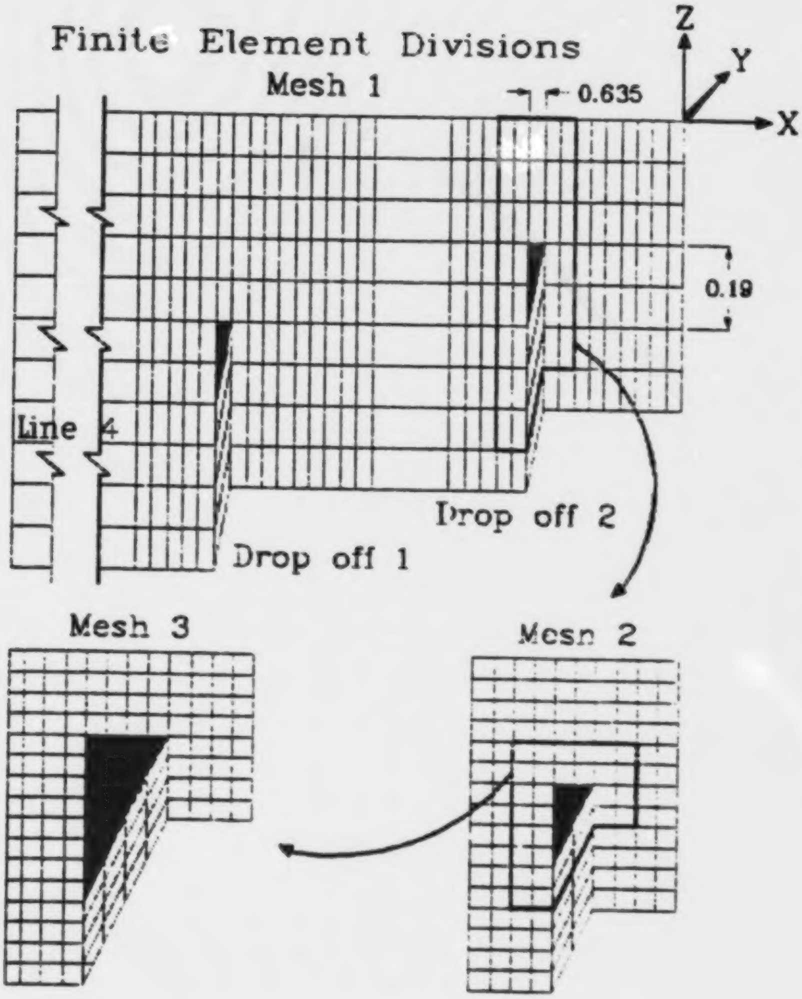
Finite Element Divisions
Z
Y
X
Mesh 1
0.635
0.19
Line 4
Drop off 2
Drop off 1
Mesh 3
Mesh 2

FIGURE 11: Finite element model and refinements

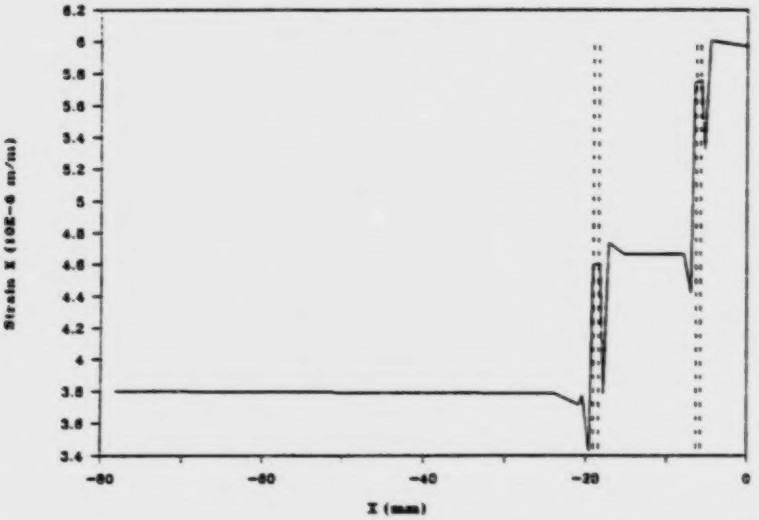

FIGURE 12a: Normal strain ε_x distribution along X axis at 6.35 mm < y < 12.7 mm at line 4 (graphite/epoxy)

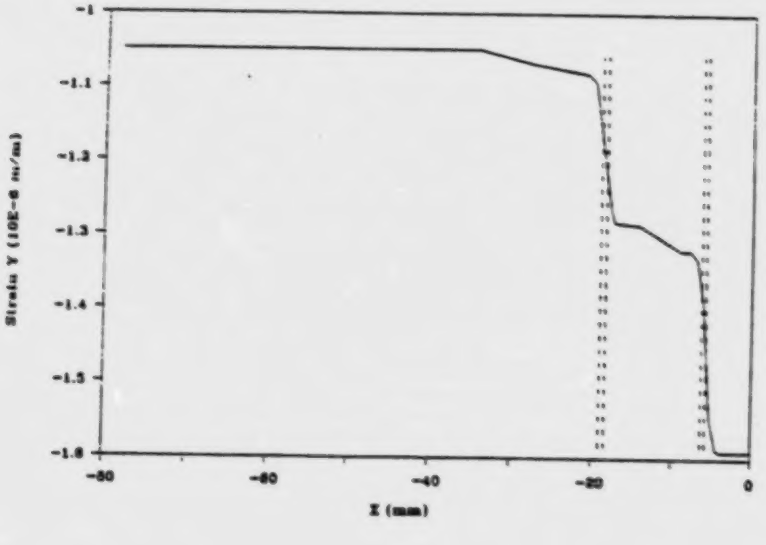

FIGURE 12b: Normal strain ε_y distribution along X axis at 6.35 mm < y < 12.7 mm (graphite/epoxy)

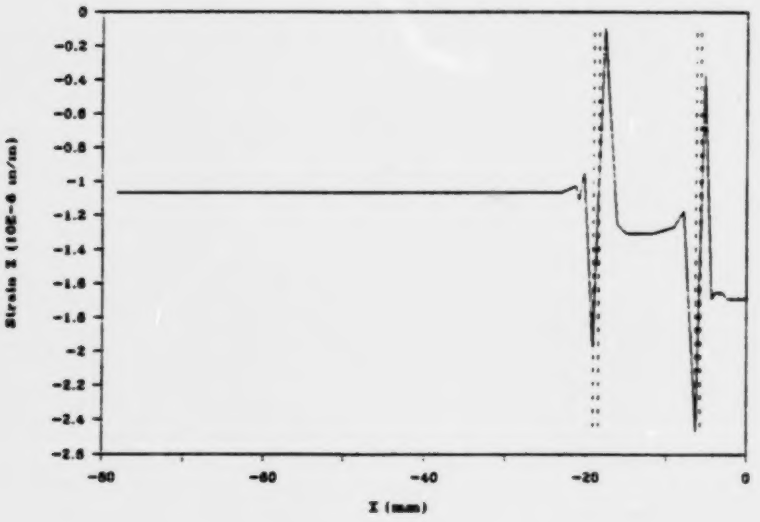

FIGURE 12c: Normal strain ε_z distribution along X axis at 6.35 mm < y < 12.7 mm (graphite/epoxy)

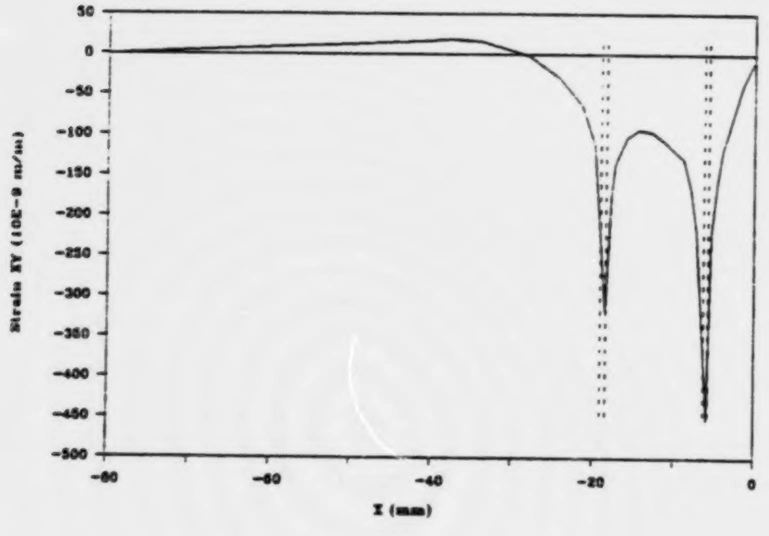

FIGURE 12d: Shear strain ε_{xy} distribution along X axis at 6.35 mm < y < 12.7 mm (graphite/epoxy)

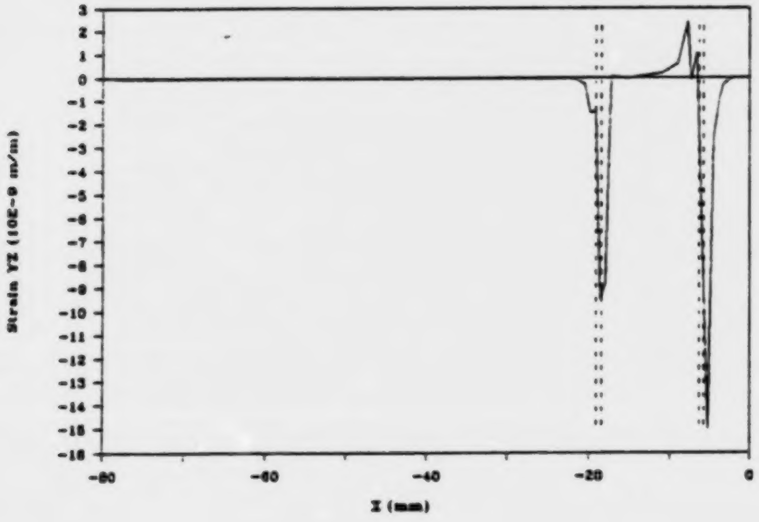

FIGURE 12e: Shear strain ε_{yz} distribution along X direction at 6.35 mm < y < 12.7 mm (graphite/epoxy)

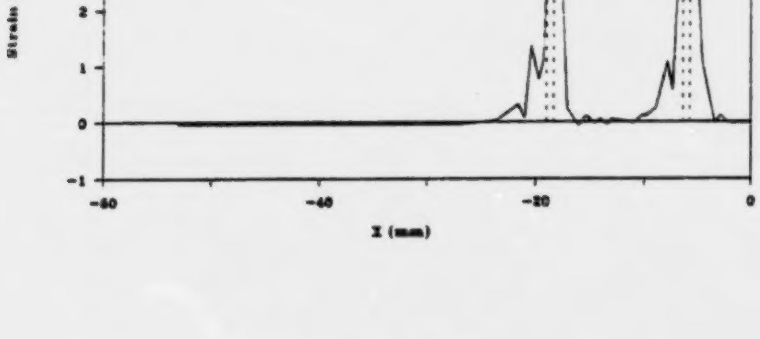

FIGURE 12f: Shear strain ε_{xz} distribution along X direction at 6.35 mm < y < 12.7 mm (graphite/epoxy)

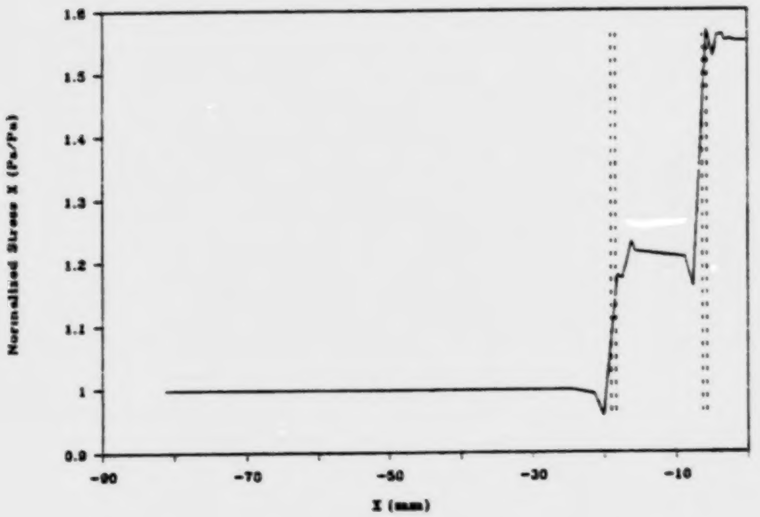

FIGURE 13a: Normalized normal stress σ_x distribution along X direction at $6.35 < y < 12.7$ mm (graphite/epoxy)

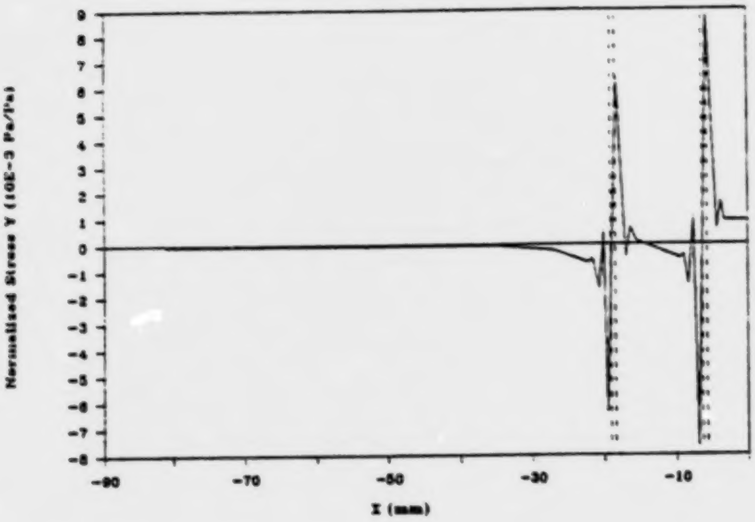

FIGURE 13b: Normalized normal stress σ_y distribution along X direction at $6.35 < y < 12.7$ mm (graphite/epoxy)

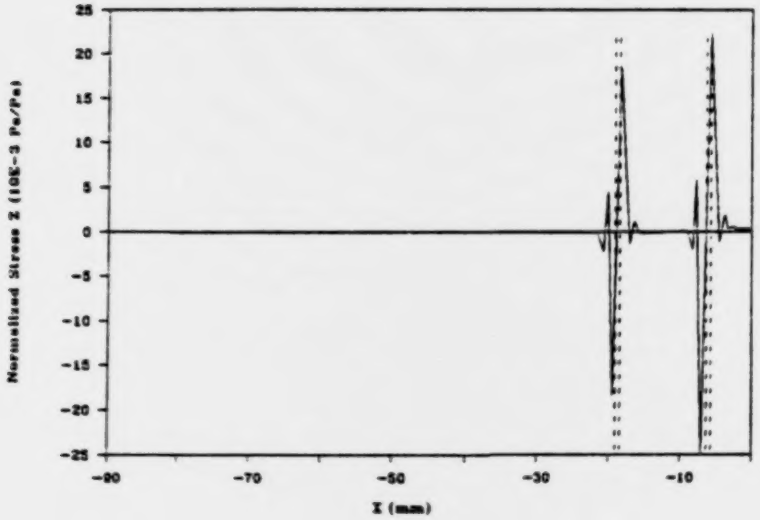

FIGURE 13c: Normalized normal stress σ_z distribution along X direction at $6.35 < y < 12.7$ mm (graphite/epoxy)

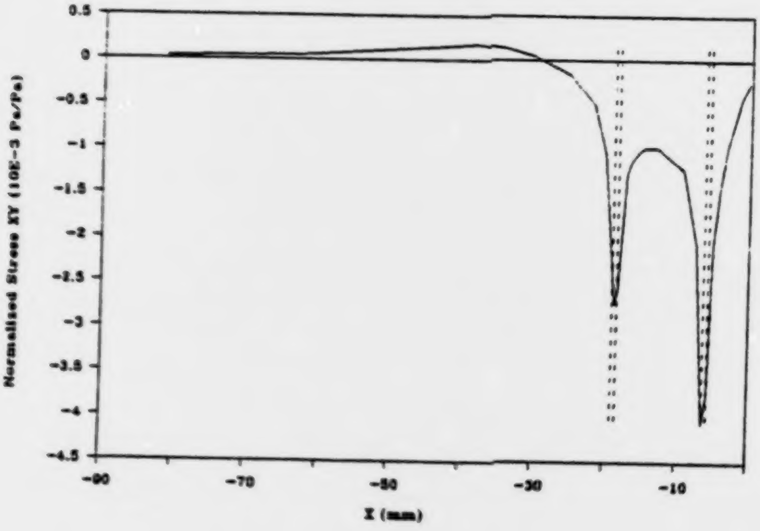

FIGURE 13d: Normalized shear stress σ_{xy} along X direction at $6.35 < y < 12.7$ mm (graphite/epoxy)

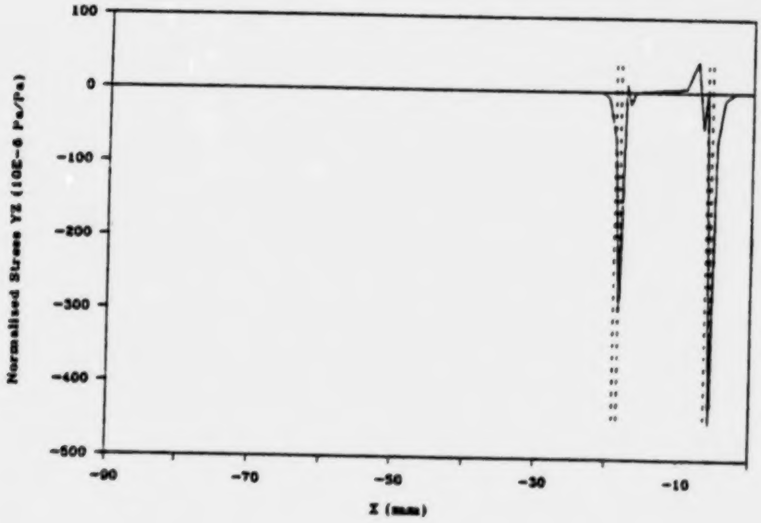

FIGURE 13e: Normalized shear stress σ_{xz} distribution along X direction at 6.35 < y < 12.7 mm (graphite/epoxy)

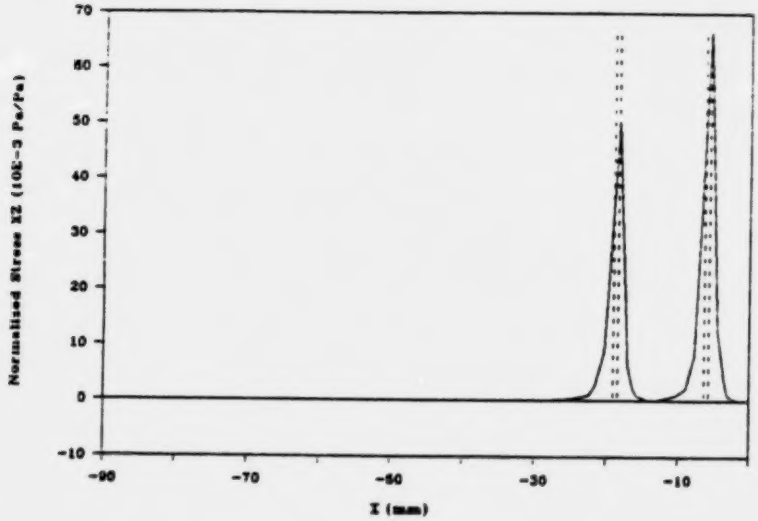

FIGURE 13f: Normalized shear stress σ_{xz} distribution along X direction at 6.35 < y < 12.7 mm (graphite/epoxy)

Table 1: Material properties used in finite element model

	graphite / epoxy*	glass / epoxy*	epoxy resin**
E_x (GPa)	181.	38.60	3.42
$E_y = E_z$ (GPa)	10.3	8.27	3.42
$G_{xy} = G_{xz}$ (GPa)	7.17	4.14	1.29
G_{yz} (GPa)	1.26	1.26	1.29
$\nu_{xy} = \nu_{xz}$	0.28	0.26	0.33
ν_{yz}	0.30	0.30	0.33
X (MPa)	1500.	1200.	72.4
Y (MPa)	40.	31.	72.4
S (MPa)	68.	72.	36.2***

* Values taken for T300/5208 and scotchply 1002 from [5]

** Values vary for different resin systems. Numbers used here are for anhydrid-cured epoxy resin system in [7]

*** Shear strength are approximated to be half of tensile strength

4. Finite element calculations:

Tapered laminates were modeled using three dimensional finite elements. Element number STIF 45 of program ANSYS was used. STIF 45 has been found to be a very good element for stress analysis in other applications. With this element, the material properties can follow the layer's dz/dx slope. Even though the element has only 8 nodes, the displacement varies quadratically with space variable giving a linear strain and stress distribution within the element [6].

Regions around the drop-off were modeled according to configurations observed on the laminates as shown in figures 5 & 6. Due to symmetry, only one eighth of the laminate is modeled. Three successive finite element meshes were used to study the effect of mesh size on the stresses. The sub-modeling is shown in figure 11. From the results of the first mesh, a section was taken out for mesh refinement in the second mesh. Nodal displacements from the first mesh were imposed on the cut out section with interpolation for displacement of new nodes on the boundary. Similar approach was performed as one goes from mesh 2 to mesh 3. A uniform tension σ_x of 0.69 MPa was applied at the larger end of the model. Data used for finite element model are shown in table 1.

Stress and strain variations obtained from finite element mesh 1 are shown in figures 12 and 13. Figures 12a - 12f show the strain distributions along the x direction at elements between y = 6.35 and 12.7 mm. Among the six strains ϵ_x, ϵ_y ϵ_z and ϵ_{xz} are of the order of 10^{-6} whereas strains ϵ_{xy} and ϵ_{yz} are of the order of 10^{-9}. The strain distributions are uniform and only peak out in the small vicinity of the drop-off. The width of this small disturbed region is about 3 mm. Figures 13a - 13f show the normalized stress distribution along the x direction between y = 6.35

mm and 12.7 mm. These stresses are normalized by dividing by the applied stress of 0.69 MPa. Normalized stress σ_x varies between 1 from the end of the laminate to a value of 1.57 at the other end. Apart from the fluctuations, this increase is not due to the discontinuity at the drop-offs, but due to the reduction in area at the center of the laminate (7 layers at the center as compared to 11 layers at the end, $11/7 = 1.57$). Normalized stress σ_y is small (1%) and does show fluctuation at the drop-off. Normalized stress σ_z show a similar distribution as σ_y but magnitudes of σ_z are about 2 times as large. Among the three normalized shear stresses, σ_{xz} exhibits largest values (about 7% of the applied stress). The strain and stress results show that strains ϵ_z, ϵ_{xz} and stresses σ_z, σ_{xz} are most severe. This corresponds with the delamination along the trailing edge of the drop as observed in figures 9 and 10.

Due to the steep gradients of strain and stress distribution in the vicinity of the drop-offs in figures 12 and 13, only the distribution should be valid, the absolute values should be examined further in finer meshes of finite elements. The nature of fluctuations in σ_z and σ_{xz} distributions show that singularity exists at the drop-off. In that case, the use of finer and finer meshes can only approach the results but may not give exact values. Due to constraints of computer resources, only two further meshes were used as shown in figure 11. For glass/epoxy, maximum values of normalized σ_{xz} in going from coarse to finer meshes are 0.17, 0.33 and 0.42. The difference between the second and the first is 94% and that between the 3rd and 2nd result is 27%. This decrease in difference indicates the results are converging. A similar behavior is observed for the normalized stress σ_z.

5. Comparison between finite element and experimental results:

Examination of figure 8 shows that the acoustic emission event occurred at stresses in the thinnest (middle) section of from 140 to 240 MPa. This translates into an applied stress at the thick section of 89.09 to 152.7 MPa. Using the finest mesh finite element result, the interlaminar stress σ_{xz} varies from 37.4 MPa (89.09 x 0.42) to 64.1 MPa (152.7 x 0.42). Using the approximated value of shear strength S of glass/epoxy and pure epoxy in table 1, the calculated value is more than shear strength of pure epoxy and less than that of glass/epoxy. Corresponding values for σ_z are smaller but similar comparison between the stress σ_z and strength Y can also be observed.

The above comparison is subjected to the approximated nature of the finite element mesh and the determination of the load at which acoustic emission event occurred.

Note that while interlaminar stresses exceed interlaminar strengths, stress σ_x is 89.09 - 152.7 MPa which is much smaller than the uniaxial strength X of 1020 MPa.

6. Conclusion:

The agreement between finite element results and experimental results allow the following conclusions:

1- A reasonable finite element mesh has been established for the determination of interlaminar stresses in tapered laminates made of unidirectional layers.

2- For unidirectional layered tapered laminates, ordinary "acoustic emission" can be used to determine the first sign of delamination.

3- Interlaminar normal stress σ_z and shear stress σ_{xz} are mainly responsible for first delamination failure in unidirectional tapered laminates.

The above conclusions are restricted to unidirectional tapered laminates. To come closer to real laminates (tapered laminates made with layers of different fiber orientations), tapered laminates of unidirectional off-axis fiber orientation have to be investigated.

7. Acknowledgement:

The financial support from Industrial Materials Research Institute and the C scan done by National Aeronautical Establishment are appreciated. Thanks are also extended to Bell Helicopter Textron Canada for the glass/epoxy prepregs and discussions with engineering personnel.

REFERENCES

1- Kulkarny, S.V., Stone, R. G., Toland, R. H., "Prototype development of an optimized, tapered-thickness, graphite/epoxy composite flywheel". University of California, Laurence Livermore Laboratory, Report No. UCRL-52623. pp.1-37, November 1978.

2- Wu, C. M. L., Webber, J. P. H., "Analysis of tapered (in steps) laminated plates under uniform inplane load". Composite structures, vol.5 (1986) p.87.

3- Webber, J.-P. H. and Wu, C.M.L. "Theoretical investigation of stress concentration in damaged carbon fiber reinforced plastic plate structures", Progress Report 10, MOD Res. Ag. No. ER/A/9/4/2034/064. Department of Aeronautical Engineering, University of Bristol, Dec 1984.

4- Lucking, W.M., Hoa, S.V. and Sankar, T.S., "The effect of geometry on interlaminar stresses of $[0/90]_s$ Composite laminates with circular holes", Journal of Composite Materials, Vol.18, March 1984, p.188.

5- Tsai, S. W., Hahn, H. T. "Introduction to composite materials". Technomic publishing Co., Lancaster Pennsylvania. 1980.

6- Wilson, E.L., Taylor, R.L., Doherty, W.P. and Ghaboussi, J., "Incompatible displacement model", in Numerical and Computer Methods in Structural Mechanics, ed. S.J. Fenves et al, Academic Press, 1973.

7- Lubin, G., Handbook of Composites, Van Nostrand Rheinhold, 1982.

A NOVEL METHOD FOR THE MEASUREMENT OF MODE II DELAMINATION IN AEROSPACE COMPOSITES

by

D.S. Matsumoto, S.K. Gifford and M. Vallance
General Electric Company, Schenectady, New York, U.S.A.

(Manuscript not received on time. Please communicate with the authors.)

MONITORING PROGRESSION OF MODE II DELAMINATION DURING FATIGUE LOADING THROUGH ACOUSTIC EMISSION IN LAMINATED GLASS FIBER COMPOSITE

by

C. Roy and M. El Ghorba
Department of Chemical Engineering
Université de Sherbrooke
Sherbrooke, Que., Canada, J1K 2R1

Presented at the 8th annual NRCC/IMRI symposium "Composites-'87",
November 5 and 6, 1987, Boucherville, Que., Canada

ABSTRACT

Acoustic emission (AE) was used to monitor damage development in a glass fiber/epoxy composite during monotonic and cyclic Mode II loadings of DCB specimens. AE parameters such as event count rates and accumulative event counts together with the distribution of events by time and location in the DCB specimen were used as proper indicators of the damage growth at various stages during testing. AE proved to be a powerful technique to predict in real-time the interlaminar failure stress (delamination in Mode II) in both the static and the dynamic tests. An S-N curve constructed entirely on the AE signatures recorded during fatigue testing exhibits three distinct stages enabling to delineate the period of damage initiation, the period of damage growth and finally the occurrence of delamination. A generalized expression based on the nonlinear cumulative damage model was developed in order to correlate AE activity with the damage development in the composite during cyclic loading. The fatigue data to date agree well with this method of prediction of the fatigue life.

1. INTRODUCTION

Advanced composites have now been employed as load carrying structural material for aircraft and helicopter for many years. The composite components have to withstand various combinations of loading demanding sometimes a complicated combination of lamina orientations in the lay-up fabrication. Non destructive evaluation (NDE) is used extensively during development of the component manufacturing process and thereafter the production inspection is aimed at a broad characterization of the material quality which, in effect, is as good as the quality of the component proved acceptable mechanically. Recent reviews of NDE of composites (1-3) indicate that in service inspection remains a serious problem since the most universally employed methods do not provide real-time or dynamic monitoring of damage in composite materials. The direct costs of the inspection to assess the material condition are large in terms of lost time and equipment required.

In addition to providing information about the local failure mechanisms (4), acoustic emission (AE) show the most promise to monitor structures during service and to assess the damage at various stages during the life of a composite structure. Significant improvements in the AE instrumentation as well as in the analytical techniques including signal analysis (4-5) coupled with faster data acquisition systems to display information in real-time, make the AE method a prime candidate technique to predict the levels of damage that influence the structure's mechanical performance.

The aim of this study is to assess the sensitivity of the AE method to monitor in real time damage progression localization and delamination in DCB specimens subjected to cyclic loading. The characteristic fatigue (S-N) curve of a glass fiber reinforced epoxy laminate is constructed using AE signatures as the main indicator of the fatigue damage growth.

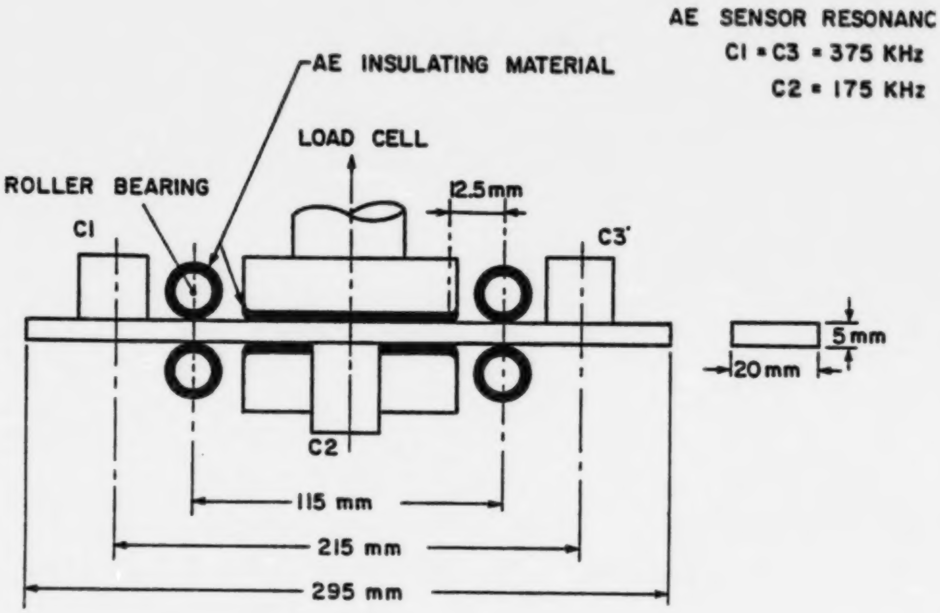
AE SENSOR RESONANC
C1 = C3 = 375 KHz
C2 = 175 KHz
AE INSULATING MATERIAL
LOAD CELL
ROLLER BEARING
12.5mm
C1
C3'
5mm
20mm
C2
115 mm
215 mm
295 mm

Fig. 1(a) Shematic diagram of mode II loading configuration.

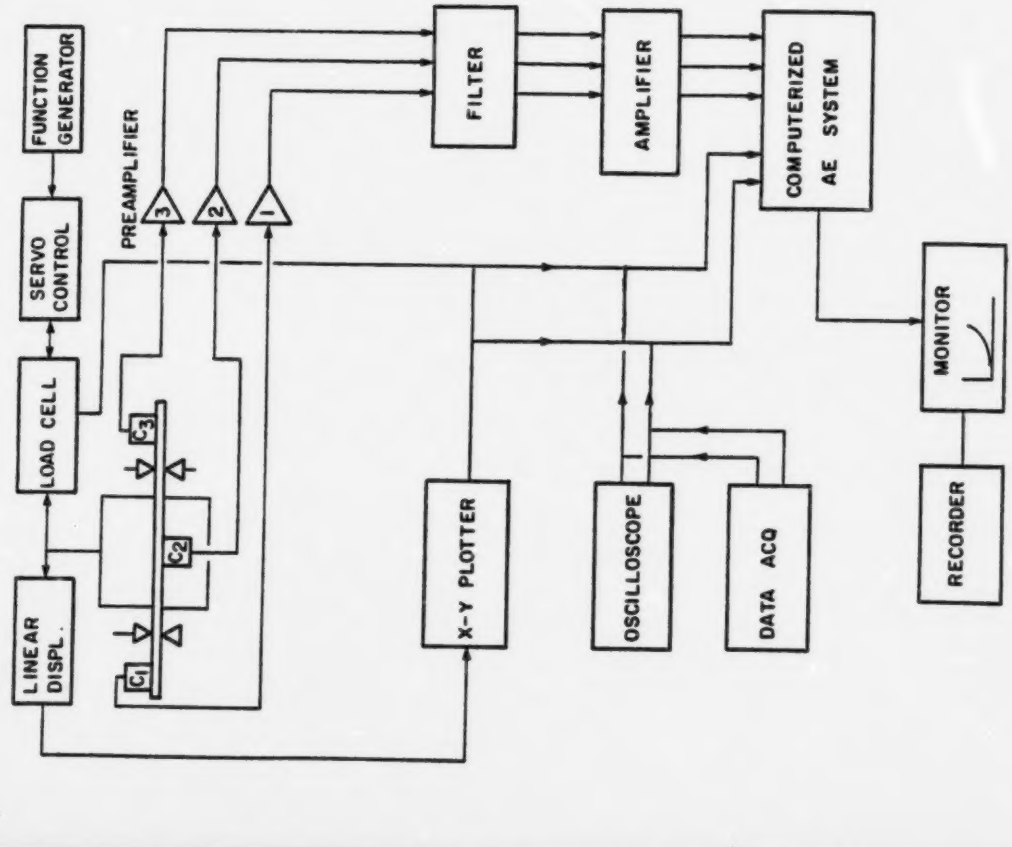
FUNCTION GENERATOR
SERVO CONTROL
LOAD CELL
LINEAR DISPL.
PREAMPLIFIER
3
2
1
C3
C2
C1
FILTER
AMPLIFIER
COMPUTERIZED AE SYSTEM
MONITOR
RECORDER
X-Y PLOTTER
OSCILLOSCOPE
DATA ACQ

Fig. 1(b) Instrumentation for acoustic emission measurement.

2. TESTING PROGRAMME

2.1 Material and laminate

The material used in this study was a (S2) glass fiber/epoxy (CE 9000-9) developed by Ferro Corporation. The laminate was autoclave cured to the manufacturers' specified cure schedule and consisted of 26 plis $[\pm 45, 0_4, \pm 45, 0_4 + 45]_s$ giving a thickness of 5 mm. The specimens (295 mm long by 20 mm wide) were cut from the panels which had been C-scanned and found to be free of detectable defects.

2.2 Interlaminar forward shearing

Mode II interlaminar fracture stress can be computed from the geometric and material properties of the specimen. Short beam theory formula proposed by Mullin and Knoell (6) were used to find the critical ratio of specimen span L to specimen thickness h which would enhance mode II delamination in the DCB specimen. The loading configuration together with the specimen dimensions shown in Fig. 1 (a) were designed to meet the mode II interlaminar fracture requirements.

2.3 The static and fatigue loading

Static tests were performed to determine the critical interlaminar fracture stress τ_{max} of the composite beam. The specimens were loaded at ambient temperature under displacement control using an MTS servo-hydraulic testing machine. A displacement rate of 0.009 mm/s was used. The applied displacement (δ) and the corresponding load (P) were recorded on a X-Y plotter and simultaneously stored using the data acquisition system of the acoustic emission system. The fatigue tests were performed under load control

TABLE 1

INTERLAMINAR FRACTURE STRESS OF THE FIBERGLASS/EPOXY DCB SPECIMENS LOADED IN MODE II

Sample No.	Cross-sectional Area-A $(mm)^2$	Load P_{max} (KN)	Shear stress τ_{max} (MPa)
M 2900	114	8.36	54.97
M 3900	113.59	8.75	57.78
M 3900 B	113.59	7.96	52.56
M 4900	115.62	8.80	57.10
M 4900 B	115.62	8.83	57.30
M 5900	112.56	7.99	53.27
M 6900	115.61	9.76	63.32
Average $\bar{X}$		8.637	56.61
Deviation S		0.618	3.59

using the same servo-hydraulic testing system. The applied load was sinusoidal at a minimum to maximum load ratio of 0.1 and a frequency of 5 Hz.

2.4 Acoustic emission monitoring

An AET 5000B computerized system in conjunction with three resonant piezoelectric transducers mounted onto the specimen as shown. Fig. 1(b) was used to detect, record and locate the acoustic signals originating from either of the two shear zones of the beam specimen. The operating parameters of the system were: signal amplification of 80 dB (40 dB in the preamplifier and 40 dB in the amplifier), system threshold level of 1 V and a dead time of 100 μs.

Envelope characteristics of the AE signals i.e. event counts, rise time, duration, amplitude, slope, energy, time of arrivals were recorded during a test; the system can process AE events at a rate as high as 2000 C/s. The time difference module of the system computes the time of arrival differences of the emissions between sensors thereby locating the AE source in the test specimen. For convenience, the specimen was divided into 295 segments along its length (150 × 1 cm divisions on either side of the central sensor) to provide location information on the AE signals emitted from either of the two shear zones.

3. RESULTS AND DISCUSSION

3.1 The static tests

The results of the critical interlaminar fracture stress τ_{max} are summarized in Table 1. For each of the seven specimens tested, the interlaminar shear strength of the composite was computed using the maximum load reached at the onset of the first delamination in one of the two shear zones

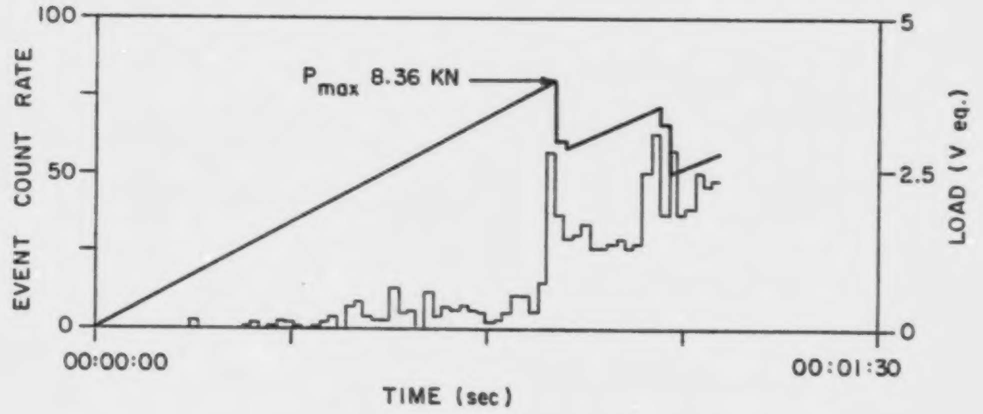

Fig. 2 Static test. Load and count rate as a function of time. Note coincidence of load and count rate peaks with onset of delamination.

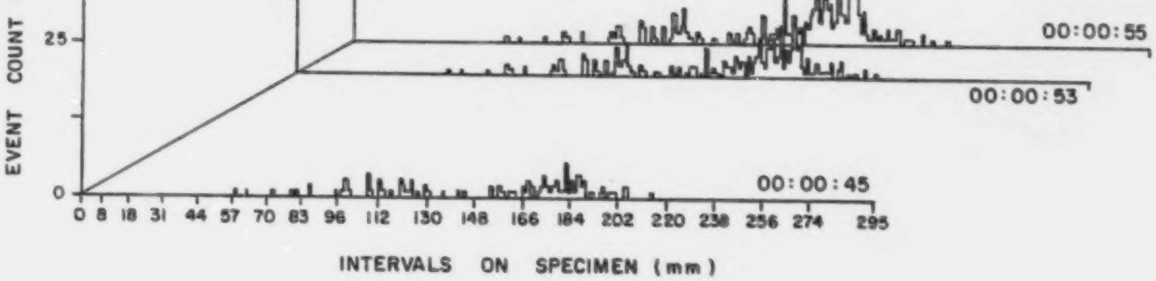

Fig. 3 Distribution of AE events in zones 1 and 2 of the specimen at three time intervals during a static test.

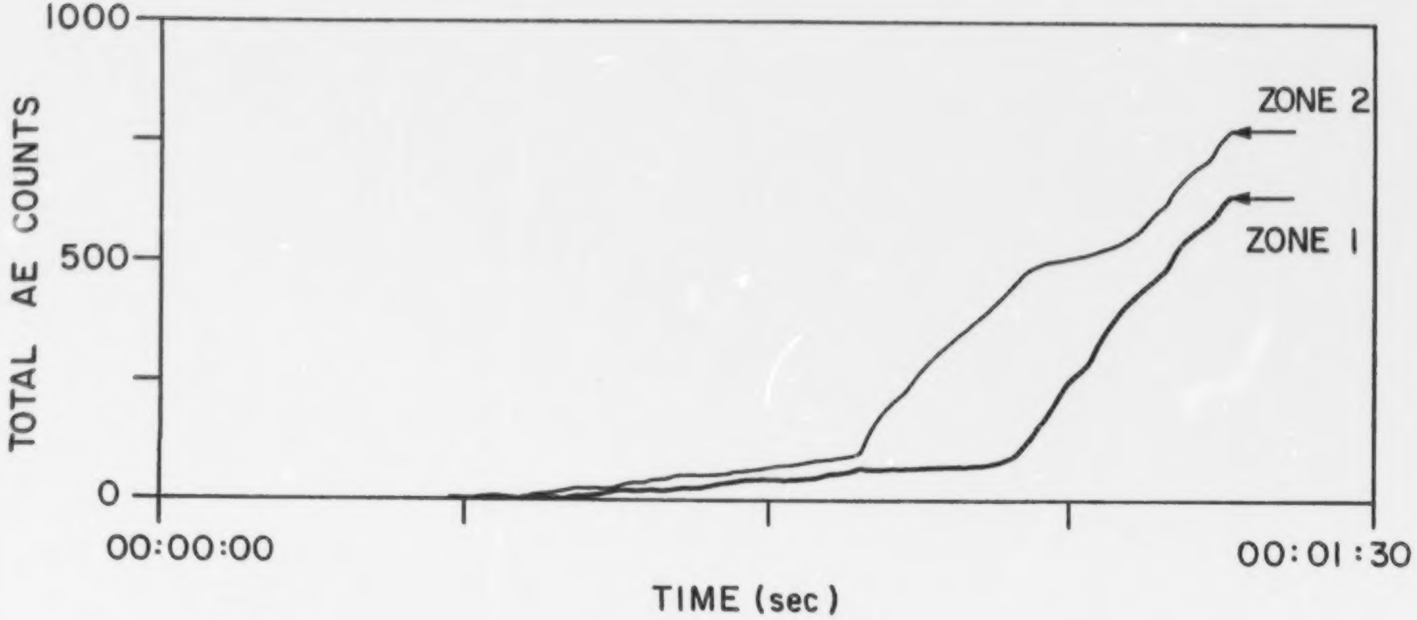

Fig. 4 Accumulative AE event counts in zone 2 and 1 respectively during a static test. Note the sudden burst of events in zone 1 after delamination in zone 2.

of the specimen. The delamination was characterized by a sudden drop in the recorded load which was followed by a temporary increase in load and a second load drop coinciding to delamination in the second shear zone. Fig. 2 illustrates a typical test in which the load was measured as a function, a time and AE activity (number of events per unit of time). The two sudden bursts of AE counts coincided to successive load drops caused by the delamination in each shear zone. The location distribution histogram shown in Fig. 3 illustrates the AE activity in the two shear zones of a specimen at three time intervals (45 s, 53 s and 55 s respectively) just prior to the occurrence of the first delamination. The data show that one of the two zones (zone 2) where the acoustic emissions was most frequent represents the area of major damage progression. The AE accumulative event counts on the respective shear zone of the specimen for the duration of the test is shown in Fig. 4. The pattern of damage growth in the respective shear zones confirmed that the AE activity in zone 2 is higher initially than in zone 1. However at the onset of the delamination in zone 2, the load bearing capacity of the composite in zone 2 is diminished thus setting up rapid rate of damage growth in zone 1; this is consistent with large accumulative event counts observed in zone 1 following delamination in zone 2.

3.2 The fatigue tests

The AE real-time response recorded during a fatigue test can be divided into the following stages:

- stage I is defined as the number of cycles N_1 below which there is no AE activity in the composite. It represents for a given level of cyclic stress, a threshold leading to irreversible damage in the material.

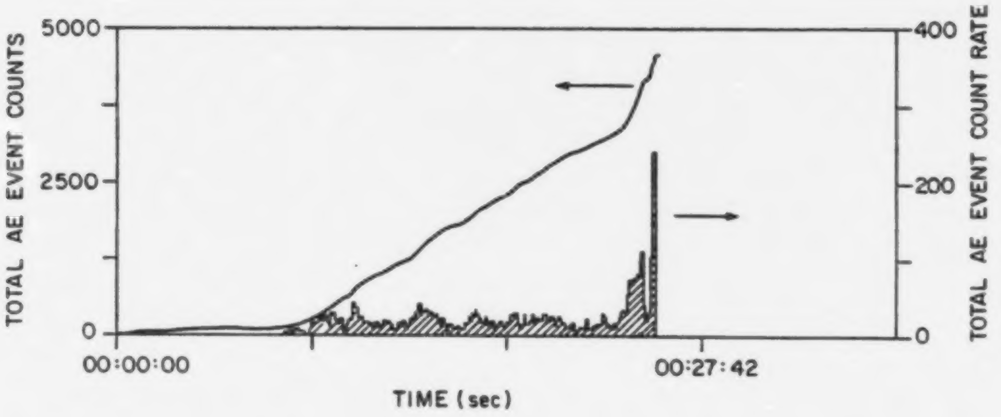

Fig. 5 The two AE parameters (accumulative event counts and event count rate) measured during a fatigue test.

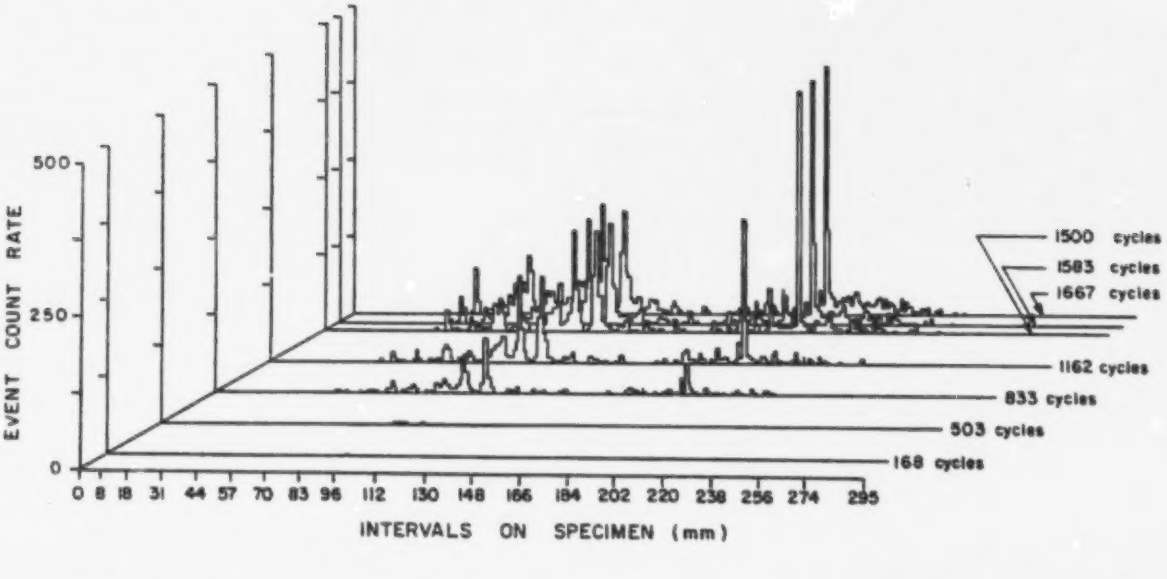

Fig. 6 Distribution of AE events in the two zones of specimen No F3900 at different intervals during the fatigue test.

TABLE 2

SUMMARY OF FATIGUE DATA

($R = 0.1$ $P_{max} = 8.64$ KN)

% P_{max}		75	75	75	70	60	50
Sample No.		F 2900	F 3900	F 1900	F 9900	F 8900	F 7900
Cross-sectional area $(mm)^2$		113.36	113.36	113.36	124.62	124.62	125.86
Shear stress (MPa)		43.46	43.46	43.46	36.89	31.62	26.09
Cyclic frequency (Hz)		1	1	1	5	5	5
Time to (s)	Damage initiation	68	68	90	317	9000	189,227
	Delamination	832	1667	907	3682	31500	-
Number of Cycles	Stage I (N_1)	68	68	90	1584	45,000	946,135
	Stage II (N_f)	832	1167	907	18,409	157,500	1,326,860
$(N_1/N_f) \times 100$		8.17	4.09	9.9	8.6	28.57	—

- stage II corresponds to the progressive growth of AE activity and its development occurs in relation to the amount of damage created in the material. The extent of this period (number of cycles N_2) is strongly dependent on stress level, with decreasing duration the higher the cyclic stress level is.
- stage III corresponds to a sudden burst of AE activity in the material analogous to the events count rate recorded at the instant of the delamination occurrence in a static test.

The results of the fatigue tests carried out at respectively 75%, 70%, 60% et 50% of the critical interlaminar fracture stress (average τ_{max} measured in the static tests) are summarized in Table 2. The data clearly delineate the three stages of the fatigue life defined above in terms of AE activity. On the basis of the current fatigue test standards for composite material, the reproducibility of the results are very good thus suggesting that the AE technique can reliably identify the damage initiation and growth and, delamination in a glass fiber reinforced epoxy composite. The Fig. 5 illustrates the AE activity during fatigue cycling of the specimen No. F3900 cycle loaded to 75% τ_{max}. It shows that the three stages of the fatigue life of the specimen are well identified by either of the two acoustic parameters chosen i.e. AE count rate or accumulative event counts. The hystogram of Fig. 6 shows the distribution of events by cycles and location in the two shear zones of the specimen. As the test progressed, the damage spread in both zones, to begin with higher activity appeared in zone 1 than in zone 2 but, at cycle number 1667, delamination occurred in zone 2. The cyclic load-displacement hysteresis loops of the composite were recorded (with the X-Y plotter) at regular intervals to compare the respective sensitivity of the mechanical and AE systems to detect the onset of the first delamination in

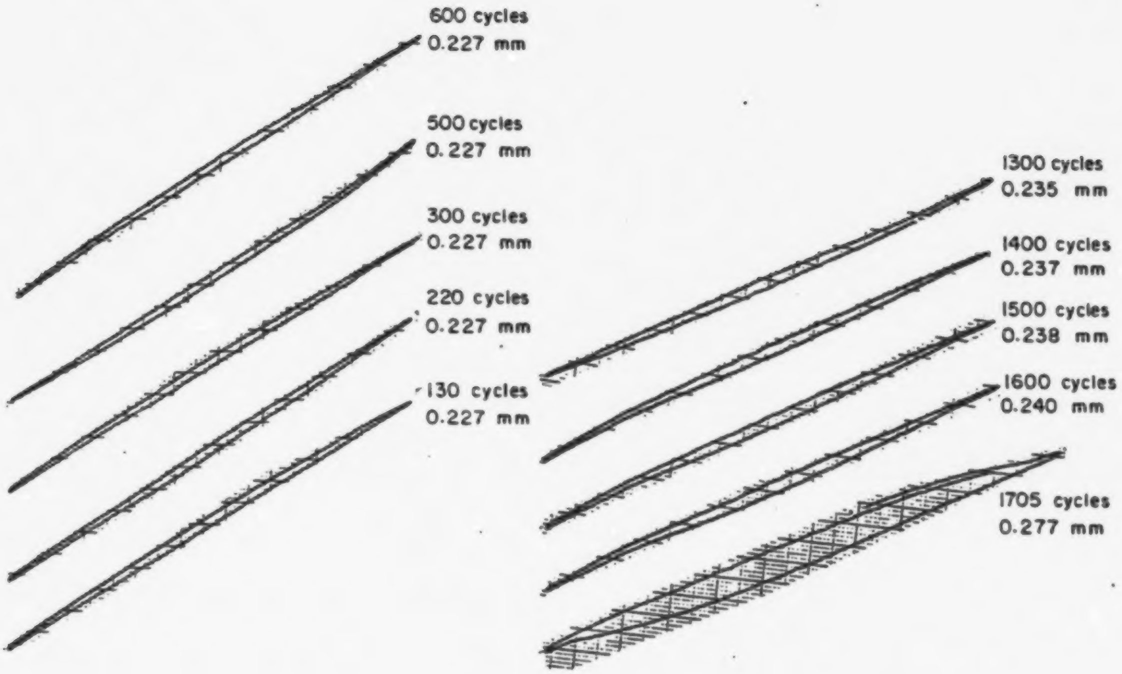

Fig. 7 Cycle hysteresis loops displaying little variation in their size or shape until the occurence of the first delamination in the specimen.

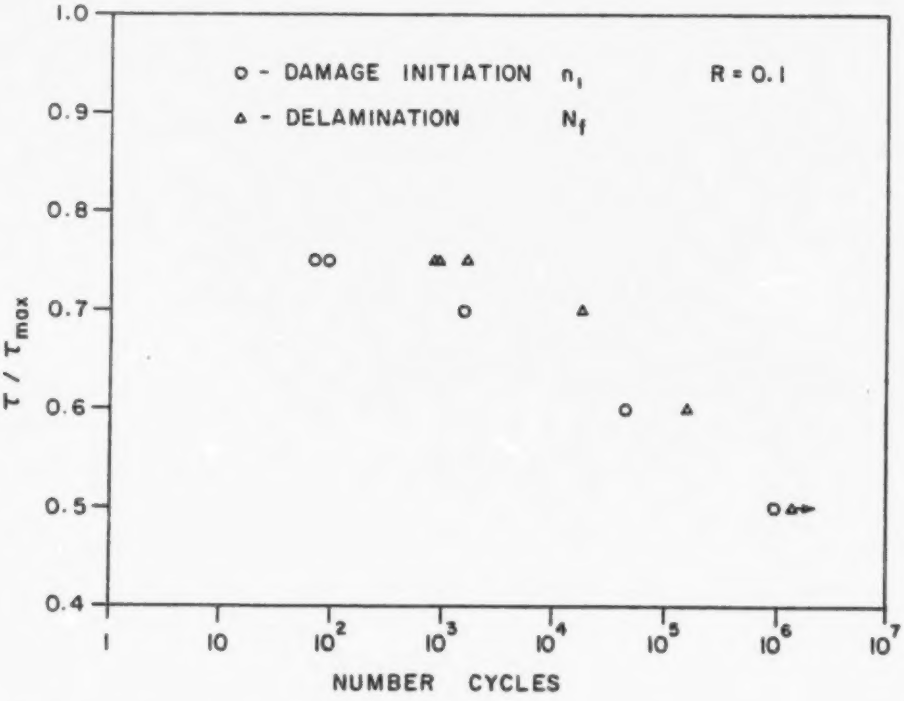

Fig. 8. S-N curve providing information on both the damage initiation and development during the fatigue life of the composite.

the specimen. The cyclic hysteresis loops at time intervals during the test are reproduced in Fig. 7. The increases in the width from tip-to-tip of the loops (i.e. the displacement) with the number of cycles was hardly measurable until the first delamination occurred at the 1705th cycle. It appears that the standard fatigue test procedures normally adopted to study the fatigue behaviour of a composite offers litte information on the damage development in the material prior to delamination.

The fatigue stress amplitude in terms of the number of N_1 (damage initiation) and N_f (first delamination) is shown in Fig. 8 as S-N curve, in which τ is a total stress amplitude and τ_{max} is the average interlaminar fracture stress determined in the static tests. It is seen that for each cycle stress amplitude the number of cycles to initiate irreversible damage in the material and to generate the delaminations are displayed as twin points enabling the fatigue life of the beam specimen to be fully characterized. For the levels of the fatigue stress amplitude investigated the three stages of the fatigue life of the composite were identified with the exception that at the low level (50% τ_{max}), the stage III (delamination) had not been attained at the end of the test (1.3×10^6 cycles). Nevertheless, the damage growth in the composite (stage II), as indicated by the AE activity recorded during the test, had progressed for some 381,000 cycles.

3.3 Damage growth modelling

It is well known (7-8) that damage in composite materials incorporates the interaction of the various types of failure mechanisms occurring at different stages of the fatigue life of the composite being studied. Any predictive methodology must therefore reflect the amount of damage which develops in the material before failure. Since the AE activity measured

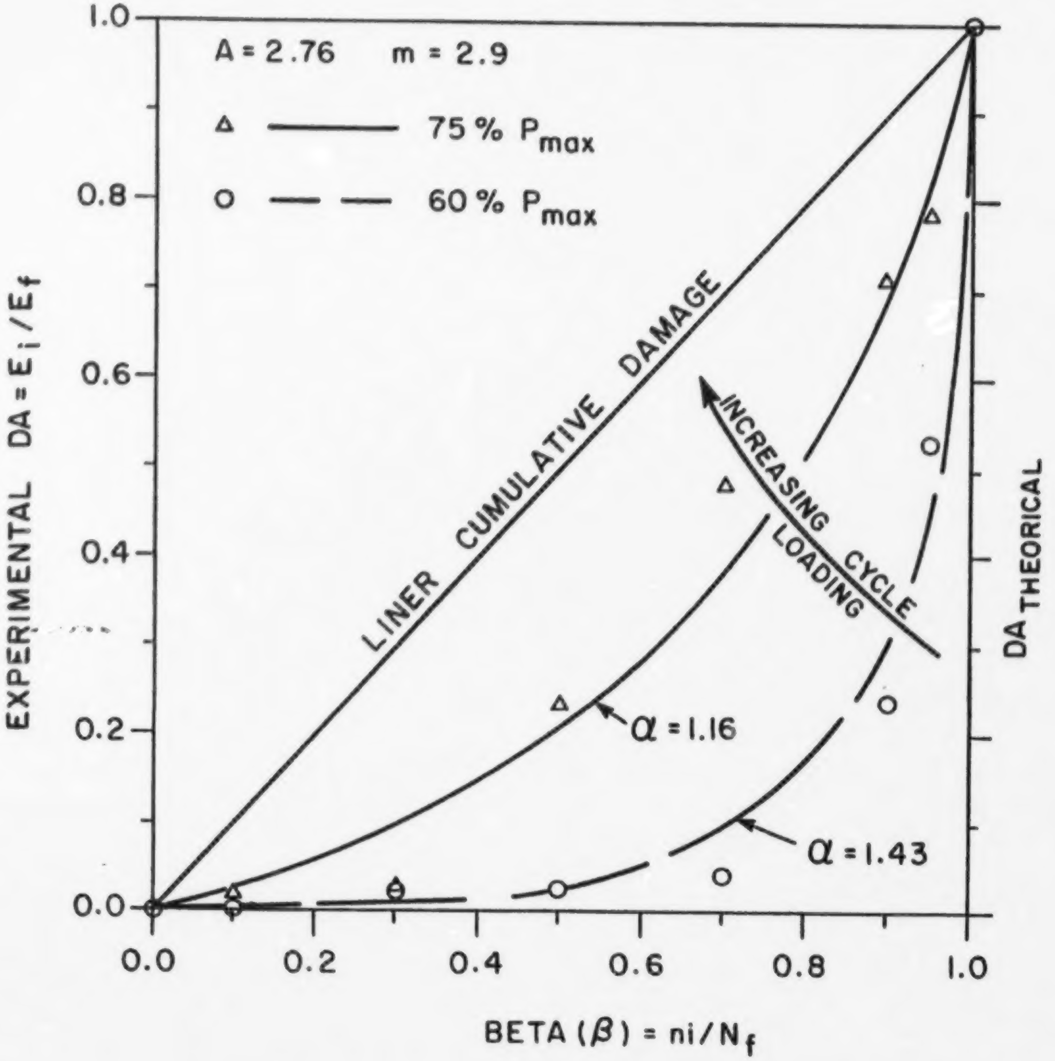

Fig. 9 The correlation between nonlinear cumulative damage curves developed and experimental data to date.

during a fatigue test enables to define the material degradation $f(n/N_f)$, it is a simple matter to express the fatigue damage in terms of the cycle ratio (n_i/N_f) where failure (delamination) is hypothesized $\sum (n_i/N_f) = 1$.

Experimentally the damage measured by acoustic emission as a function of the fractional life β of the composite can be expressed as $DA = E_i/E_f = f(\beta)$ where E_i = number of instantaneous events

E_f = number of events at failure (delamination)

where $\beta = n_i/N_f$ n_i = number of instantaneous cycles

N_f = number of cycles leading to mode II delamination.

The generalized form of the damage accumulation, DA, assessed by acoustic emission is [9]:

$$DA = \frac{\beta}{\beta + (1 - \beta)\alpha^m}$$

$\alpha = (A \frac{E_t}{E_f})$ E_t = AE accumulative event counts at failure (static test)

E_f = AE accumulative event counts at failure (fatigue test)

A and m are parametric acoustic constants

For $n_i = 0$ $\beta = 0$ and $D = 0$

For $n_i = N_f$ $\beta = 1$ and $D = 1$

The curves relating the theoretical damage development in the composite during a fatigue test are shown in Fig. 9 for two fatigue stress amplitudes.

The experimental points displayed on the curves agree well with the nonlinear model. These results strongly indicate that the damage accrues exponentially towards the end of the fatigue life of a composite; in such a circumstance the ability to nondestructively evaluate the material condition is essential.

4. CONCLUSIONS

The interlaminar fracture stress of a glass fiber/epoxy composite has been investigated using the Mode II forward shearing amenable with the DCB specimen. Specifically, the damage accumulation in the laminate beam during monotonic and cycling loading has been monitored using an acoustic emission technique. It has been possible to identify the various stages of the fatigue life of the composite and to predict the location of the impending failure (delamination). An S-N curve was constructed for this composite entirely on the AE signatures recorded during fatigue testing, which proved to be more sensitive than the usual analyses of the cyclic hysteresis loop that are carried out to evaluate the strength degradation of a material.

A cumulative damage model attempting to correlate the AE activity with damage growth in the composite has been proposed. Such a modeling procedure is important to rationalize the phenomenological aspects of the complex mode of damage development in fiber composite. It is interesting to note that the fatigue data to date agree well with a generalized form of a nonlinear cumulative damage model.

5. ACKNOWLEDGEMENTS

This paper is based on work supported by the Industrial Materials Research Institute of the National Research Council of Canada (contract # 31950-6-0013/02-SD).

The authors wish to thank Dr. T. Vu Khanh of IMRI and Dr. R.C. Fews and Mr. S. Chowdbury from Bell Helicopter Textron Canada for their support and encouragement. The authors are most grateful to a colleague M. Michel Tasnon, for his assistance with the experimental work and his helpful discussions.

6. REFERENCES

1. J.G. Scotland and C.M. Scala, "A Review of Non-Destructive Testing of Composite Materials", NDT-International, 1, 75 (1982).
2. D. Proulx, C. Roy and D.G. Zimcik. "Assessment of the State of the Art of NDE of Advanced Composite Materials", Canadian Aeronautics and Space Institute Journal, 31, 325, (1985).
3. Y. Bar-Cohen, "NDT of Fiber-Reinforced Composite Materials - A Review, Materials Evaluation, 44, (1986).
4. A. Maslouhi, C. Roy and D. Proulx, "Characterization of AE Signals Generated in Carbon Epoxy Composites 2nd Int. Symp. on AE from Reinforced Composites, Montreal, July 21-25, (1986).
5. A. Rotem, Acoustic Emission Signature of Failure Modes 2nd Int. Symp. on AE from Reinforced Composites, Montreal, July 21-25 (1986).
6. J.V. Mullin and A.C. Knoell, Mat. Res. and Stand MTRSA, 10, 16 (1970).
7. K.L. Reifsnider and R.D. Jamison, Int. J. Fatigue, 4, 187 (1982).
8. J.C. Duke et al., Non-Destructive Evaluation of Composite Materials - A Design Philosophy, ICM-4, 1, 489, Stockholm, Aug. (1983).
9. M. El Ghorba and C. Roy, "Etude préliminaire de caractérisation du délaminage en Mode II dans un matériau composite fibres de verre/epoxy par suivi d'émission acoustique", Rapport interne Département génie mécanique, Université de Sherbrooke, Sept. (1987).

Paper No. 8 by J.C. Seferis is withdrawn.

CANADAIR'S EXPERIENCE IN DEVELOPING AIRCRAFT COMPOSITE STRUCTURES

by

P. McConnell
Canadair Limited
Montreal, Que., Canada, H3C 3G9

Presented at the 8th annual NRCC/IMRI symposium "Composites-'87",
November 5 and 6, 1987, Boucherville, Que., Canada

Abstract

Canadair has been active in the field of fiber-reinforced composites as it has advanced over the past decade. We have developed methods for characterizing the structural properties of composites so that secondary and primary structures can be safely produced with them. Many secondary components have been produced, particularly for the CL-601 Challenger business jet. Primary structures have been produced for surveillance drones and in one case for the Challenger, and certification procedures for the types of structure are continually being refined.

1 Introduction

The successful introduction of new material technology requires that i) the technology provide real improvements over the status quo while being economically practical, ii) sufficient understanding of the material exists to allow it's efficient use with confidence, and iii) it be possible to demonstrate the safety of the technology to regulatory authorities.

Generally, an advance in one of these areas motivates complementary advances in the others. They must progress together, because the level of technology available for use is constrained by the least developed of the three.

Composite materials provide a good example of how these three areas must progress in a complementary manner. Throughout the 1970's, extensive efforts were made to build experience with the new technology of graphite/epoxy composites. The materials were eventually found to be limited by a lack of toughness, which led to the development of new, tougher, materials. We are now in a second period of experience building with these new materials. Thus, we have gone from a situation where a new technology required improved understanding, to one where that understanding motivated an improved technology, and then back to a situation of trying to completely understand the technology.

Component	Material	A/C	Date
Radome, MAD Boom, Rudder Insert	Fiberglass	CL-28	1954
Wing Tips, Horizontal and Vertical Stab. Tips	Fiberglass	CL-215	1972
Wing/Fuselage Fairings, Nose Cone, Tail Cone, Nose L/G Doors, Misc. Access Doors, Misc. Fairings, Flap L/E, Cowling, Vert. Stab. L/E, Misc. Ducting, Cockpit Panels, Wheel Bins	Kevlar	CL-600/601	1977
Belly Fairing, Cabin Floor, Stabilizer Fairings, Fuel System Reservoirs, Fuel Tank Access Panels, Wheel Disks, Winglet Tips	Graphite	CL-600/601	1977-1980

Table 2.1 Secondary Composite Structures.

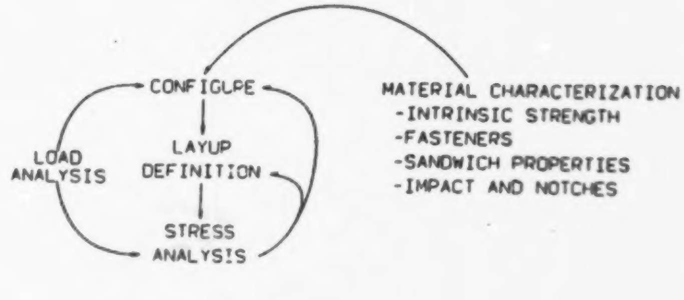
CONFIGURE
LOAD ANALYSIS
LAYUP DEFINITION
STRESS ANALYSIS
MATERIAL CHARACTERIZATION
-INTRINSIC STRENGTH
-FASTENERS
-SANDWICH PROPERTIES
-IMPACT AND NOTCHES

Figure 2.1

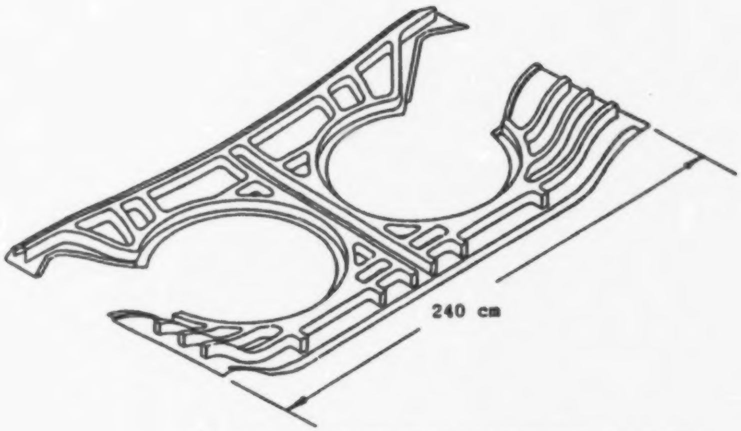

Figure 2.2 CL-601 Main Landing Gear Fairing

These ongoing changes in the technology have been accompanied by the development of methods that can be used to certify structures made from the new materials. Fortunately, even though the state of the art is continuously changing, the certification methods that are emerging are fairly general and can be applied to many different composite material systems.

Canadair has been active in this field as the new materials have developed. We have developed design methods for composites based upon our understanding of these materials, and we have also been developing certification procedures. This paper is a brief description of the design and certification procedures that Canadair has used to bring various components into production.

2 Secondary Structure

Design Methods

Table 2.1 lists most of the secondary composite components that have been produced at Canadair.

The approach used for the design of secondary composite structures is outlined in figure 2.1.

The test data required for these designs consists of material stiffness and ultimate strength values, fastener strength data, and sandwich panel data. Strength values are usually B-basis allowables.

The component configuration is based on the designer's assessment of the loading situation and the overall part geometry, while allowance is made for manufacturing capabilities. The initial layup is based on the designer's experience and simple calculations.

When specifying the layup, the designer is guided by some simple rules. Nearly all of these components are made out of balanced fabrics, so the choice is limited to θ/(90-θ) plies. For tractability and by tradition, the selection is usually limited to 0/90 and ±45 plies arranged in a symmetric layup. The percentage of each type of ply is assigned after an initial assessment of the relative magnitudes of the normal and shear stresses

When the initial design is ready, a stress analysis is performed. This is usually done with the aid of a finite element analysis package, unless the loading and geometry lend themselves to hand calculation. The results of the analysis are used in conjunction with the material data and a failure criterion to derive margins of safety for each ply. The margin of safety is usually calculated with respect to the ultimate load, which is taken as 1.5 times the limit load (the highest load that the component is expected to experience in it's lifetime).

Margins of safety with respect to other relevant failure modes are also calculated. These may include buckling, fastener failure, impact damage propagation, and various sandwich construction failure modes.

If any margin of safety is found to be negative, the design is modified, and the analysis is repeated. This continues until all margins of safety are positive.

For parts with small structural loads, like some cabin ducting, the choice of configuration and layup is based on the requirements of handleability and installation. Only limited strength analysis is performed in these cases.

As an example of a secondary component, consider the CL-601 main landing gear fairing, illustrated in figure 2.2. This component was originally designed and produced in aluminium, but was later redesigned in graphite/epoxy for weight savings.

The material system used in the fairing is Celion 3000 graphite fabric in a balanced 24 yarn-per-inch 8-harness satin weave reinforcing Narmco 5208 epoxy resin. Mechanical design data for this material system was generated by an extensive testing program which is described in the next section on primary structure.

Component	Material	A/C	Date
Experimental			
Wing preliminary design exercise, stiffened panels manufactured.	Graphite	--	1985
Pre-Production			
Outboard Flap Vane	Graphite	CL-601	1982
Production			
Rotor Blade	Glass, Kevlar	CL-227	1983

Table 3.1 Primary Composite Structures.

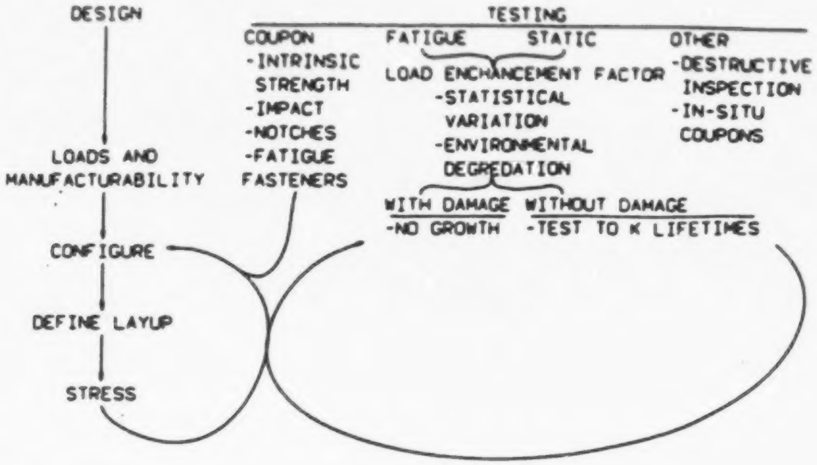
DESIGN
LOADS AND MANUFACTURABILITY
CONFIGURE
DEFINE LAYUP
STRESS
TESTING
COUPON
-INTRINSIC STRENGTH
-IMPACT
-NOTCHES
-FATIGUE FASTENERS
FATIGUE
STATIC
LOAD ENCHANCEMENT FACTOR
-STATISTICAL VARIATION
-ENVIRONMENTAL DEGREDATION
WITH DAMAGE
-NO GROWTH
WITHOUT DAMAGE
-TEST TO K LIFETIMES
OTHER
-DESTRUCTIVE INSPECTION
-IN-SITU COUPONS

Figure 3.1

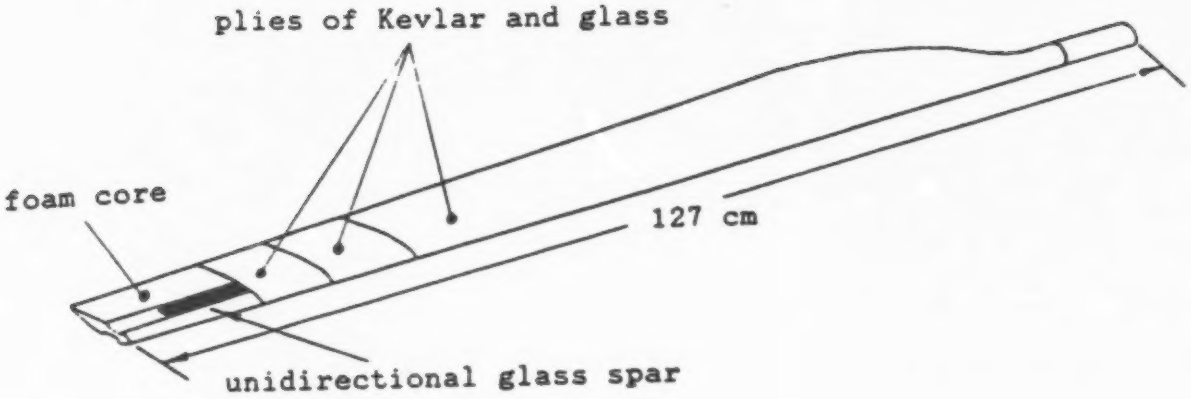
plies of Kevlar and glass
foam core
127 cm
unidirectional glass spar

Figure 3.2 CL-227 Rotor Blade

The pattern of stiffeners on the component was chosen by a designer to match the anticipated load paths. A 0/90 layup was chosen because significant shear was not expected, and because the skin is only two plies thick in some areas. The layup could not have been symmetrical in those regions if both 0/90 and ±45-type plies had been included.

The success of this design is evidenced by the following figures: comparing the metal to the composite design, the part count was reduced by 126, the cost was reduced by 40%, and the weight was reduced by 34%.

3 Primary Structure

Design Methods

Table 3.1 lists all of the primary composite components that have been produced at Canadair.

The approach used for the design of primary composite structures is outlined in figure 3.1.

An extensive program of coupon tests is used to determine the intrinsic strength of any material system that is to be used in the design of primary structures. The strength quantities of interest are: longitudinal tension and compression, shear, flexure, short beam shear, and transverse tensile and compression strength. Tests are carried out at high and low temperature, and the effects of chemical exposure are assessed. A and B-basis allowables are derived, these are the population's lower 1 and 10 percentiles respectively, given with a 95% confidence level.

A-basis allowables are usually used in the design of primary structure.

Studies are carried out to obtain design data on the material's fastener-bearing, fatigue, and impact properties, and it's notch sensitivity.

The design of the component is based upon the coupon-level data, plus loading data and current manufacturing capabilities. Selection of the layup requires consideration of buckling, edge stresses, and the strength envelope of the layup. As was described for secondary structures, margins of safety are calculated for all potentially critical failure modes.

Static, fatigue, and damage-tolerance tests are normally carried out on full-sized production components.

The static test normally proceeds to failure, and is considered successful if the failure load is somewhat greater than ultimate. The amount by which the test should exceed ultimate is determined by material variability (the test part is assumed to be fabricated from unusually strong material), and by environmental degradation of material strength (the material is assumed to realize it's 'unconditioned' strength during the test). The test component is therefore assumed to be stronger than the "weakest" possible production component that has experienced environmental degradation.

The fatigue test is also run at enhanced loads, for multiple lifetimes. The full-sized component fatigue test is normally run at constant-amplitude, so studies of the fatigue spectrum are made to determine an equivalent constant-amplitude fatigue load.

The damage tolerance test is carried out to show that flaws induced by normal service will not grow under service loading. The flaws are usually 'barely visible' impact artifacts, although saw cuts have been used in the past. The loading is usually the same as that used in the fatigue test.

CL-227 Rotor Blade

This component is a fiberglass/Kevlar/graphite/epoxy structure with a foam core. This component and it's construction is illustrated in figure 3.2.

The analysis of the blade proceeded in two basic steps: a beam-type model was first used to model dynamic behavior, and later a plate-type model analyzed the stresses. The Tsai-Wu failure criterion was used to predict the margins of safety with respect to material failure.

Coupon tests were used to define the strength of proposed skin lay-ups, and design strains were restricted to account for impact damage. Fatigue studies of candidate skins led to the selection of an optimum layup

The static test was run up to 153% of ultimate to account for material variability and environmental degradation. The fatigue test was run at a constant amplitude equal to 100% of limit load. Damage tolerance tests, which have yet to be completed, will be performed on both a static and a fatigue article.

Additional testing was performed to determine the compressive strength of test coupons taken from an actual production blade, verifying the production process.

A unique aspect of the design of this structure was the interrelationship between the manufacturing process (closed mold/expandable core) and the material properties. The manufacturing methods used to make coupons for material characterization tests did not necessarily simulate the curing environment of the actual component. This was the motivation for testing coupons taken from the actual production item.

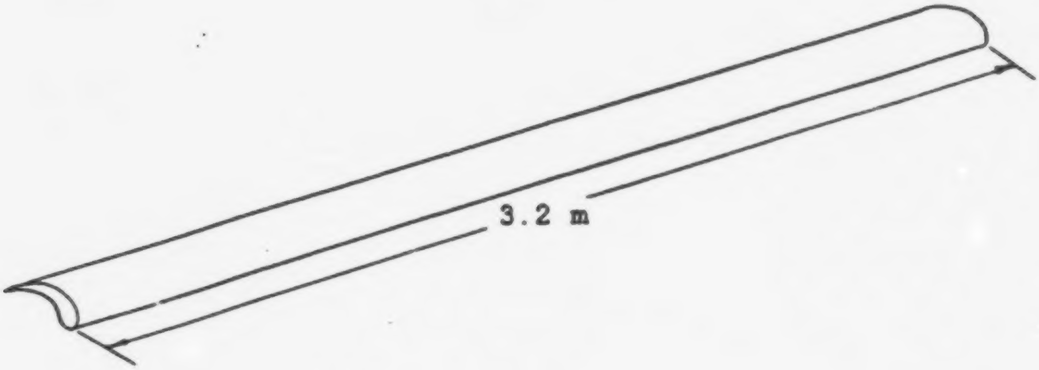

Figure 3.3 CL-601 Flap Vane

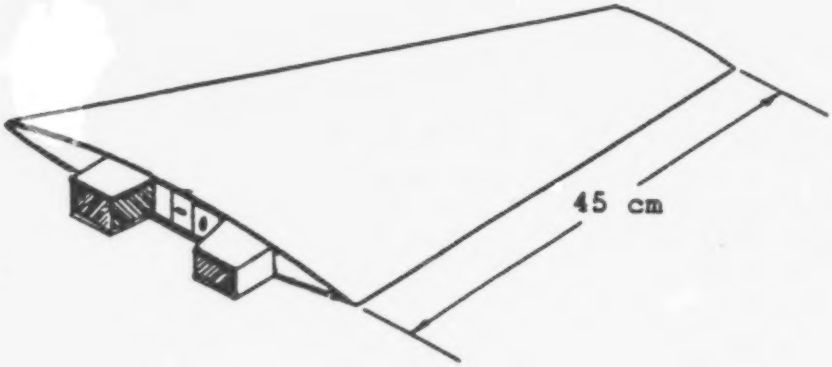

Figure 3.4 CL-289 Wing

CL-601 Flap Vane

This component, shown in figure 3.3, is a graphite fabric/epoxy structure.

This was a relatively simple component to analyze. Some of the preliminary work was done treating the component as a beam with distributed loads. Later, refined modelling was carried out using finite elements with plate-type elements.

Static, fatigue, and damage tolerance tests were carried out on full-sized test components.

The structure was subjected to two static loading tests, one to design limit load, and another to failure. Failure occurred at 133% of design ultimate load.

Fatigue testing was carried out to simulate 5 lifetimes of takeoff and landing cycles. One lifetime was taken to be 190000 cycles, and testing was carried out in blocks of 9500 landing cycles followed by 9500 takeoff cycles. No changes in the structure were observed during the fatigue test.

The damage tolerance test consisted of a fatigue test carried out after a saw cut had been made in the region of maximum bending moment. It was found that no growth of damage occurred during fatigue when the flaw was smaller than the size at which it failed catastrophically.

The structure was also tested in flight. Between December 1984 and June 1985 the vane saw 31 flights, accumulating 60.3 hours of unrestricted flight. No changes in the condition of the vane occurred during the flight tests.

CL-289 Wing

The CL-289 wing, shown in figure 3.4, is a Kevlar/epoxy structure.

Kevlar/epoxy was chosen as the structural material due to it's radar transparency, and because of it's weight advantage over aluminum. Development work began in 1973, and, due to the extended nature of the program, only pre-production wings have been made to date.

The wing was designed according to static strength and stiffness criteria. Fatigue and damage tolerance issues were neglected because of the limited life of the components. Each vehicle requires four wings, two of which are destroyed on each flight, meaning that each wing is only used for two flights.

The pre-production design was tested statically for stiffness and strength. The production design will be further tested at high and low temperature with absorbed moisture, and for erosion due to rain and dust, for the effects of salt fog, and for strength under shock loading.

Wing Design Exercise

This project was undertaken to identify the technologies that Canadair would have to develop to allow the production and certification of large primary composite structures.

A material selection procedure was undertaken to identify the optimum available material system based on certain desired material properties. These properties were, in order of importance: toughness, density, delivery reliability, shelf life, hot/wet properties, difficulty of fabrication, flow during cure, technical support, purchase price, toxicity, compatibility with other resins, cure cycle complexity, qualification time and cost, repairability, exothermic properties, and flammability. As a result of this analysis, Hercules IM6/Narmco 5245C was selected as the preferred material system for external areas where low-velocity impact was a concern. Union Carbide T300/Narmco 5208 was selected for use in internal areas where such impact events were not a concern.

The configuration of the wing was selected after trade-off studies of three alternatives: all honeycomb, multi-spar, and two-spar multi-rib. The final selection favored the two-spar design due to considerations of design, manufacturing, inspection, and repair. "Double Z" stiffeners were selected over hat stiffeners after consideration of manufacturability, inspectability, and airworthiness certification requirements.

An extensive series of coupon tests was conducted to confirm the assumed design strain of .5%. A total of 248 specimens were tested to determine the effects of stacking sequence, spectrum loading, notches, low velocity impact, and environmental exposure.

It was found that the design strain was limited to .42% by compressive strength after impact.

Sub-component tests were carried out on stiffened panels that represented typical compression surface skin areas. Analysis methods were developed to predict buckling levels and post-buckling behavior.

Compression tests of the skin sections showed that failure occurred by separation of the stiffeners from the skin. This failure mode was investigated using a fracture mechanics approach, and testing was continued after the area was reinforced. It was found that the reinforcement elevated the failure load, and changed the mode from stringer separation to material compressive failure.

One of the benefits of this exercise was the understanding it gave of the effort required to design and certify a large primary composite structure for a civilian aircraft. In particular, the material characterization effort was, not surprisingly, found to be much greater that would be required for an equivalent design effort using aluminum, since all common aluminum alloys are well characterized.

4 Conclusions

Canadair has designed and brought into production a great number of secondary structural components fabricated out of advanced composite materials. The design of these structures required a complete understanding of the properties of the material systems used, an understanding which was accumulated by several years of basic research.

The amount of primary structure designed has been much less, mostly because of the great effort required in terms of material characterization and component testing that is required for certification. In the future, as the efficiency of the material systems improve, and the certification procedures become established, the design of flight vehicle structures in composites should become more common.

MANUFACTURING OF FIBRE COMPOSITE COMPONENTS BY FILAMENT WINDING

by

M. Munro
Department of Mechanical Engineering
University of Ottawa
Ottawa, Ontario, K1N 6N5

Presented at the 8th annual NRCC/IMRI symposium "Composites-'87",
November 5 and 6, 1987, Boucherville, Que., Canada

ABSTRACT

The paper begins with a summary of the simple to very complex fibre composite components that have been fabricated by automated filament winding. The process of filament winding, where resin impregnated high strength, high modulus fibres are placed on a rotating mandrel (under controlled tension) in a specified geometric pattern, is then described in detail. A qualitative comparison of the filament winding of fibre composite components by conventional and robotic winding systems is presented next. The results indicate that a robotic winding system can be a viable alternative to conventional filament winding for certain applications. Finally, the concepts of lightweight winding systems, hybrid filament winding processes and advanced filament winding techniques are presented.

INTRODUCTION

Fibre reinforced polymeric materials have been very successful in replacing metallic materials in existing structures, for example, from fibreglass pipe and tanks to the graphite fibre composite wing sections of the F-18. Their use has also permitted the construction of components that were not feasible with conventional metallic materials. The most visible example for Canada is the use of the highest modulus graphite fibre available at that time (Celanese GY-70) in the stiffness-critical upper and lower boom arms of the Canadarm. This last example highlights an advantage of graphite fibres that is specific to the particular fibre. Graphite fibre composites also exhibit very good fatigue properties, low creep and good damping. Kevlar fibre composites are particularly tough while polymeric composites of glass fibres are low cost. The advantages of fibre reinforced polymers can also be of a general nature in that they apply to essentially all aligned continuous fibre composites. These include high specific properties (particularly, strength and modulus), low wastage (material is only placed where required) and design flexibility (reinforcement is oriented to meet individual component needs).

For high performance composites in which the fibre orientation, the volume fraction of fibres and the void content are critical manufacturing concerns there are a number of advanced processes available. These processes are generally automated or are being automated and include various forms of prepreg layup (manual, robotic transfer and gantry), pultrusion, braiding and filament winding. The cost effectiveness of a number of the above processes have been recently evaluated for the fabrication of graphite fibre laminates (1,2). Filament winding was shown to have a significantly lower relative cost than other processes (1). The results of Reference 2 generally indicate that pultrusion and filament winding were more cost effective than the other processes. For more complex structures the use of pultrusion is questionable due to the unidirectional fibre orientation produced by the process.

Since the introduction of filament winding in 1947 by M.W. Kellogg, a large variety of components have been fabricated. The simplest to fabricate are rings (with the fibres oriented circumferentially) suitable for fibre composite flywheels for energy storage. Helically wound tube-type components can range from fibreglass pipe to the graphite fibre composite tubes used for the MX missile and the solid rocket booster casings for the Space Shuttle which are under development. As well, automotive and helicopter drive shafts are being fabricated and have been placed in service. Both spherical and elongated fibre composite pressure vessels have been produced in the thousands of components. These range from units that are again very large (e.g. the 2.3 m. dia. Kevlar 49 fibre composite pressure vessel used for the 1st Stage Motor of the Peacekeeper rocket) to small vessels that can be held in the hand yet are capable of storing large amounts of energy on a unit weight basis. Other axisymmetric yet more complex structures include rectangular and square box sections, tapered truncated cones and ellipsoids. Non-axisymmetric structures have included pipe tees and elbows, L, S and T-shaped air ducts, connecting rods, leaf springs, steering wheels and bumper frames. In the same area of automotive products, some interest exists for the filament winding of passenger car frames. Other non-axisymmetric structures that have been built include a grain hopper car, storage silos, aircraft radomes, helicopter blades and boom sections, wind turbine blades and aircraft fuselages. The Beech Starship I corporate jet has a filament wound graphite fibre composite fuselage. Thus, the complexity of the component does not seem to be a limit of the filament winding process.

The majority of the components just listed have been fabricated using computer-controlled conventional or robotic winding systems. Thus, the purposes of this paper are to (1) review filament winding equipment and concepts with particular emphasis on computer control and (2) compare the filament winding of fibre composite components by conventional and robotic winding systems. The details presented in the following sections have been taken from References 3 to 34. Due to the general nature of most of the articles, References will be noted only for very specific details.

BASIC FILAMENT WINDING PROCESS

The process of the filament winding of fibre reinforced polymeric composites consists of placing resin impregnated bands of fibres under controlled tension through a payout eye on a rotating mould (mandrel) in

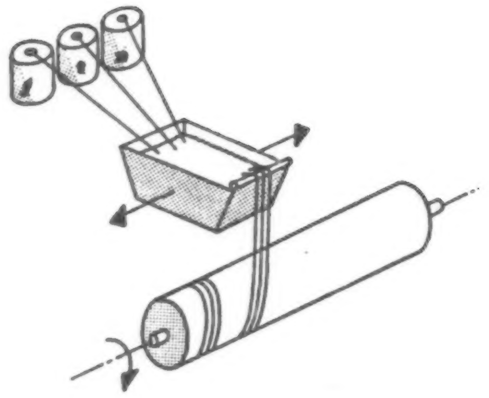

Figure 1. Classic filament winding (Courtesy McLean Anderson).

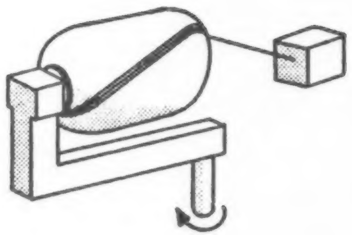

Figure 2. Polar (planar) filament winding (Courtesy McLean Anderson).

a prescribed geometric path. This path is described by the wind angle which is the acute angle between the fibre band path and the longitudinal axis of the mandrel. The fibre bands may be impregnated in a wet fashion during the winding process (schematically illustrated in Figure 1) or the fibre bands may be pre-impregnated by the material supplier with either a thermosetting or thermoplastic resin. For high quality, high performance fibre composite components very precise control of the tension in the fibre bands must be maintained. The placement of the fibre bands on the rotating mandrel requires precise control of the payout eye with respect to the rotating mandrel. The nature of this control depends upon the type of filament winder as explained in the following sections.

CONVENTIONAL FILAMENT WINDING EQUIPMENT

A typical filament winding system consists of a number of components. The first is the machine itself in which the relative motion of a number of axes is controlled. Either dry or pre-impregnated bands of fibres (referred to as strands, rovings or tows) are drawn from racks (creel) of fibre spools that may travel with the payout eye or are stationary. Tensioning devices control the tension in the fibre bands typically at the creel. In wet winding, the fibre bands after being drawn from the creel are impregnated with resin in a resin bath. The mandrels on which the resin impregnated fibres are wrapped can be removable or can remain as part of the component. Each of these components will now be discussed in more detail.

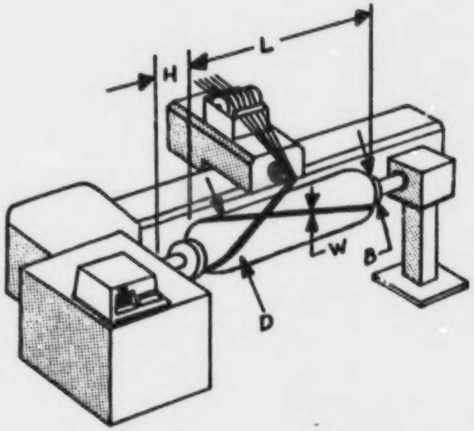

Figure 3. Helical filament winding (Courtesy McLean Anderson).

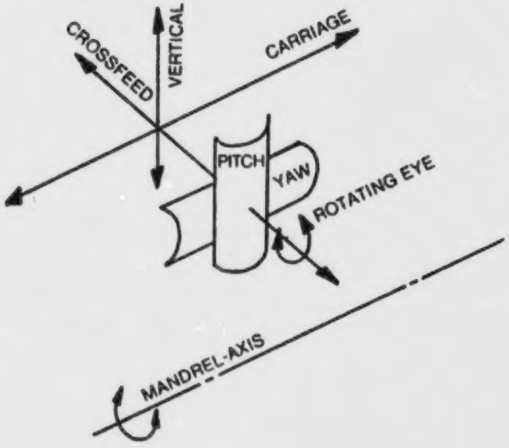
CROSSFEED
VERTICAL
CARRIAGE
PITCH
YAW
ROTATING EYE
MANDREL-AXIS

Figure 4. Typical axes of control for a computer-controlled helical filament winder (Courtesy McLean Anderson).

Conventional Filament Winding Machines

The standard conventional filament winding machines are generally available in two forms-for polar (planar) and helical winding patterns. The polar winding machines are generally mechanically-controlled devices in which the mandrel is stationary and the payout eye rotates around the mandrel or the mandrel rotates and the payout eye remains stationary (Figure 2). These latter machines are sometimes referred to as tumble winders. Coverage of the mandrel is accomplished by indexing the mandrel at the end of each polar circuit. The polar winding machines are suitable for large production runs typically of closed-end pressure vessels with low aspect ratios (length/diameter) and fibres predominantly aligned within 15° of the longitudinal axis of the vessel. The control is mechanical in nature in that the relative motion of the axes are governed by a mechanical transmission employing typically gears, cams and chain components. The helical-type winding machines of Figure 3 can also be mechanically controlled. They are particularly suited for large production runs of cylindrical components in which the wind angle is constant. Closed-end pressure vessels can also be fabricated, however, the fibre band path over the ends is limited to sinusoidal or elliptical paths. For low values of wind angle the production of these fibre band paths requires excessive overtravel of the payout eye. Various techniques can be used to reduce the overtravel, however, many machines now have additional axes which are computer-controlled.

The basic computer-controlled helical-type filament winder consists of two axes-mandrel rotation and carriage transverse (Figure 4). The addition of a crossfeed or vertical axis greatly simplifies the winding of closed end pressure vessels. For tape winding of sophisticated mandrel surface changes, payout eye rotation is required. Other axes can include the remaining vertical or crossfeed, yaw and pitch.

Other methods of control that were used in the development of the control systems have included punched paper tape, cam servos and photo control which are explained in detail in Reference 6. The original computer-controlled filament winding machines utilized standard computerized numerical control (CNC) that provided point to point motion. The standard CNC controllers generally required specific functions for filament winding to be written by the filament winding machine suppliers. Many of the present sophisticated control systems are microprocessor-based in which the positions of the dependent axes (controlled with respect to the mandrel axis) are calculated from the inputted parameters which describe the component. The computer-controlled filament winders are capable of controlling both linear and non-linear motions between mandrel rotation and carriage traverse.

The actual position and velocity data for the various axes can come from a variety of sources. The filament winding machine suppliers can furnish application programmes for the winding of standard shapes such as rings, pipes, cones and closed-end pressure vessels. The operator simply inputs the required component parameters such as diameter, length, helical wind angle, number of layers, etc., and the filament winding machine will generate the required coordinate data. For more complex structures, the required CAM data could be calculated for a subsequent section while the machine is winding the present section. Another approach would be to download from a more sophisticated and computationally faster computer. The third approach is to use a teach mode in which the required path is first marked on the mandrel. The payout eye is then positioned using joy sticks in an incremental or dynamic fashion such that the fibre band lays along the marked line on the mandrel. Various coordinate points are stored along the path. It is then possible to step forward and backward from one point to the next as well as smooth and edit the pattern in particular to remove regions of high acceleration. The smoothing and editing abilities come from the use of sophisticated and highly interactive graphics packages. Thus, it is also possible to enter data points using the interactive graphics package. In order to shorten the winding time, some of these packages can also simulate the winding of a component at a constant fibre feed rate instead of the usual constant mandrel rotation rate. For the constant fibre feed rate case it is necessary to verify that the velocity and acceleration limits of the machine have not been exceeded. One final feature is that of scaling the axes. This permits the relative motions of the axes to handle sub-scale to full scale changes as well as adjusting for the build-up of sequential layers on a wound component.

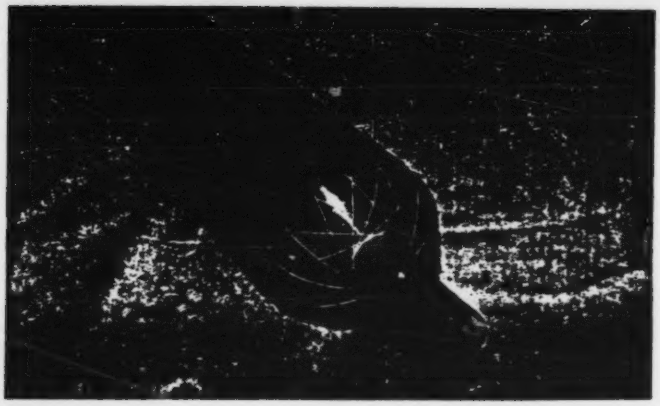

Figure 5. Geodesic path over end dome of closed-end helical pressure vessel wound with twine on silicone treated mandrel.

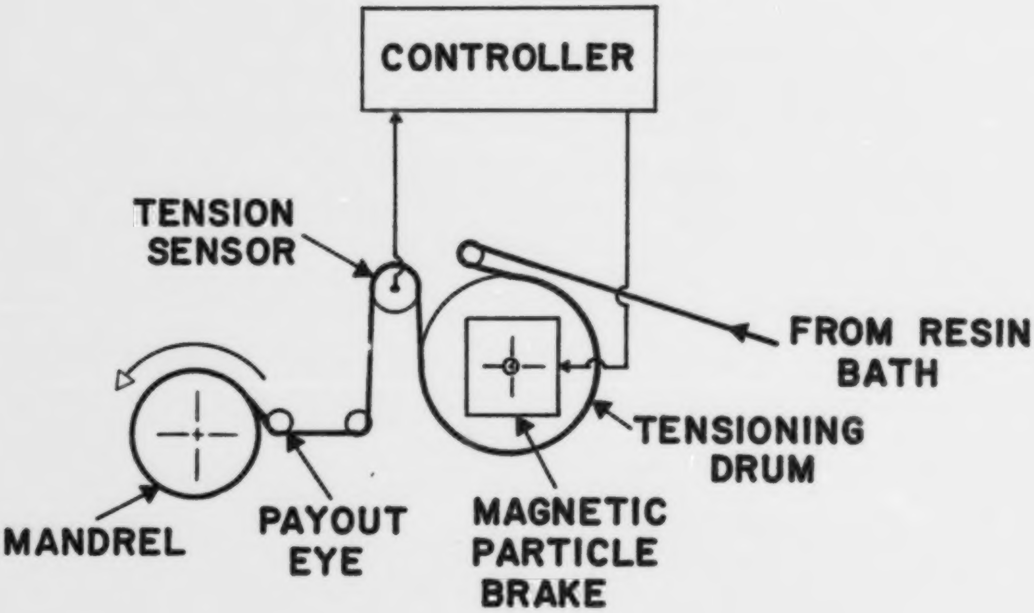
CONTROLLER
TENSION SENSOR
FROM RESIN BATH
TENSIONING DRUM
MANDREL
PAYOUT EYE
MAGNETIC PARTICLE BRAKE

Figure 6. System for applying and controlling fibre band tension after resin impregnation.

The use of a graphics package is also part of fully integrated CAD/CAM systems that have been developed for filament winding (15, 16). In these systems a 3-D solids graphics package is first used to model the component. The geodesic paths (paths on which the fibre bands are stable and do not slip even when tensioned) as illustrated in Figure 5 are then calculated and simulated on the model using the graphics package. If the pattern covers the component and is windable, a finite element mesh is automatically generated. The material stiffness constants for each element are determined from known lamina constants and the orientation and thickness of the layers determined during the simulation. The stresses and strains form the imposed loading are then compared with the failure criteria. If no values are exceeded, then the filament winder is automatically programmed to fabricate the component. Thus, as in other CAD/CAM systems, it is possible to verify the various aspects of component design and manufacture using simulations rather than a more experimental approach.

Tensioning Devices

Besides accurate placement of the fibre bands on the mandrel, the control of the tension in the fibre bands as they are being placed on the mandrel is of very practical importance. The winding tension has a direct effect on the fibre volume fraction, fibre alignment and void content. For wet winding, commercial filament winders employ a number of approaches (electrical, mechanical or pneumatic) to control the initial tension of the fibre bands typically before the resin bath, i.e., at the spool from which the fibre band is being unwound. Since fibre tension will change as it passes around guide pulleys and through the resin bath, the author has used a tension sensor/ magnetic brake closed loop feedback system to control the tension of the wetted fibre bands after the resin bath (Figure 6). This technique provides very accurate and consistent constant tensioning and is more appropriate for variable tension profiles. However, for practical reasons it is limited to single fibre band winding. For winding with thermosetting or thermoplastic pre-preg tapes tensioning could be applied using either method.

Resin Bath

For wet filament winding, three approaches are used to impregnate the fibres with the thermosetting resin. The first (which is particularly suited to low viscosity resins) consists of passing the fibre bands over the top of of a resin covered rotating drum. The drum is rotating in a resin bath and a constant thickness of resin on the drum is maintained using a doctor blade. For higher viscosity resins, faster winding speeds or heated resin baths the fibre bands are passed over and under a series of transverse fingers immersed in the resin bath. In both of the previous cases resin scrapers at the exit of the bath are used to remove the excess resin. For applications requiring a very controlled resin to fibre ratio, the resin can be metered onto the fibre bands in proportion to the fibre band feed rate (21, 22, 23).

Mandrels

There are essentially two types of mandrels - permanent and removable. The permanent mandrels are typically for pressure vessels that are of the load sharing type, i.e. thick metallic inner liner or non-load sharing employing a thin metallic inner liner simply to provide an impervious seal to gases or liquids and act as mandrel for winding. For open-end structures, annular or solid steel or aluminum removable mandrels are appropriate. For closed-end structures the removable mandrels can be made of sand and binder (polyvinyl alcohol, sodium silicate) or soluble plaster that is dissolved by water after curing, eutectic metals or salts that are melted out or inflatable elastomeric bags. For large diameter components mandrels can be made of frangible plaster or metallic collapsible segments that are removed from the inside after curing.

Auxiliary Function

Modern computer-controlled filament winding systems not only perform the functions described in the previous sections, they also monitor and control other functions and document the entire winding process. It is possible to monitor and control such functions as fibre delivery rate and amount, fibre breakage, resin bath level and temperature and the temperature at the pre-preg head or of the mandrel. These functions, as well as operator interruptions, can be documented in a hard copy at the end of the process thus providing detailed information for each component fabricated.

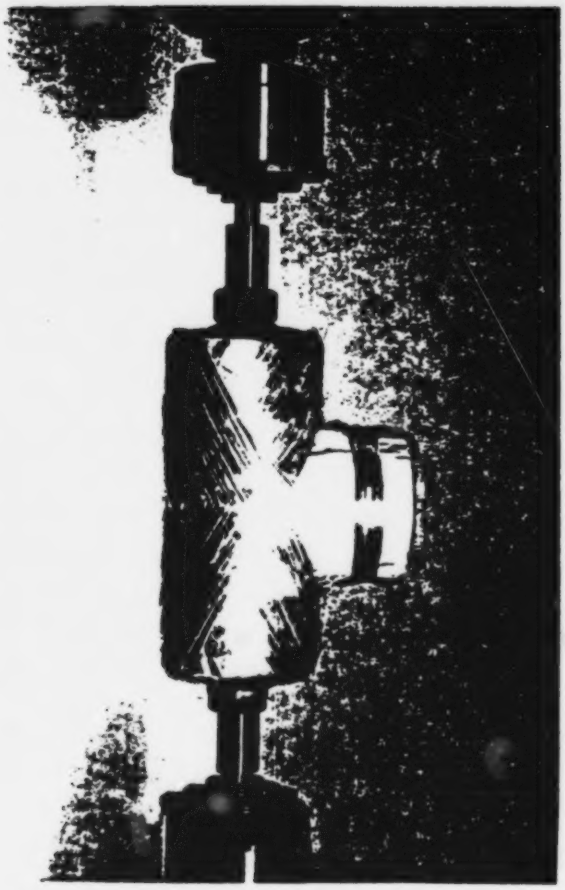

(a)

(b)

Figure 7. Fibre composite proof-of-concept components fabricated by a robotic winding system.

(a) fibreglass pipe tee preform
(b) closed end pressure vessel wound with graphite fibre prepreg tape.

ROBOTIC FILAMENT WINDING

The fabrication of fibre composite components by a robotic winding system is being studied in Europe, the United States and Canada. The European systems have been developed by Professor W. Menges of the University of Aachen to fabricate a variety of components (28). Northrop's Ventura Division is using one of Professor Menges' 7-axis robotic winding systems to fabricate different types of complicated ducting components (19). Automated Dynamics Corporation of Troy, New York has developed a winding head that attaches to an industrial robot for filament winding of fibre composite components on a stationary mandrel (19). The author has also evaluated the use of an industrial robot with an auxiliary rotating mandrel for the fabrication of proof-of-concept pressure vessels with pre-preg tape and fibreglass pipe tees (Figure 7). The above robotic winding systems have been developed in competition with conventional filament winding systems for certain production situations. A qualitative comparison of the two manufacturing approaches is given in the next section.

COMPARISON OF FILAMENT WINDING OF FIBRE COMPOSITE COMPONENTS BY CONVENTIONAL AND ROBOTIC WINDING SYSTEMS

A comparison of these two processes is very dependent on the size and the component that is being manufactured. Typical conventional helical-type filament winding machines have adjustable tailstocks and long beds that can accommodate high aspect ratio (ℓ/d) mandrels. At the moment, the robotic winding systems have used stationary robots. The

COMPARISON OF FILAMENT WINDING OF FIBRE COMPOSITE COMPONENTS BY CONVENTIONAL AND ROBOTIC WINDING SYSTEMS

CRITERION	CONVENTIONAL FILAMENT WINDER	ROBOTIC FILAMENT WINDER
COST (Can. $)	$250,000 (min.)	$180,000 (min.)
SYSTEM RESPONSE		
- max. traverse speeds	~ 0.7m/sec	~1m/sec
- max. payout eye rotation	~ 0.5rev/sec	~0.5rev/sec
ACCURACY/REPEATABILITY	similar (~±0.2mm)	
AUTOMATIC MANDREL CHANGING	possible, especially for large production runs of one component	possible, even for mixed components
PROGRAMMING		
- teach mode	yes	yes
- application software	available	available
- down loading	yes	yes
ADDITIONAL PROCESSES		
- chopper gun spraying	available	possible
- roller impregnation	possible	possible
- tape laying	possible	possible
- trimming, drilling	?	possible
- painting	?	possible

working envelope of the robots is quite small when compared to that of the conventional filament winding machines. Thus the basis for comparison will be for systems that would be used to fabricate small yet complex fibre composite components. It is expected that at least four axes of control will be required so as to permit filament winding with pre-preg tapes. A summary of the results is given in Table I with details outlined below.

The cost of a complete winding facility obviously depends upon the options selected and the actual unit considered. For this comparison, a cost was estimated for a basic 4-axis conventional filament winding machine. Microprocessor-based control was assumed for the conventional filament winder while the 5-axis robotic system included the robot controller, a microcomputer, the microcomputer/robot controller interface software and an auxiliary mandrel drive.

The response of the two systems was mainly judged on the maximum traverse rates and payout eye rotation rate. Accuracy and repeatability can be specified for a conventional filament winding machine as part of the purchase specification. For the industrial robots this is generally a specified pre-determined value. Both parameters are also very much a function of the operating speed and speed changes. In summary, it can be said that both systems are accurate and repeatable to the same degree.

In a fully automated flexible manufacturing system, it is desirable to remove the operator form the process as much as possible. In addition, many of the resin systems are toxic or carcinogenic. It is, therefore, desirable to have the bare mandrels automatically loaded and automatically unloaded after winding. This can be accomplished with a robotic system by simply changing the end effector on the robot. The robotic system should be able to handle a large variety of mandrel types and transfer them form or to any position within its working envelope. Automatic mandrel changing has been developed for conventional filament winding machines, however, the complexity increases with different mandrel sizes and types.

In terms of programming the fibre band path, both systems are available with teach mode. Application software for simple shapes is probably more available for the conventional filament winding systems. Downloading of CAM data from larger computers is possible with both systems.

The robotic winding system is readily capable of doing many other types of manufacturing operations as listed in Table I due to its large work envelope, two extra axes of control and since changing end effectors is a natural process for industrial robots.

The previous discussions have shown that robotic filament winding is a possible manufacturing system for some types of components. In order to increase the acceptance of robotic filament winding systems, the robots must operate at fast speeds. This will require faster hardware, improved software algorithms and lightweight arms to be developed. The

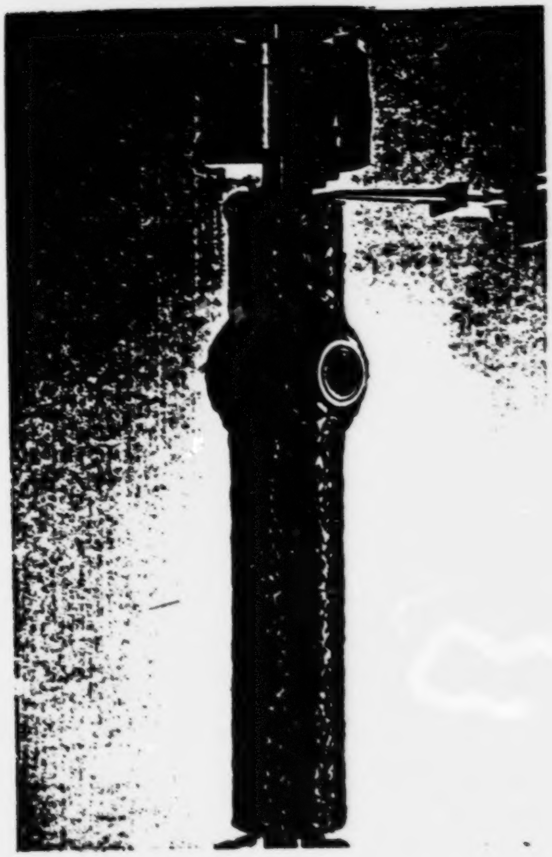

Figure 8. Proof-of-concept dry winding of a graphite fibre composite robotic arm with integral metallic housing.

concept of lightweight filament winding machines in general is discussed in the next section.

FIBRE COMPOSITE FILAMENT WINDERS

One possible approach to increase the speed of conventional filament winding machines is to fabricate as many of the carriage components out of lightweight fibre composites. Braun (31) has also suggested the use of lightweight graphite fibre composite robots to replace the conventional carriage and payout eye assembly. There has been significant activity in the development of graphite fibre composite robots both in North America and Japan (32). It is believed by the author that the development should be centred on filament winding where an integral metallic housing (for bearings or direct drive motors) is wound in at the same time. A proof-of-concept mandrel with a dry preform winding of carbon fibres is shown in Figure 8.

HYBRID FILAMENT WINDING PROCESSES

The process of filament winding can also be coupled with other promising fibre composite manufacturing processes (33). One of the most promising processes for fibre composite automotive parts is resin transfer moulding. One of the major problems with resin transfer moulding is the preparation of the dry fibre preform (34). Filament winding can be used where the resin is replaced by a binder solution for the high-speed automated production of the preforms. Wet filament winding can also be used in combination with compression moulding where the filament winding process is used to prepare a wet wound slab-type preform which is then compression moulded to final size and shape.

ADVANCED FILAMENT WINDING CONCEPTS

Filament winding systems are available for the filament winding along geodesic paths of complex axisymmetric and non-axisymmetric components. For non-symmetric components there is no single geodesic path that is repeated many times to completely cover the mandrel surface but in fact individual paths for each circuit must be calculated. This will probably be performed by CAD systems or mainframe computers and the coordinate data for winding will then be downloaded to the filament winding machine microcomputer.

Other areas of advanced research are in non-geodesic winding and winding in reverse curvature areas (i.e. concave contours). Both approaches involve placing fibre bands where they might slip due to the applied tension. Some mechanical methods to solve this problem that have been employed include winding around pins, relying on friction or compressing pre-preg tapes onto the surface. Cure related techniques include rapid in-situ curing by ultra violet light (if appropriate) or by the winding of thermoplastic pre-preg tapes where melting and solidification occurs at the point of tape laydown on the mandrel before any shifting can occur.

ACKNOWLEDGEMENTS

The author wishes to acknowledge the financial support of the Natural Sciences and Engineering Research Council of Canada and the University of Ottawa. The contribution of graphite fibre prepreg tape from Boeing Canada Limited is greatly appreciated.

CONCLUSIONS

The filament winding process can be used to fabricate both simple and very complex fibre composite structures. This paper has reviewed the different types and components of filament winding equipment. Future promising directions of robotic winding systems, winding with thermoplastic materials and winding of non-geodesic and reverse curvature structures have been indicated.

REFERENCES

1. W.T. Freeman, Filament Winding Clinic, Society of Manufacturing Engineers, Anaheim, California, Paper No. 6, (1985).

2. S. Krolewski and T. Gutowski, SAMPE Journal 23, 3, 21 (1987).

3. J.F. Kober, 35th Annual Technical Conference, Reinforced Plastics/Composites Institute, Section 19-A, 1 (1980).

4. D.E. Beck, 36th Annual Technical Conference, Reinforced Plastics/Composites Institite, Section 5-B, 1 (1981).

5. C.D. Hermansen and R.R. Roser, ibid, Section 5-A, 1 (1981).

6. M.L. Skinner, R.R. Roser and K.J. Samowitz, IEEE, Paper No. 82CH1817-6, (1982).

7. T.M. Harper and J.S. Roberts, 39th Annual Technical Conference, Reinforced Plastics/Composites Institute, Section 9-E, 1 (1984).

8. R.R. Roser, 29th National SAMPE Symposium and Exhibition 29, 73 (1984).

9. R.R. Roser, 30th National SAMPE Symposium and Exhibition 30, 1231 (1985).

10. R.R. Roser, Society of Manufacturing Engineers, Paper No. MF85-504.

11. M. Munro, A. Miyase, J. McCrea and R.C. Flanagan, 17th Intersociety Energy Conversion Engineering Conference, 1967 (1982).

12. J-C. Leon and G. Wells, 1st European Conference on Composite Materials, 532 (1985).

13. R.R. Roser, M.L. Skinner, K.J. Samowitz, K.L. Kemp and B.L. Folsom, 31th International SAMPE Symposium, 810 (1986).

14. M.J. Owen, V. Middleton, D.G. Elliman, H.D. Rees, K.L. Edwards, K.W. Young and N. Weatherby, Institution of Mechanical Engineers Paper No. C29/86, (1986).

15. G.M. Wells and G.C. Eckold, 1st International Conference on Automated Composites, 6/1 (1986).

16. V. Middleton, K.W. Young, D.G. Elliman and M.J. Owen, ibid, 9/1 (1986).

17. C. Kirkland, Plastics Technology 10, 5, 77 (1980).

18. T.L. Elegante, Mechanical Engineering 108, 12, 32 (1986).

19. L.M. Sheppard, Advanced Materials and Processes 7, 31 (1987).

20. D.J. Gayman, Manufacturing Engineering 99, 1, 26, (1987).

21. G. Lubin, "Handbook of Composites", p. 448, Van Nostrand Reinhold, New York (1982).

22. R.R. Zeits, AVRADCOM Report No. TR79-15, (1979).

23. Sales Literature, Josef Baer Maschinenfabrik.

24. Sales Literature, McLean-Anderson.

25. Sales Literature, Engineering Technology Inc.

26. Sales Literature, Goldsworthy Engineering Inc.

27. Sales Literature, Pultrex Limited.

28. G. Menges and E. Neise, 5th International Conference on Composite Materials, 457 (1985).

29. G. Menges and E. Neise, 40th Annual Technical Conference, Reinforced Plastics/Composites Institute, Paper 19-B, 1 (1985).

30. G. Menges, E. Schmachtenberg and K. Kirberg, Second ASM Conference on Advanced Composites, 163 (1986).

31. W. Braun, 1st International Conference on Automated Composites, 11/1 (1986).

32. A. Fahim, M. Munro and H. Sarrazin, DREP/RRMC Workshop on Military Robotic Applications, Victoria, B.C., (1987).

33. D.J. Zeier, 1st ASM Conference on Advanced Composites, 107 (1985).

34. C. Johnson, Automotive Applications of Plastic and Advanced Composites Today and in the Future, Toronto, Ontario, Presentation No. 7, (1986).

SIMULATION OF FLOW IN INTERNAL MIXERS AND TWIN SCREW EXTRUDERS

by

J.L. White, W. Szydlowski, J. Kim and K. Min
Center for Polymer Engineering
University of Akron
Akron, Ohio, U.S.A.

(Manuscript not received on time. Please communicate with the authors.)

RHEOLOGY OF MICA-FILLED POLYPROPYLENE AS INFLUENCED BY COUPLING AGENTS

by

A. Rochette, L. Choplin, P.A. Tanguy
Université Laval
Québec, Canada

(Manuscript not received on time. Please communicate with the authors.)

MECHANICAL AND RHEOLOGICAL PROPERTIES OF CARBON BLACK FILLED POLYETHYLENES

by

T. Malik, P.J. Carreau and M. Grmela
Department of Chemical Engineering
Ecole Polytechnique de Montreal
Montreal, Que., Canada

(Manuscript not received on time. Please communicate with the authors.)

PROCESSING SEQUENCE AND THE PROPERTIES OF VINYL COMPOUNDS

by

E. Trujillo, C. Richard and H.P. Schreiber
Department of Chemical Engineering
Ecole Polytechnique de Montreal
Montreal, Que., Canada

Presented at the 8th annual NRCC/IMRI symposium "Composites-'87",
November 5 and 6, 1987, Boucherville, Que., Canada

PROCESSING SEQUENCE AND THE PROPERTIES OF VINYL COMPOUNDS.

E. TRUJILLO, C. RICHARD AND H.P. SCHREIBER
Department of Chemical Engineering, Ecole Polytechnique de Montreal.

ABSTRACT.

Acid - base interaction parameters were measured by inverse gas chromatography over broad temperature ranges for PVC, plasticizer and $CaCO_3$ fillers used as components in formulations which were mixed in a torque rheometer. Mixing was performed by three different routes: In one, all components were added simultaneously, whilst in other schemes two of the components were premixed with the third ingredient added subsequently. Mixing was carried on to equilibrium torque readings. Energy requirements for the mixing processes were evaluated from areas under torque vs. time diagrams, and the mechanical properties of resulting compounds were represented by stress - strain data. The latter were re-evaluated following aging periods at controlled temperature. Energy requirements for the attainment of equilibrium torques were shown to vary with the interaction balance among components, confirming similar earlier findings. Furthermore, these energies varied significantly with mixing sequences, minimum requirements being associated with the simultaneous dispersion of all ingredients. In other processing schemes, higher energies were needed, presumably because equilibrium partitioning of components was influenced by the imposed premixing schemes. Initial mechanical properties of compounds showed relatively slight variation with selected mixing sequences, but upon aging, property variations clearly distinguished among the compounds. Component repartitioning, driven by shifting acid-base interaction balances at aging and test (room) temperatures, was more rapidly attained in compounds with all ingredients mixed simultaneously. Specific interactions among compound constituents also influenced absolute values of mechanical property parameters along with rates of property reattainment following controlled temperature variations.

INTRODUCTION;

The question of interactions among the materials involved in a multi-component polymer system has been given much attention in recent times. Focal points are methods whereby these interactions may be evaluated quantitatively, and relationships between component interactions and various properties of the system. Acid/base concepts have gained credence in representing other than dispersion force interactions, Fowkes (1) having reviewed the subject recently. The method of inverse gas chromatography (IGC) has been adapted in our work(2,3) to serve as a convenient route to the evaluation of quantitative.comparative indexes of acid/base interaction. Use of this approach has enabled us to rationalize dispersion behavior of particulates in polymer matrixes, and the responses of polymer mechanical properties to the presence of various particulate additives.

The concept of interactions is applied, in the present work, to the diverse routes that may be taken in compounding a system to its final composition. This reflects on a widespread practise to prepare masterbatches or concentrates of some of the components in a system, and then to dilute to final compositions. The practise may bring into play a wide range of component interactions,the more so since compounding operations are generally conducted at elevated temperatures, while storage and eventual use of the compounds takes place at near-ambient temperatures. Acid/base and other specific interactions related to enthalpic and entropic factors being temperature dependent(4), it seems possible that significant shifts in interaction forces occur during these phases of a system's handling, creating(at least transient)local compositional heterogeneities and transient property balances. Filled, plasticized PVC compounds were well suited for present purposes, and this report expands on earlier data given in ref.(3).

EXPERIMENTAL SECTION;

Materials and compounding sequences: The host resin was a commercial, suspension polymerized PVC (K value of 65). Di n-octyl phthalate (DnOP) was used as plasticizer at 40 phr of PVC. Compounds were filled with two grades of $CaCO3$: One (-I) had a BET surface area of 2.7 m^2/g and an average particle size of 2.6µm; the second (-II) reported 2.4 m^2/g of surface and a mean particle size of 2.4 µm. Both fillers were commercial, surface coated samples. A commercial tribase stabilizer also was involved.

TABLE I

COMPOSITION OF TEST SPECIMENS*

Compound Comp (phr)		PVC	DnOP	$CaCO_3$-I	$CaCO_3$-II
Mix-Sequence:	Comp. Code:				
A	A-1	100	40	20	–
	A-2	100	40	–	20
	A-3	100	40	40	–
	A-4	100	40	–	40
B	B-1	100	40	20	–
	B-2	100	40	–	20
	B-3	100	40	40	–
	B-4	100	40	–	40
C	C-1	100	40	20	–
	C-2	100	40	–	20
	C-3	100	40	40	–
	C-4	100	40	–	40

* All compounds also contain 3 phr. lead tribase stabilizer.

Each of the compounds used in this work was prepared by three different routes. Throughout, however, compounding was done in a Brabender mixer at T= 190C and 50 rpm motor speed, so that the compounds shared the same shear - and thermal-history(5). Further, the mixer was always operated under constant volume -loading (45 cm.^{3}). The following were the mixing sequences:

SEQUENCE A: All components of the system were premixed by hand, and introduced into the Brabender. The mixer was operated to constant torque, and an additional 2 minutes of mixing was allowed to ensure attainment of steady-state dispersion.
SEQUENCE B: A filled,rigid PVC mass was prepared by fusing polymer and fillers in the Brabender (190C); plasticizer was then added and mixed to constant torque plus 2 mins.
SEQUENCE C: Polymer and DnOP were premixed in the Brabender (190C); fillers were then added to the plasticized mass and milled to constant torque plus 2 mins.
The composition of specimens used in this work and their identification codes are shown in Table I.

Test procedures:
The interaction potential of materials used in this work was determined by IGC procedures reported previously (2,3). Chromatographic columns for PVC and DnOP were prepared by coating Chromosorb W support particles, while the fillers were tumbled with glass spheres 0.5 mm. in diameter, and the coated spheres were used as substrates in IGC determinations. Specific retention volumes, $(V_g)_o$, were determined for very dilute injections of n-butanol and n-butyl amine. Determinations were in quintuplicate, with a reproducibility of ± 3% for PVC and plasticizer, and ± 7% for the fillers. Investigation covered the temperature range 30-110 C. The choice of vapors followed the acid/base concepts of Drago and coworkers (6), and of Prausnitz (7); thus the alcohol serves as a Lewis acid probe, and the amine as a Lewis base. The interaction potential of the stationary phase in the IGC procedure is then evaluated from the parameter Ω, as follows(2):

$\Omega = 1 - (V_g^\circ)_b/(V_g^\circ)_a$ when V_g° for the amine > than for the alcohol, and

$\Omega = (V_g^\circ)_a/(V_g^\circ)_b - 1$, when the V_g° for alcohol > for amine.

Thus negative values of Ω denote a Lewis acid, and positive ones a Lewis base.

Parameters characterizing the dispersion performance of the system were drawn from the Brabender mixing trace,

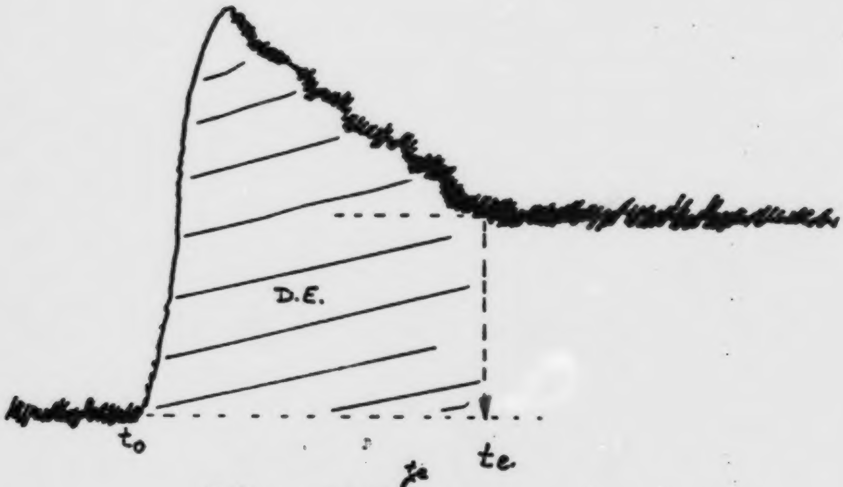

$$D.E. = 2\pi N \int_{t_o}^{t_e} \tau \cdot dt.$$

Fig.1. Typical Brabender dispersion trace for filler in PVC host polymer.

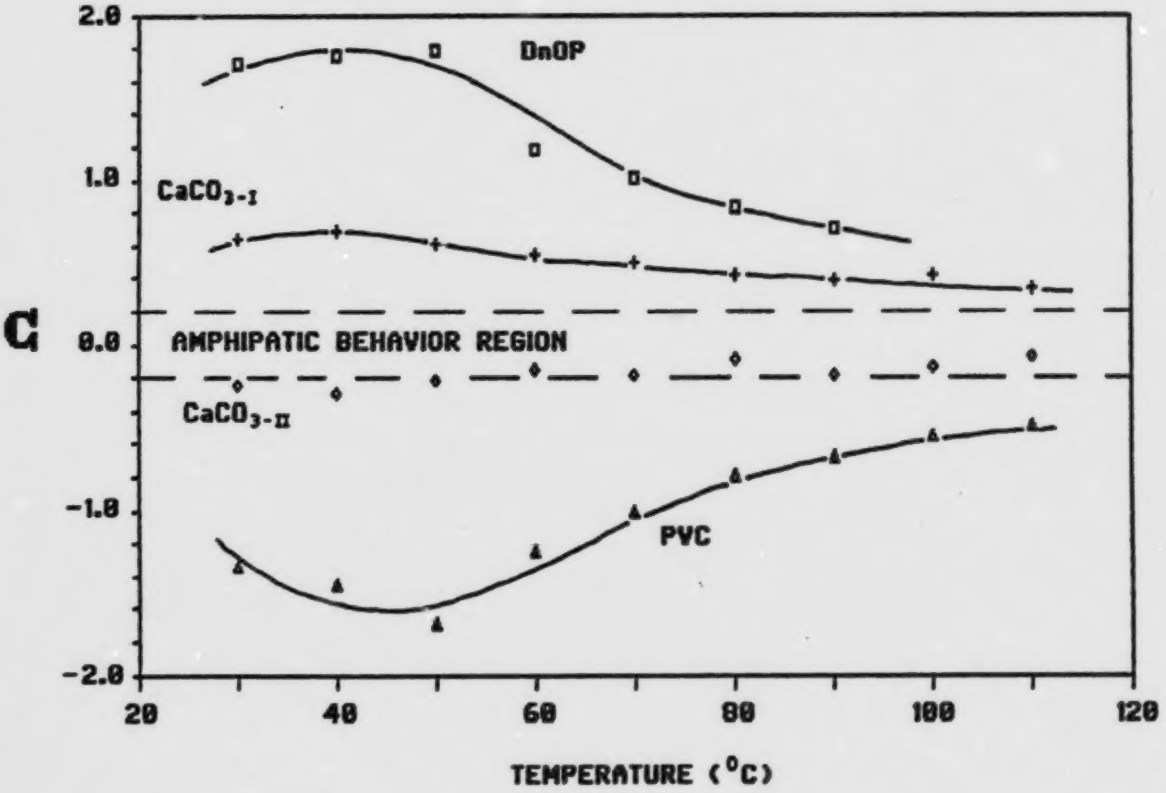

Fig.2. Temperature variation of acid/base interaction parameter for components of filled polymers.

as illustrated in Fig.1. Here t_o marks the time when the instrument is loaded, and t_e is the time for attainment of a torque equilibrium. The area under the curve, as shown, is termed a "dispersion energy" parameter (D.E.) and is defined by:

$$\text{D.E.} = 2N\pi \int_{t_o}^{t_e} \tau dt,$$

where N is the rotational speed of the mixer, and τ is the torque.

Mechanical properties of test compounds were measured by stress-strain data, using an Instron table-model tester at a drawing speed of 5 cm/min. Test specimens were prepared by compression molding at 190C,2000 psi for 2 min., then quenching the plates in cold water. Mechanical testing was performed on samples as prepared, following equilibration at 45C for selected periods,and also following extended conditioning at 110C, as annotated in appropriate sections of this paper.Circulating-air ovens were employed for thermal conditioning.

RESULTS AND DISCUSSION.

Interaction characteristics: Values of Ω for PVC, DnOP and the two versions of $CaCO_3$, are shown in Fig 2 over the entire temperature range studied. The experimental uncertainties of Ω determinations suggest that a band be defined in the region of $\Omega = 0$, into which should fall materials able to interact through dispersion forces alone, and amphipatic materials with balanced acidic and basic interaction sites. Filler -II falls into this band, the surface coating applied to this commercial sample evidently mitigating the basic tendencies displayed by -I. Though a mild temperature variation of Ω is discernible, particularly in -I, this is much less than the T-dependence shown by the PVC and the plasticizer. The inherently acidic polymer attains an Ω minimum near 50C, and correspondingly,the inherently basic plasticizer a maximum in the 50-60C range. This is attributed to the stronger bonding between acid/base pairs than between like pairs at probe/substrate contacts. The different activation energies for debonding vapor molecules from surface sites would then tend to accentuate inherent acid or base tendencies in substrates, until sufficient thermal energy had been supplied to the system to reduce these debonding energies to those associated with longer-range, but weaker dispersion forces.

Certain consequences are suggested by the data in Fig.2. These include:

.. Strong acid/base interaction should bond plasticizer and polymer at lower (eg use) temperatures, but at

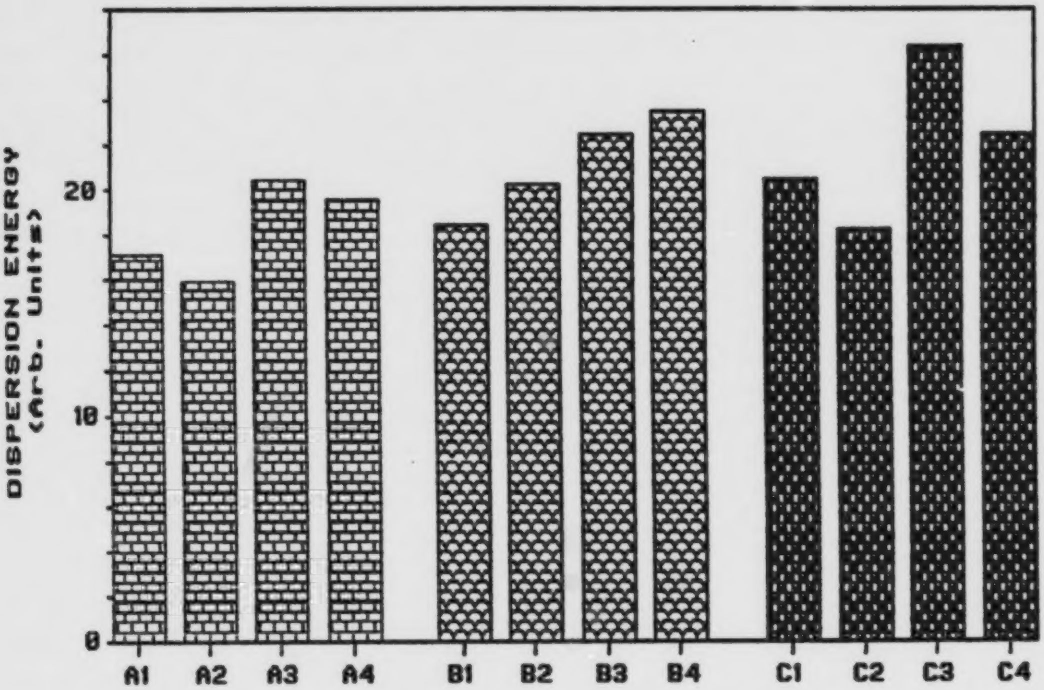

Fig.3. Dispersion energy demand for PVC formulations prepared by alternate compounding strategies.

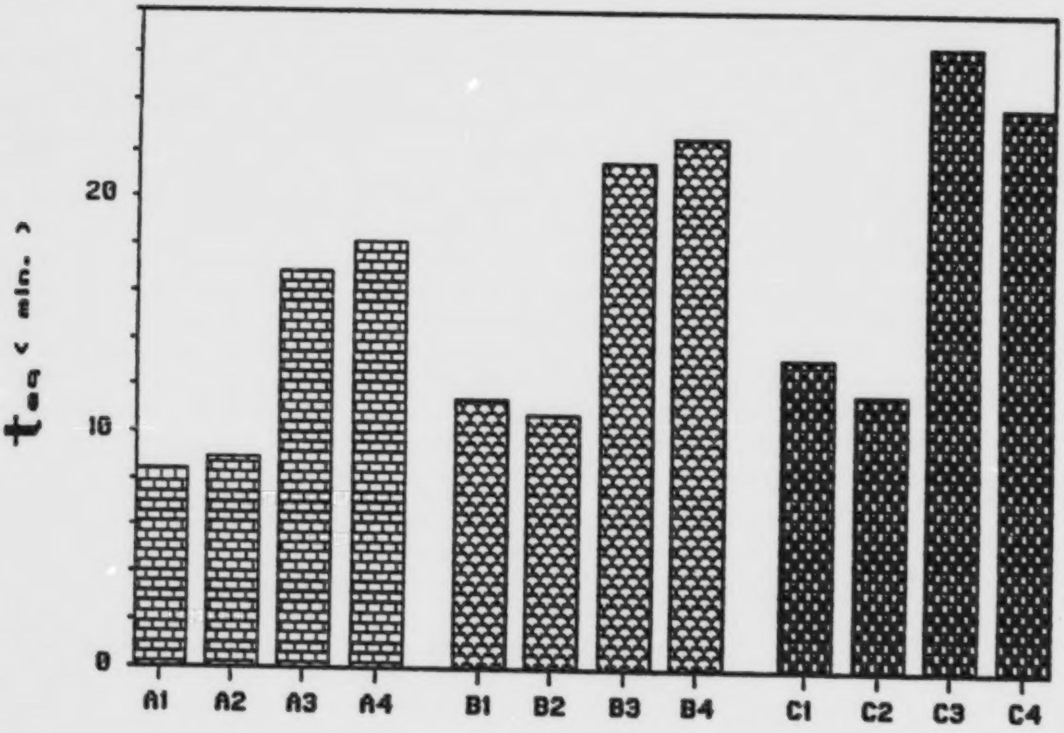

Fig.4. Dispersion times for PVC formulations by alternate compounding strategies.

mixing and processing temperatures (>110C) these forces appear to be much reduced. Freshly prepared compounds may therefore be in transient states of plasticizer distribution.

.. Filler -I will tend to associate appreciably with the host polymer,but will be relatively hostile to contacts with the plasticizer. Competition between filler/polymer and plasticizer/polymer contacts should therefore be expected to influence both mixing and solid-state properties.

.. Filler -II should act as a good "bridging" material, being able to interact with plasticizer and with polymer constituents. Compounds with ostensibly equivalent compositions, but containing fillers with different surface coatings, may therefore be variously heterogeneous. Indeed, it might be argued that when specific (eg. acid/base) interactions exist in a polymer system, compositional heterogeneity at local (eg. molecular,domain,etc) levels is a general condition (8,9).

Dispersion behavior: First evidence that the mixing sequences adopted for this work lead to different properties of the present systems, thereby affecting performance parameters,is to be found in Figs.3 and 4. The former shows variations in the dispersion energy parameter,D.E., the latter in the time required to attain steady-state torques in the mixing experiments.For any given compound, the most efficient mixing sequence is A - i.e. the simultaneous charging of all constituents into the mixing chamber. This leads to lowest values of both D.E. and t[illegible]. Sequence B is noticeably more time- and energy-consuming, and sequence C is the least effective mixing procedure.

A qualitative rationalization of these findings is based on the ease of partitioning the diverse materials according to acid/base (thermodynamic) driving forces.Under the influence of a high shear field at elevated temperature the materials mixed by sequence A may be assumed to partition randomly. Steady states are attained rapidly, with little differentiation between compounds using filler -I or -II. This does not mean, of course, that the distribution of components attained is the thermodynamically favored one. In sequence B, the basic DnOP must dilute a premilled masterbatch of PVC/filler. Since there is finite specific interaction between these materials, the rates of steady-state attainment are reduced relative to sequence A. The performance of samples with filler -I and -II, again, is quite similar - this in spite of stronger competition offered to DnOP/PVC contacts by the basic filler -I (see Fig.2). The performance variations in sequence C are pronounced; here the seemingly restricted capability of the basic filler (-I) to

TABLE II INITIAL MECHANICAL PROPERTIES OF PVC COMPOUNDS

Compound	In. Modulus (MPa)	El. at rupture (%)
A-1	126	355
A-2	108	380
A-3	175	160
A-4	143	190
B-1	140	310
B-2	122	330
B-3	212	115
B-4	168	125
C-1	110	330
C-2	110	330
C-3	152	125
C-4	145	135

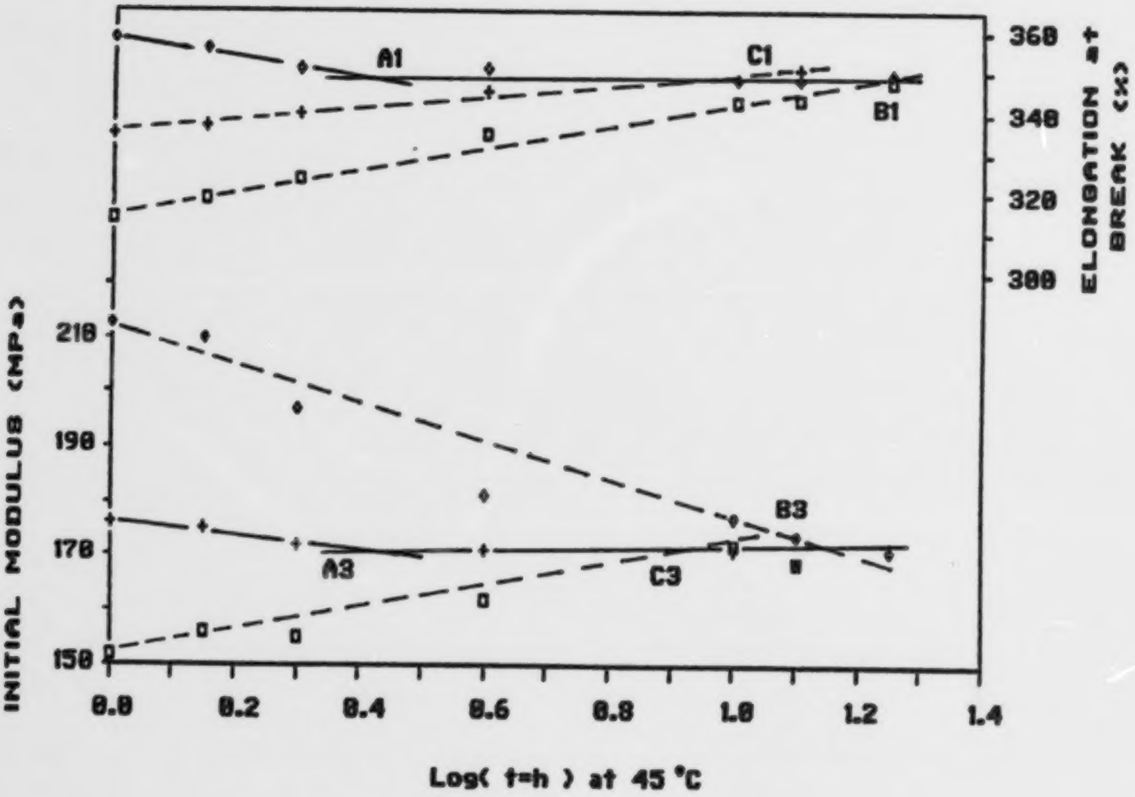

Fig.5. Time-dependent changes in modulus and elongation on 45C annealing: Illustration for compounds using filler I, prepared by routes A,B and C.

promote the partitioning of the mobile plasticizer results in significant increases in both D.E. and t_{eq}..The C sequence is, in this comparison, the least attractive compounding option.

Initial mechanical responses: Initial moduli and elongations at rupture were the parameters selected to characterize the mechanical responses of the test materials. A summary of these data is given in Table II. The preparation procedures, involving quenching of compression-molded plaques, are unlikely to result in equilibrium properties. Indeed, considerable variation is in evidence; the modulus is affected significantly by a change in compounding procedure, particularly when filler -I is used. Moduli tend to be highest for procedure B, and lowest for sequence C. Correspondingly, lower elongational properties are observed for B than for the other mixing sequences. Hypothetically, the stronger bonding tendency between the acidic polymer and the basic filler -I,may lead to preferential association between these constituents, thus accounting for the observations.

It is, of course, thermodynamically inadmissible for one composition of matter to display several values of a given property, and it follows therefore that at least some,and possibly all of the data points reported in Table II describe the system in some specific non-equilibrium state. Test specimens were therefore annealed at 45 C, as already noted, in order to permit adequate relaxation time for the attainment of property equilibria. Test data at the reference T=30C, following specified annealing times, are presented in Fig. 5, for systems A-1,B-1,C-1 and A-3,B-3,C-3. Data for systems using filler -II followed paths similar to those shown. For convenience, a log time abscissa has been chosen. Clearly, none of the initial compound properties are equilibrium responses, those obtained for compounds made by sequence A being closest to the mark. Evidently,when all constituents are introduced into the mixing chamber simultaneously, the tendencies for non-equilibrium partitioning are reduced. As already suggested, the strong coupling between PVC and filler -I,inherent in their acid/base balances,is best realized in compounding sequence B, leading to large increments in modulus, and corresponding decreases in ductility. Sequence C, of course, has opposite effects. Pre-plasticization tends to produce lower compound stiffness, though the deviation from properties shown by compounds from sequence A is not as pronounced as that incurred by sequence B. The times alotted in the mixing sequences, albeit producing steady-state torques, are inadequate to generate equilibrium partitioning of the constituents. That partitioning takes place presumably by diffusion-dependent

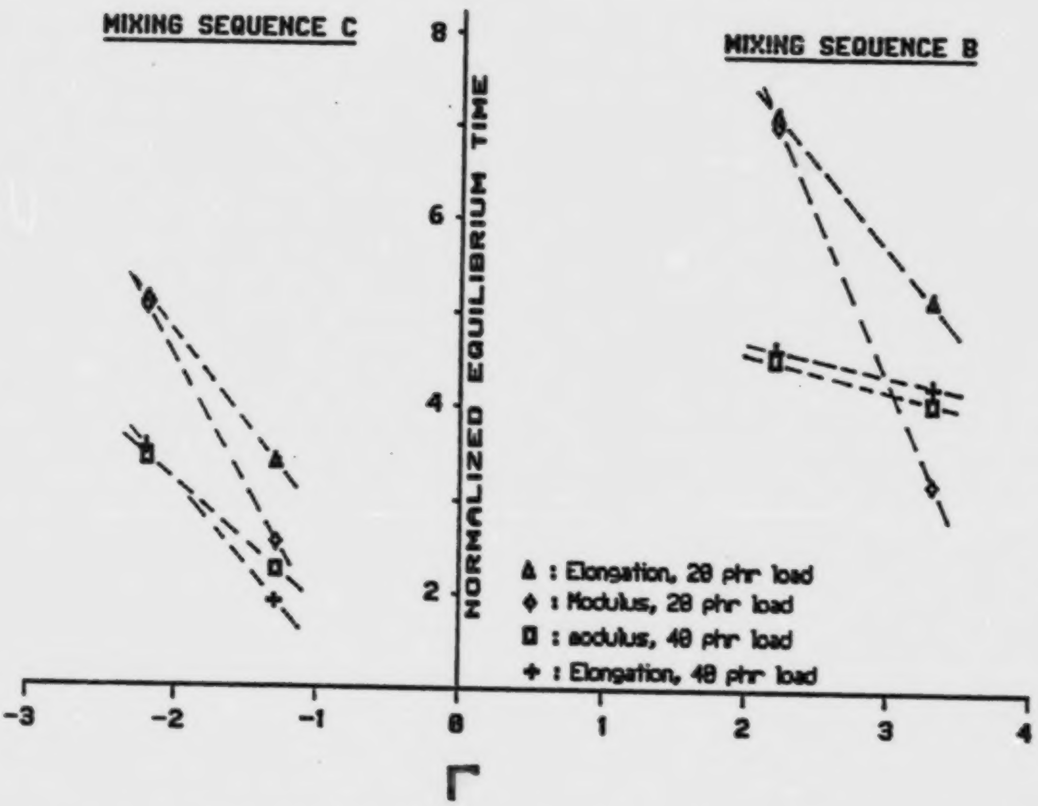

Fig.6. Time demand for attaining equilibrium properties as function of partitioning power of DOP (seq.B) and filler (seq.C).

TABLE III

EQUILIBRATION TIMES & NORMALIZATION FOR ANNEALING AT 45°C

Property:	In. Modulus		Elongation	
Teq. (h) for		Norm. Value		Norm. Value
A-1	2.1	1.0	2.3	1.0
A-2	1.8	1.0	1.2	1.0
A-3	2.6	1.0	3.0	1.0
A-4	1.5	1.0	1.9	1.0
B-1	14.5	6.9	16.0	7.0
B-2	5.7	3.2	6.1	5.1
B-3	11.5	4.4	13.4	4.5
B-4	6.0	4.0	8.0	4.2
C-1	10.6	5.0	11.5	5.0
C-2	4.5	2.5	4.0	3.3
C-3	8.5	3.3	10.1	3.4
C-4	3.3	2.2	3.7	1.9

mechanisms, similar to those documented in the behavior of PVC compounds modified by solution-and shearing processes(10).

The times needed to attain property equilibria can extend to 10-20h at 45 C, as shown in the Figure. Another view of the time factor is provided via Table III. Here the time requirements for attaining equilibrium values of moduli and ductilities are given in extenso, and also as normalized to those pertaining to mixing sequence A. The superior effectiveness of method A in attaining steady-state properties is shown particularly well by the normalized set of values. The same data may be used to test the hypothesis that the diverse routes taken to property equilibria are a reflection of the different degrees to which inherent acid/base interactions can take place under the particular mixing operations represented by the present sequences. In order to proceed, we introduce an empirical parameter of component pair interactions, based on the tabled Ω values. We assume that under condition A, interaction balances are in a reference state defined by the temperature and shear field conditions pertaining to that operation. The new parameter, Γ, then expresses the "partitioning strength" of the component introduced in the final stage of operations B and C. For example, in operation B, DOP is added to a preblend of PVC and filler. As demonstrated, compound properties differ from those made by sequence A; the time needed to attain equilibrium properties at stated T is therefore assumed to depend on the partitioning strength of the DOP at that T. At 45 C, the value of Γ is calculated from the difference between the interaction strengths of the pairs DOP/PVC and DOP/$CaCO_3$. For filler -I, then,

$$\Gamma = (\Omega_{DOP} - \Omega_{PVC}) - (\Omega_{DOP} - \Omega_{I}) = 2.27 \ ,$$

while for filler -II the value of $\Gamma = 3.31$.

Similar approaches taken for mixing sequence C produce Γ values of -2.21 and -1.30 for fillers -I and -II respectively.

Values of Γ are plotted against normalized equilibration times in Fig. 6 (equilibration times from Table III). The data available admittedly do not justify firm conclusions to be made. They do suggest however, that both modulus and ductility respond to annealing in a manner consistent with the premise that specific (acid/base) interactions provide the driving force for the rates at which equilibria are sought.

Mechanical responses after thermal conditioning : The retention of compound properties following accelerated

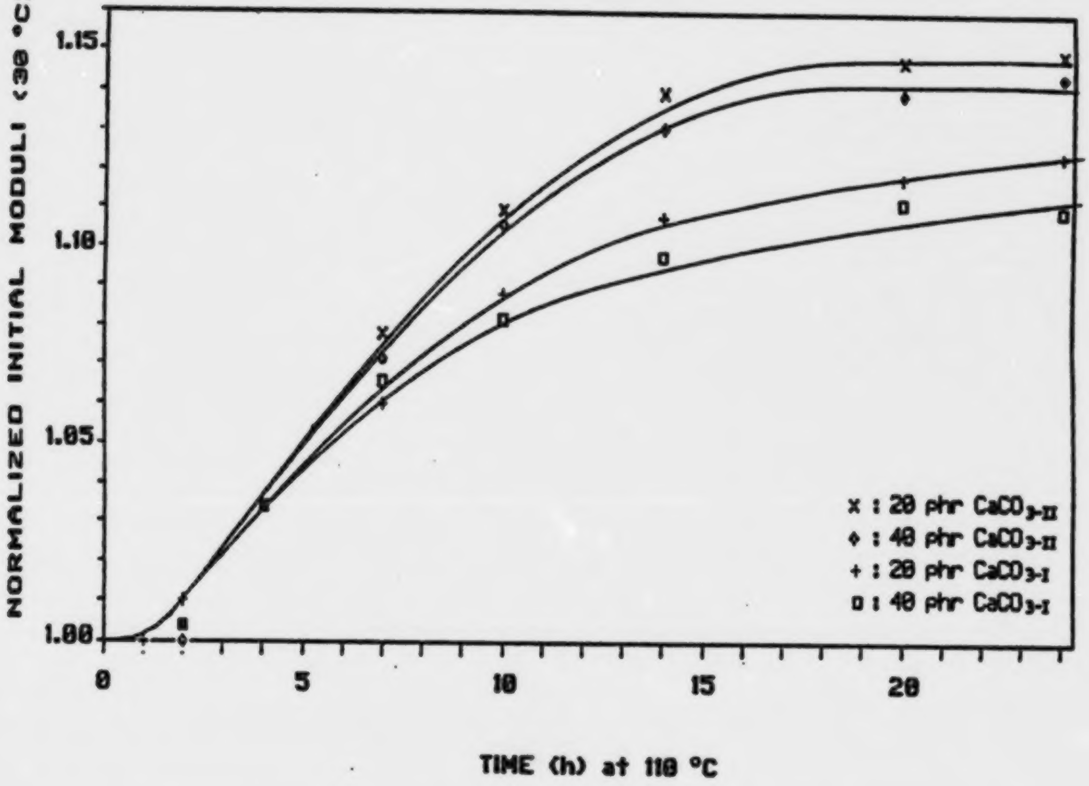

Fig.7. Effect of dwell time at 110C on modulus at 30C: Data normalized to unannealed value. All specimens prepared by method A.

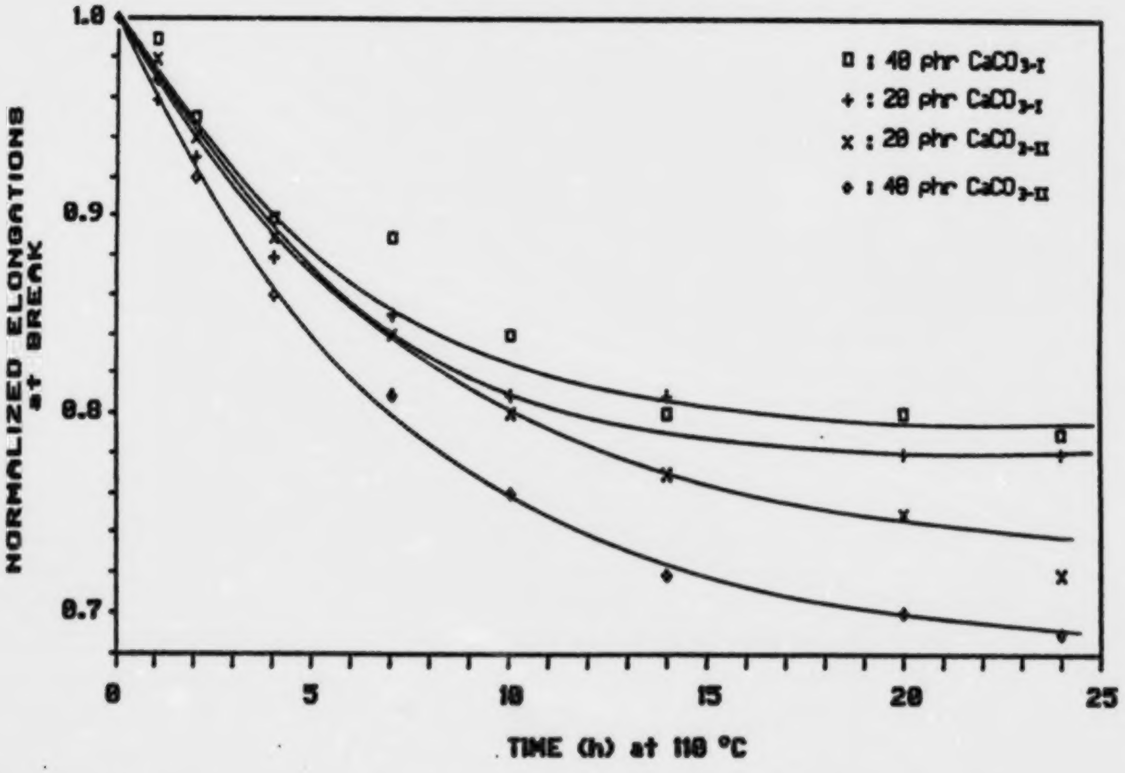

Fig.8. As in Fig.7; property displayed is elongation at rupture.

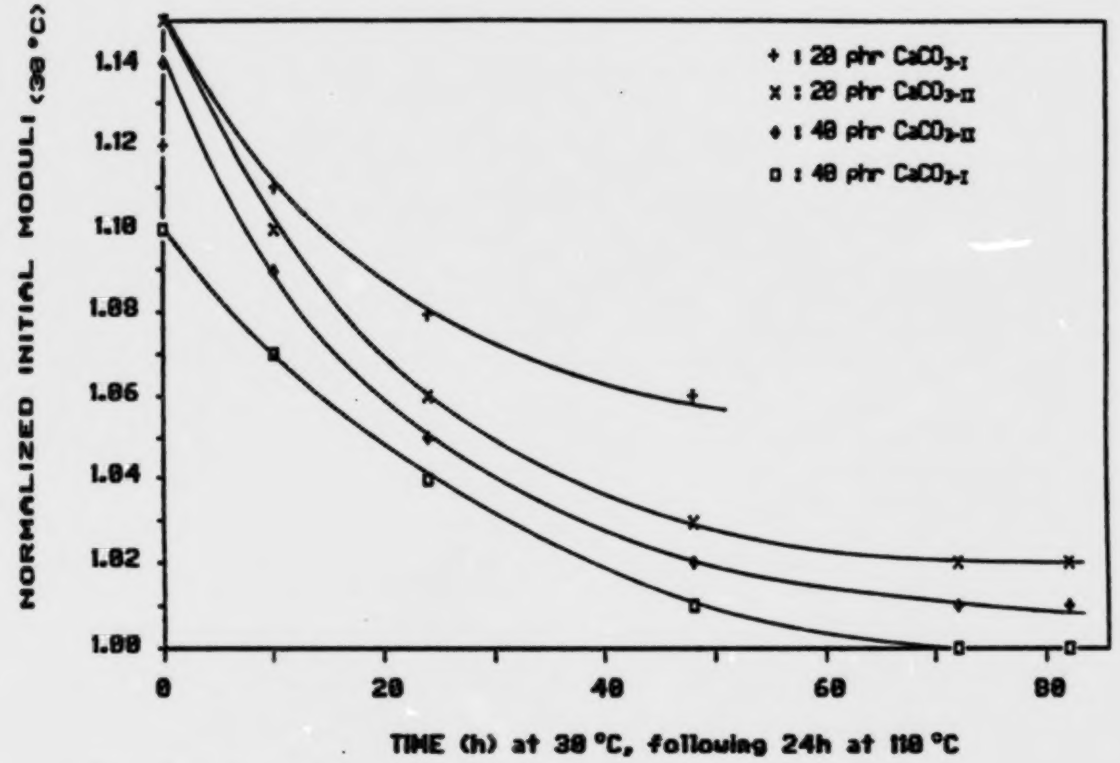

Fig.9. Revertion rates for initial modulus (30C) for compounds prepared by method A and exposed 24h. at 110C.

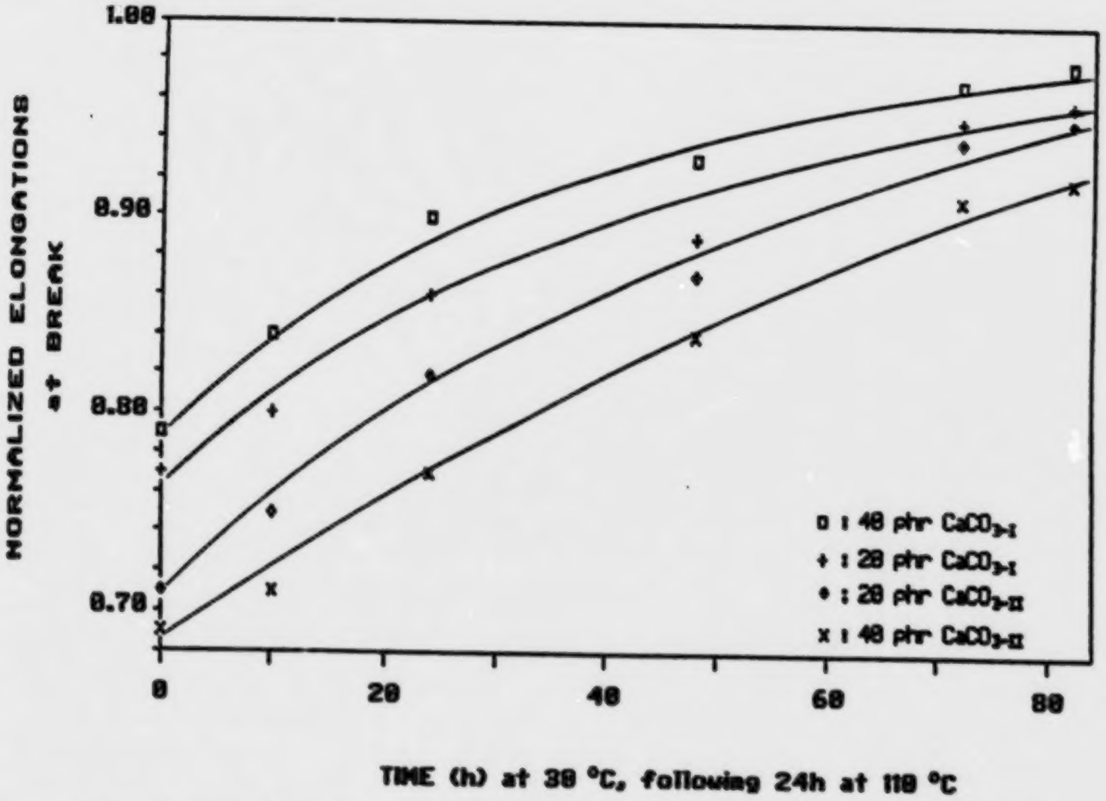

Fig.10 As in Fig.9: Property displayed is elongation at rupture.

aging, such as exposure to elevated temperatures, is a frequently applied criterion of compound "stability". In the light of data presented in Fig.2, it is evident that in systems such as filled, plasticized PVC, interaction balances will change radically at elevated temperatures, and with them changes may also be expected in the mechanical properties of the compounds. The point was made with PVC compounds freshly prepared by sequence A, which had then been exposed to 110C for selected periods, conditioned at 30C for 2 h., and then tested for modulus and ductility at the 30C reference T. The progressive changes in these characteristics as a function of dwell time at 110C are shown in Figs.7 and 8.

Exposure to elevated T generates systematic increases in initial modulus, and corresponding decreases in ductility. The kinetics of these changes are such that property steady-states are attained following some 24h. of exposure. The direction in which properties change is consistent with the indication of altered interaction balances. At 110C the respective Ω values of all constituents in the system approach the "neutral" or amphipatic band, and selective associations -e.g. between polymer and plasticizer - will be weakened or will disappear. In comparison with the initial compound, the thermally conditioned system will tend to be underplasticized, unless sufficient time is allotted for equilibrium to be reattained at the test T of 30C. This, of course, had not been the case in our experimental design. Further in connection with these Figures, a slight difference in behavior is discerned between systems using fillers I and II, the latter generating somewhat higher modulus increments and ductility decrements. Arguably this might be due to the greater residual interaction tendency at 110C between filler II and the plasticizer,- a tendency carried over to the test results at 30C, as shown.

It follows also that unless chemical or compositional changes had occurred during high temperature exposure, then the compound properties should revert, within experimental error, to those reported for the unaged controls,again provided the equilibration time was sufficiently long. To test the assumption, samples were exposed to 110C for 24 h. thus generating responses equivalent to those reported in the preceding figures. Moduli and ductilities were then re-investigated for samples which were given extended reconditioning at 30C. The results of this procedure are given in Figs.9 and 10. As before, the ordinates show moduli and ductilities relative to those of the unaged controls prepared by sequence A. As expected, the mechanical responses at first reflect the exposure to 110C, and then shift toward the steady-state values

TABLE IV

RESPONSE OF MODULUS, ELONGATION TO THERMAL CONDITIONING

(All materials brought to equilibrium @ 30°C prior to additional conditioning)

	Equilibration time (h)			
	100°C Conditioning		Following return to 30°C	
Filler:	Modulus	Elongation	Modulus	Elongation
20% $CaCO_3$ I	26	19	66	>72
20% $CaCO_3$ II	20	12	56	>72
40% $CaCO_3$ I	22	19	52	80
40% $CaCO_3$ II	22	25	49	-

pertinent to 30C, but much more slowly than noted in the procedures leading to Figs. 8 and 9. The drive for re-partitioning components, created by the difference in specific interactions at 110 and 30C, must now occur against the much higher viscous resistance offered by the polymer system. Although steady-states were not attained in all of the cases shown in Figs. 9 and 10, it is apparent that some deviation from initial steady-state values will persist. Thus, moduli appear to have been augmented by some 5%, and a similar small reduction in ductilities is implied by the data. These slight changes in property may be due to some permanent loss of plasticizer, incurred during the repeated handling of test specimens.

It is instructive to compare the times needed for the attainment of property equilibria when thermal conditioning is applied to the plasticized, filled compounds. This is done in Table IV. Among the main points of interest:

- Very long equilibration times, far exceeding 24 h. are needed to restore properties which had been perturbed by an exposure to elevated temperature.
- Compounds using filler II attain equilibrate slighly more quickly than those using filler I.

The findings of this work impart serious consequences; among these the following are noted in particular.

- Test routines designed to specify the "durability" of multi-component polymer systems should take in account the dependence of component interactions on variables such as T, and provide adequate time for property steady-states to be atained in the performance of the tests.

- Since in use, multi-component polymer systems are often exposed to fluctuating environmental conditions, it is possible that properties are in a continuing state of flux, as interaction balances seek to respond to these changing conditions. This factor may contribute to the accumulation of stresses in a system, and affect its use-life.

- The existence of preferential associations in a polymer system, for example as caused by acid/base interactions, indicates that such systems are generally heterogeneous, local compositional variations being a consequence of such interactions. This confirms the view expressed by Guthrie and coworkers(8).

- The mixing sequence used in preparing multi-component systems influences dispersion processes as well as initial properties of the polymer compound.

. In view of the influence exerted by acid/base balances on the processability and the bulk properties of the system, interaction criteria should be applied in selecting materials for a multi-component system. This seems particularly germane to the surface characteristics of particulates used in the system.

ACKNOWLEGMENTS.

This work was supported by grants from the Natural Sciences and Engineering Research Council. Canada. Additional material support was kindly provided by Northern Telecom Inc., Lachine, Canada. Useful discussions with Drs. J. Checkland and M. Kapuscinski of that organisation are acknowledged with pleasure.

REFERENCES.

(1). F.M. Fowkes. J.Adhesion Sci.Tech.1.7 (1987).

(2). Y.M. Boluk and H.P. Schreiber. Polym.Composites.7.295 (1986).

(3). C. Richard.K.Hing and H.P. Schreiber.Polym.Composites.6. 201 (1985).

(4). V.Gutmann, The Donor-Acceptor Approach to Molecular Interactions. Plenum Press. New York.(1978).

(5). H.P. Schreiber and M.Kapuscinski.Polym.Eng.Sci.21.433 (1981).

(6). R.S.Drago.G.C.Vogel and T.E. Needham.J.Amer. Chem.Soc.93.6014 (1971).

(7). P.M. Cuckor and J.M. Prausnitz,J.Phys.Chem.76.598 (1972).

(8). G.Alexander.S.Bradshaw,K.Dodd.J.T.Guthrie and T.Mason. XIII International Conference in Organic Coatings Science and Technology.Proceedings 13.Athens Greece. July 1987., p.133.

(9). H.P. Schreiber XIII International Conference in Organic Coatings Science and Technology. Proceedings 13.Athens. Greece. July 1987.p.367.

(10). A.Ajji.H.P. Schreiber and A. Rudin.J.Appl.Polym.Sci.33.2493 (1987).

APPLICATIONS OF DIFFUSE REFLECTANCE FT-IR TO FIBER-REINFORCED COMPOSITES

by

K.C. Cole, D. Noël and J.-J. Hechler
National Research Council Canada
Industrial Materials Research Institute
75 De Mortagne, Boucherville, Que., Canada, J4B 6Y4

Presented at the 8th annual NRCC/IMRI symposium "Composites-'87",
November 5 and 6, 1987, Boucherville, Que., Canada

SUMMARY

Diffuse reflectance Fourier transform infrared (FT-IR) spectroscopy can be used to obtain infrared spectra directly from the surface of composite materials with little or no sample preparation. It is thus of interest as a nondestructive method for industrial inspection. In many cases, the IR spectra provide detailed information concerning the chemical composition and molecular structure of the material. The technique works particularly well for carbon-fibre composites. This paper describes the principles involved, some factors which influence the quality of the spectra, and a number of examples of applications. These include the characterization of epoxy matrices (composition, curing, degradation), the detection of surface contamination, and the determination of the degree of crystallinity in PPS-based composites.

RÉSUMÉ

La spectroscopie infrarouge à transformée de Fourier en réflectance diffuse permet d'obtenir des spectres infrarouge directement de la surface des matériaux composites avec très peu de préparation de l'échantillon. Elle s'avère donc très intéressante comme méthode d'analyse non-destructive pour l'inspection industrielle. Le spectre infrarouge peut fournir des informations détaillées concernant la composition chimique et la structure moléculaire du matériau. La technique fonctionne particulièrement bien pour les produits renforcés avec des fibres de carbone. L'article décrit les principes de la méthode, quelques facteurs qui influent sur la qualité du spectre, et quelques exemples d'applications: la caractérisation des matrices époxydes (composition, réticulation, dégradation), la détection de la contamination de surface, et la détermination du degré de cristallinité dans les matériaux composites à base de polysulfure de phénylène.

INTRODUCTION

The ever-increasing usage of composite materials based on fiber-reinforced polymers is largely due to their high strength-to-weight ratio, which makes them particularly suitable for applications such as the aerospace industry. Since the performance of these materials is closely related to their chemical and molecular structure, it is important to have sensitive and reliable methods for characterizing these properties. One of the most versatile and widely used techniques for this purpose is infrared spectroscopy, which can give quite detailed information. Unfortunately, because of the highly absorbing nature of most materials in the infrared region, meaningful transmission spectra can only be obtained if the sample is in the form of a dilute solution, a thin film, or a fine powder. Thus many industrial materials do not lend themselves to such measurements without destructive sample preparation.

Reflectance measurements offer an alternative sampling method, but in the past were hampered by a lack of sensitivity. Fourier transform instruments, with their rapid-scanning capability and optical advantages, have changed this (1). In particular, the diffuse reflectance (DR) technique has proved to be extremely sensitive and useful in a number of applications (2-5). However, although the general utility of FT-IR for characterizing fiber-resin composites is well known (6), there have been relatively few reports of the use of diffuse reflectance for such materials. Apart from our own preliminary results (7,8), these have come mainly from groups at NASA Langley Research Center and Case Western Reserve University. The first group has used diffuse reflectance FT-IR to study both epoxy and polyimide resins in carbon-fiber-reinforced composites (9-12), whereas the second has investigated silane-treated glass fibers (13-15) and Kevlar® fibers (16).

The principal advantage of diffuse reflectance for the study of composites is the fact that it is essentially a nondestructive method. The infrared beam is directed onto the sample surface, which may be rough and inhomogeneous, and a part of the scattered back-reflected radiation is captured and analyzed. Hence the method has the potential for application to real parts in a manufacturing environment. However, the spectra obtained are not identical to those which would be obtained in transmission, and care must be exercised in their interpretation. The nature of the spectrum, and the amount of information which can be gleaned from it, varies depending on the type of sample. The object of this article is to describe a few examples of the application of diffuse reflectance to industrial composites, at the same time using the results to illustrate certain factors which influence the quality of the spectra and their interpretation.

EXPERIMENTAL

Materials

The composite systems studied were Narmco Rigidite 5208/WC3000 from Narmco Materials (a division of BASF Structural Materials Inc.), Ferropreg CE-306/281 from Ferro Corporation Composites Division, and Ryton AC40-60 from Phillips Petroleum Company.

Narmco Rigidite 5208/WC3000 is a carbon-epoxy system. The reinforcement consists of Celion 3000 carbon fibers woven in an 8-harness satin pattern (each fill yarn passing alternately over seven warp yarns and under one warp yarn). This is impregnated with partially cured Narmco 5208 resin to give "prepreg" with a nominal resin content of 42% by weight. The main components of Narmco 5208 are an epoxy resin based on tetraglycidyl-diaminodiphenylmethane, a second epoxy based on a bisphenol A Novolac, and the amine hardener diaminodiphenylsulfone. Cured panels were made from four layers of prepreg by vacuum bag autoclave curing according to the recommended temperature program (a two-hour dwell at 135°C followed by three hours curing at 177°C).

Ferropreg CE-306/281 is a Kevlar®-epoxy system. The reinforcement, woven in a plain weave pattern, is impregnated with CE-306 resin to a level of 53% by weight. The infrared spectra indicate that the main components are an epoxy resin of the bisphenol A type and the hardener dicyandiamide. Panels were made from four plies of prepreg by vacuum bag autoclave curing for one hour at 127°C.

Ryton AC40-60 is based on the thermoplastic polymer polyphenylene sulfide (PPS). It contains 40% by weight PPS and 60% unidirectional carbon fiber reinforcement. A moulded panel was made by hot pressing four plies of prepreg in a mould for 5 minutes at 315°C and 1.03 MPa, then cooling at a rate of 11°C per minute.

Instrumentation

Infrared spectra were recorded using a Nicolet 170SX Fourier transform instrument equipped with a mercury cadmium telluride detector. For diffuse reflectance measurements, a "praying mantis" type accessory from Harrick Scientific Corporation was used. Samples consisting of small squares about 1 cm x 1 cm were cut with scissors where possible or with a jigsaw when necessary. These were mounted with double-sided adhesive tape on a flat horizontal support whose height could be adjusted to maximize the energy throughput. Powdered potassium bromide, compacted with a spatula to give a smooth level surface, was used as a reference to record the instrumental background. Specular reflectance spectra were measured using an External Specular Reflectance Accessory with an angle of incidence of 30°, also from Harrick Scientific. An aluminized mirror was used as reference. All spectra were measured using an accumulation of 128 scans.

RESULTS AND DISCUSSION

Reflection versus Transmission

Before any results are presented, it is important to underline some differences between transmission and reflection spectra. The optical properties of a material may be defined in terms of two variables, the index of refraction n and the absorption coefficient α, both of which vary as a function of the wavelength of the radiation. Analytical spectroscopy is generally concerned only with α. For many substances, the curve of α versus $\tilde{\nu}$, where

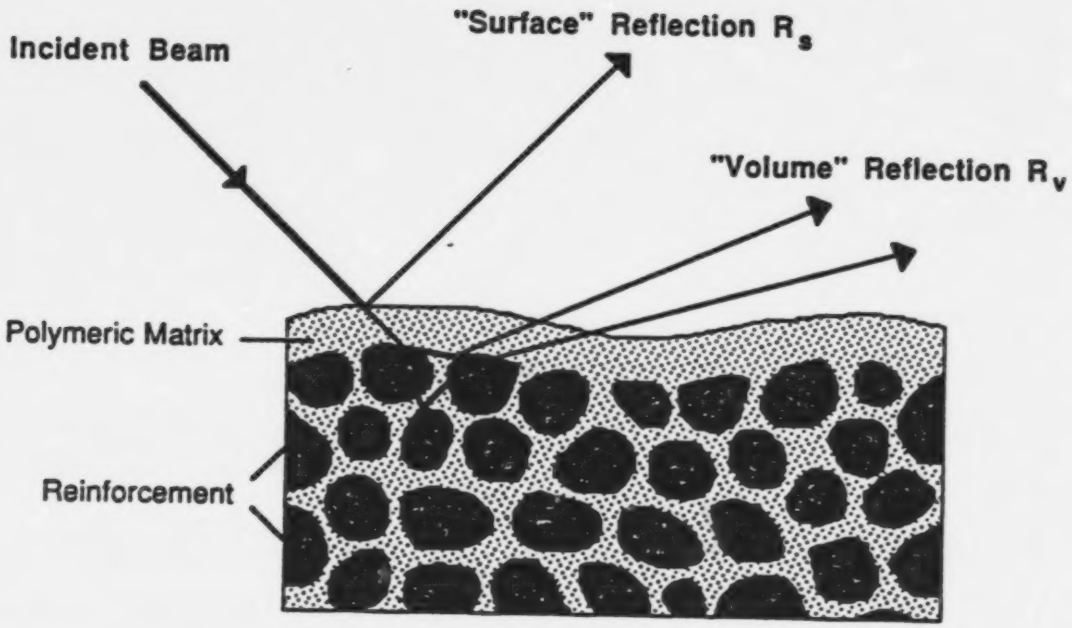
"Surface" Reflection R_s
Incident Beam
"Volume" Reflection R_v
Polymeric Matrix
Reinforcement

Fig. 1. Schematic illustration of diffuse reflectance in a reinforced polymer.

$\bar{\nu}$ (cm^{-1}) is the reciprocal of the wavelength, shows distinct peaks, particularly in the infrared region. These are often sufficient to identify the material and can sometimes be used to perform quantitative analysis. Ideally, the variation of α is determined by measuring the transmittance T of a sample of thickness b, since T is related to α by the Lambert Absorption Law:

$$T = \exp(-\alpha b) \tag{1}$$

Except for the most precise work, the contribution of the refractive index can be neglected. Taking the logarithm of T gives the absorbance A, which is directly proportional to α:

$$A = -\log_{10} T = 0.4343\, b\, \alpha \tag{2}$$

The treatment of diffuse reflection, which is more complicated, has been discussed in detail by others (17-19). Figure 1 illustrates the case of a reinforced polymer. When the incident infrared beam impinges on the sample surface, part of it is reflected immediately before it ever enters the sample. We designate this component as "surface" reflection R_s. The reflectance is governed by the laws of Fresnel (20), and depends on the angle of incidence, the polarization of the beam, the index of refraction n of the material, and the absorption coefficient α. The general relationship is quite complex, but for the special case of normal incidence it reduces to:

$$R_s = \frac{(n-1)^2 + \left(\frac{\alpha}{4\pi\bar{\nu}}\right)^2}{(n+1)^2 + \left(\frac{\alpha}{4\pi\bar{\nu}}\right)^2} \tag{3}$$

At wavelengths where there is no absorption ($\alpha = 0$), n is approximately constant, and for a typical polymeric material ($n \approx 1.5$), R_s is of the order of 4%. In the region of an absorption band, α passes through a maximum while n varies according to a dispersion-type curve. The variation of R_s reflects that of both n and α. Paradoxically, at wavelengths where the sample strongly absorbs (large α), R_s tends to 1, or 100%. This is known as the "reststrahlen effect".

That part of the beam which enters the sample undergoes attenuation according to the Lambert Absorption Law. Eventually it encounters a fiber-matrix interface, where it is partly reflected and partly transmitted, the exact proportion depending on the materials involved. After one or more such encounters, it can leave the sample. Following Vincent and Hunt (17), we designate this component as "volume" reflectance R_V. Its frequency dependence can be quite different from that of R_S. Because it has actually passed through the sample, it tends to resemble that of a transmission spectrum. Both R_s and R_v are detected by the infrared detector, and the form of the resulting spectrum depends on the relative contributions of the two, which in turn depend on the nature of the sample. In some cases (for example, organic powders dispersed in nonabsorbing KBr powder), R_s is negligible and the spectrum is very similar to the transmission spectrum. In other cases (for example, highly absorbing materials or inorganic materials with a high index of refraction), R_s can dominate the spectrum to the point where it is almost unrecognizable compared to the transmission spectrum.

Even when R_s is negligible, the diffuse reflectance spectrum differs somewhat from the transmission spectrum, since the Lambert Law is not directly applicable. Instead, diffuse reflectance spectra are usually analyzed in terms of the Kubelka-Munk function (18, 19):

$$F(R_\infty) = \frac{\alpha}{s} = \frac{(1 - R_\infty)^2}{2R_\infty} \qquad (4)$$

In this equation, R_∞ is the diffuse reflectance of the sample, which is assumed to be "infinitely thick", α is the absorption coefficient, and s is a scattering coefficient. Both $F(R_\infty)$ and the

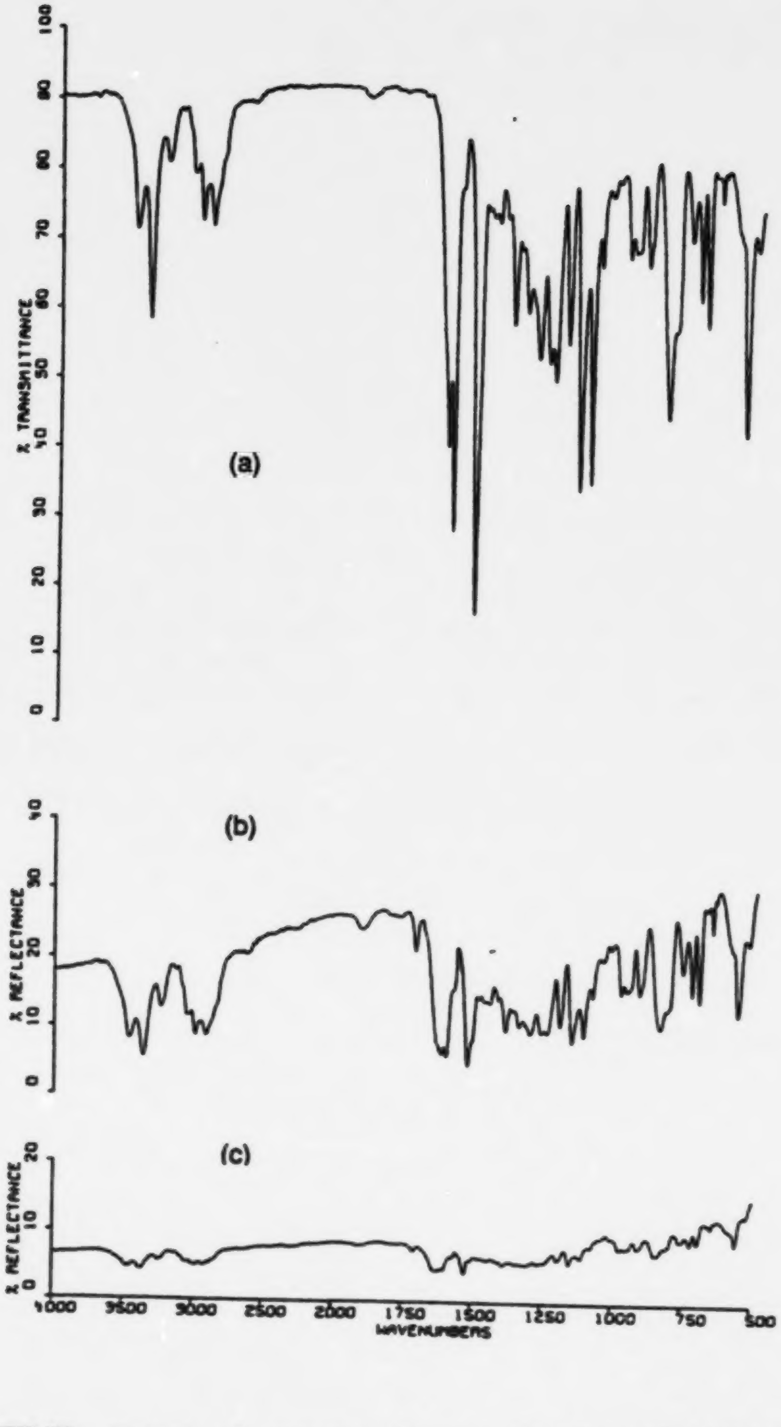

Fig. 2. FT-IR spectra of uncured Narmco Rigidite 5208/WC3000, as recorded: (a) transmission spectrum of thin film of neat resin cast from acetone solution on KBr window; (b) diffuse reflectance spectrum of prepreg, measured with principal fiber direction parallel to beam direction; (c) diffuse reflectance spectrum obtained with principal fiber direction perpendicular to beam direction.

absorbance A of Eq (2) are related to the absorption coefficient α, but whereas b is a constant, the scattering coefficient s varies with frequency. Usually, however, the variation is gradual, and a diffuse reflectance spectrum converted to Kubelka-Munk units is similar to a transmission spectrum converted to absorbance units. The Kubelka-Munk equation was derived for the case of an isotropically scattering powdered sample, and works particularly well for a moderately-absorbing powder diluted in a nonabsorbing matrix. It may not be entirely suitable for the analysis of spectra of samples such as fiber-reinforced polymers.

In the remainder of the paper, various diffuse reflectance spectra will be presented and interpreted in view of the above considerations.

Characterization of Carbon-Epoxy Prepreg

Figure 2 shows some typical spectra of the Narmco 5208/WC3000 system. The first (Figure 2a) is the transmission spectrum of a thin film of resin, obtained by extracting the prepreg with acetone, depositing a few drops of the extract on a KBr window, and evaporating the solvent under vacuum. The spectrum shows numerous peaks which provide information concerning the resin chemistry. For instance, the strong peaks at 1146 and 1105 cm^{-1} arise from sulfone groups present in the DDS hardener, while the small peaks between 1000 and 900 cm^{-1} correspond to epoxide rings in the epoxy resin. A more complete discussion of the spectrum and its use for quantitative analysis will be published elsewhere (21). The other two spectra in Figure 2 were recorded directly from prepreg by diffuse reflectance using two different orientations of the sample. As a result of the type of weave used (8-harness satin), on a given prepreg surface seven-eighths of the total area is covered by fibres aligned in one particular direction, which we designate the "principal fiber direction". For the spectrum of Figure 2b, this direction was parallel to the beam direction of the instrument, whereas for Figure 2c it was perpendicular. It is obvious that the sample orientation influences the quality of the spectrum, and that with the "praying mantis" accessory used, the best results

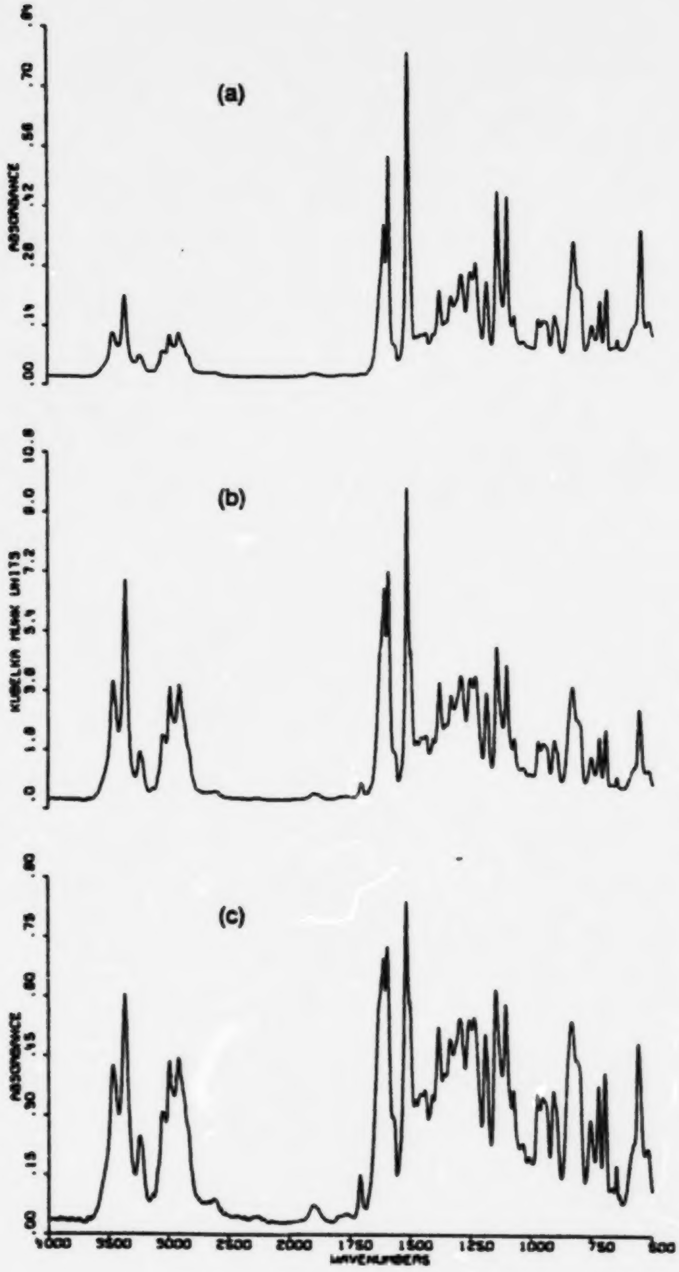

Fig. 3. FT-IR spectra of Narmco Rigidite 5208/WC3000, after conversion of units and baseline correction: (a) transmission spectrum of Figure 2a, expressed in absorbance units; (b) DR spectrum of Figure 2b, expressed in Kubelka-Munk units; (c) DR spectrum of Figure 2b, expressed in "pseudo-absorbance" units.

are obtained with the principal fiber direction parallel to the beam direction. Even in this case, however, a strong background absorption prevents the overall reflectance from exceeding about 40%. This is due at least in part to absorption by the carbon fibers, which absorb at all frequencies without showing any distinct peaks.

To properly compare the DR spectrum with the transmission one, they must be converted to similar units. The transmission spectrum of Figure 2a was converted to absorbance and the result is shown in Figure 3a. For the prepreg DR spectrum, neither absorbance nor Kubelka-Munk units are strictly correct, but since there is no more rigourous treatment available, both were tried in order to determine which corresponds best to the "true" absorbance spectrum. Figure 3b shows the DR spectrum of Figure 2b after conversion to Kubelka-Munk units followed by baseline correction to remove most of the background absorption. Figure 3c shows the same spectrum expressed in "pseudo-absorbance" units. Of the two, the Kubelka-Munk transformation appears to give the best match to Figure 3a, in terms of relative peak intensities and overall shape. Kubelka-Munk units are thus preferred, even though the agreement is not exact. This is undoubtedly because of contributions from front-surface reflection and scattering effects, as well as the fact that the prepreg is not an isotropically-scattering powder. However, all the details of the transmission spectrum are evident in the DR spectrum, and the latter is certainly sufficient for identification of the resin chemistry, with considerably less effort than is involved in obtaining the transmission spectrum.

In fact, the DR spectrum provides more information than the transmission one. The small peak at 1708 cm^{-1} appears only in reflectance. It disappears from the spectrum if the prepreg is exposed to the atmosphere for a few days or heated for a short time, so it corresponds to a volatile component. A small amount was collected by heating some prepreg and was identified from its infrared spectrum as acetone, presumably residual solvent left from the prepregging process. It does not appear in the transmission spectrum because acetone was used to extract the resin and then completely evaporated before recording the

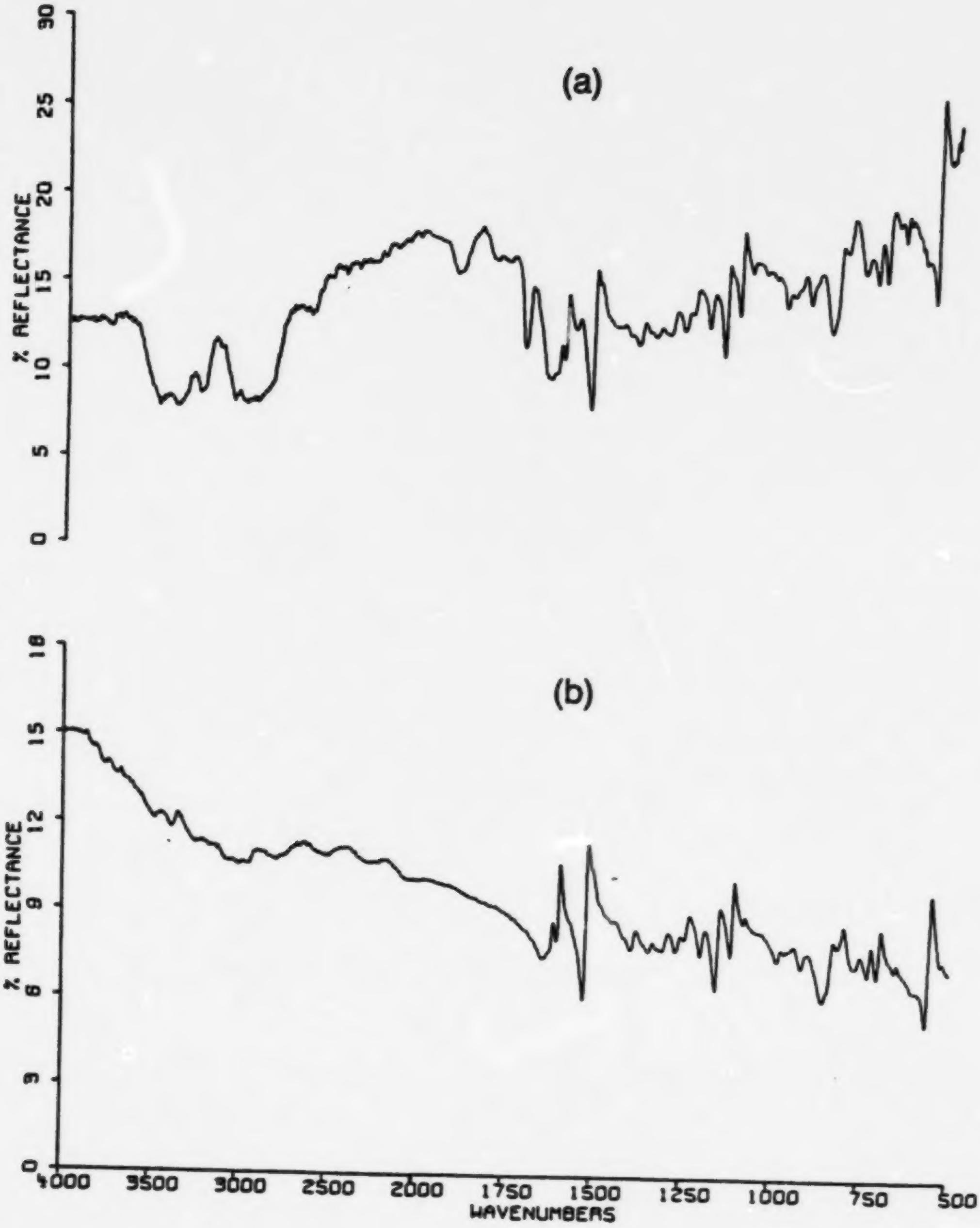

Fig. 4. (a) DR spectrum of resin-rich area of Narmco 5208/WC3000 prepreg; (b) front-surface (specular) reflectance spectrum of neat film of Narmco 5208 resin.

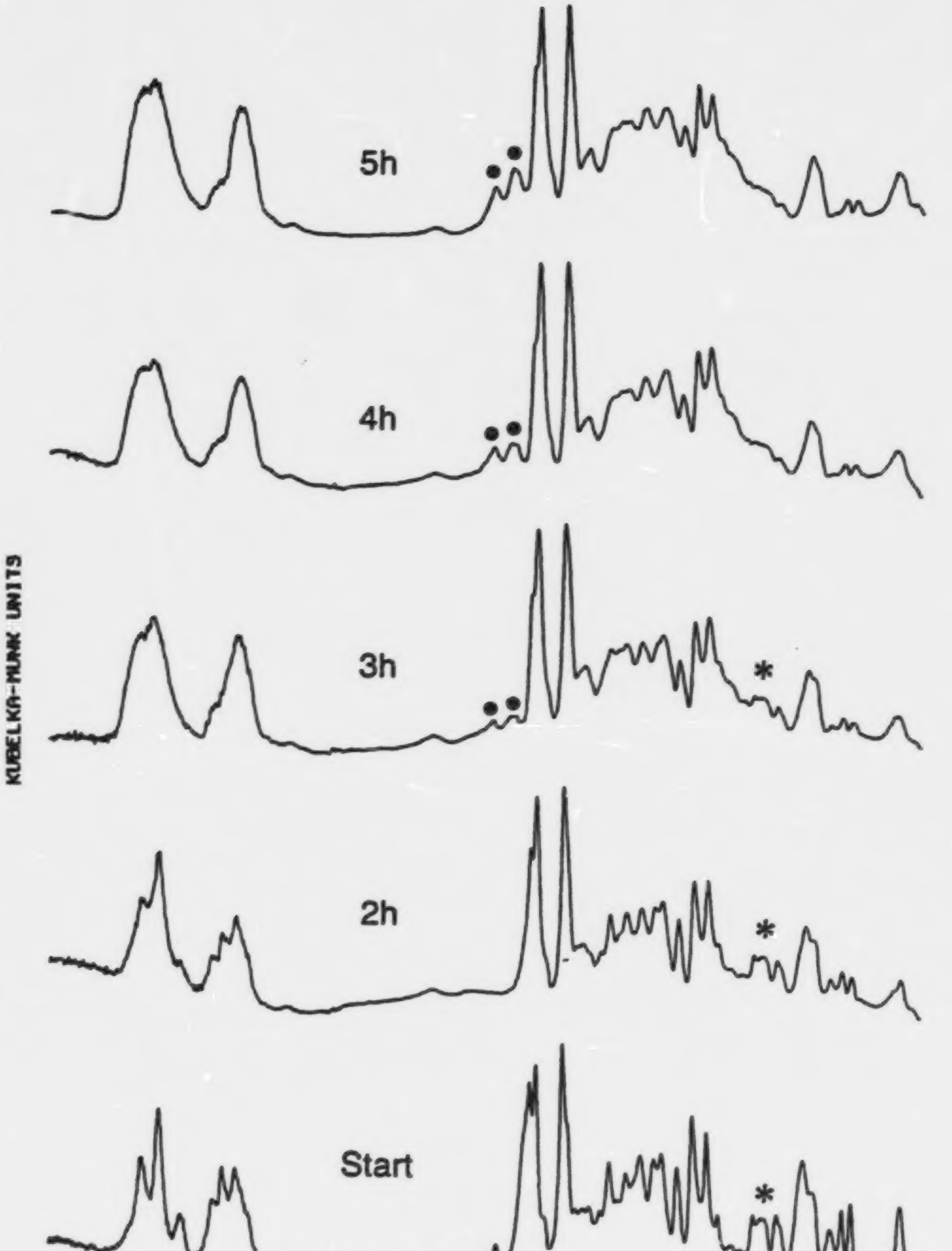

Fig. 5. Evolution of DR spectrum of Narmco 5208/WC3000 prepreg during cure (2 h at 135°C followed by 3 h at 177°C).

spectrum. This is a good example of the "nondestructive" advantage of the diffuse reflectance method.

Quantitative Analysis

Infrared spectroscopy can be used for quantitative analysis of the resins in prepreg systems, to check the proportions of the different components as well as the degree of polymerization, or "B-staging", of the resin. If diffuse reflectance could be used for this purpose instead of transmission, it would mean considerable time savings in sample preparation. Unfortunately, our investigation (21) of this possibility for the Narmco 5208 system has shown that the DR results are not sufficiently reproducible for quantitative work in this case. The relative standard deviation of the indices measured is as high as 28%. The main reason appears to be the contribution of the front-surface reflection R_S, which causes an apparent deformation of band shapes because of the effect of the refractive index. The relative importance of R_S and R_V varies somewhat from specimen to specimen, depending on the thickness of the layer of resin on the prepreg surface. Figure 4a shows an extreme case involving a particularly "resin-rich" specimen. Comparison with Figure 2 shows that the peaks are considerably deformed. That this is due to front-surface reflection is confirmed by Figure 4b, which is a reasonably "pure" front-surface reflection spectrum obtained from a film of neat resin using a specular reflectance accessory. The peaks take on a dispersion-type character as a result of the refractive index contribution.

Curing of Carbon-Epoxy Prepreg

One important advantage of the DR method is that it can be applied to samples at all stages of curing. Figure 5 shows DR spectra obtained from a rather simple curing study done by placing samples of Narmco 5208/WC3000 prepreg in an air-circulation oven for two hours at 135°C followed by three hours at 177°C. All the spectra are of good quality. The progress

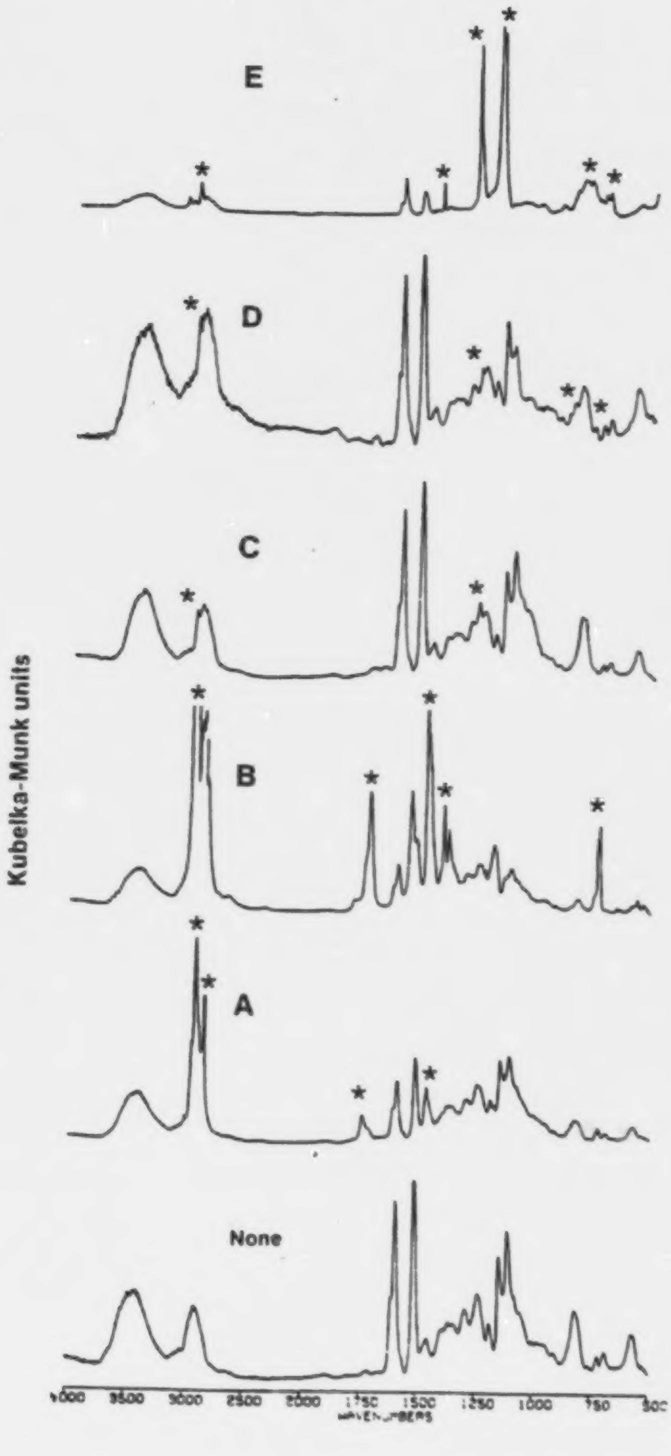

Fig. 6. DR spectra of Narmco 5208/WC3000 cured panel with commercial release agents (designated A to E) deposited on surface. Estimated coverage, in mg/cm^2: A, 2.8; B, 4.8; C, 1.2; D, 0.7; E, 21.

of the curing reaction is obvious, as shown by the disappearance of the epoxide ring peaks at 1000-900 cm^{-1} (indicated by a "*" in the figure) and the changes which occur in the N-H and O-H stretching region (3600-3200 cm^{-1}). Also of interest are the peaks which appear at 1724 and 1668 cm^{-1} in the later stages of cure (indicated by a "•" in the figure). These are due to carbonyl groups formed by atmospheric oxidation. The DR technique can thus be used for cured parts to check both the completion of cure and the occurrence of degradation. Similar studies have been reported involving polyimides as well as epoxies (10, 11). It is unfortunate that the DR technique is not suitable for precise quantitative work, because it would be ideal for studying the kinetics of curing. This is often done by transmission, using a thin film between KBr windows, but it has been reported (22), and our (unpublished) results confirm, that the apparent reaction rate in such conditions is higher than when the resin is cured in the absence of KBr.

Detection of Mold Release Agents on Composite Surfaces

In fabricating parts from composite materials, a mold release agent is often applied to the mold surface in order to facilitate removal of the part. If transferred to the part surface, it can interfere with subsequent operations such as painting or adhesive bonding, so it is advisable to check the surface for contamination. We have investigated the possibility of using diffuse reflectance FT-IR for this purpose (23). To obtain an idea of the sensitivity, samples were prepared by depositing known quantities of five different commercial release agents (designated "A" to "E") on specimens cut from a Narmco 5208/WC3000 cured panel. Figure 6 shows the DR spectra. In all cases, peaks arising from the release agent can be seen and are indicated by asterisks. The detection limit is rather difficult to determine, because the different release agents give different peaks, but it was estimated to be generally of the order of 200 $\mu g/cm^2$. Subtraction of the "control" spectrum corresponding to no release agent may be necessary in some cases to show up weak release agent peaks.

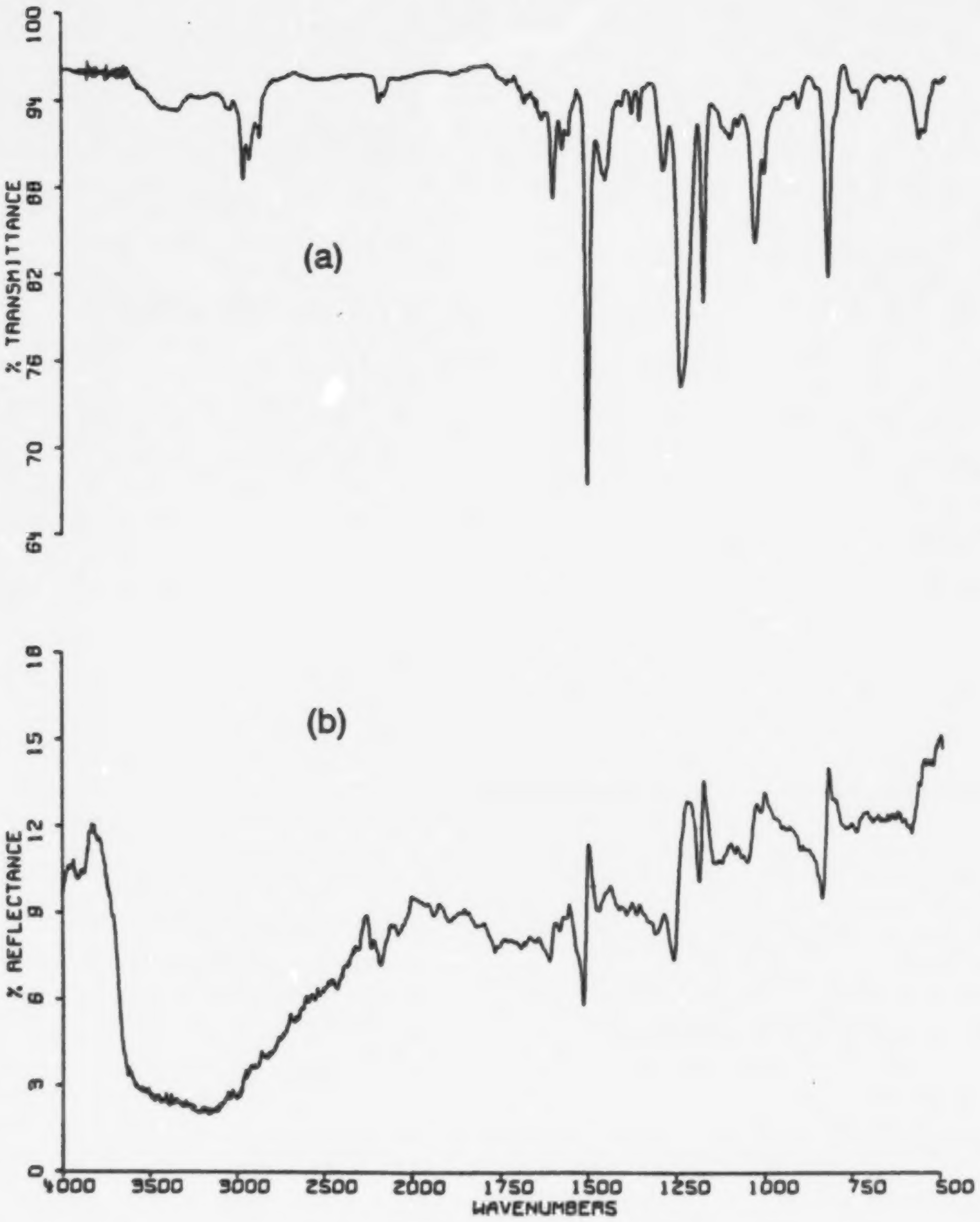

Fig. 7. FT-IR spectra of cured Ferropreg CE-306/281: (a) transmission spectrum of thin cured film between KBr windows; (b) diffuse reflectance spectrum of cured panel.

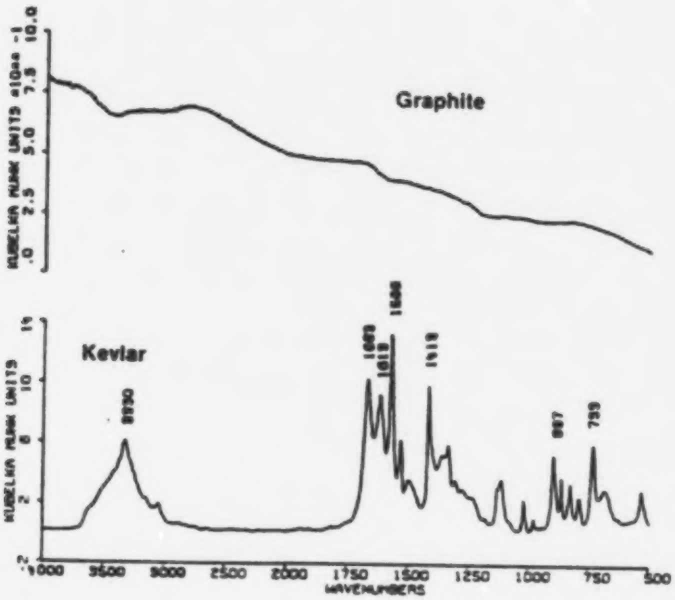

Fig. 8. Diffuse reflectance FT-IR spectra of woven graphite fiber cloth (8-harness satin weave) and woven Kevlar cloth (plain weave).

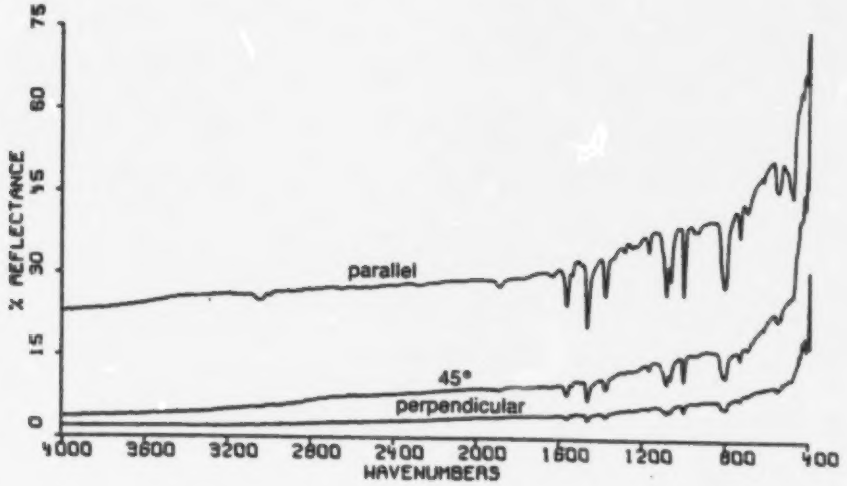

Fig. 10. Diffuse reflectance FT-IR spectra of Ryton AC40-60 prepreg recorded with different sample orientations (fiber direction with respect to beam direction).

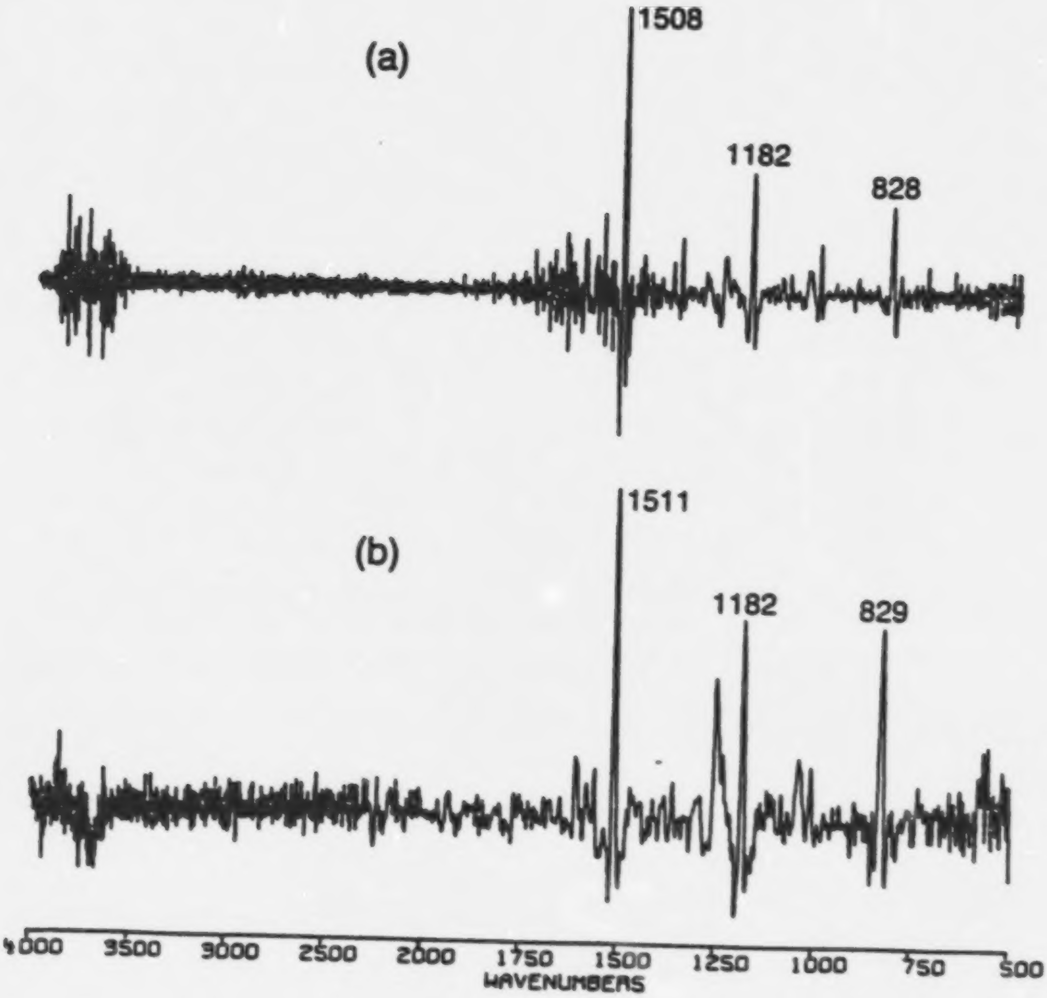

Fig. 9. Comparison of derivative traces obtained from spectra shown in Figure 7.

Kevlar®-Epoxy Composites

Figure 7b shows the DR spectrum of a cured panel made from Ferropreg CE-306/281 prepreg. It is quite different from the transmission spectrum of a cured film of CE-306 resin, shown in Figure 7a. The overall reflectance is quite low (less than 15%). The peaks occur at about the same frequencies as in the transmission spectrum, but they have the dispersion-type shape characteristic of front-surface reflection. There is no sign of peaks arising from the Kevlar® reinforcement, whose DR spectrum is shown in Figure 8. It would appear that the index of refraction of the Kevlar® is close to that of the matrix, so that the reflectance at the matrix-fibre interface is very low and that part of the IR beam which penetrates the sample is not returned towards the detecting mirror. In other words, the R_v component of the reflected radiation is small and the R_s component dominates. This limits the amount of information obtainable from the DR spectrum, since many of the details seen in the transmission spectrum are lost. Nevertheless, the DR spectrum can serve to identify the system. It is interesting to note that comparison of the DR and transmission spectra is facilitated by taking appropriate derivatives. Figure 9 compares the first derivative of the DR spectrum with the second derivative of the resin's transmission spectrum. In spite of the high noise level, it can be seen that the two traces are quite similar and show distinct peaks at much the same frequencies. Thus, in the case of composite samples which give DR spectra dominated by front-surface reflection, it may be possible to extract useful information by taking the derivative.

Crystallinity in PPS-Carbon Composites

Although most composite systems currently used in high-performance applications are based on thermosetting polymers, there is growing interest in the use of thermoplastic matrices such as polyphenylene sulfide. These also must be properly characterized, but the requirements are different from those of thermosets. For instance, instead of the degree of

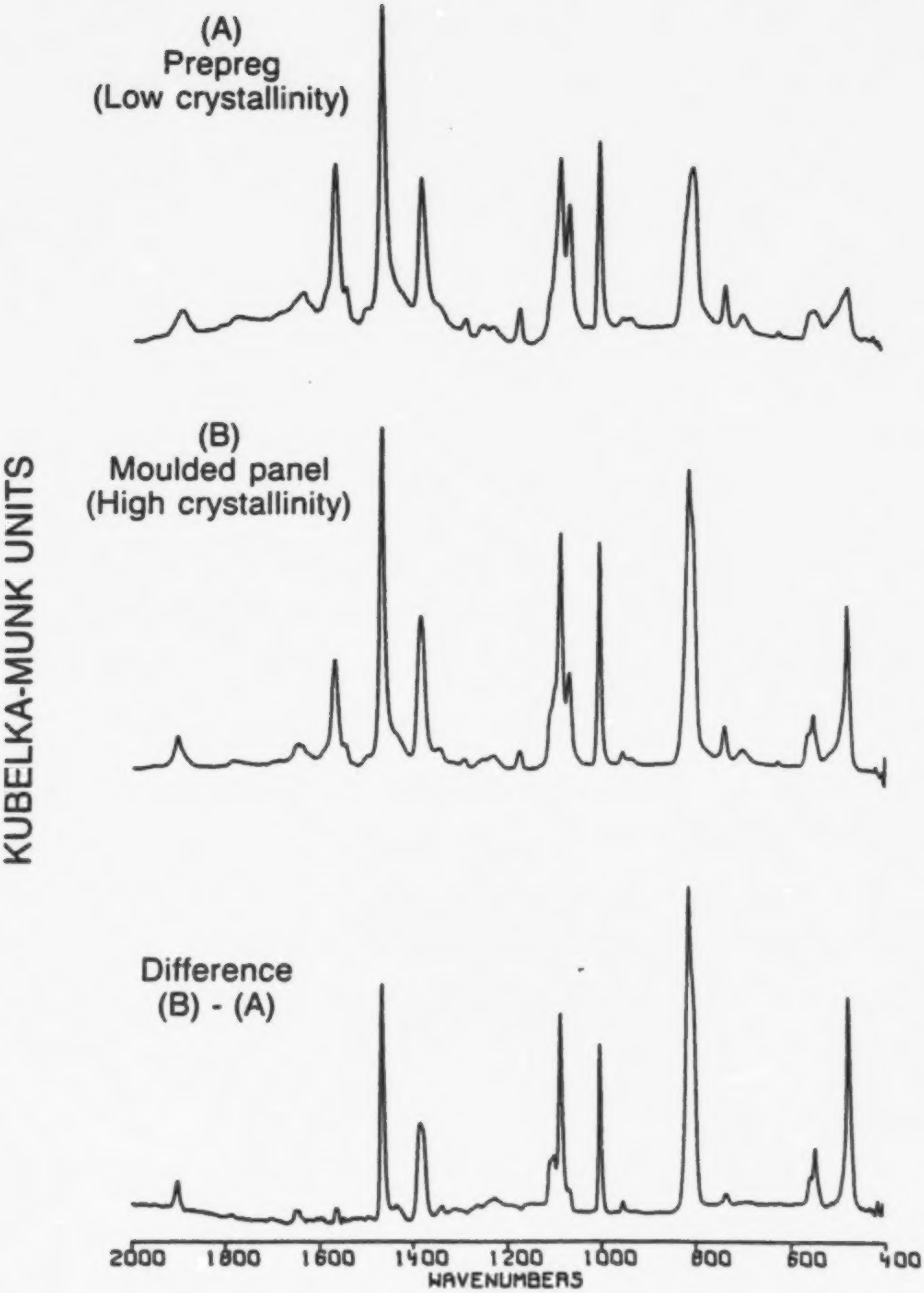

Fig. 11. DR spectra of Ryton AC40-60 prepreg and molded panel, after conversion to Kubelka-Munk units and baseline correction, showing differences resulting from change in degree of crystallinity.

cure, it is the crystallinity which must be controlled, since many of the physical properties are related to it. Diffuse reflectance FT-IR can be used to check the crystallinity of the surface of finished parts in a nondestructive manner (24). Figure 10 shows DR spectra for a sample of Ryton AC40-60 prepreg. Since the fibers are unidirectionally aligned, the sample orientation is even more important than for the Narmco 5208/WC3000 prepreg; as in that case, the parallel orientation is the best. The spectrum is of good quality and there is no evidence of peak distortion. Apparently the optical constants of the PPS and the thickness of the surface layer of polymer are such that front-surface reflection effects are small in this case. Figure 11a shows the prepreg spectrum after conversion to Kubelka-Munk units and baseline correction, while Figure 11b is a similar spectrum obtained from a molded panel made from the prepreg as described in the Experimental Section. Differential scanning calorimetry showed that the prepreg was highly amorphous while the panel had achieved maximum crystallinity. This results in significant differences in the spectra, which are sufficiently good to allow a spectral subtraction to be performed (Figure 11). It shows that certain peaks increase in intensity on crystallization, while others remain unchanged. Thus, for example, the ratio of the heights of the overlapping peaks at 1075 and 1093 cm^{-1} changes from 0.73 in the prepreg to 0.44 in the panel. This ratio was found to be sufficiently reproducible for use as a quantitative indicator of the degree of crystallinity. When a series of samples was prepared by annealing prepreg at 105°C for different periods of time, an excellent correlation was observed between the 1075/1093 ratio and the enthalpy of crystallization as measured by DSC (24).

CONCLUSIONS

Diffuse reflectance FT-IR can be very useful for the rapid nondestructive characterization of composite materials based on fiber-reinforced polymers, particularly those involving carbon fibers. The main problem in its application is the contribution of front-surface reflection, whose importance varies depending on the optical constants of the particular materials involved. For PPS-carbon composites, its effect is small enough so that DR can be used for quantitative characterization of the degree of crystallinity. For carbon-epoxy materials, it is more important, particularly in samples with a thicker layer of resin on the surface. This precludes the use of DR for quantitative analysis, but for qualitative purposes it gives excellent spectra. It can be used to identify the type of resin, to check the degree of cure, to detect oxidation, and to detect surface contamination. For Kevlar®-epoxy samples, front-surface reflection dominates the spectrum. This limits the amount of information obtainable but still allows use of the spectrum for identification purposes.

ACKNOWLEDGEMENTS

The authors would like to thank K. C. Overbury, A. Chouliotis, C. Lehto, and D. Wilson of Canadair Limited, Montréal, for providing the samples and André Pilon of NRCC/IMRI for recording many of the spectra.

REFERENCES

1. P. R. Griffiths and J. A. de Haseth, "Fourier Transform Infrared Spectrometry" (Chemical Analysis Series Vol. 83), John Wiley and Sons, New York (1986).
2. M. P. Fuller and P. Griffiths, *Anal. Chem.* **50,** 1906 (1978).
3. M. P. Fuller and P. Griffiths, *Appl. Spectrosc.* **34,** 533 (1980).
4. P. R. Griffiths and M. P. Fuller, *Adv. Infrared Raman Spectrosc.* **9,** 63 (1982).
5. J. M. Chalmers and M. W. Mackenzie, *Appl. Spectrosc.* **39,** 634 (1985).
6. Y. T. Liao and J. L. Koenig, *Dev. Reinf. Plast.* **4,** 31 (1984).
7. K. C. Cole, D. Noël, and J.-J. Hechler, *Nat. SAMPE Symp./Exhib. [Proc.]* **30,** 624 (1985).

8. K. C. Cole, D. Noël, and J.-J. Hechler, *Proc. Soc. Photo-Opt. Instrum. Eng.* **553,** 114 (1985).

9. P. R. Young, B. A. Stein, and A. C. Chang, *Nat. SAMPE Symp./Exhib. [Proc.]* **28,** 824 (1983).

10. P. R. Young and A. C. Chang, *Nat. SAMPE Tech. Conf.* **16,** 136 (1984).

11. P. R. Young and A. C. Chang, *SAMPE Journal* **22**(2), 70 (March/April 1986).

12. P. R. Young and A. C. Chang, *SAMPE Quarterly* **17**(4), 32 (July 1986).

13. R. T. Graf, J. L. Koenig, and H. Ishida, *Anal. Chem.* **56,** 773 (1984).

14. M. T. McKenzie, S. R. Culler, and J. L. Koenig, *Appl. Spectrosc.* **38,** 786 (1984).

15. M. T. McKenzie and J. L. Koenig, *Appl. Spectrosc.* **39,** 408 (1985).

16. E. G. Chatzi, H. Ishida, and J. L. Koenig, *Appl. Spectrosc.* **40,** 847 (1986).

17. R. K. Vincent and G. R. Hunt, *Appl. Opt.* **7,** 53 (1968).

18. P. J. Brimmer, P. R. Griffiths, and N. J. Harrick, *Appl. Spectrosc.* **40,** 258 (1986).

19. P. J. Brimmer and P. R. Griffiths, *Appl. Spectrosc.* **41,** 791 (1987).

20. W. W. Wendlandt and H. G. Hecht, "Reflectance Spectroscopy", Interscience, New York (1966).

21. K. C. Cole, A. Pilon, D. Noël, J.-J. Hechler, A. Chouliotis, K. C. Overbury, "Comparison of infrared spectroscopic methods for the quantitative analysis of epoxy resins used in carbon-epoxy composite materials", paper submitted for publication in *Applied Spectroscopy* .

22. G. C. Stevens, *J. Appl. Polym. Sci.* **26,** 4259 (1981).

23. K. C. Cole, C. Lehto, and M. Yuhasz, *Proc. Soc. Photo-Opt. Instrum. Eng.* **665,** 243 (1986).

24. K. C. Cole, D. Noël, J.-J. Hechler, and D. Wilson, to be published.

HIGH TEMPERATURE POLYIMIDES, CHEMISTRY AND PROPERTIES

by

Daniel A. Scola
United Technologies Research Center
East Hartford, CT 06108, U.S.A.

Presented at the 8th annual NRCC/IMRI symposium "Composites-'87",
November 5 and 6, 1987, Boucherville, Que., Canada

ABSTRACT

Selected polyimide resins are capable of long term use at 316°C for over thousands of hours in an inert atmosphere, and approximately 2000 hours in air. This attractive feature of polyimides has provided an avenue for applications at elevated temperatue (316°C) as adhesives, coatings and secondary structures in the form of fiber reinforced polyimide composites.

The chemistry and properties of thermoplastic and crosslinked polyimides including addition type polyimides will be discussed. Selected mechanical and fracture toughness properties of polyimides and polyimide composites will also be presented. The chemical considerations of both commercial and experimental material systems, Avimid N, PMR-15, Larc TPI and others as they effect processing will also be discussed.

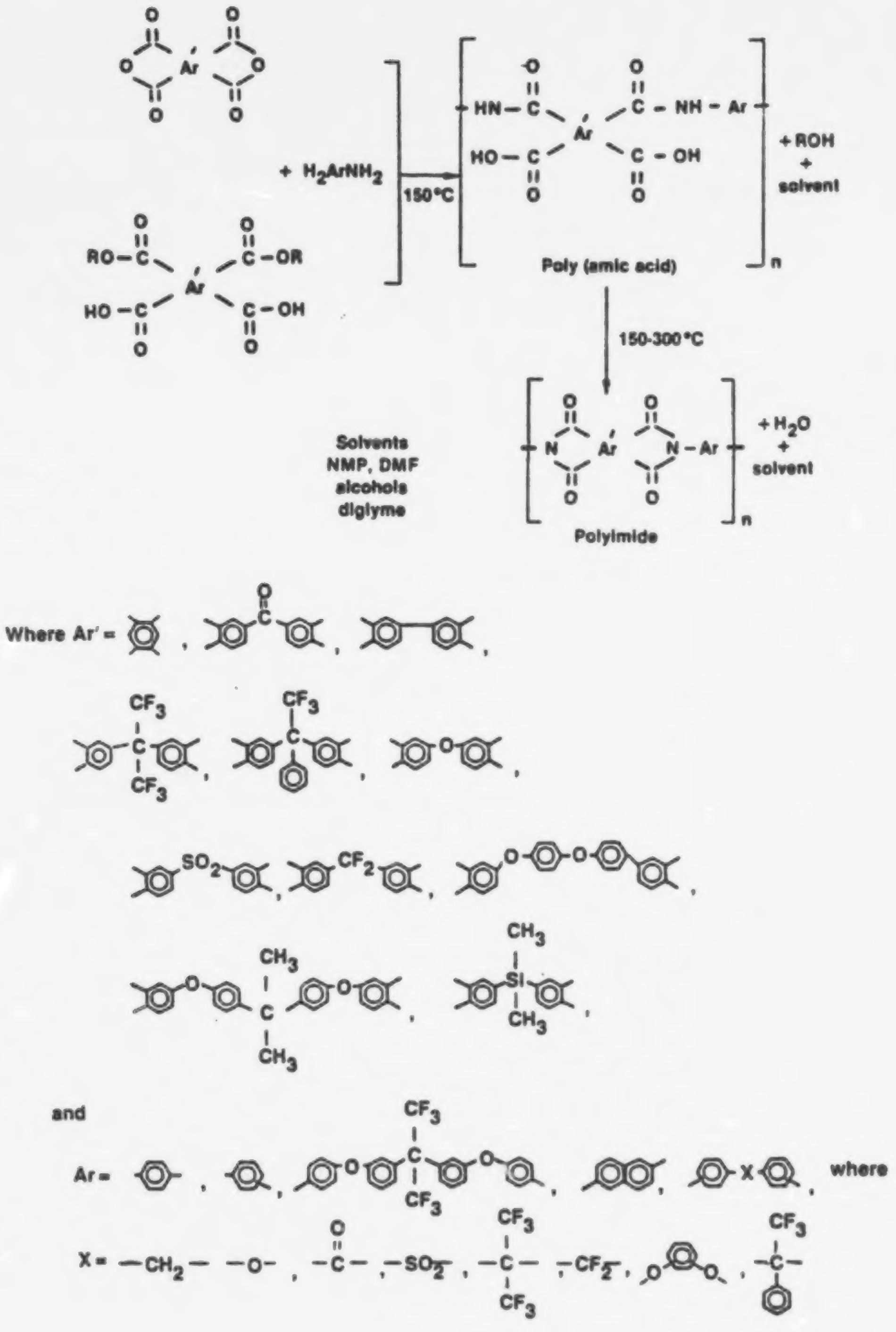
+ H$_2$ArNH$_2$
150°C
Poly (amic acid)
+ROH + solvent
150-300°C
Solvents NMP, DMF alcohols diglyme
Polyimide
+H$_2$O + solvent
Where Ar' =
and
Ar =
where
X = —CH$_2$— —O— , —C(=O)— , —SO$_2$— , —C(CF$_3$)$_2$— , —CF$_2$— ,
85-2-32-11

Fig. 1. Condensation polyimides.

HIGH TEMPERATURE POLYIMIDES, CHEMISTRY AND PROPERTIES

Daniel A. Scola
United Technologies Research Center
East Hartford, CT 06108

INTRODUCTION

Condensation Polyimides, discovered by Bogert and Renshaw in 1908 (1) and made practical by Edwards and Robertson (2) are derived from dianhydride or dianhydride derivatives and diamines. The intermediate polyamic acids are produced by a series of step-growth reactions at room temperature which control the molecular weight of the final polyimide product. The general reactions for polyimide formation is illustrated in Fig. 1.

For high temperature structural applications in the range 300 to 350°C the dianhydride Aryl (Ar) and diamine Aryl (Ar') groups can comprise of stiff aramatic structures.

For lower temperature structural applications, for example inthe temperature region from 200 to 275°C, the Ar and Ar' groups may contain arom[illegible] and aliphatic structures, ether linkages, and thioether linkages thereby lowering the glass transition temperature and also use temperature. The number of commercially available high temperature polyimides have been increasing steadily over the past three years. These represent a range of systems which can be rated in terms of their

Table 1

Commercial Types of Polyimides For Potential Use in Advanced Structural Composites

Condensation Type

- Monsanto's Skybond 700, 703
- DuPont NR-150B2 (Avimid N)
- LARC TPI
- Avimid K-111
- Ultem 1000
- Amoco Torlon
- Eymyd L-20
- Eymyd L-30

Addition Type

PMR-15	Reverse Diels-Alder Nadic end-capped
LARC 160	Reverse Diels-Alder Nadic end-capped
Thermid 600	Acetylene end-capped
BMI's	Bismaleimides, Maleimide end-capped

Table 2

Physical and Mechanical Properties of Polyimides[1]

	Avimid[1,2] K-111	Skybond[1,3] 701	PMR-15[1,4,5]	NR-150B2[1,6,7]	Thermid[1,8,9] MC-600	UpJohn[1] 2080	Ultem[1] 1000	Torlon[1] 4203	Larc TPI[1,10]
Density g/cc	1.31	1.35	1.32	1.40	1.34	1.40	1.27	1.38	1.37
Tensile strength MPa (ksi)	102 (14.8)	69 (10.0)	38.6 (5.6)	110 (16.0)	83 (12.0)	120 (17.1)	104 (15.2)	186 (27)	114 (16.6)[11]
Tensile modulus, GPa (10^6psi)	2.9 (.42)	4.1 (.60)	3.9 (0.57)	4.1 (.6)	4.1 (.60)	1.3 (.19)	3.0 (.43)	4.4 (.64)	3.5 (0.51)[11]
Flexural strength, MPa (ksi)	-	-	176 (25.5)	-	145 (21.0)	117 (17.0)	145 (21)	211 (30.1)	159 (23)
Flexural Modulus Gpa (10^6 psi)	-	-	4.0 (.58)	-	4.5 (.66)	3.4 (.48)	3.4 (.48)	4.5 (0.66)	-
Izod impact strength notched, J/m (ft. lbs/in.)	-	53.4 (1.0)	53.4 (1.0)	42.7 (.8)	48 (.9)	37.4 (.7)	53.4 (1.0)	133.5 (2.5)	(0.4)
Strain-to-failure, %	11	1.0	1.5	6.0	1.5	10	60	20	8.5[11]
Glass transition temp, °C (°F)	250 (482)	330 (626)	340 (644)[4]	340 (644)	320 (608)	280 (536)	210 (426)	267 (512)	256 (510)
Fracture Toughness G_{IC}[2] J/m^2 (in-lb/in)	1,900 (11.0)	-	280[5] (1.57)	2400 (13.4)	-	-	-	3900 (21.9)	-

1. Properties taken from commercial data sheets and technical literature as noted.
2. Ref. 3
3. Ref. 4
4. Ref. 5
5. Ref. 6
6. Ref. 7
7. Ref. 8
8. Ref. 9
9. Ref. 10
10. Ref. 11
11. Properties of film.

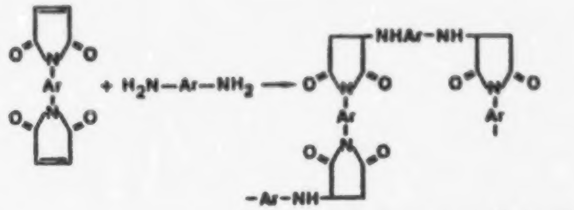
+ H₂N—Ar—NH₂
NHAr—NH
Ar
—Ar—NH

Amine crosslinked polybismaleimide

Michael addition BMI's

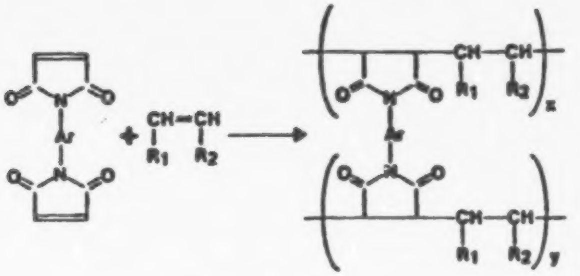
Ar
CH=CH
R₁ R₂
CH—CH
x
y

Bismaleimide — Olefin Copolymers

86-2-32-14

Fig. 2. Addition-type polyimides, bismaleimides.

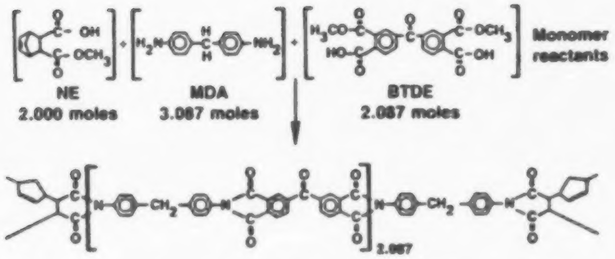
Monomer reactants
NE
2.000 moles
MDA
3.087 moles
BTDE
2.087 moles
2.087

Thermally cross-linked polyimide PMR-15

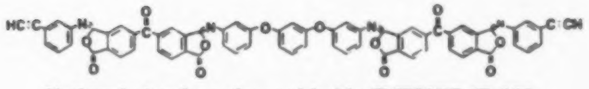

National starch preformed imide THERMID IP-600

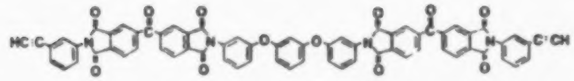

National starch preformed isoimide THERMID MC-600

87-1-51-1

Fig. 3. Addition type polyimides.

temperature capabilities. The types of commerically available polyimides are shown in Table 1.

In terms of their chemistry, there are two general types of commercial polyimides. The first type, thermoplastic polyimides derived from a condensation reaction as shown in Figure 1, and the second type, crosslinked polyimides, are derived from preformed imide monomer or oligomers, such as bismaleimides (Figure 2), the Reverse-Diels Alder (RDA) polyimide PMR-15, and the acetylene-ferminated polyimide MC-600 or IP-600, illustrated in Figure 3. This paper will address both the condensation and addition-type polyimides with the exception of the bismaleimides.

General Physical And Mechanical Properties

Table 2 lists some general physical and mechanical properties of commercial polyimides. Both the condensation and additions type are listed in Table 2. The properties of these materials were taken from commercial data sheets or technical literature as noted. For application to advanced composites, the properties which are of significance are (1) the glass transition temperature Tg, which sets the limit for its upper temperature use in composites, (2) the resin modulus, which controls the stiffness required to maintain rigidly between fibers and allows transfer of the load between fiber to fiber, (3) the strain-to-failure, which allows the fibers to exhibit their strain capability without matrix microcracking, and (4) fracture toughness, which is related to strain-to-failure and modulus and which allows the composite to resist delamination, peel and shear failure. The resin property which is not listed in Table 2 is the bonding capability of each polymer material with a given fiber. This material property can only be determined in an adhesion bond test by means of a tensile lap shear test or in a composite by means of an interlaminar shear test.

Table 3

Some Thermal Properties of Polyimides

Condensation Type	Tg's °C(°F)	Upper Temp. Capability °C(°F)
Skybond 700 Series	330 (626)	316 (600)
Avimid N (NR-150B2)	340 (644)	316 (600)
LARC TPI	265 (510)	300 (572)
Avimid K-III	250 (482)	225 (432)
Eymyd™ L-20	310 (590)	300 (572)
Eymyd™ L-30	350 (662)	316 (600)
UpJohn 2080	280 (536)	275 (528)
Ultem 1000	210 (426)	267 (512)
Sixef 44™	260 (500)	316 (600)
Addition Type		
PMR-15	340 (644)	316 (600)
LARC 160	330 (626)	316 (600)
Thermid MC-600 or IR 600	320 (608)	288 (550)
BMI's	230-290 (446-554)	232 (450)

Table 4

Thermo-Oxidative Stability Of High Temperature Polymers At 316°C In Air Flow, 100 CC/min

	Wt. % loss after, hrs								
Polymer	91	408	504	670	840	1079	1583	2927	4122
NR-150 B2	0.8	1.3	1.5	1.7	2.1	2.4	3.5	5.8	10.7
p-PPQ	0.7	2.9	3.9	6.5	9.6	12.1	20.3	51.1	74.9
PMR-15	2.3	5.7	7.1	8.7	11.1	13.4	22.2	55.4	84.9
IP-600	1.8	8.2	10.0	13.2	16.8	19.8	33.9	68.5	89.2
Larc TPI	6.8	12.1	13.7	16.6	17.7	19.9	28.2	46.5	82.2
L-20	1.9	6.6	7.3	10.0	12.8	21.3	46.5	72.8	100
L-30	1.5	5.8	8.1	10.4	13.5	20.9	45.4	86.1	100
PBI	0.4	11.5	14.6	19.6	27.4	40.8	65.7	100	-

Table 5

Thermo-Oxidative Stability of Polymer Materials at 316°C (600°F) in Flowing Air (100 cc/min)

Polymer Material	Relative Level of Stability at 316°C	Estimated Useful Life at 316°C, hrs	
		~ 10% Wt loss	~ 20% Wt loss
Avimid N(NR 150B2)	1	4000	>4000
Polyphenylquinoxaline (PPQ)	2	1500	1500
PMR-15	2	1000	1500
Larc TPI	3	500	1000
IP-600	3	500	1000
Eymyd L-20	3	600	1000
Eymyd L-30	3	600	1000
PBI	4	400	700

Table 6

Condensation Polyimides

Process Conditions for Resins and Composite

Polymer System	Solvent System	Amidization Conditions	Imidization Conditions	Postcure
Avidimid N (NR-150B2)	Ethanol DMAC	150°C/1.25 hr	200°C/1 hr auto clave, 250 psi or 2000 psi, compression + 316°C/1 hr 250 psi auto clave or 2000 psi compression	200°C/4 hrs 210°C/1 hr 310°C/4 hrs 330°C/4 hrs 370°C/4 hrs
Skybond 700 Series	NMP Xylene	100°C/1 hr	200°C/1 hr vacuum + 343°C/2 hrs (Auto clave) 200 psi or 2500 psi compression	370°C/2 hrs
Larc TPI	Diglyme, DMAC or mixtures	Supplied as Polyamic Acid	220°C/1 hr + 300°C/1 hr 1000 psi compression	340°C/2 hrs
Eymyd L-20	DMAC	Supplied AS Polyamic Acid	232°C/2 hrs 335°C/1 hr 1500 psi	375/2 hrs
Eymyd L-30	DMAC	Supplied As Polyamic Acid	232°C/ 2 hrs + 375°C/2 hrs 2000 psi	375/2 hrs

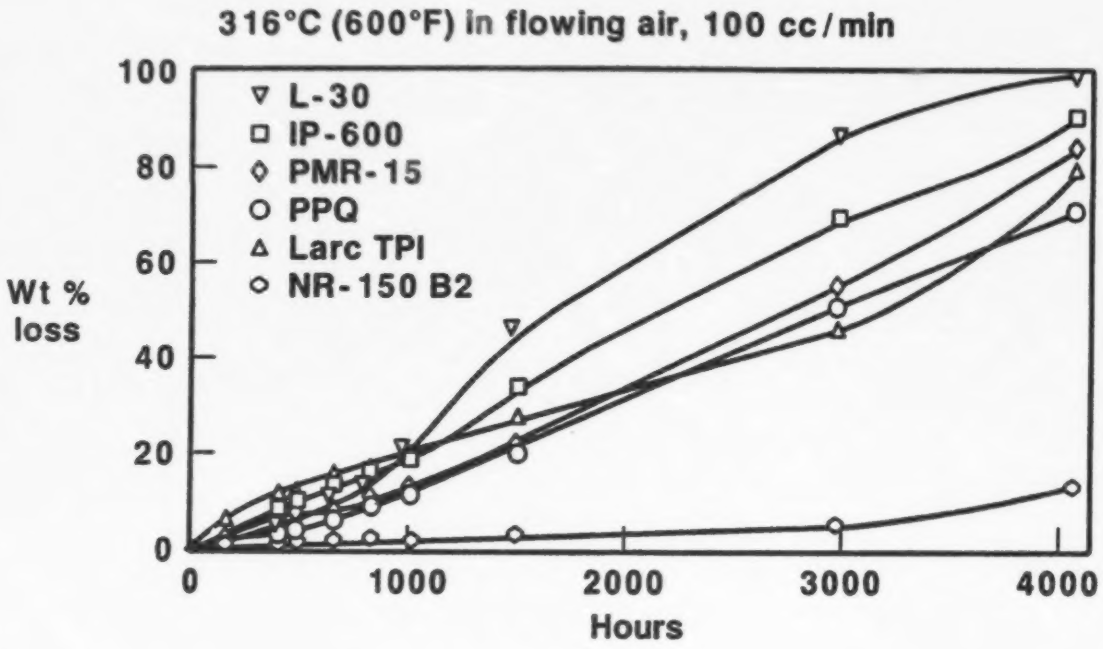

Fig. 4. Thermo-oxidative stability of high temperature polymer. (316°C (600°F) in flowing air, 100 cc/min)

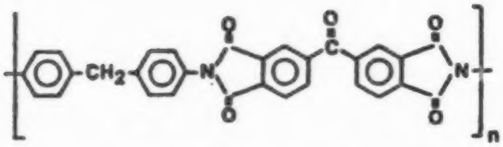

Monsanto Skybond 701

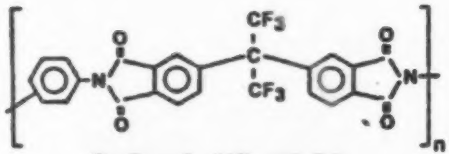

DuPont's NR-150 B2
Thermoplastic

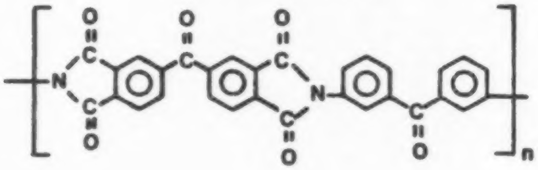

Larc TPI

86-2-32-17

Fig. 5. Thermoplastic polyimides derived from a condensation reaction.

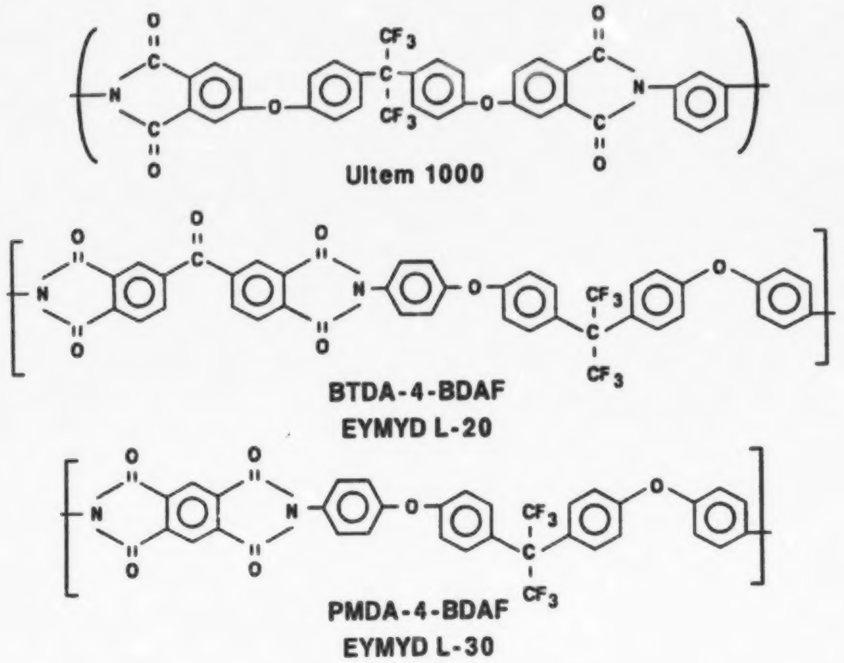
Ultem 1000
BTDA-4-BDAF
EYMYD L-20
PMDA-4-BDAF
EYMYD L-30

Fig. 6. Thermoplastic polyimides derived from a condensation reaction.

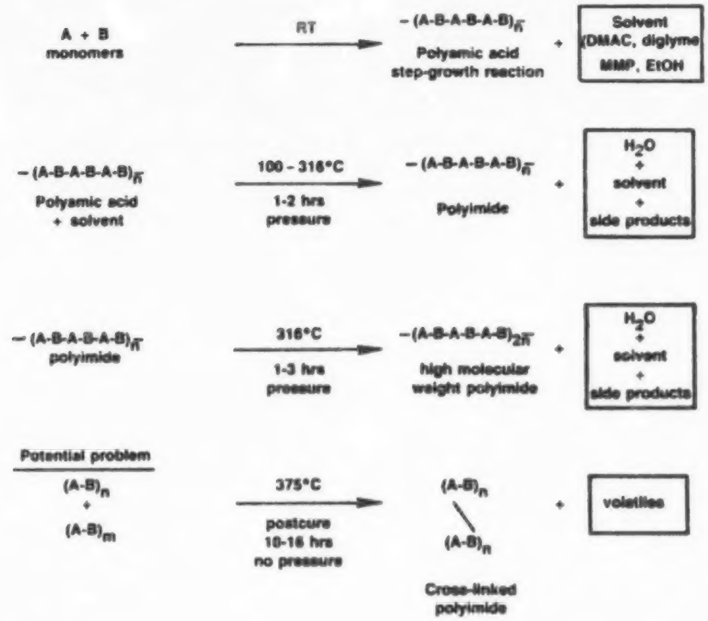
A + B
monomers
RT
–(A-B-A-B-A-B)n–
Polyamic acid
step-growth reaction
+
Solvent
(DMAC, diglyme
MMP, EtOH
–(A-B-A-B-A-B)n–
Polyamic acid
+ solvent
100 - 316°C
1-2 hrs
pressure
–(A-B-A-B-A-B)n–
Polyimide
+
H2O
+
solvent
+
side products
–(A-B-A-B-A-B)n–
polyimide
316°C
1-3 hrs
pressure
–(A-B-A-B-A-B)2n–
high molecular
weight polyimide
+
H2O
+
solvent
+
side products
Potential problem
(A-B)n
+
(A-B)m
375°C
postcure
10-16 hrs
no pressure
(A-B)n
(A-B)n
Cross-linked
polyimide
+
volatiles

Compression molding-low void, 2-3%
Autoclave molding-high void, 5-8%

Fig. 7. Processing of condensation polyimides.

Thermal Properties And Thermo-Oxidative Stability

The glass temperature and upper temperature capabilities of the polyimides are listed in Table 3. The glass transition temperature Tg, which is a second order transition, is the region where the polymer undergoes a transition from the rigid glassy state to a soft rubbery state. In this region there is a sharp change in the modulus (stiffness), and the ability of the polymer system to sustain a load. Therefore, the Tg of the resin defines the upper temperature limit for use in a structural application, which is approximately 30 to 40°C below the Tg. In a non-structural coating application, the polymer system can be used above the Tg, providing it has the thermo-oxidative stability and adhesive characteristics required for the application.

The long term isothermal thermo-oxidative stability of various polymers was determined at 316°C (600°F) in flowing air. The thermo-oxidative stability was measured based on weight loss or gain. The data is shown in Table 4 and illustrated in Figure 4, form the basis of ranking the polymer systems into four levels of thermo-oxidative stability. The level of stability an estimate of the useful life at 316°C, are listed in Table 5.

Process Characteristics

Condensation Polyimides.

The condensation polymers, examples of which are shown in Figure 5 & 6, are processed in-situ into high molecular weight polymers by a series of step-growth reactions. Table 6 lists process conditions and postcure cycle.

The first step in the molecular weight build-up is the formation of amic acid oligomers (Fig. 7). This occurs over a temperature range from RT to 150°C with the elimination of moisture and/or ethanol and solvent. The solvent used in most condensation type systems is either ethanol or solutions of ethanol/NMP, DMAC or NMP/xylene. The NMP or DMAC solvents are high boiling and must be removed in the course of the processing consolidation steps. During amic acid formation, no consolidation of the oligomer occurs. The second step of the reaction, imidization, occurs with the elimination of water or ethanol or other alcohol, depending on the ester used. This occurs over a temperature range approximately 150°C to 316°C. During the imidization process, chain extension occurs, the viscosity of the polymer increases, and pressure must be applied to consolidate the polymer as this process occurs. As mentioned above, in addition to removal of volatile by-products, residual solvent must also be removed during this consolidation step. Therefore, the critical aspect of the process is the removal of by-products and solvent during consolidation.

Addition-Type Polyimides

The Reverse Diel-Alder (RDA) PI's

The Reverse-Diels-Alder (RDA) addition type polyimides[12,13] represented by PMR-15 not only undergo the amidation and imidization reactions to form low molecular weight oligomers, typical of condensation polyimides, but also undergo an irreversible Diels-Alder reaction leading to high molecular weight cross-linked polyimides. Processing of this resin is further complicated by isomerization of the endo nadic end-capped oligomer to the exo-isomer. These latter two reactions distinguish the RDA addition polyimides from the condensation polyimides. The

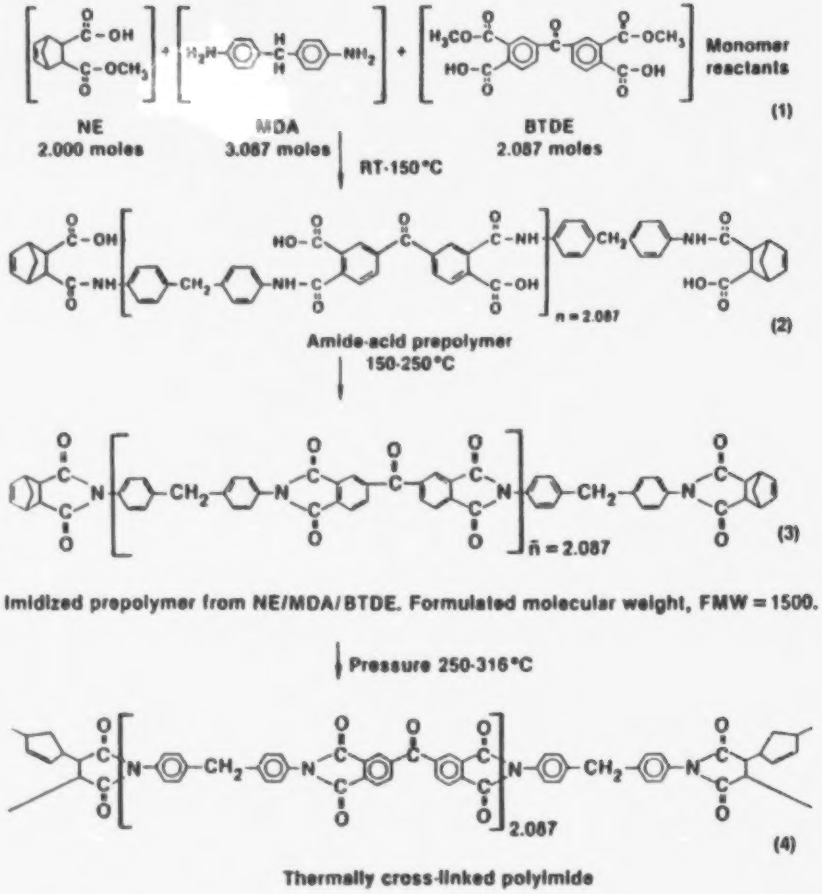
Monomer reactants
(1)
NE
2.000 moles
MDA
3.087 moles
BTDE
2.087 moles
RT-150°C
n = 2.087
(2)
Amide-acid prepolymer
150-250°C
ñ = 2.087
(3)
Imidized prepolymer from NE/MDA/BTDE. Formulated molecular weight, FMW = 1500.
Pressure 250-316°C
2.087
(4)
Thermally cross-linked polyimide

86–2–32–8

Fig. 8. General reaction scheme for PMR-15 reverse Diels-Alder polyimide.

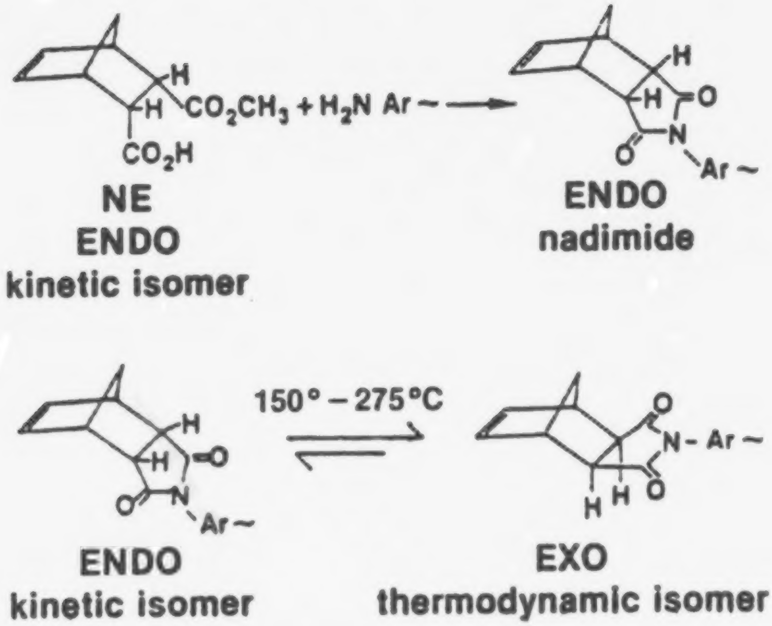
H
H
$CO_2CH_3 + H_2N$ Ar ~
CO_2H
NE
ENDO
kinetic isomer
H
H
O
N
O
Ar ~
ENDO
nadimide
H
H
O
N
O
Ar ~
150° – 275°C
O
N - Ar ~
O
H H
ENDO
kinetic isomer
EXO
thermodynamic isomer

88-2-32-6

Fig. 9. Isomerization during PMR-15 polymerization.

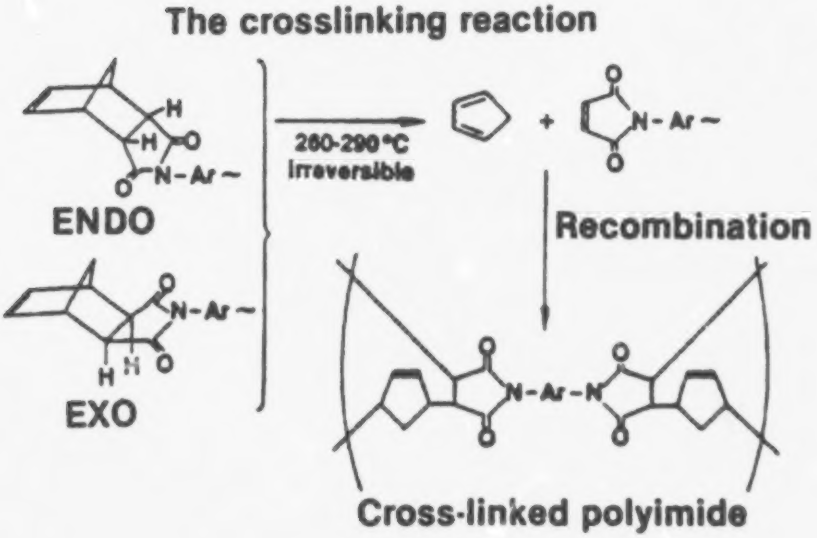
The crosslinking reaction
H
H
O
O
N - Ar ~
ENDO
O
N - Ar ~
O
H H
EXO
260-290°C
irreversible
+
O
N - Ar ~
O
Recombination
O
N - Ar - N
O
O
O
Cross-linked polyimide

88-2-32-7

Fig. 10. Reverse Diels-Alder during cure.

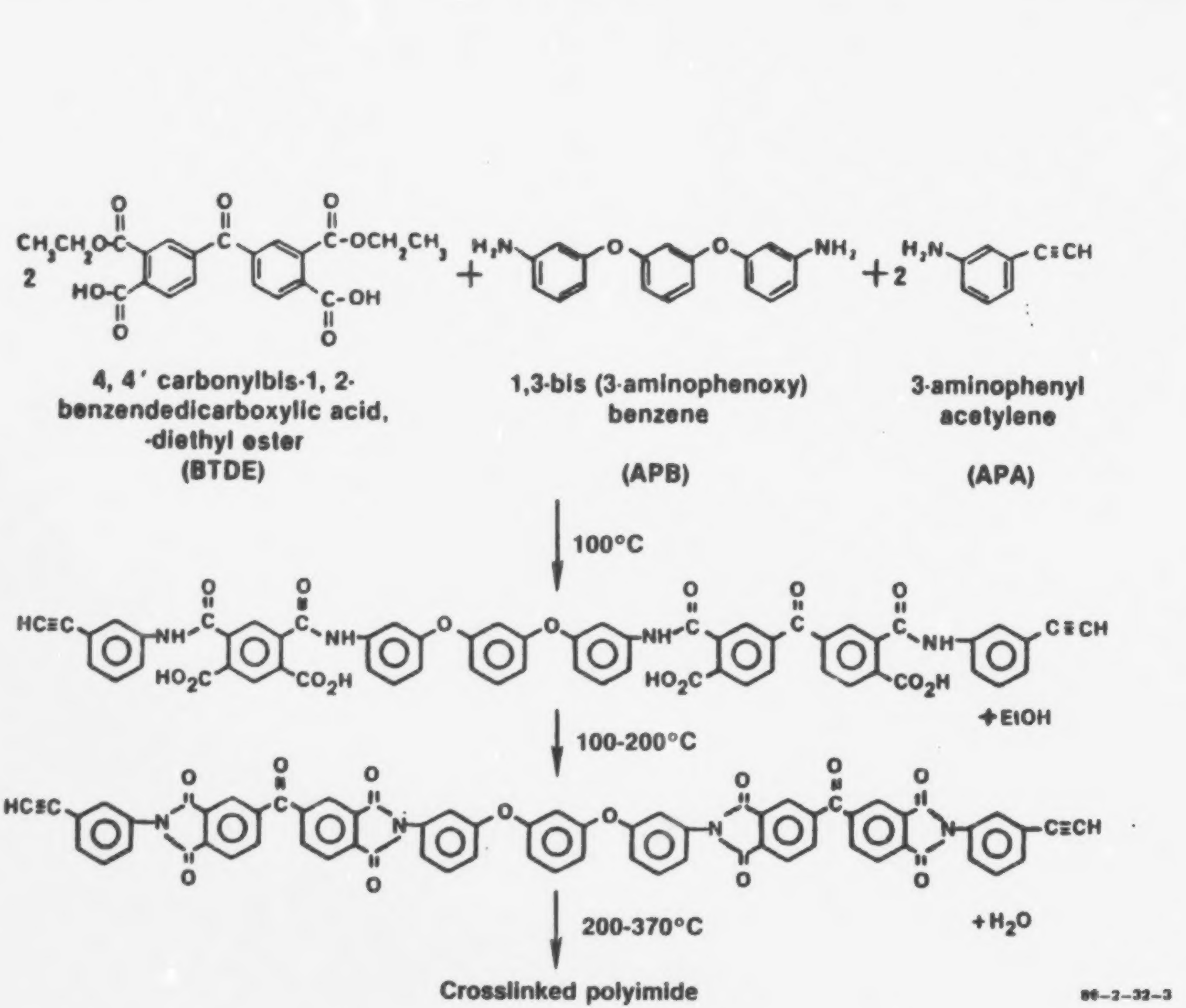
2
4, 4′ carbonylbis-1, 2-benzendedicarboxylic acid, -diethyl ester
(BTDE)
+
1,3-bis (3-aminophenoxy) benzene
(APB)
+2
3-aminophenyl acetylene
(APA)
100°C
+EtOH
100-200°C
+H2O
200-370°C
Crosslinked polyimide
86-2-32-3

Fig. 11. PMR acetylene end-capped Thermid Al-600.

process steps are as follows: Amide formation occurs in the first step between 40 to 150°C (Fig. 8). In the second step imidization occurs over a temperature range 150 to 250°C, and above (Fig. 8). Simultaneously, in the temperature range 175 to 260°C, isomerization of the endo-isomer to the exo-isomer occurs (Fig. 9).[14,15] Finally, in step 4, an irreversible Diels-Alder reaction of the endo/exo oligomers occurs yielding the reactive intermediates, cyclopentadiene and bimaleimide oligomer (Fig. 10). These recombine to form a stable cross-linked polyimide. The critical steps in the processing of this polyimide is the removal of residual by-products due to the imidization reaction and removal of low molecular weight components formed during the various process steps, as consolidation occurs.

Acetylene End-Capped PI's

The acetylene end-capped addition polyimide, Thermid 600[16] can be processed from monomers, AI-600 (Fig. 11), similarly to the RDA polyimide PMR-15 and condensation PI's in its initial stages of oligomer imide formation. The acetylene end-capped polyimide can be processed from preformed solid oligomer powder, The imide MC-600 or isoimide IP-600 (Fig. 3). The monomers combine to form acetylene terminated amic acids oligomers over the temperature range 40 to 150°C, with the removal of ethanol and/or water and solvent. The second step involves formation of the acetylene terminated Thermid 600 oligomer imide with the elimination of water and solvent over the temperature range 150 to 250°C. Simultaneously, during imide formation, the acetylene end-cap undergoes homopolymerization to form a poly (eneimide) over the temperature range 175°C to 350°C. If the starting oligomer is MC-600 or IP-600, cross-linking occurs over the temperature range 150 to 250°C and continued reaction and thermal stabilization occurs over the temperature range 250 to 350°C. As with the other polyimides the critical steps are elimination of the

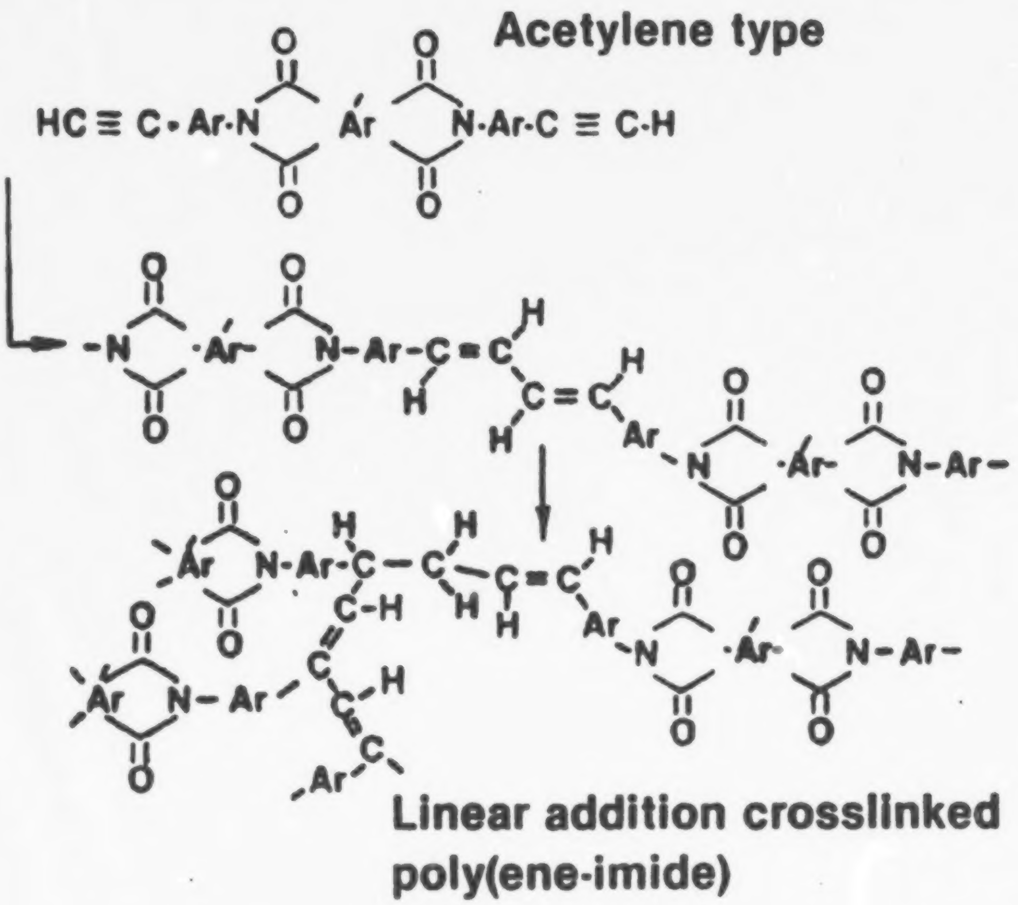
Acetylene type
Linear addition crosslinked poly(ene-imide)

3-2-32-2

Fig. 12. Cross-linking reaction of acetylene addition polyimides.

Table 7

Mechanical Properties Of
High Temperature Polymer/
Graphite Fiber Composites

Composite system	Unaged Shear strength, ksi RT	 316°C	 % Ret.	 Flex strength ksi RT	 316°C	 Ret.
PMR-15/Celion 6000[1]	15.0	7.5	50	275	160	58
NR-150B2/Celion 6000[2]	15.0	7.0	47	225	128	57
Thermid 600/HTS[3]	12. 1	8.0	66	195	148	76
m-PPQ/HMS[4]	6.2	3.4	55	122	55.8	46
Larc TPI/Celion 6000[5]	10.0	-	-	232	-	-

1. (Ref. 17) R. H. Pater, 13th SAMPE National Tech Conference SAMPE, 13, 38-52 (1981).
2. (Ref. 18) D. C. Aldrich - DuPont High Temple Workshop V, Monterey, Calif. March 5-7 (1985).
3. National Starch and Chem Corp Data Sheet on Thermid 600.
4. P. Hergenrother, NASA Langley Res. Center. private communication.
5. (Ref. 11) A. K. St. Claire and T. L. St. Claire, 26th National SAMPE symposium, SAMPE 26, 165-178 (1981).

Table 8

MECHANICAL PROPERTIES OF
HIGH TEMPERATURE POLYMER/
GRAPHITE FIBER COMPOSITES
Ages 1000 hrs at 316°C in air

	Shear strength, ksi 316°C*	 316°C	% Ret	Flex strength ksi 316°C*	 316°C	% Ret
PMR-15/Celion 6000[1]	6.5	7.50	100	134	147	109
NR-150B2/E-glass[2]	3.4	3.90	115	35	43	123
Thermid 600/HTS[3]	8.0	-	-	35	83	56
m-PPQ/HMS[4]	3.4	1.65	49	56	36	64

*Unaged

1. (Ref. 17) R. H. Pater, 13th SAMPE National Tech Conference SAMPE 13, 38-52 (1981).
2. DuPont Data Sheets on NR-150B2.
3. National Starch and Chem Corp Data Sheet on Thermid 600.
4. H. Hergenrother, NASA Langley Res. Ctr. private communication.

by-product off gases and residual solvent during the consolidation step over the temperature range 175°C to 350°C. In Thermid MC-600, pressure is applied at 200°C, and maintained up to 316°C. The cross-linking reaction is illustrated in Fig. 12. In order to arrive at a high glass transition temperature, high strength and stiffness, the resin is postcurred at 375°C for 24 hrs.

The formation of a stiff, cross-linked polyimide material by an addition reaction, both for PMR-15 and thermid 600, implies that by-product gases and solvent do not complicate the fabrication process. However, this is misleading because water, alcohol and low molecular by-products of an unknown nature are formed during the process steps for both polymer systems. If provisions are not made to remove these materials during the process steps, they become trapped in the structure. The presence of voids and blister formation during post cure in many cases can be attributed to these by-product gases, volatile solvents and unknown low molecular weight by-products.

Properties of Polyimide Resin Composites

Unaged mechanical properties of polyimide resins reinforced with graphite fibers are listed in Tables 7. Some mechanical properties after aging 1000 hrs at 316°C are listed in Table 8. For the limited data available, it is clear that NR-150B2 and PMR-15 retain their unaged 316°C strength properties after 1000° hours at 316°C in air. The unavailability of long term isothermal aging data for the high temperature polymer composite systems suggests that additional efforts should be placed in this area to develop a sound technology base.

ACKNOWLEDGEMENT

The author would like to acknowledge J. H. Vontell who assisted in thermo-oxidative stability and process studies.

REFERENCES

1. T. M. Bogert and R. R. Renshaw, J. Am. Chem. Soc., 30, 1140 (1908), W. M. Edwards and I. M. Robertson, US Patent 2,710, 853 (1955).

2. W. M. Edwards and I. M. Robertson, US Patent 2,710,853 (1955).

3. H. Gibbs, "The Interdisciplinary Workshop on the Chemistry and Properties of Polyimides", sponsored by Div, Poly. Chem. of ACS, MGM Grand Hotel, Reno Nevada, June 25-28, (1985).

4. Monsanto Product Technical Bulletins, Nos. 5042 and 623 A.

5. P. J. Cavana and W. F. Winters, PMR-15 Polyimide/Graphite Fiber Composite Fan Blade, NAS CR 135113, Feb. (1976).

6. D. A. Scola, unpublished results.

7. H. Gibbs, Proceedings of the 28th Annual Technical Conference, Reinforced Plastics/Composites Institute, SPI, Inc., Section 2-D (1973).

8. H. Gibbs, Proceedings of the 29th Annual Technical Conference, Reinforced Plastics/Composites Institute, SPI, Inc., Section 11-D (1974).

9. A. L. Landis and A. B. Naselo W, SAMPE 14, 236-242 (1982).

10. N. Bilow, ACS Symposium Series, 132 A. A. May, Editor p. 139-150, (1980).

11. A. K. St. Claire and T. L. St. Claire, 26th National SAMPE Symposium, SAMPE 26, 165-178 (1981).

12. H. R. Lubowitz, US Patent 3,528,590, Sept. 15, (1970).

13. T. T. Serafini, P. Delvigs, & G. R,. Lightsey, J. Appl. Poly Sci., 16, (4), 905-916, (1972). US Patent 3, 765,149, July, (1973).

14. P. R. Young and A. C. Chang; J. Heterocyclic Chem. 20, 177 (1983).

15. D. A. Scola and J. H. Vontell, 2nd International Polyimide Conference, Proceedings, Nevelle Country Club, Ellenville, NY, Oct. 30-Nov. 1, 247-252 (1985). "Recent Advances in Polyimide Science and Technology," Society of Plastics Engineers, Publishers, W. D. Weber and M. R. Gupta, Editors, 324-335 (1987).

16. A. L. Landis, N. Bilow, R. H. Boschan, R. E. Lawrence and A. T. Aponyi, Am. Chec. Socl Div., Coatings & Plastics, 15, (2), 537-541 (1974).

17. R. H. Pater 13th SAMPE National Tech. Conference, SAMPE, 13, 38-52 (1981).

18. D. C. Aldrich - High Temple Workshop V, Monterey, Calif. March 5-7, (1985).

RADIATION-CURABLE CARBON FIBER PREPREG COMPOSITES

by

C.B. Saunders, L.W. Dickson, A. Singh, A.A. Carmichael and V.J. Lopata
Atomic Energy of Canada Limited Research Company
Radiation Applications Research Branch
Pinawa, Manitoba, Canada, R0E 1L0

Presented at the 8th annual NRCC/IMRI symposium "Composites-'87",
November 5 and 6, 1987, Boucherville, Que., Canada

RADIATION-CURABLE CARBON FIBER PREPREG COMPOSITES

Chris B. Saunders, Lawrence W. Dickson, Ajit Singh,
Alistair A. Carmichael and Vince J. Lopata

Radiation Applications Research Branch
Whiteshell Nuclear Research Establishment
Atomic Energy of Canada Limited Research Company
Pinawa, Manitoba, Canada ROE 1LO

Radiation processing is the utilization of ionizing radiation, usually photons or electron beams, to produce useful physical and chemical changes in a material. A potential application for electron beam processing for composite manufacturing is for curing carbon fiber prepregs. These prepregs, carbon fibers or fabrics preimpregnated with liquid polymer resin, are commonly used in the aircraft industry. Their use, however, can be time consuming and labour intensive. The advantages of radiation curing over thermal or chemical curing methods include improved rate control, reduced curing times, and curing at ambient temperature. There is also no need for chemical initiators.

A radiation-curable prepreg has been designed to meet the mechanical and physical property specifications of a leading aircraft manufacturing company. The resin is a mixture of an epoxy diacrylate, polybutadiene diacrylate and a multifunctional monomer. This resin was used to impregnate a plain weave carbon fabric, at a loading of 35% (by mass), using a solvent process.

Preliminary characterization studies show that the cured polymer produced by irradiation in air to a dose of 40 kGy is amorphous with a maximum gel fraction of 85%. The softening point of the polymer varied from 228°C (30-kGy sample) to 237°C (50-kGy sample). The linear thermal expansion coefficient of the polymer was 1.7×10^{-4} cm/cm°C from 25 to 150°C and was unaffected by varying the applied dose from 30 to 50 kGy.

INTRODUCTION

Basic and applied research and development in the field of radiation treatment of polymers and composites have continued since the first observed radiation polymerization reported by Hopwood and Phillips in 1938 (1). Several reviews of the radiation chemistry of monomers and polymers have been published (1-4) and there has been a continuous interest in research and product development for new applications of radiation treatment of plastics and composites (5,6). Industrial use of radiation processing began about 25 years ago.

One application of ionizing radiation is the polymerization of selected polymer systems. The interaction of high-energy radiation with organic compounds produces a variety of potential initiators, including anions, cations and free radicals. Radiation-induced polymerization generally proceeds by the single mechanism that is most favoured by the conditions of the system (monomer type, temperature, impurities present, etc.). Monomers that polymerize by a free radical mechanism such as the vinyl-type monomers, are excellent candidates for radiation-induced polymerization. A free radical polymerization process consists of chain initiation, propagation and termination reactions and proceeds by the following type of mechanism (2,4,7,8):

$R\cdot + M \rightarrow RM\cdot$ (initiation) (1)

$RM_n^{\cdot} + M \rightarrow RM_{n+1}^{\cdot}$ (propogation) (2)

$RM_n^{\cdot} + R\cdot \rightarrow RM_nR$ (termination) (3)

$RM_n^{\cdot} + RM_x^{\cdot} \rightarrow RM_{n+x}R$ (termination) (4)

$RM_n^{\cdot} + S \rightarrow RM_nS\cdot$ (termination) (5)

where $R\cdot$ is an initiating free radical, M is a monomer, $RM\cdot$ is the chain-propogating intermediate, S is a free radical scavenger and $RM_nS\cdot$ is a non-propogating radical. The initiation and propagation reactions are straightforward sequential addition of monomer units to a free radical initiator. Chain termination may occur by reaction of the propagating intermediate with a free radical initiator, another intermediate or a free radical scavenger such as molecular oxygen. Because of the inhibiting effect of oxygen on free radical polymerizations, some monomers must be polymerized in an inert atmosphere, e.g., nitrogen or vacuum. Many resin formulations have now been design that are less sensitive to this oxygen effect and the need for an inert gas blanket was thus eliminated. The dose range required for most polymerization processes is 10 to 50 kGy, depending on the process objective and the material to be irradiated (9).

Cationic and anionic polymerization reactions occur by a similar mechanism, except that the initiator and chain-propagating intermediates are ions and the non-scavenged termination step is an ion-pair recombination reaction.

The rates of ionic polymerization reactions are about 100 times faster than those of free radical processes since the activation energies of the propagation step tend to be significantly lower for the ionic mechanisms (2,4). Low temperatures favour ionic polymerization mechanisms because of the higher activation barriers for the free radical reactions and because of the reduced rate of the ionic chain termination reactions. Ionic polymerization may be terminated by reaction of the propogating intermediate with water. Cyclic compounds, such as epoxides, ethers, and sulphides, must be dried carefully prior to radiation-induced, ring-opening polymerization, which almost invariably proceeds by an ionic mechanism.

High-energy irradiation of polymers also causes crosslinking and scission (1,3,4,9). Controlled crosslinking leads to an improvement of the mechanical properties of the irradiated polymer, whereas scission usually leads to a deterioration of mechanical properties. Crosslinking and scission occur simultaneously when polymeric materials are irradiated, but one process usually dominates: polyethylene, polyamides and polyesters crosslink, but polyisobutylene, polymethylmethacrylate and cellulose undergo scission. The irradiation conditions may also favour crosslinking over scission. Crosslinking is favoured during irradiation in vacuum and inert atmospheres, and at high dose rate. The dose range required for most crosslinking applications is 50 to 200 kGy.

High-energy radiation may also be used to form chemical bonds between polymers and other materials: this process is termed grafting (1,4,9). Grafting may be effected either by the simultaneous irradiation of a monomer and the substrate (9) or by post-irradiation grafting involving prior irradiation of a substrate known to retain the ability to induce polymerization of a monomer long after irradiation as a result of residual free radicals or the formation of peroxzides on the surface. The post-irradiation grafting of monomers onto organic polymers is due to the formation of long-lived peroxides during irradiation of the polymer in an oxygen-containing atmosphere. These peroxides decompose by reaction with monomer molecules, thereby initiating polymerization of the monomer and creating chemical bonds between the two materials. The dose range for most grafting applications is 50 to 200 kGy.

Radiation processing of plastics is an established industry. The advantages of radiation curing over other curing methods include improved rate control, reduced curing times, and curing at ambient temperature without the need for chemical initiators or solvents. Electron beam (EB) accelerators, dominating the industry with about 500 individual units worldwide, are used for plastics and composite production (10). Ultraviolet radiation sources are also extensively used for thin coating applications. The penetration limit for industrial high-energy EB accelerators (10-MeV beam voltage) is about 9 cm for two-sided treatment of unit-density material. The dose is distributed throughout the thickness of the material with approximately 25%

variation (11). The penetration limit is also inversely proportional to the density of the material to be treated. If the density is 2 g/cm^3, the penetration limit for two-sided 10-MeV electron treatment is 4.5 cm.

Five general product categories account for over 95% of the current worldwide EB plastics production capacity (12,13,14):

1. Crosslinked wire and cable insulation to increase shape stability at elevated temperatures and improve resistance to solvents and environmental stress cracking;

2. Crosslinked semi-crystalline polyethylene to produce heat shrinkable sheet, film and tubes;

3. Partially vulcanizated rubber sheet to improve physical properties and form stability during tire assembly and final vulcanization;

4. Crosslinked polyolefins, usually polyethylene to produce an improved foam product. EB treatment improves the mechanical and chemical properties of the foam and enable the process and pore size to be accurately controlled; and

5. Radiation-curable coatings and adhesives. EB treatment is very quick and curing is done at ambient temperatures. Solvents are not required either, eliminating a potential pollution problem.

At present, radiation processing can not be considered a part of the commercial fiber-reinforced composite manufacturing industry. Nevertheless, EB processing does seem to have potential applications for several reasons. These reasons include:

1. The ever-continuing search for new matrix-fiber systems that can be easily processed and have the required mechanical and chemical properties. Thermoplastic composites are easily processed, but they often do not have the high-temperature properties of thermosets required for many applications, primarily in the aircraft and aerospace industry and the automotive industry. Radiation processing can convert a thermoplastic resin to a thermoset polymer. The processing ease of thermoplastics can be exploited, while still obtaining the high-temperature properties of thermosets.

2. The importance of automation of processes using fiber-reinforced composites to increase their use in high-volume consumer-oriented industries such as the automotive industry. Production speed is of primary importance and extensive cure cycles limit production. EB processing should be able to eliminate long cure cycles for some free radical-initiated resin systems, which would significantly increase production speeds.

3. Radiation processing can be easily retrofitted to many types of process lines, such as pultruders, pulformers and extruders. Radiation processing can also be an off-line process to treat selected products as required from a large processing facility, providing production flexibility.

One potential application for electron beam processing of composites is for curing carbon fiber prepregs. These prepregs, carbon-fibers or fabrics preimpregnated with liquid resin, are used in the aircraft industry for hand lay-up application, producing a high - strength, low - weight construction material. Epoxy resins are commonly used to manufacture these prepregs, but the curing cycle is both time consuming and expensive. Radiation polymerization of most epoxy compounds proceeds by a cationic mechanism (15). These cationic reactions are inhibited by water, even at trace levels, and thus, most epoxies are not currently good candidates for industrial-scale radiation polymerization. Good radiation curing properties can be imparted to an epoxy resin, however, by acrylating the terminal epoxy groups of an epoxy oligomer (15).

The mechanical properties of carbon fibers are not deleteriously affected by irradiation when irradiated in a vacuum to a dose of 50 MGy (16). This excellent radiation stability makes these fibers well suited for radiation-curable prepregs. The expected dose required to cure these prepregs is less than 50 kGy.

The objective of this experimental program is to design and manufacture a radiation-curable polymer-carbon fiber prepreg that meets all of the mechanical and physical property specifications set by a leading manufacturer of aircraft components. The program was divided into two phases: designing the prepregs and characterizing the selected resin system, and mechanical and physical testing of the radiation-cured material. This paper describes our current work involving designing these prepregs and characterizing the selected resin system, and it also outlines our future testing program.

Table 1. Recommended Radiation-Curable Resin Formulations

Compound Name	Sartomer Product Number	Recommended Formulations (wt.%) A	B	C	D	E	F
Dipentaerythritol Monohydroxypentaacrylate	SR-399	80	80	20	20	20	20
C_{14}-C_{15} Diol Diacrylate	SR-2000	20	-	30	30	-	-
Polybutadiene Diacrylate	SR-5000	-	20	50	-	30	30
Aliphatic Urethane Diacrylate	SR-9503	-	-	-	50	50	-
Epoxy Diacrylate	SR-3000	-	-	-	-	-	50

Table 2. Relative Product Characteristics for Selected Compounds

Property	SELECTED COMPOUNDS[1] Dipentaerythritol Monohydroxypenta-acrylate (SR-399)	C_{14}-C_{15} Diol Diacrylate (SR-2000)	Polybutadiene Diacrylate (SR-5000)	Aliphatic Urethane Diacrylate (SR-9503)	Epoxy Diacrylate (SR-3000)
Abrasion Resistance	X			X	X
Adhesion	X	X	X		X
Chemical Resistance	X				X
Flexibility	X	X	X	X	
Hardness	X				X
Heat Resistance	X			X	X
Impact Resistance		X	X		
Low Shrinkage		X	X	X	X
Water Resistance		X	X		X
Weatherability	X			X	
Molecular Weight	525	~300	3000	2000	428
Reactive Esters, %	97.5	99+	99+	99	98+
Specific Gravity (@25°C)	1.19	0.934	0.940	1.200	1.200
Viscosity (pa.s @ 25°C)	15.25	0.01-0.02	0.01-0.02	~2000	~1000

(1) X means that when the compound is included in a resin formulation, the specified property is imparted to the cured polymer.

EXPERIMENTAL

Materials

The Sartomer Company, a leader in the supply of radiation curable polymer resins, was asked to recommend resin formulations that could be impregnated in a specified carbon fabric and radiation cured, producing a composite that would meet or exceed the aircraft industry's material specifications for epoxy preimpregnated carbon fiber tapes and woven fabrics (Specification BMS 8-212J,1985). Table 1 lists the six recommended resin formulations.

Five acrylated compounds were selected to prepare the six resin formulations. Dipentaerythritol monohydroxypentaacrylate (SR-399) is a multifunctional monomer with low volatility and very low toxicity. The diol diacrylate (SR-2000) is a reactive diluent, also with low volatility and toxicity. The remaining three compounds, polybutadienne diacrylate (SR-5000), aliphatic urethane diacrylate (SR-9503) and epoxy diacrylate (SR-3000), are all oligomers.

The relative product characteristics of these compounds must be examined to understand why these particular resin formulations have been recommended for manufacturing of a radiation-curable prepreg. Table 2 lists these relative product characteristics.

Resin formulations A and B (Table 1) are each 80% SR-399 monomer, which has good product characteristics except for impact

Table 3. Carbon Fabric Specifications
Fiber Properties

Specificiation/Property	Value
Fabric Weave	Plain
Filaments/Tow	3000
Fabric Areal Weight (g/m^2)	193
Cured Fabric Thickness (mm)	0.2
Fiber Tensile Strength (MPa)	3790
Fiber Tensile Modulus (GPa)	234
Fiber Tensile Strain (%)	1.5
Fiber Density (g/cm^3)	1.8
Prepreg Resin Content (wt.%)	35 ± 2.0
Resin Composition (wt.%)	
SR-3000	50
SR-5000	30
SR-399	20

resistance, low shrinkage and water resistance. SR-2000 (in Resin A) and SR-5000 (in Resin B) are mixed with SR-399 to improve these deficiencies. Formulation C combines all three compounds. SR-9503, accounting for 50% of formulations D and E, has poor adhesion characteristics, chemical resistance, hardness, impact resistance and water resistance. SR-2000 (in Resin D) and SR-5000 (in Resin E) are added in these formulations at the 30% level to improve adhesion, impact resistance, and water resistance. The remaining 20% of each formulation is SR-399, added to increase adhesion, chemical resistance and hardness. Formulation F combines SR-3000 (50%), SR-5000 (30%) and SR-399 (20%). SR-5000 is added to improve the flexibility and impact resistance to the epoxy acrylate and SR-399 is added to improve the flexibility and weatherability of the formulation.

The epoxy diacrylate resin system (Resin F) was selected for manufacturing of the radiation-curable prepregs because of its epoxy structure, which is similar to the resins presently used for prepregs, and the superior product characteristics of SR-3000 as compared to the oligomers used in the other formulations, SR-5000 and SR-9503.

A plain weave carbon fabric, manufactured by Hercules, has been selected from the aircraft industry's qualified products list. Hercules also manufactured our prepregs using a solvent process. Table 3 lists the product specifications for the carbon fabric and the radiation-curable prepreg and the typical properties of the carbon fibers.

Hercules' carbon fibers are produced from polyacrylonitrile precursor (PAN) using a thermal decomposition process. A typical decomposition process involves a slow oxidation of PAN fibers at 150 to 300°C under stretched conditions to produce a crosslinked ladder polymer structure, followed by a heat treatment at 1000 to 3000°C, depending on the required final properties of the fibers.

Procedure

A Gammacell-220 (dose rate = 17 kGy/h) was used to irradiate all samples in an air atmosphere at ambient temperature and pressure. The dose range was 0 to 50 kGy. A Stanton Redcroft STA-781 thermalanalysis system and a linear thermal expansion apparatus were used to study the thermal characteristics of the cured polymer as a function of radiation dose. The radiation effect on the gel fraction of the polymer and the molecular weight distribution of the extract from the gel fraction experiments were also studied using standard soxhlet extraction techniques and gel permeation chromatography (GPC). Chloroform was the solvent for the extraction and the mobile phase for the GPC. Polystyrene standards were used to convert GPC retention times into a molecular weight scale. A Haake RV3 rotary viscometer was used to determine the effect of radiation on the viscosity of the selected resin formulation as a function of temperature. The resin viscosity is an important variable for prepreg manufacturing, affecting the flow-out properties and the resin wetting characteristics in the prepregging process.

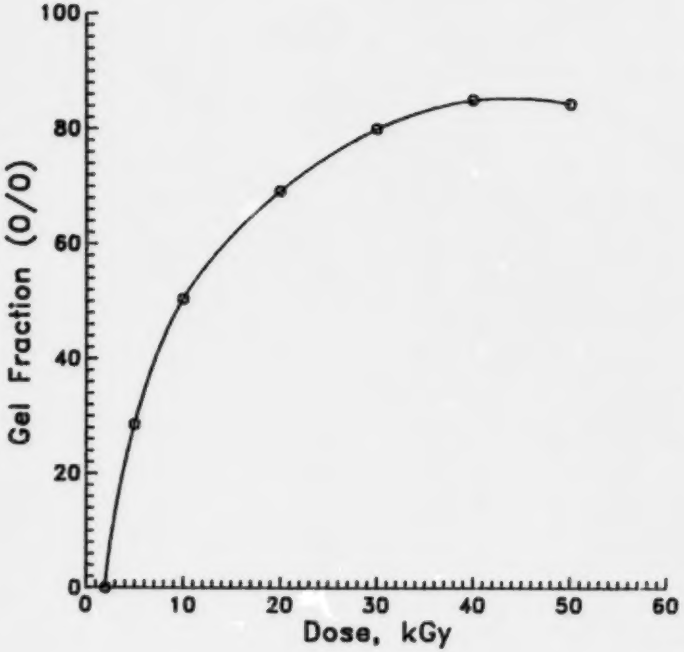

Fig. 1. The gel fraction of the cured polymer vs. irradiation dose.

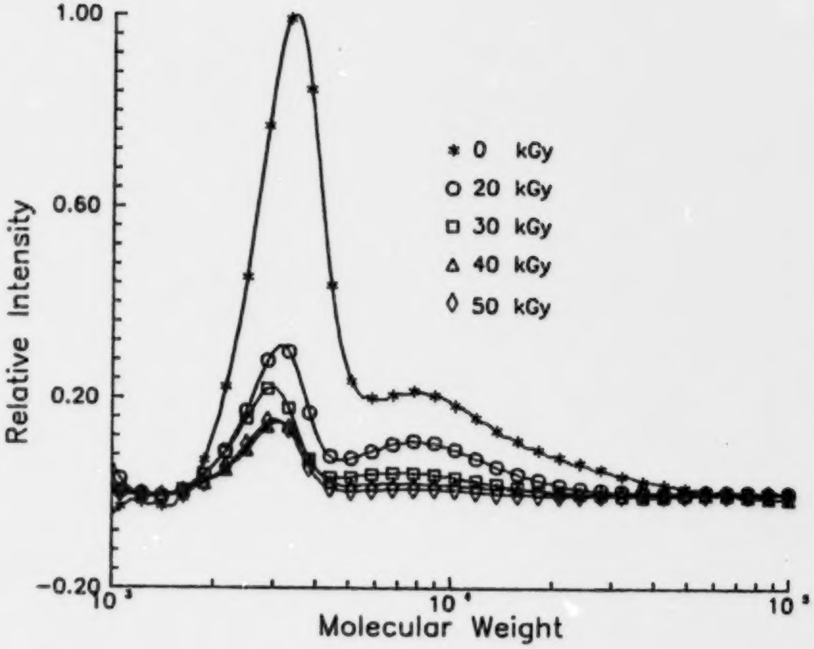

Fig. 2. The effect of irradiation on the molcular weight distribution of the extracted polymer.

RESULTS AND DISCUSSION

Gelation and Molecular Weight Distribution

Figure 1 illustrates the effect of irradiation on the gel fraction of the polymer. The radiation dose required to initiate gelation, the gel point, was 2 to 3 kGy. The gel fraction then increased rapidly with dose, reaching its constant maximum level of approximately 85% at a dose of 40 kGy. Since crosslinking and scission are occurring simultaneously during irradiation, 100% gelation would not occur in this polymer at ambient temperature and pressure.

Figure 2 displays the molecular weight distribution of the extracted portion of the polymer. The GPC data show that the amount of low molecular weight material decreases as the radiation dose increases to 40 kGy. At doses above 40 kGy, the molecular weight distribution of the extract is independent of the radiation dose, again suggesting that crosslinking and scission effects are in equilibrium under these experimental conditions.

Thermal Characteristics

Differential thermal analysis (DTA) of the cured polymer in an argon atmosphere showed a characteristic peak at about 230°C. The DTA heating rate was 5°C/min. X-ray diffraction analysis of cured polymer samples (dose = 50 kGy) heated to 300°C showed that the polymer was amorphous and unchanged from the control samples; therefore, the DTA peak was not a result of crystallization of the polymer.

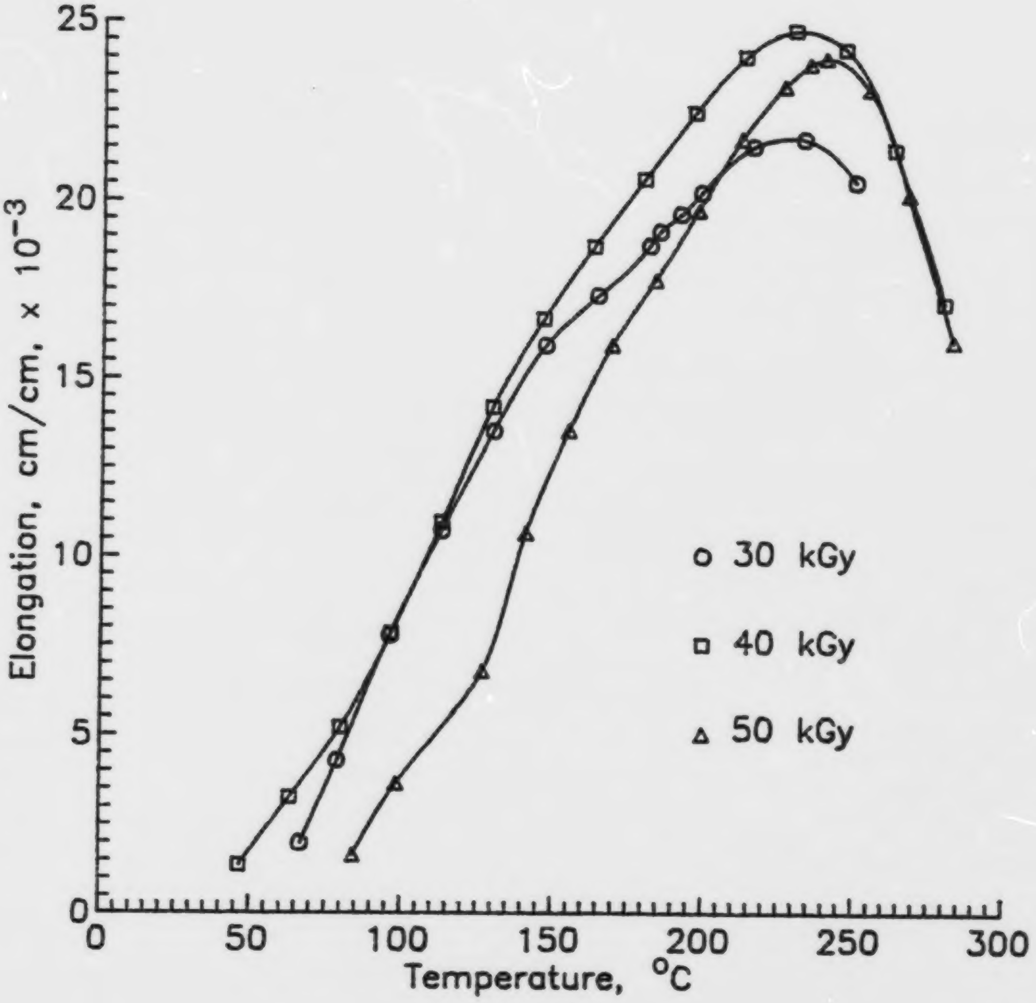

Fig. 3. Linear thermal expansion vs. temperature

Linear thermal expansion analysis confirmed that the DTA peak was due to polymer softening. Figure 3 is a plot of the elongation of the cured polymer (30, 40 and 50 kGy) as a function of temperature. The polymer softening point is affected only slightly by irradiation, increasing from about 228°C for the 30-kGy sample to about 237°C for the 50-kGy sample. The slope of each curve below 150°C, the linear thermal expansion coefficient, is also unaffected by irradiation up to 50 kGy. The expansion coefficient is approximately 1.7 x 10 cm/cm°C for all three polymer samples (30, 40 and 50 kGy). The elucidation of the effect of irradiation on the thermal expansion of the polymer above 150°C requires further investigation. The expansion curves in Figure 3 do not have any rapid slope increases, suggesting that the cured polymer may not have a detectable glass transition temperature (Tg). Differential scanning calorimetry (DSC) is being used at the present time in an attempt to detect a Tg for the polymer.

Miscellaneous

The density of the resin was 1.11 g/cm^3. Curing the resin with a radiation dose of 5.0 kGy (gel fraction ~ 85%) did not significantly affect the density. The viscosity of the resin was approximately 10 poise at 80°C. This viscosity is well above the required 100 centipoise limit for hot melt prepregging. Solvent prepregging, using methylethylketone was, therefore, the specified process for the program.

CONCLUSIONS

A radiation-curable polymer-carbon fiber prepreg material has been designed to meet the mechanical and physical property specifications set by a major aircraft company. The selected resin formulation is a mixture of epoxy diacrylate (50%), polybutadiene diacrylate (30%) and dipentaerythritol monohydroxypentaacrylate (20%) resins. A plain weave carbon fabric was selected for the prepreg material. A solvent process using methylethylketone was used to impregnate the fabric with about 35% (by mass) of the resin.

The maximum gel fraction for the cured polymer was about 85% at a radiation dose of 40 kGy in an air atmosphere. The gel point was at 2 to 3 kGy. X-ray diffraction showed that the polymer was amorphous and remained amorphous at 300°C. The softening point of the cured polymer varied from 228°C (30-kGy sample) to 237°C (50-kGy sample). The linear thermal expansion coefficient of the polymer was about 1.7×10^{-4} cm/cm°C up to 150°C and was independent of the curing dose up to 50 kGy.

Table 4. Industrial Carbon Fabric - Epoxy Prepreg Laminate Specifications[1]

Property	ASTM[2] No.	Temperature[3] (°C)	Minimum[4] Average	Minimum Value
Ultimate Tensile Strength (MPa)	E4	20-130	1275	1100
Tensile Modulus (GPa)	E4	20-130	145	117
Tensile Strain (-cm/cm)	E4	20	9500	7500
		130	9000	7000
Ultimate Compression Strength (MPa)	D695	20	1140	1030
		70	1070	900
		130	930	760
Compression Modulus (GPa)	D695	20-130	131	97
Compression Strain (cm/cm)	D695	20	8500	-
		70	7700	-
		130	7000	-
Wet Compression Strength (mPa)[5]	D695	20	483	345
		70	414	310
		130	241	172

(1) The laminate contains 14 plys all in the same fiber orientation (± 1°).

(2) American Standard of Testing and Materials.

(3) The time specified at the test temperature prior to the test is 10 ± 3 minutes for all dry test and 2 ± 1 minutes for all wet tests.

(4) At least five specimens are to be tested.

(5) Specimen conditioning: soaked in water at 71°C for 14 days prior to the test.

FUTURE WORK

The second phase of this experimental program is the characterization and mechanical and physical testing of the radiation-cured carbon-epoxy prepregs. All tests are being done by the accepted American Standard of Testing and Materials (ASTM).

The prepreg physical tests include measuring the resin content, volatile content, moisture content, resin flow and ply thickness. Table 4 lists the mechanical specifications for a 14-ply laminate made of carbon fabric-epoxy prepregs (BMS 8-212J, 1985). The radiation-curable prepregs will be used to produce a similar laminate for mechanical testing over the listed temperature range of 20 to 130°C (Table 4). Samples will be irradiated in a vacuum bag assembly. Each property listed in Table 4 will be measured for the radiation-cured laminate and the results will be compared with the specifications.

ACKNOWLEDGEMENT

The authors would like to thank the Sartomer Company for recommending the radiation-curable resin formulations, Hercules Incorporated for producing the prepregs with our specified resin and Dr. P. Hayward and Dr. E. Vance for their advice and technical support.

REFERENCES

1. A.Chapiro, "Radiation Chemistry of Polymeric Systems," Interscience Publishers, New York (1962).

2. T.F. Williams, "Fundamental Process in Radiation Chemistry," Ch.8, Interscience Publishers, New York (1968).

3. M. Dole, "The Radiation Chemistry of Macromolecules," Vols. 1 and 2, Academic Press, New York (1973).

4. J.E. Wilson, "Radiation Chemistry of Monomers, Polymers and Plastics," Marcel Dekker, New York (1979)

5. S.V. Nablo, Radiat. Phys. Chem.,25 (1985).

6. Proceedings of the 6th International Meeting on Radiation Processing, Ottawa, 1987, to be published in Radiat. Phys. Chem.

7. F.W. Billmeyer, Jr., "Textbook of Polymer Science," Wiley-Interscience, New York (1984).

8. H.R. Allcock and F.W. Lampe "Contemporary Polymer Chemistry," Prentice-Hall, Englewood Cliffs, New Jersey (1981).

9. R.S. Mellberg, "Radiation Processing," SRI International Research Report No. 618, California (1979).

10. R.A. Peters, "The Quiet Revolution: Electron Beam, Ultra-Violet and Other High Energy Radiation Processing," Omega Research Associates Report, Pittsburg (1984).

11. J. McKeown, IEEE Trans. Nucl. Sci., NS-32,5, 3292 (1985).

12. R.W. Singleton and R.J.T. Clabburn, Progress in Rubber and Plastics Technology, 2(2)10 (1986).

13. S. Ota, Radiat. Phys.Chem., 18 (1-2) 81, 1981.

14. S.A.H. Mohammed and J. Walker, Rubber Chem. Technol., 59(3) 482 (1986).

15. L.V. Dickson and A. Singh, "Radiation Curing of Epoxies," Proceedings of the 6th International Meeting on Radiation Processing, Ottawa (1987).

16. R.E. Fornes, J.D. Memory and N. Naranong, J. Appl. Polymer Sci., 26, 2061 (1981).

LONG-TIME MECHANICAL RELAXATION IN PARTICLE-POLYMER BLEND SYSTEMS

by

T. Masuda and L. Li
Kyoto University
Kyoto, Japan

(Manuscript not received on time. Please communicate with the authors.)

ROLE OF MORPHOLOGY AND COUPLING AGENT IN FRACTURE PERFORMANCE OF GLASS-FILLED POLYPROPYLENE

by

J. Denault and T. Vu-Khanh
National Research Council Canada
Industrial Materials Research Institute
75 De Mortagne, Boucherville, Que., Canada, J4B 6Y4

Presented at the 8th annual NRCC/IMRI symposium "Composites-'87",
November 5 and 6, 1987, Boucherville, Que., Canada

ROLE OF MORPHOLOGY AND COUPLING AGENT IN FRACTURE PERFORMANCE OF GLASS-FILLED POLYPROPYLENE

J. Denault and T. Vu-Khanh

National Research Council Canada
Industrial Material Research Institute
75, De Mortagne
Boucherville, Québec, Canada, J4B 6Y4

ABSTRACT

The effect of silane coupling agent on the morphology and fracture performance of particulates filled polypropylene was investigated. The onset of the crystallization at the filler matrix interface was observed by optical microscopy. This analysis shows that the silane alters the matrix morphology by inducing nucleation at the filler/matrix interface. This effect was attributed to the physisorbed layer of silane on the filler.

The fracture performance of the composites was analysed by the post yield fracture mechanics approach. The effect of coupling agent on the fracture performance was found to occur at a very low concentration whereas subsequent increase in silane concentration has no effect. Furthermore, the effect of coupling agent depends on concentration of filler. Silane treatment has a detrimental effect at low concentration of filler. However, at high concentration of filler, an improvement in the filler/matrix adhesion has a beneficial effect on the fracture performance. Two phenomena, the morphological effect and the competition between the contribution of the matrix/filler interface and the contribution of the matrix, were found to be possible explanations for the variation of K_{Rmax} with filler concentration and adhesion at the matrix/filler interface.

INTRODUCTION

The incorporation of fillers into polymers has been widely used commercially to improve the physical properties of the polymers for specific applications. The most commonly sought after improvements are strength and rigidity. For this purpose the adhesion between matrix and reinforcements is a very important parameter determining the mechanical performance of composites. The addition of coupling agent should promote adhesion in composites. The main function of the interface is to permit an efficient stress transfer from the matrix to the reinforcing filler.

However, the effect of coupling agent on fracture performance remains unclear. While the modulus and the strength increase, a reduction of the Izod fracture energy of mica-filled polypropylene in the presence of coupling agent has been noted (1). In practice, due to the propagation of cracks originating from flaws which exist in most structures, the performance of a given material is often related to its resistance to crack growth. In a previous study on the fracture behaviour of silane treated mica reinforced polypropylene (2) it was found that increasing the adhesion between mica flakes and matrix led to a decrease of the maximum crack growth resistance. This decrease in the fracture performance has been attributed to the reduction of the matrix ductility in the composite in the presence of coupling agent. The crack growth resistance of the composite was governed by a competition between voiding and stretching effects in the matrix. Voiding was formed under hydrostatic stress in the bulk region and drawing was promoted by shear plastic deformation around the filler boundary. A better interface could therefore increase the triaxiality of stress by reducing the matrix/filler debonding. Consequently, even though the debonding energy is increased by the use of coupling agent, the above effect can lead to a reduction in the fracture energy of the composite under certain conditions.

In the case of composites made with mineral fillers and a thermoplastic matrix, a concept of an interpenetrating network at the interface has been suggested (3,4) to be an important factor in the reinforcement mechanism. Following this concept the coupling agent/matrix interface is a diffuse boundary where intermixing takes place due to the penetration of the matrix into the coupling agent layer and the migration of the coupling agent molecules into the matrix phase. Consequently, in addition to the enhanced adhesion, the use of coupling agent can affect the morphology of the matrix and hence the mechanical performance of the interphase. It has been shown that interphase plays an important role in the mechanical performance of composites. The rigidity and strength of the latters are directly governed by the modulus and strength of the interphase (5,6).

The purpose of this work was to investigate in more detail the effect of coupling agent on fracture performance of the particulate-filled polypropylene.

EXPERIMENTAL

Materials

The polypropylene used in this study was an injection grade resin, Profax 6301, from Himont Canada Ltd. The resin was in powder form, and had a melt index of 12g/10 min (ASTM 1238). Milled glass fibers 1/32" and glass flakes (Hammer-milled Flake Glass 1/64") were obtained from Owens Corning Fiber Glass, Toledo, OH. The glass beads were obtained from Potters Industries, Laprairie, Quebec, grade No. 1922 (diameter 150-200 μm).

Dow Corning Z-6032 silane, having the chemical fromula $(CH_3O)_3$-Si-$CH_2CH_2CH_2NHCH_2CH_2NHCH_2$-ϕ-CH=$CH_2$.HCl and designated as N-β-(N-vinyl benzylamino) ethyl-γ-aminopropyl trimetoxy silane, was applied on the mineral fillers by the dry blend technique. A 10% solution of silane in methanol was pulverized on the glass fillers while blending in an Attritor mixer. This process was done at approximately 60°C to evaporate the methanol. To complete the condensation of silanol groups at the glass surface, the treated fillers were heated at 140°C for 10 minutes. The uncoated fillers were also stirred in the mixer to simulate the degradation of the fillers during the mixing.

Sample preparation

Polypropylene powders were dry blended with the glass fillers in a Welex high intensity mixer (Model ESK-80). The tensile specimens were injection molded (ASTM D638, Type I). For the fracture tests, three-point bend specimens of 3 by 12 by 60 mm were cut out from compression molded plates. The initial cracks (a_o) created with three-point-bend specimens were 4.8 mm long, giving a ratio of initial crack length to specimen width (a_o/D) of 0,4. A prenotch was first made by a saw cut and the final crack was created by forcing a razor blade into the specimen in a special jig on a laboratory press, giving a crack tip radius of less than 30 μm.

Mechanical Testing

All tests were performed on a standard testing machine (Instron Model 1125). The tensile tests were performed with a cross-head speed of 10 mm/min. The deformations were measured by a strain gage extensometer Instron, Model N° A325-242630-004, having a gage length of 1 inch. The tensile strength was determined as the maximum load divided by the initial section of the specimen.

The critical stress intensity factor during crack propagation was calculated using the calibration factor $f(a/D)$ for the three-point-bend specimens provided in (7):

$$K_R = \frac{PS}{BD^{3/2}} \left(\frac{a_{eff}}{D}\right) \tag{1}$$

where P is the load, S is the support span, B is the specimen thickness, D is the specimen width, and a_{eff} is the effective crack length which is the physical crack size augmented for the dimension of the plastic zone ahead of the crack tip. At each load level on the load-deflection diagram, the effective crack length (a_{eff}) was calculated from the

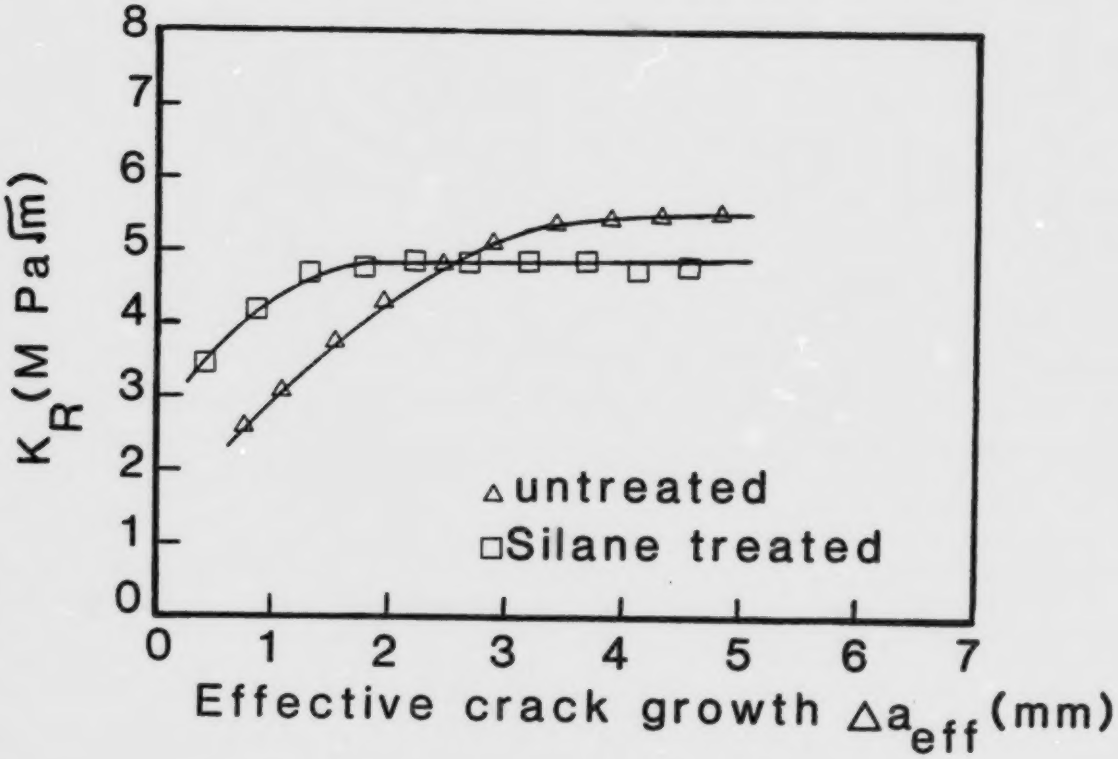

Figure 1 - Crack growth resistance vs effective crack extension for the silane treated and the untreated glass flakes polypropylene composites (30% of glass flakes).

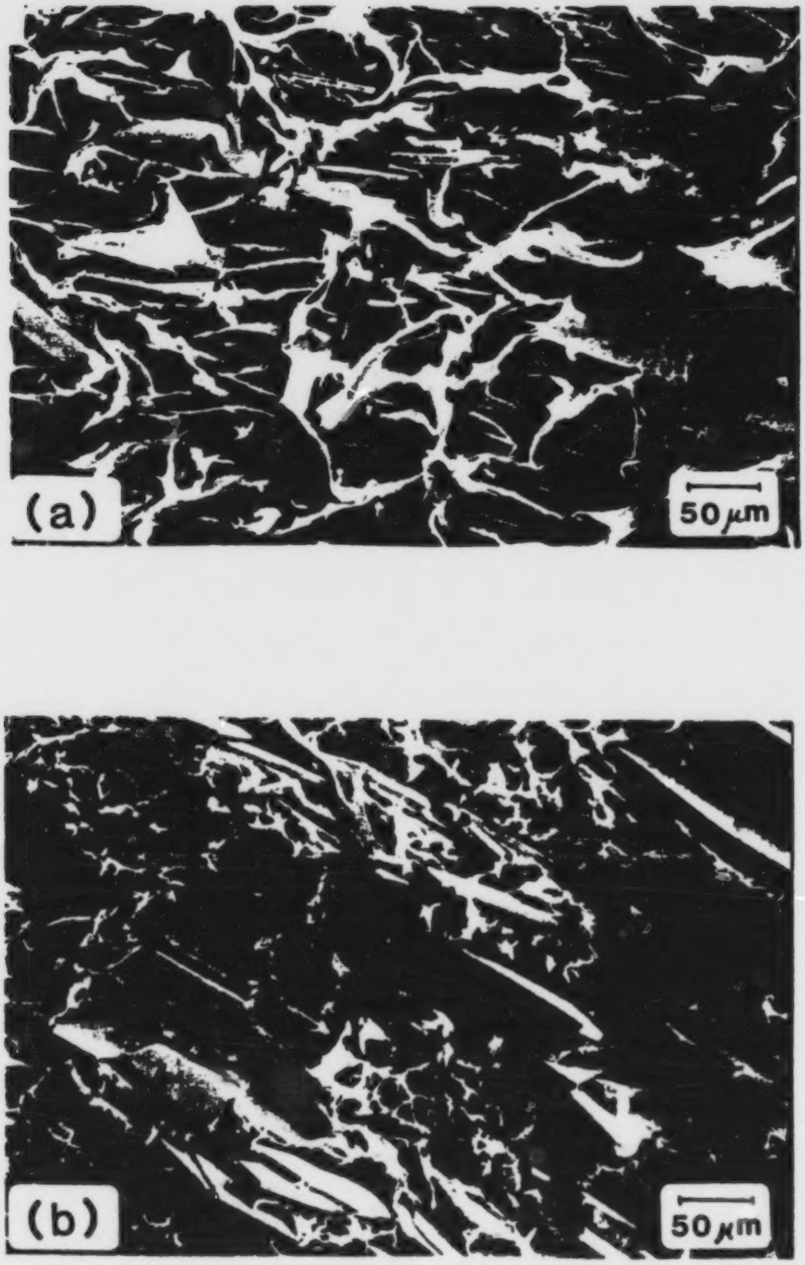

Figure 2 - Micrographs of fracture surface of polypropylene reinforced by 30% of: (a) untreated glass flakes and (b) silane treated glass flakes.

instantaneous compliance, C, determined by the secant passing through the origin of the load-deflection curve as discussed (8). The calculated critical stress intensity factor, which represents the crack growth resistance of the material, was then plotted as a function of effective crack growth Δa_{eff} ($a_{eff} - a_o$). For all the mechanical tests, an average value was determined from at least 4 samples.

Microscopy

A scanning electron microscope (Type Jeol 35CF) was used to examine the fracture surfaces of the composites. The optical microscope used was a Leitz/Wetzlar, Dialux 20. Micrographs of polypropylene crystallization at 120°C were taken with crossed polarizers in presence of filter.

RESULTS AND DISCUSSIONS

Figure 1 shows the effect of silane treatment on the crack growth resistance, K_R, as a function of the effective crack extension Δa_{eff} for the glass-flake reinforced polypropylene composite, containing 30% by weight of filler. It can be seen that the silane treatment decreases the maximum crack growth resistance of the composite as was previously observed in the case of silane treated mica polypropylene composite of the same composition. This reduction is in accordance with the previous observation of the microductility of particulates filled polypropylene (2,9-12). It was suggested that the microscopic plastic deformation of the matrix was promoted by the debonding at the interface between the filler and the matrix. The debonding permitted the matrix to deform away from the filler and to stretch. Better adhesion between the filler and the matrix can reduce the material's ability to debond at the interface and to deform.

Figure 2 shows the micrographs of the fracture surfaces of the untreated and the silane treated glass flakes reinforced polypropylene. In the case of treated glass flakes, the matrix stretching appeared less pronounced than in the case of untreated glass flakes. However, a close

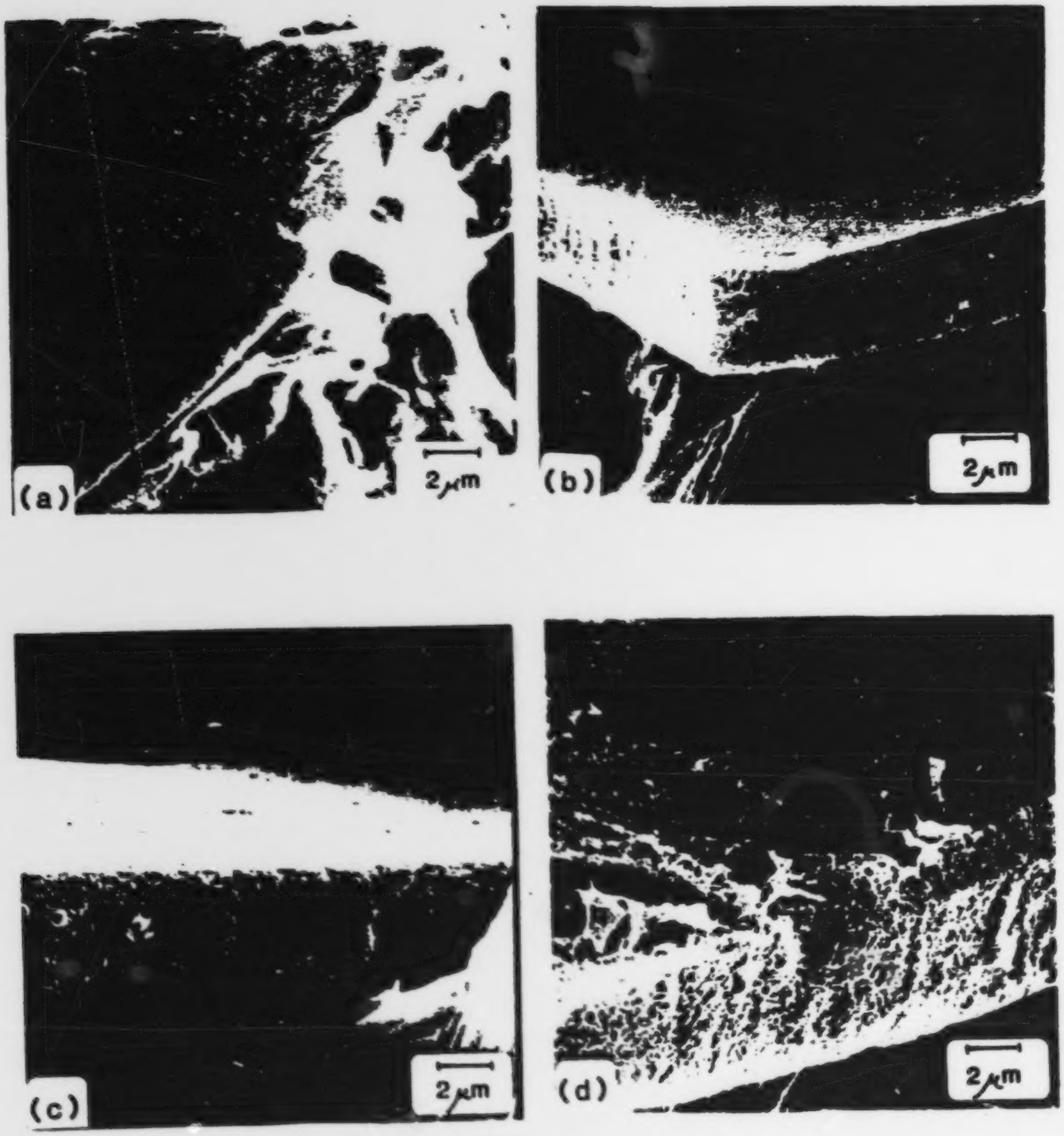

Figure 3 - Micrographs at high magnification of fracture surface of polypropylene reinforced by 30% of glass flakes treated with different concentration of silane coupling agent: (a) 0%, (b) 0,25%, (c) 0,4% and 0,8% (by weight of filler).

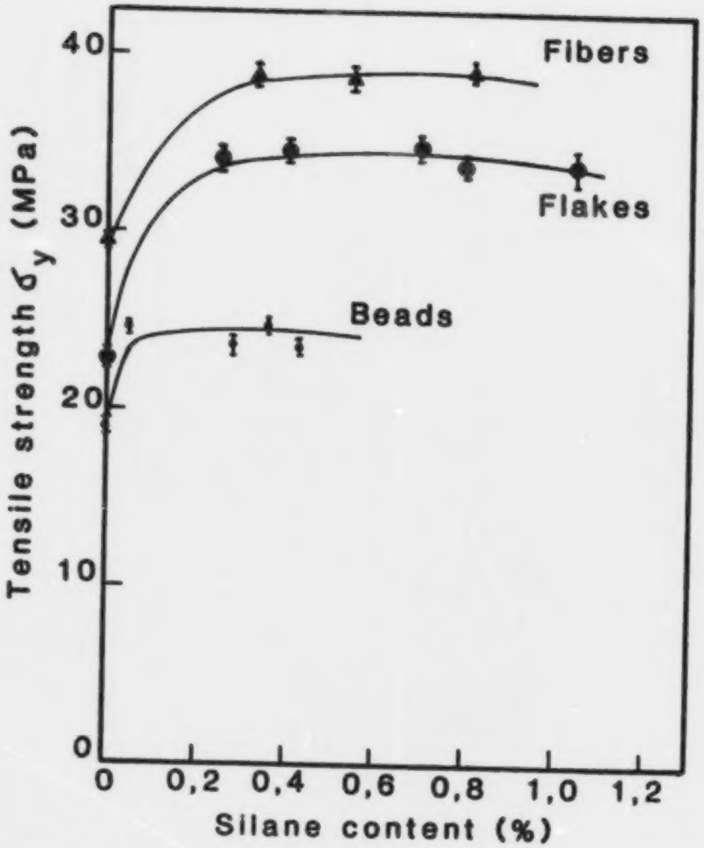

Figure 4 - Tensile strength of polypropylene reinforced by 30% by weight of glass-flakes, glass-fibers and glass beads as a function of silane concentration.

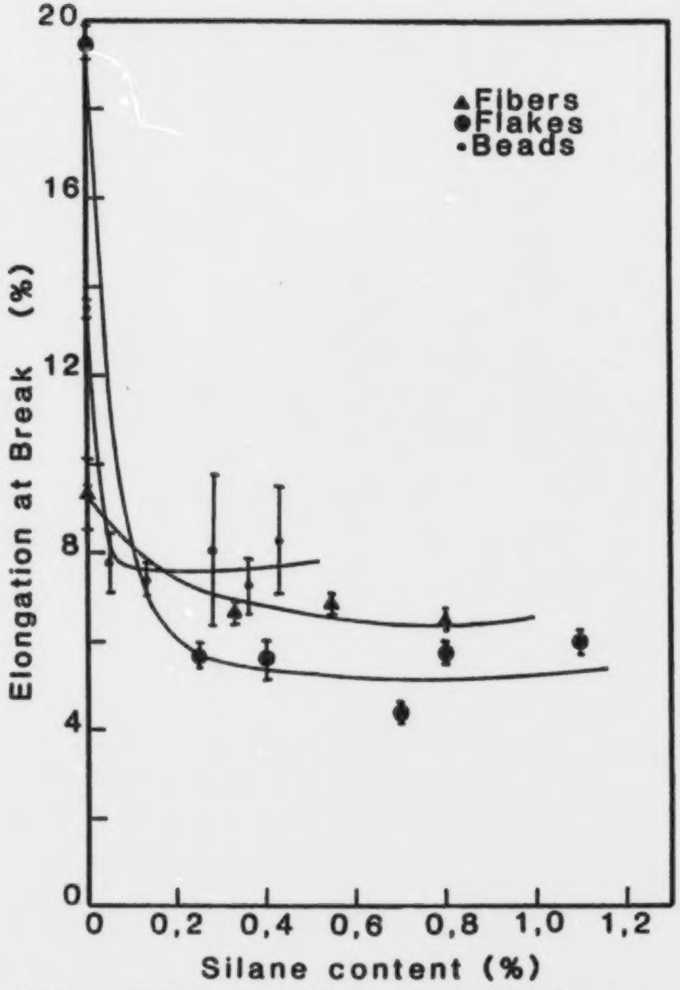

Figure 5 - Percentage of elongation at break of polypropylene reinforced by 30% by weight of glass-flakes, glass-fibers and glass beads as a function of silane concentration.

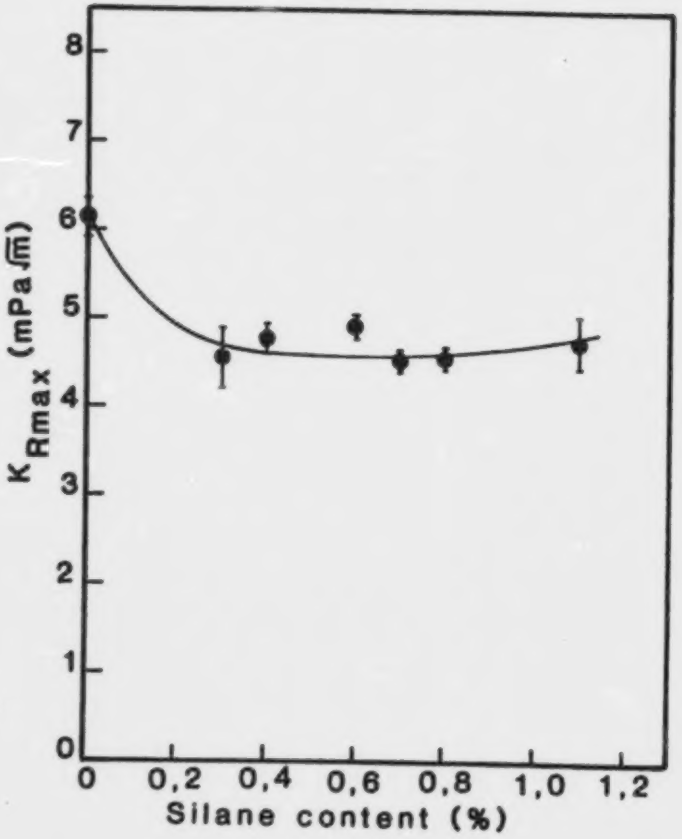

Figure 6 - Maximum crack growth resistance of polypropylene reinforced by 30% by weight of glass-flakes as a function of silane concentration.

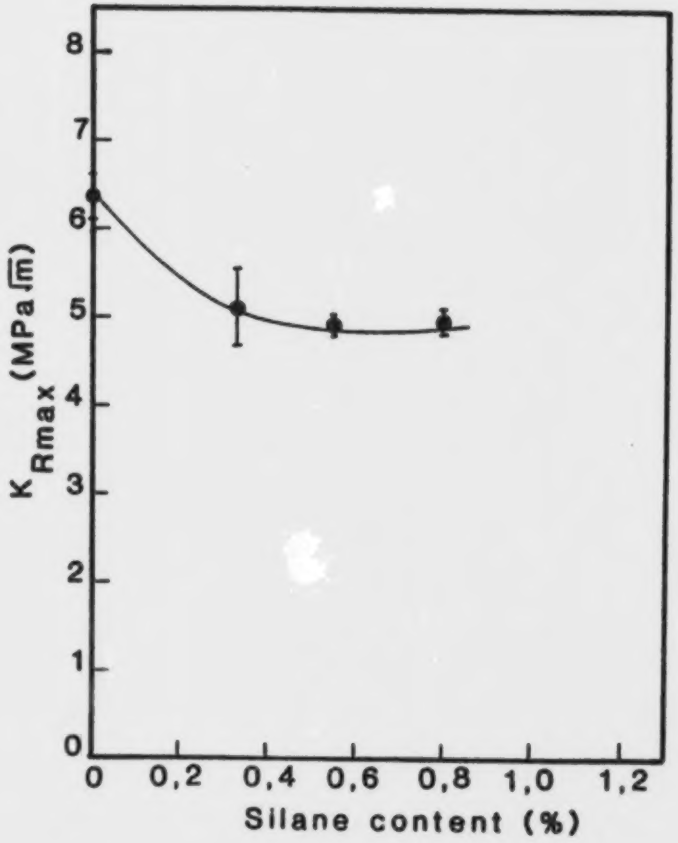

Figure 7 - Maximum crack growth resistance of polypropylene reinforced by 30% by weight of glass fibers as a function of silane concentration.

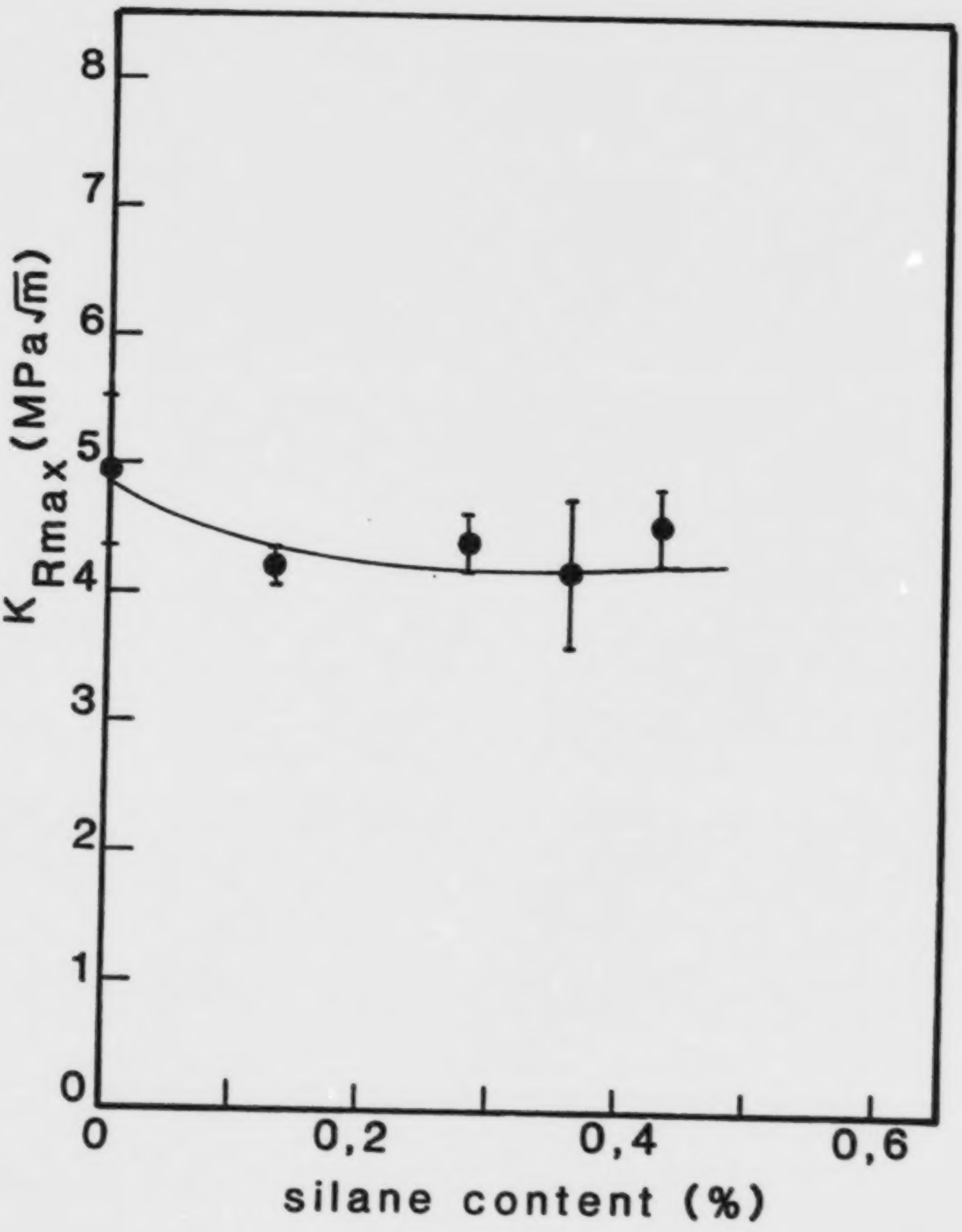

Figure 8 - Maximum crack growth resistance of polypropylene reinforced by 30% by weight of glass-beads as a function of silane concentration.

examination of the interphase revealed that in the presence of coupling agent, there is a microscopic drawing of the matrix at the interface.

The fracture surfaces of glass flakes reinforced polypropylene treated with different amounts of silane coupling agent is shown at high magnification in Figure 3. In the case of untreated glass flakes the surface of the fillers after fracture appears very clean. However, in the case of silane treated filler it is possible to observe that the matrix adheres to the filler after fracture. The amount of matrix remaining on the filler surface seems to depend on the amount of silane added to the filler. Increasing the concentration of silane in the composites leads to more residu on the fillers. The matrix remaining on the filler surface exhibits a microscopic drawing, suggesting that there is a strong interaction between the filler and the matrix. These microscopic observations lead to the conclusion that increasing the amount of silane on the filler gives an extension of the interfacial effect to the bulk of the matrix as suggested by the concept of an interpenetrating network.

Effects of Silane concentration

The effects of silane-coupling-agent concentration on the tensile strength and on the elongation at break of the composite for different classes of reinforcement with composition of 30% by weight of filler is shown in Figures 4 and 5 respectively. Figures 6 to 8 show the variation of the maximum crack growth resistance as a function of silane concentration for the same classes of reinforcement. For all filler types, the addition of coupling agent increases the tensile strength, reduces the percentage of elongation at break and the maximum crack growth resistance. The effects of coupling agent occur at very low concentration. As the concentration of coupling agent increases, the above parameters rapidly attain a plateau region in which the variation of silane concentration has no effect on the mechanical performances of the composites. The plateau region is reached at lower fraction of silane in the case of beads, due to the fact that the surface occupied by the beads is much lower than that of flakes and fibers. Surprisingly enough,

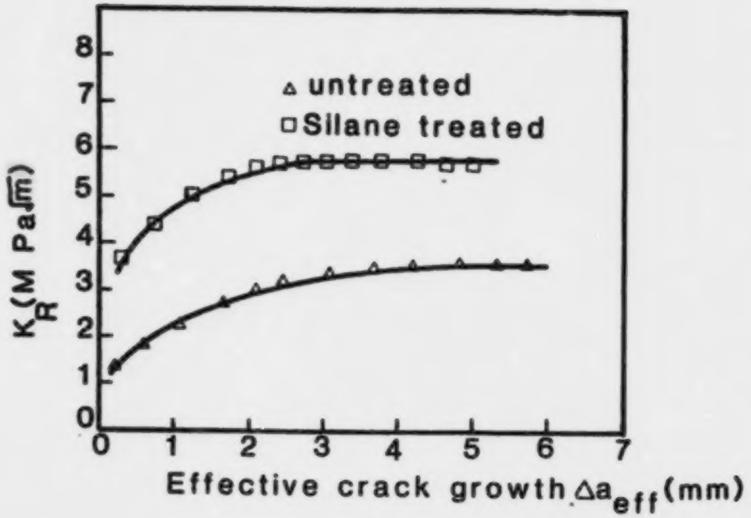

Figure 9 - Crack growth resistance vs effective crack extension for the silane treated and the untreated glass flakes polypropylene composites (70% of glass-flakes).

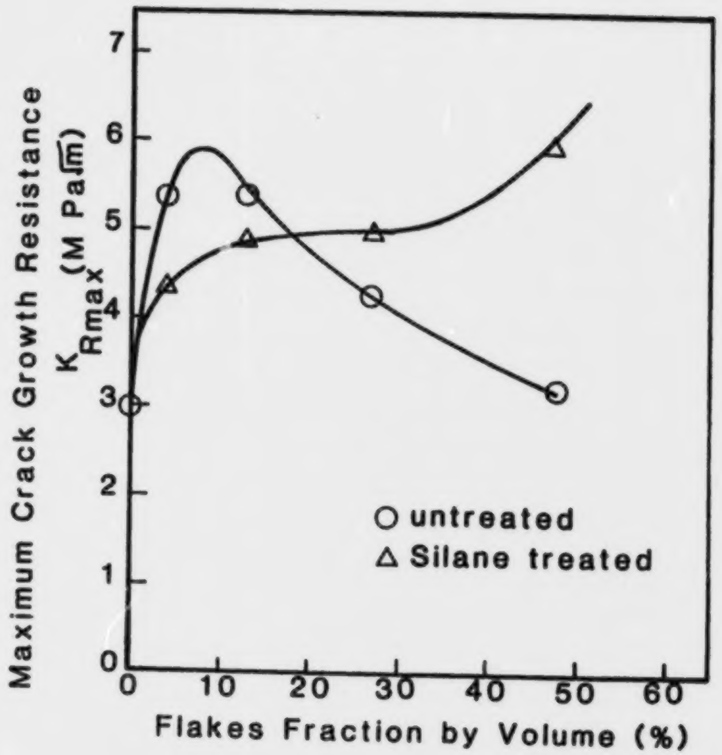

Figure 10 - Maximum crack growth resistance as a function of filler concentration for the untreated and the silane treated glass-flakes reinforced polypropylene.

extending the interfacial effect by increasing the amount of silane on the fillers does not affect the mechanical properties as in Figures 4 to 8.

Effect of filler concentration

The previous work (9,11) on the microductility of particulated filled polypropylene has shown that the fracture performance also depends on the concentration of filler. The maximum crack growth resistance of mica and glass flakes polypropylene composites shows an optimum value as a function of filler concentration. Adding fillers to polypropylene results in a significant improvement in crack propagation resistance at low concentration. However, as the filler fraction is increased, the effective amount of the matrix material is reduced, resulting in a reduction of the energy dissipated in the plastic deformation of the matrix and therefore a decrease of the fracture energy of the composite. In such a situation, one could expect that better filler/matrix adhesion would have a beneficial effect on the fracture performance of the composites. Measurements were made on composites containing 70% by weight of glass flakes. Figure 9 shows the comparison between the untreated and silane treated glass flake composites. It demonstrates that silane treatment indeed results in a strong increase in the crack growth resistance of the composite.

This result can be qualitatively explained in terms of the simple rule of mixture in the same manner as that which has been used to explain the thickness effect (13). Considering the case of a completely random system of fillers of any shape, from the law of mixture, the maximum crack growth resistance of the composite can be expressed, as a first approximation, in the form:

$$K_{Rmax} = K_m(\phi) + (K_i - K_m(\phi))\,\phi \qquad (2)$$

in which ϕ is the filler volume fraction, K_i represents the contribution of the matrix/filler interface to the crack growth resistance and $K_m(\phi)$ is that of the matrix, which is actually a function of the filler volume

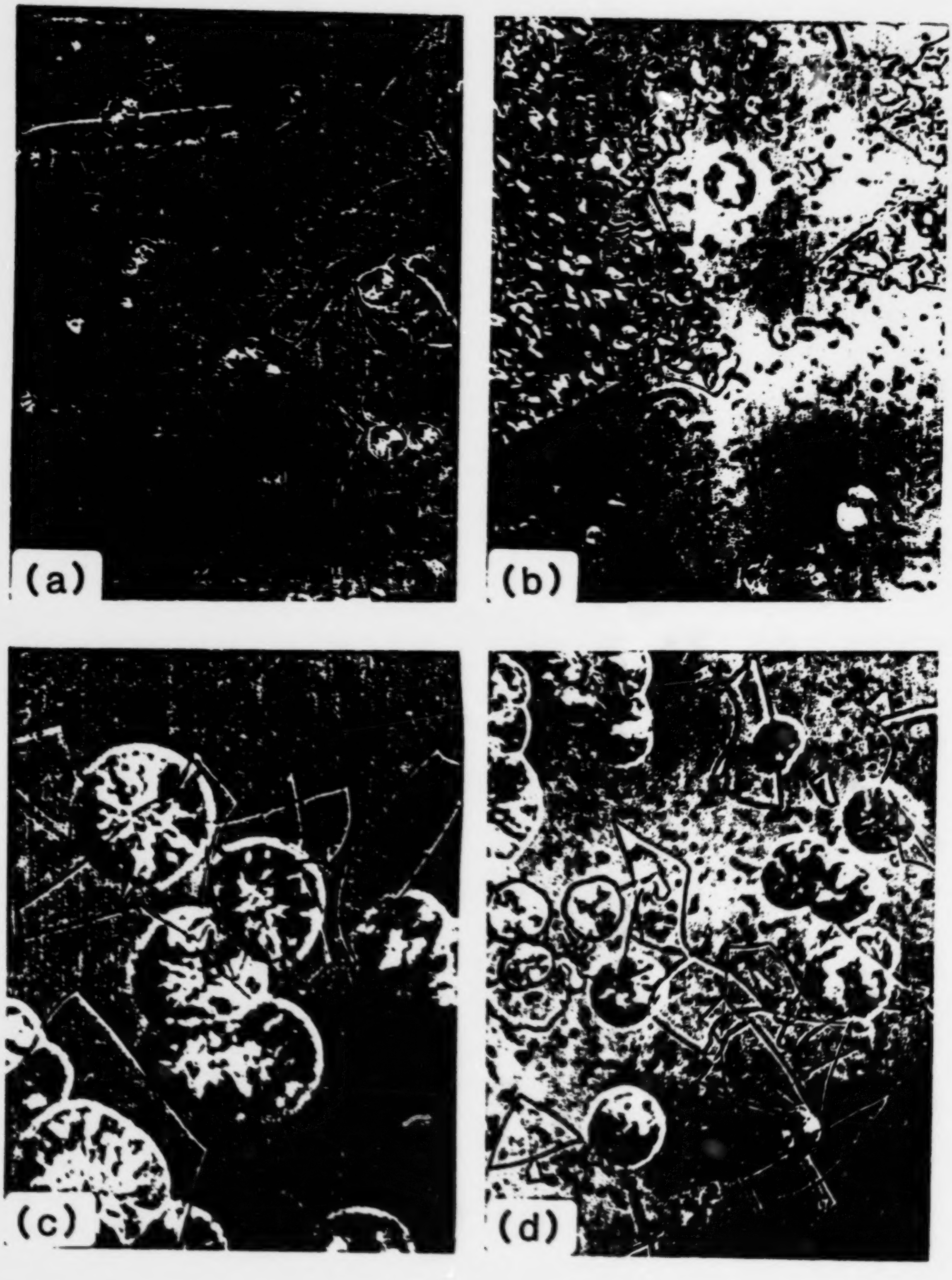

Figure 11 - Micrograph of the onset of crystallization of polypropylene in the presence of: (a) untreated glass-flakes, (b) dry blend silane treated glass-flakes, (c) solution treated glass-flakes and (d) dry blend silane treated glass-flakes boiled in water for 2 hours.

fractions. From the above expression, it can be seen that when K_i is higher than $K_m(\phi)$, K_{Rmax} could increase with filler concentraton. Measurements made on silane-treated-glass-flake composites at various concentrations are summarized in Figure 10. The result confirms the form eq. (2), showing an increase in K_{Rmax} with ϕ at high concentration, as apposed to that observed in the case of untreated filler. At low volume fraction, the contribution of K_i is small with respect to that of $K_m(\phi)$. The rise in K_{Rmax} is mainly due to a rise in $K_m(\phi)$ with increasing ϕ. The result also seems to show a region in which $dK_{Rmax}/d\phi = 0$ at $\phi \sim 25\%$. This volume fraction also seems to correspond to the transition between detrimental and beneficial effects of the filler/matrix adhesion. Above this volume fraction, since $K_m(\phi)$ decreases with increasing ϕ due to a reduction in the effective amount of the matrix material as discussed earlier, K_{Rmax} increases strongly with ϕ. The competition between K_i and $K_m(\phi)$ could therefore be a good explanation for the variation of K_{Rmax} with filler concentration and adhesion at the matrix/filler interface.

However, it is worth noting that the above process is not the only possible explanation. It is well known that coupling agent affects the matrix morphology. The change in morphology, induced by the presence of silane, can also be responsible for the variation in K_{Rmax}.

The effect of the silane treatment on the matrix morphology was investigated by optical microscopy. Figure 11a) shows the optical microscopic observation of the onset of the crystallization of polypropylene in presence of untreated glass flakes. The untreated glass flakes do not act as nucleating sites since no specific crystallization can be observed on the glass flakes, and the crystallization begins in the bulk of the matrix. However, when silane coupling agent is added it is possible to observe a preferential crystallization on the fillers (Figure 11b) and hence the treated glass flakes act as nucleating sites. It can therefore be concluded that changes in the matrix morphology possibly play a role in the variation of K_{Rmax}.

On the other hand, the observed silane-induced nucleating effect is rather surprising since it has been demonstrated that silane inhibits the nucleating effect of mica in polypropylene (14). These opposite effects could be explained by the following differences: firstly, the composition of mica and glass-flake fillers and secondly the method used to apply silane. In the previous study (14), the silane was applied to the mica by solution treatment whereas the dry blend technique was used in the present work. To adequately compare these two systems, the glass flakes were treated by immersion in a 2% aquous solution of the silane. Figure 11 c) shows the onset of the crystallization of polypropylene in presence of glass flakes treated in solution. When applied from solution, the silane coupling agent does not induce crystallization on glass flakes. Hence we can conclude that the silane coupling agent may affect the morphology of the polypropylene matrix at the interface depending upon the method used to apply silane. The principal difference between the solution and the dry blend treatment is in the structure adopted by the silane molecules at the filler surface. It has been found (15,16), that dry blend results in a major portion of physisorbed silane leaving approximately a monolayer quantity of chemisorbed silane whose coverage on the filler surface is imperfect. The solution treatment results in a more uniform coverage and, although it has been well established that a significant amount of physisorbed silane exists on the solution treated fillers, dry blend increases the content of the physisorbed silane dramatically. It is, however, possible to extract the physisorbed layer of silane without removing the chemisorbed layer by boiling the treated fillers in water for two hours (17). The microscopic observation of polypropylene crystallization in the presence of the dry blend silane treated glass flakes after the extraction of its silane physisorbed layer is shown in Figure 11 d). The extraction of the physisorbed layer of silane inhibits the nucleating ability of the dry blend silane treated glass flakes. From this latter observation it can be concluded that the morphological changes observed at the polypropylene/glass flake interface can be attributed to the physisorbed layer of silane. So, the next part of this work will be the investigation of the morphological effect on K_{Rmax}.

SUMMARY AND CONCLUSION

The addition of silane coupling agent glass-flakes polypropylene composites containing 30% by weight of filler increases the tensile strength and decreases the elongation at break as well as the maximum crack growth resistance. The effects of coupling agent occur at a very low concentration and the mechanical properties rapidly reach a plateau region where the subsequent variation of silane concentration has no effect. This result was obtained in spite of an extension of the interfacial effect produced by an increase of the silane concentration on the filler as observed on the fracture surfaces of these composites.

However, it was found that the effect of silane is dependent on the filler concentration in the composite. In fact, an increase in the filler/matrix adhesion modified the fracture behavior of glass-flakes polypropylene composites. The maximum crak growth resistance of the untreated glass flake composites shows an optimum value as a function of filler concentration, whereas silane treatment results in a continuous increase. The results also showed that the improvement in the adhesion between filler and matrix has a beneficial effect on the fracture performance at high filler concentrations. This result has been qualitatively explained in terms of the simple mixture's law. The competition between the contribution of the matrix/filler interface and the contribution of the matrix, which is a function of the filler volume fraction was found to be a good explanation for the variation of K_{Rmax} with filler concentration and adhesion at the matrix/filler interface.

In addition to the adhesion effect, the presence of coupling agent was found to modify the morphology at the filler/matrix interface. However, this effect seems to depend on the method used to apply silane. When the silane coupling agent is applied to the filler by the dry blend technique it was found to induce nucleation in the glass flake polypropylene composite, while the slurry treament seems to produce no morphological change at the filler matrix interface. It was demonstrated that the nucleation ability of the dry-blend-silane-treated glass flakes can be attributed to the large amount of physisorbed silane present on the filler.

It is assumed that the morphological change at the filler/matrix interface produced by the silane coupling agent applied by the dry blend technique can also be responsible for the variation in K_{Rmax}. Further studies are needed to understand the effect of matrix morphology on the fracture performance of these composites.

REFERENCES

1. C. Busigin, R. Lahtinen, G.M. Martinez, G. Thomas and R.T. Wookhams, Polym. Eng. Sci., 24, 169 (1984).
2. T. Vu-Khanh and B. Fisa, Polym. Comp., 7, 219 (1986).
3. E.P. Plueddemann and G.L. Slark in "Proc. 35th Ann. Tech. Conf. Reinf. Plastics/Composites Div.", SPI, Section 20-B (1980)
4. H. Ishida, J.L. Koening, J. Polym. Sci., Phys., 18, 1931 (1980).
5. M. R. Piggott, Composites 86 Symposium, NRCC/IMRI, Boucherville, Québec, Canada, pp.1.1-1.21, Nov. 25-26 (1986).
6. P.S. Theocaris, Adv. Polym. Sci., 66, 149 (1985).
7. E 399 Standard Test Method for Plane Strain Fracture Toughness of Metallic Materials, Annual Book of ASTM Standards (1983).
8. T. Vu-Khanh, B. Sanschagrin, and B. Fisa, Composites 85 Symposium, NRCC/IMRI, Boucherville, Québec, Canada, pp.9.1-9.47, Nov. 20 (1983).
9. T. Vu-Khanh, B. Sanschagrin, and B. Fisa, Polym. Comp., 6, 249 (1985).
10. T. Vu-Khanh and B. Fisa, Polym. Comp., 7, 375 (1986).
11. T. Vu-Khanh, S.P.E. Techn. Papers, 33, 503 (1987).
12. T. Vu-Khanh and B. Fisa, S.P.E. Techn. Papers, 31, 1145 (1985).
13. J.G. Williams, "Fracture Mechanics of Polymers", John Wiley & Sons, New York (1984).
14. A. Garton, S.W. Kim and D.M. Wiles, J. Polym. Sci., Polym. Let. Ed., 20, 273 (1982).
15. K.D. Kilnari and E.D. Goddard in "Proc. 35th An. Tech. Conf., Reinf. Plastics/Composites Div.", SPI, Section 20-E (1980).
16. H. Ishida, Polym. Comp., 5, 101 (1984).
17. B.D. Favis, L.P. Blanchard, J. Leonard and R.E. Prud'Homme, J. Appl. Polym. Sci., 28, 1235 (1983).

FIGURE CAPTIONS

Figure 1 - Crack growth resistance vs effective crack extension for the silane treated and the untreated glass flakes polypropylene composites (30% of glass flakes).

Figure 2 - Micrographs of fracture surface of polypropylene reinforced by 30% of: (a) untreated glass flakes and (b) silane treated glass flakes.

Figure 3 - Micrographs at high magnification of fracture surface of polypropylene reinforced by 30% of glass flakes treated with different concentration of silane coupling agent: (a) 0%, (b) 0,25%, (c) 0,4% and 0,8% (by weight of filler).

Figure 4 - Tensile strength of polypropylene reinforced by 30% by weight of glass-flakes, glass-fibers and glass beads as a function of silane concentration.

Figure 5 - Percentage of elongation at break of polypropylene reinforced by 30% by weight of glass-flakes, glass-fibers and glass beads as a function of silane concentration.

Figure 6 - Maximum crack growth resistance of polypropylene reinforced by 30% by weight of glass-flakes as a function of silane concentration.

Figure 7 - Maximum crack growth resistance of polypropylene reinforced by 30% by weight of glass fibers as a function of silane concentration.

Figure 8 - Maximum crack growth resistance of polypropylene reinforced by 30% by weight of glass-beads as a function of silane

Figure 9 - Crack growth resistance vs effective crack extension for the silane treated and the untreated glass flakes polypropylene

Figure 10 - Maximum crack growth resistance as a function of filler concentration for the untreated and the silane treated glass-flakes reinforced polypropylene.

Figure 11 - Micrograph of the onset of crystallization of polypropylene in the presence of: (a) untreated glass-flakes, (b) dry blend silane treated glass-flakes, (c) solution treated glass-flakes and (d) dry blend silane treated glass-flakes boiled in water for 2 hours.

USE OF WOOD FIBERS IN THERMOPLASTIC COMPOSITES: VI. ISOCYANATE AS A BONDING AGENT FOR POLYETHYLENE-WOOD FIBER COMPOSITES

by

R.G. Raj, B.V. Kokta, D. Maldas and C. Daneault
Centre de recherche en pâtes et papiers
Université du Québec à Trois-Rivières
C.P. 500, Trois-Rivières, Québec, Canada, G9A 5H7

Presented at the 8th annual NRCC/IMRI symposium "Composites-'87",
November 5 and 6, 1987, Boucherville, Que., Canada

USE OF WOOD FIBERS IN THERMOPLASTIC COMPOSITES: VI. ISOCYANATE AS A BONDING AGENT FOR POLYETHYLENE - WOOD FIBER COMPOSITES

by

R.G. RAJ, B.V. KOKTA, D. MALDAS AND C. DANEAULT
Centre de recherche en pâtes et papiers
Université du Québec à Trois-Rivières
C.P. 500, Trois-Rivières, Québec
G9A 5H7

ABSTRACT

Linear low density (LLDPE) and High density (HDPE) polyethylenes were reinforced with wood fibers of aspen chemithermomechanical (CTMP) pulp. The different isocyanates (i) polymethylene (polyphenyl isocyanate), (ii) Toulene -2-4- diisocyanate, (iii) 1-6 Hexamethylene - diisocyanate and (iv) Ethyl isocyanate used as bonding agents improved the tensile properties of the composites. HDPE performed better in comparison with LLDPE composites. Also, shorter fibers (mesh size 60) produced higher tensile strength and modulus in HDPE. The comparison of HDPE reinforced with aspen, mica and glass fibers showed the effectiveness of wood fibers interms of their cost and performance.

INTRODUCTION

The use of cellulose fibers as a reinforcement has been limited in comparison with mineral and glass fibers[1]. The performance of the composite material depends significantly on the type of bonding between the reinforcing fiber and matrix. This is greatly influenced by the role of interface which is often the short fall of wood fibers as reinforcing fillers in thermoplastics. On the other hand, the wood fibers posses strength and modulus properties which compare favorably with glass fibers when one considers the density of the fibers[2]. In addition the cellulose fibers have a number of advantages such as cost, light weight and little damage during processing[3].

The use of cellulose fibers in polymer composites was reviewed by Seymour[4] who used wood flour as a reinforcement in different polymers including high density polyethylene and polypropylene. Schneider and Brebner[5] studied the chemical modification of wood by alkoxysilane coupling agents. They reported good dimensional stability and antishrink efficiencies comparable to other chemical wood modifiers. The mechanical properties of silane treated wood pulps and polyethylene grafted wood pulps with low density polyethylene was compared by Kokta et al.[6]. They found the grafted CTMP fibers improved the mechanical properties of the composite by a factor of 2.6 for modulus, 2.3 for stress and 2.1 for energy at yield.

Self-bonding of wood particles with the addition of 2.5%-5.0% of synthetic resins (phenol-formaldehyde and isocyanate) was reported by Avella and de Lhoneux[7]. They found enchanced swelling resistance and flexural strength with isocyanate resin. Activation of wood surface by different methods of bonding and their effect in the variation of mechanical properties of the products were studied by Zavin[8]. The chemistry of diisocyanates, and possible reactions as wood binders were reviewed by Johns[9] who also examined the reasons for the excellent bonding efficiencies of disocyanates. Different methods of mixing the cellulosic fibers with polyethylene and polypropylene and their influence on mechanical properties of the composites was studied by Michell et al.[10]. They found the flexural modulus at different humidity levels showed improvement compared to polymer.

In the present investigation, the use of various isocyanates as bonding agent for wood fibers (aspen) and polyethylene (low density and high density) was studied. The effect of isocyanate type on mechanical properties of the composites was also examined. A comparative study on other types of reinforcements, such as mica and glass fiber with polyethylene was also carried out.

Table 1. Typical properties of polyethylenes as supplied by manufacturer

Physical properties	LLDPE GR-0534-A	LLDPE GF-0118-A	HDPE GRSN-8907
Density (g/cm^3)	0.934	0.918	0.954
Melt index (g/10min)	5.0	1.0	7.5
Tensile strength (MPa) at maximum load	15.8	40.0	--
Elongation at maximum load (%)	620	600	--
Secant modulus at 1% elongation (MPa)	427	220	--

Table 2. Preparation conditions and properties of aspen pulp

Cooking conditions		Properties	
Temperature max (°C)	126	Drainage index (CSF), ml	119
Retention time (min)	5	Brightness, Elrepho (%)	60.9
Pressure (psig)	20	Opacity, (%)	91.4
Na_2So_3 (%)	5	Breaking length, km	4.46
NaOH (%)	5	Elongation (%)	1.79
pH	12.9	Tear index, mN.m^2/g	7.20
Consistance during refining (%)	23.9	Burst index, KPa.m^2/g	2.59
Refining energy, MJ/kg	5.15	Yield (%)	92.0
Refiner output, kg/h	45.6	Kappa index No	121.7
		Lignin (%)	17.9

EXPERIMENTAL

Materials

The different types of polyethylene used in this study, linear low density polyethylenes (LLDPE), Novapol LLGR-0534-A and Novapol LLGF-0118-A and a high density polyethylene (HDPE) GRSN-8907 were supplied by Novacor Chemicals Ltd.. The reported properties of polyethylenes are summarized in Table 1.

The chemithermomechanical pulp (CTMP) of aspen used for reinforcing the polyethylene was prepared in a Sund Defibrator under the conditions listed in Table 2.

Mica-200-NP-Suzorite (200 mesh, coated) was supplied by Marietta Co., Montreal and Glass fibers 731 BA 1/32 (0.8 mm, coated) was supplied by fiber glass of Canada via Mia chemicals, Montreal.

The following isocyanates were used as bonding agent between the polymer and wood fibers:

i) Polymethylene (polyphenyl isocyanate)
ii) Toulene -2-4-diisocyanate

iii) 1-6 Hexamethylene diisocyanate

iv) Ethyl isocyanate

The isocyanates were supplied by polysciences Inc. All chemicals utilized in this work were used as supplied by the manufacturers.

Fiber treatment

The CTMP aspen pulp was dried at 55°C in an air circulating oven before it was ground to mesh size 60 mixture. The composition of the mixture has the following fiber sizes: 60.5% mesh 60, 20.2% mesh 80, 15.5% mesh 100, and 3.5% mesh 200.

Isocyanate treatment

The treatment of isocyanate was carried out either by direct mixing with polymer or by using it with coated wood fibers.

In the first case, the isocyanate was added (3.0% by weight based on polymer) directly to the polymer (45 g) and mixed thoroughly, then the fibers were added at 0-40 weight fractions.

Coated fibers

The aspen fibers were coated with different chemical agents in a roll mill (C.W. Barbender Laboratory prep. mill, No. 065).

Aspen coated fibers [1]

A typical coating mixture consists of aspen fibers (mesh size 60, 15g), isocyanate (9.0% by weight based on fiber), polymer (HDPE or LLDPE, 4.5 g) and 2.0 g of maleated propylene wax (Eastman chemical E 43) added gradually in a preheated roll mill at 165°C.

Mixing was carried out 4-5 times with re-mixing to achieve better dispersion. Then the coated fibers were ground to mesh size 20.

Aspen coated fibers [2]

The aspen fibers were mixed with maleic anhydride (1.0 g) polymer (HDPE or LLDPE, 4.5 g) and di-t butyl peroxide (0.3 g) which serve as an initiator. The mixing was done in a roll mill at 160°C and then the fibers were ground to 20 mesh size.

Aspen coated fibers [3]

In this case, the amount of maleic anhydride was increased (4.5 g) along with the initiator concentration (0.8 g). The polymer (HDPE or LLDPE, 4.5 g) was added to the mixture and the aspen fibers were coated at 160°C in a roll mill and then finally ground to 20 mesh size.

Preparation of Composites

The aspen fibers were mixed at different weight fractions (0-40%) with polymer (LLDPE or HDPE) and extruded in a laboratory CS1 Max Mixing Extruder (Model CS194) at 150°C to 160°C. The extruded samples were ground to 20 mesh size.

The above mixture was molded into shoulder type tensile test specimens (24 at the same time) in a mold which was covered by metal plates on both sides. The specimens were molded at a temperature of 150°C for 15 minutes with a pressure of 3.3MPa. The samples were taken out after 15 minutes of cooling to room temperature with the pressure maintained during the process. The same procedure was used for mica and glass fiber composites.

Mechanical tests

The tensile properties of the composites were measured using an Instron (Model 4201) according to ASTM D638 method. The properties reported were measured at yield point. The secant modulus was based on an original point defined by force 5N, and other points defined by load at set elongation (LASE) 0.1, 0.5, 1.0 and 5.0 percent. The full-scale load was 500 N, gauge length 17 mm, and a cross-head speed of 10 mm/min was used. Typical specimen dimensions were: 17.0 mm between grips, 3.267 mm in width, and 1.545 mm in thickness.

At least four specimens were tested each time with 6 to 8 specimens in most cases. The properties measured by Instron 4201 were automatically calculated by HP86B using the Instron 2412005 General Tensile Test Program. Average coefficients of variation for mechanical properties were as follows: stress, 3.8%-7.2%; strain, 4.3%-6.9%; energy, 5.4%-8.1%; modulus 2.3%-5.8%.

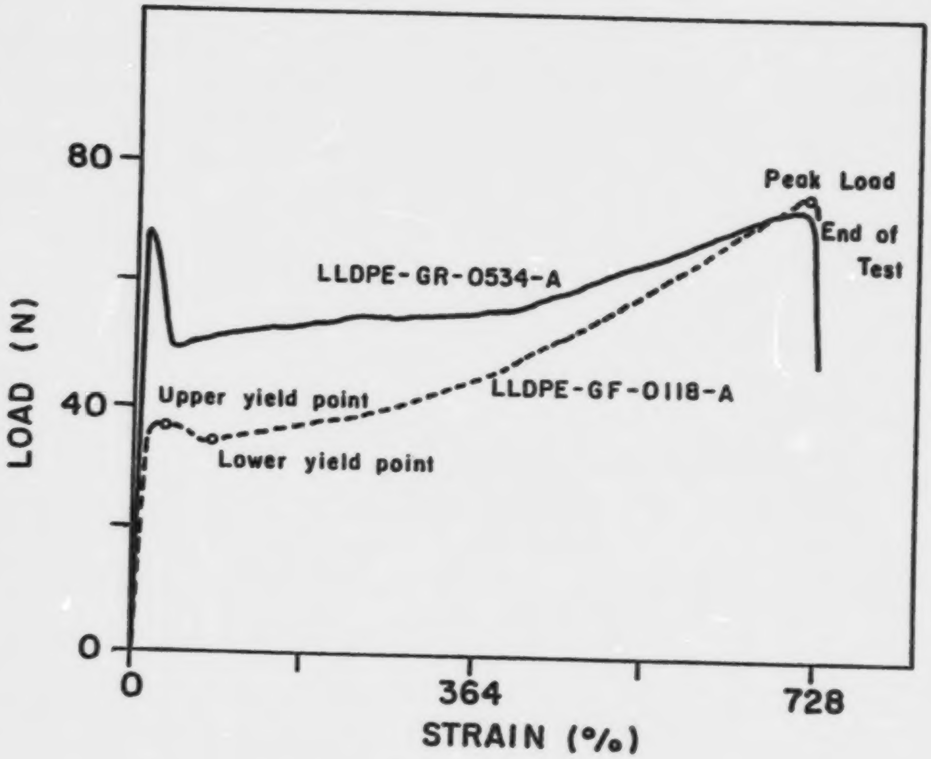

Fig. 1 Load vs strain curves for LLDPE-GR-0534-A and GF-0118-A without fiber addition

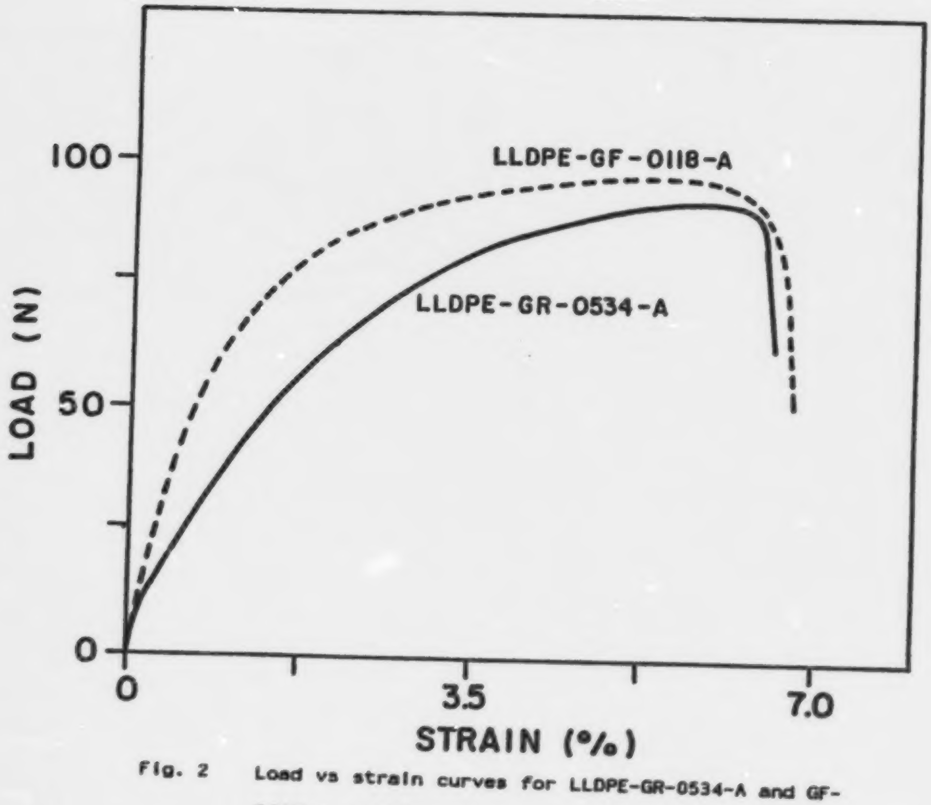

Fig. 2 Load vs strain curves for LLDPE-GR-0534-A and GF-0118-A reinforced with coated$_3$ fibers (20.0%) fiber weight)

Table 3. Composites of untreated aspen fibers

Polymer	Stress (MPa)				Energy (KJx10^{-5})				Elongation (%)				Modulus (MPa)			
Fibers (wt %)	10	20	30	40	10	20	30	40	10	20	30	40	10	20	30	40
HDPE (GRSN-8907) Composites	22.4	17.4	15.1	11.2	10.7	6.5	4.6	1.6	5.1	5.4	5.0	1.0	978	1016	1095	1327
HDPE		21.7				15.1				5.1				966		
LLDPE$_1$ (GF-0534) Composites	13.4	12.6	10.9	10.1	9.3	5.0	2.5	1.6	5.1	5.4	5.1	1.0	670	759	958	1353
LLDPE$_1$		14.7				10.7				11.1				347		
LLDPE$_2$ (GF-0118) Composites	9.4	8.2	6.9	4.1	6.2	3.7	2.6	0.8	10.5	5.3	5.4	5.1	351	387	418	546
LLDPE$_2$		9.2				31.7				42.4				206		

Table 4. Composites of aspen (CTMP) coated$_1$ fibers

Polymer	Stress (MPa)				Energy (KJx10^{-5})				Elongation (%)				Modulus (MPa)			
Fibers (wt %)	10	20	30	40	10	20	30	40	10	20	30	40	10	20	30	40
HDPE (GRSN-8907) Composites	23.4	26.7	—	31.9	16.8	9.7	—	11.9	7.2	5.2	—	3.7	1035	1203	—	1962
HDPE		21.7				15.1				5.1				966		
LLDPE$_1$ (GF-0534) Composites	14.5	16.4	—	23.0	11.1	8.3	—	10.2	5.1	5.1	—	5.1	610	664	—	1017
LLDPE$_1$		14.7				10.7				11.1				347		
LLDPE$_2$ (GF-0118) Composites	11.4	12.1	12.9	14.6	15.9	25.6	21.6	15.7	20.2	5.1	5.1	5.1	366	404	540	577
LLDPE$_2$		9.2				31.7				42.4				206		

RESULTS AND DISCUSSION

Typical stress-strain curves for polymer and their composites appear in Figs.1 and 2. The polyethylenes showed upper and lower yield points with peak load at the end of the test. The reported values in this study were calculated at upper yield point, whereas in Table 1 the values are reported at maximum load. After the addition of wood fibers in polyethylene, the yield point shifts towards peak load (Fig. 2).

Non-treated aspen (CTMP) composites

The results presented in Table 3 indicate the modulus of the composites increased in all cases. The increase was nearly four times in LLDPE (GF-0534) at 40.0 percent filler in the composites. The stress and energy values decreased with increase in filler content. This could be due to the poor adhesion at the polymer-fiber interface. The elongation was maintained in HDPE composites, but it decreased in LLDPE composites.

Coated aspen fiber composites

To improve the bonding between the polymer and fiber the

Table 5. Composites of aspen (CTMP) coated$_2$ fibers

Polymer	Stress (MPa)				Energy (KJx10^{8})				Elongation (%)				Modulus (MPa)			
Fibers (wt %)	10	20	30	40	10	20	30	40	10	20	30	40	10	20	30	40
HDPE (GRSN-8907) Composites	23.2	23.6	22.3	22.4	11.3	8.6	5.7	4.9	5.1	5.3	2.6	2.0	1020	1230	1557	1821
HDPE		21.7				15.1				5.1				966		
LLDPE$_1$ (GF-0534) Composites	12.6	13.9	14.3	11.4	9.3	6.7	3.8	1.9	5.1	5.3	5.4	1.7	564	628	933	1103
LLDPE$_1$		14.7				10.7				11.1				347		
LLDPE$_2$ (GF-0118) Composites	9.4	10.1	9.9	9.3	6.7	4.7	3.9	2.2	11.6	8.0	5.3	5.1	298	388	454	518
LLDPE$_2$		9.2				31.7				42.4				206		

Table 6. Composites of aspen (CTMP) coated$_3$ fibers

Polymer	Stress (MPa)				Energy (KJx10^{-8})				Elongation (%)				Modulus (MPa)			
Fibers (wt %)	10	20	30	40	10	20	30	40	10	20	30	40	10	20	30	40
HDPE (GRSN-8907) Composites	23.6	22.5	21.0	21.0	11.5	8.0	5.9	5.2	4.9	3.6	2.8	2.5	793	1032	1321	1595
HDPE		21.7				15.1				5.1				966		
LLDPE$_1$ (GF-0534) Composites	15.3	15.9	17.0	15.6	9.7	6.1	4.7	3.1	5.1	5.3	5.7	2.0	625	731	947	1172
LLDPE$_1$		14.7				10.7				11.1				347		
LLDPE$_2$ (GF-0118) Composites	10.7	11.4	10.8	—	7.5	6.5	5.8	—	10.3	9.1	8.3	—	351	399	391	—
LLDPE$_2$		9.2				31.7				42.4				206		

Table 7. PMPPICY treated aspen (CTMP) composites

Polymer	Stress (MPa)				Energy ($KJx10^{-3}$)				Elongation (%)				Modulus (MPa)			
Fibers (wt %)	10	20	30	40	10	20	30	40	10	20	30	40	10	20	30	40
HDPE (GRSN-8907) Composites	25.3	29.4	35.1	33.2	17.0	19.1	19.4	9.2	5.1	5.1	5.2	2.8	1013	1143	1634	1862
HDPE		21.7				15.1				5.1				966		
LLDPE$_1$ (GF-0534) Composites	13.4	16.0	22.3	26.3	5.5	6.3	8.1	7.9	5.1	5.1	5.4	5.2	489	739	1004	1235
LLDPE$_1$		14.7				10.7				11.1				347		
LLDPE$_2$ (GF-0118) Composites	12.6	12.2	14.1	—	11.2	21.2	21.4	—	8.9	5.0	5.1	—	377	416	536	—
LLDPE$_2$		9.2				31.7				42.4				206		

Table 8. Toluene diisocyanate treated aspen (CTMP) composites

Polymer	Stress (MPa)				Energy ($KJx10^{-3}$)				Elongation (%)				Modulus (MPa)			
Fibers (wt %)	10	20	30	40	10	20	30	40	10	20	30	40	10	20	30	40
HDPE (GRSN-8907) Composites	22.3	28.1	30.7	29.2	10.8	14.1	10.0	9.6	5.1	5.1	5.1	3.3	1012	1209	1501	1943
HDPE		21.7				15.1				5.1				966		
LLDPE$_1$ (GF-0534) Composites	14.4	18.1	19.0	14.7	8.2	6.6	5.8	4.3	5.1	5.1	5.4	5.1	547	646	912	1200
LLDPE$_1$		14.7				10.7				11.1				347		
LLDPE$_2$ (GF-0118) Composites	11.0	11.1	14.0	—	13.5	10.0	8.6	—	16.3	7.3	6.2	—	252	388	478	—
LLDPE$_2$		9.2				31.7				42.4				206		

aspen fibers were coated with different chemical agents. Tables 4-6 show the influence of chemical agents, used for coating, on the mechanical properties of the composites. The polymethylene (polyphenyl isocyanate) (PMPPIC) coated fibers generally showed better improvement in stress and modulus (Table 4).

The maleic anhydride coating on fiber do not result in significant improvement of the properties (Table 5). But, when a greater amount of anhydride was included in the coated fiber, stress and modulus values showed better improvement for LLDPE composites as seen in Table 6.

Isocyanate treated Polymer - Aspen Composites

The effective role of isocyanate as bonding agent is demonstrated by the increase in stress and modulus values of the composites (Tables 7-9). In HDPE composites, the stress increased from 21.7 MPa to 35.1 MPa. The stress values reached nearly twice the original polymer for LLDPE (GF-0534) composites. The modulus also increased from 347 MPa to 1235 MPa at 40.0 percent filler level in the composites. A similar trend was observed in LLDPE (GF-0118) composites. The increase in the strength of composites after isocyanate

Table 9. Hexamethylene diisocyanate treated aspen (CTMP) composites

Polymer	Stress (MPa)				Energy ($KJx10^{-6}$)				Elongation (%)				Modulus (MPa)			
Fibers (wt %)	10	20	30	40	10	20	30	40	10	20	30	40	10	20	30	40
HDPE (GRSN-8907) Composites	25.6	28.0	27.5	25.2	10.9	9.3	13.8	5.9	5.2	5.2	5.0	2.3	1076	1333	1542	1950
HDPE		21.7				15.1				5.1				966		
$LLDPE_1$ (GF-0534) Composites	16.2	17.8	21.3	—	6.6	8.8	9.4	—	5.2	5.0	4.4	—	651	708	941	—
$LLDPE_1$		14.7				10.7				11.1				347		
$LLDPE_2$ (GF-0118) Composites	11.2	11.3	11.9	—	11.1	10.9	5.9	—	13.1	9.7	5.2	—	294	368	499	—
$LLDPE_2$		9.2				31.7				42.4				206		

Table 10. Different isocyanate treatment in HDPE-aspen (CTMP) composites

Different isocyanates used with HDPE (1.0% weight of polymer)	Stress (MPa)				Energy ($KJx10^{-6}$)				Elongation (%)				Modulus (MPa)			
Fibers (wt %)	10	20	30	40	10	20	30	40	10	20	30	40	10	20	30	40
Polymethylene (polyphenyl isocyanate)	27.7	29.6	33.2	29.9	19.5	20.0	10.9	8.1	7.0	6.8	5.2	2.7	1091	1332	1471	1979
Toulene diisocyanate	24.0	27.5	30.7	24.8	10.9	14.2	8.7	5.5	5.2	5.2	5.2	2.2	1070	1370	1527	1961
Hexamethylene diisocyanate	26.3	27.1	24.7	25.3	15.2	11.0	7.6	6.2	5.8	4.0	3.1	2.4	1057	1329	1699	2015
Ethyl isocyanate	23.6	22.0	12.4	15.0	9.9	5.8	3.2	2.0	5.3	5.5	1.2	1.1	1192	1322	1536	1931
HDPE		21.7				15.1				5.1				966		

treatment was also observed by Coran and Patel[11] in the the case of cellulose fibers and grafted olefin polymers.

The polymers treated with toulene diisocyanate and hexamethylene diisocyanate also showed better mechanical properties as seen in Tables 8 and 9. HDPE-aspen fiber composites exhibited superior values in stress and modulus. In LLDPE (GF-0534) composites, the modulus increased almost four times the original polymer (Table 8). The stress increased from 9.2 MPa to 14.0 MPa and the modulus from 206 MPa to 478 MPa at 30 percent fiber concentration in LLDPE (GF-0118) composites. A gradual increase in stress with the addition of fibers was observed in LLDPE (GF-0534) composites (Table 9). The improvement in modulus was more significant in LLDPE than in HDPE composites. However, the retention of elongation was poor in LLDPE composites.

Since the HDPE-Aspen composites showed overall improvement in properties, further studies were carried out to reach the optimum amount of isocyanate needed to achieve improved adhesion between the fiber and polymer. Table 10 shows the mechanical properties of HDPE composites after different isocyanate treatment. The stress and modulus values had increased even with the addition of 1.0 percent isocyanate.

The PMPPIC treated composites showed better results compared to other isocyanates studied. The stress increased from 21.7 MPa to 33.2 MPa and the modulus values were more than two times the original HDPE. The maximum modulus of 2015 MPa was observed for 40.0 percent fiber composites after hexamethylene diisocyanate treatment. The ethyl isocyanate treated HDPE-Aspen composites showed an increase in modulus but the stress did not change. The poor performance of stress in ethyl isocyanate can be due to the short chain molecules which do not effectively cover the fiber surface area. While the better improvement in properties of PMPPIC treated composites can be attributed to the uniform coating of long chain molecules at the fiber surface, which led to good adhesion.

The possible type of bonding at the interface can be illustrated in the following way

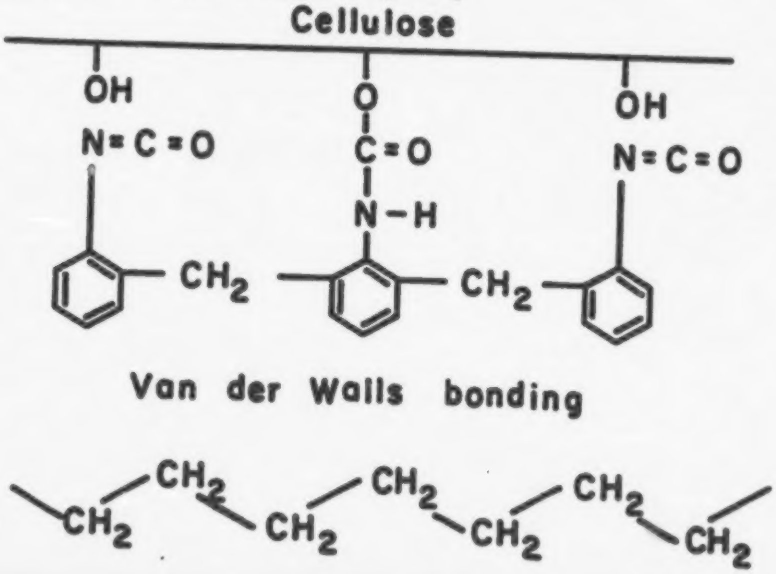

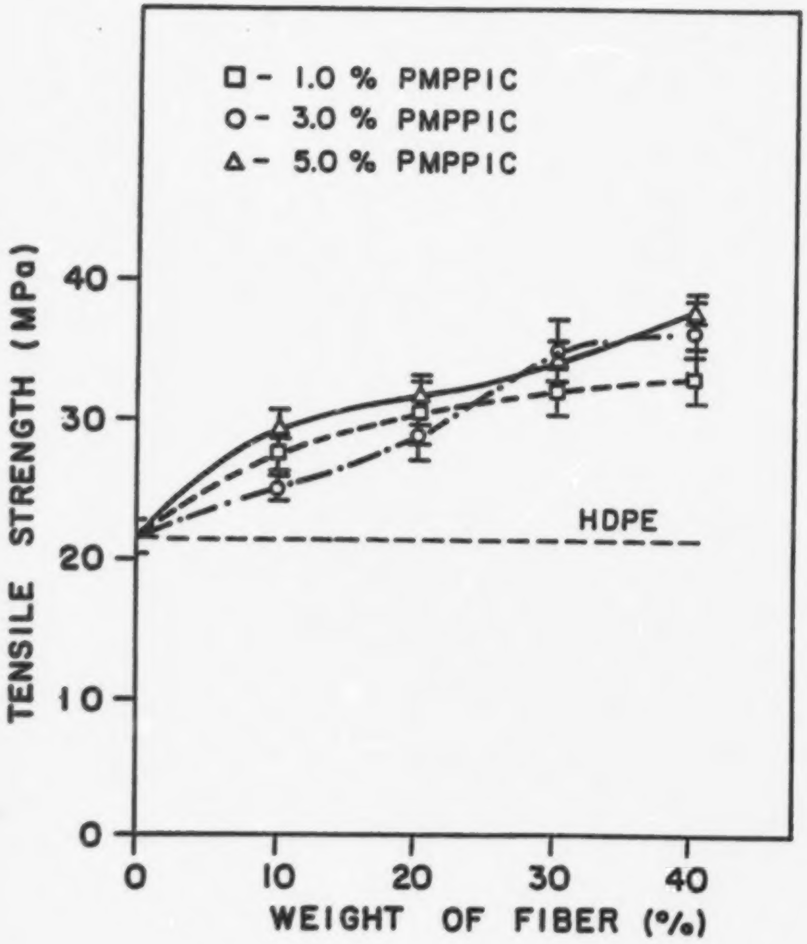

Fig. 3 Effect of PMPPICY concentration on tensile strength of HDPE-aspen composites

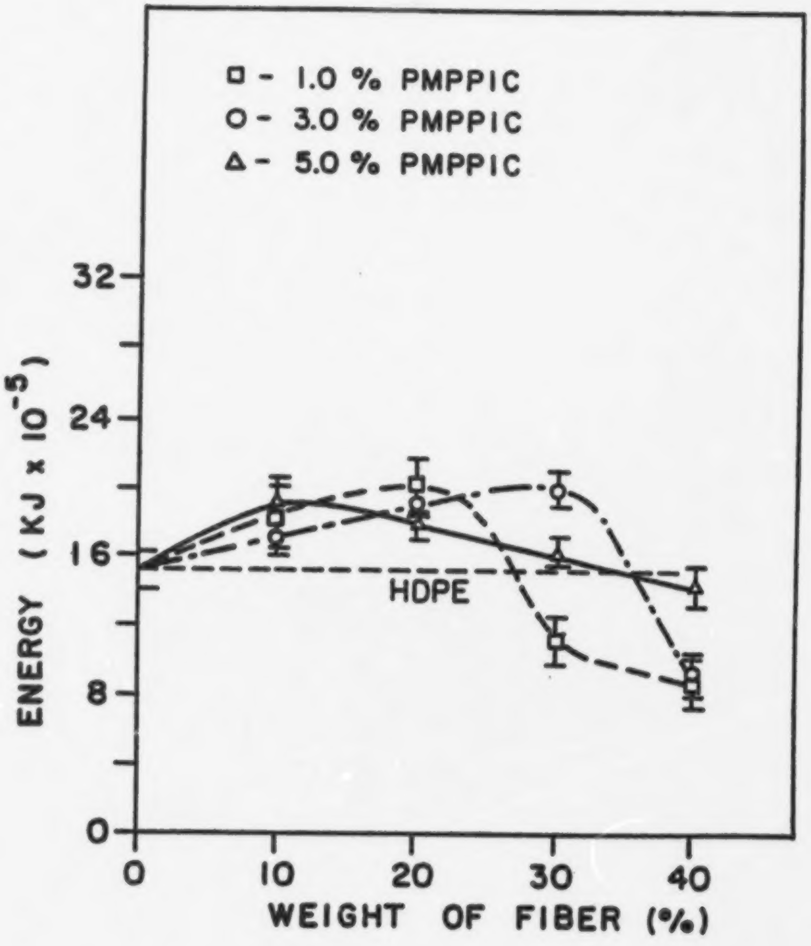

Fig. 4 Effect ofPMPPICY concentration on energy values of HDPE-aspen composites

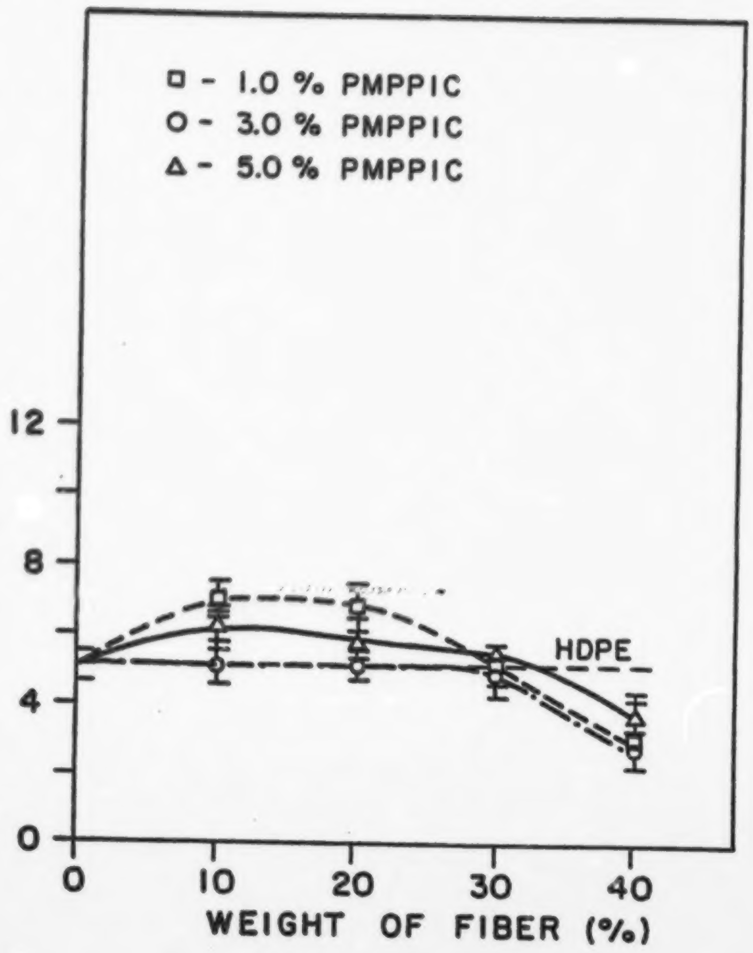

Fig. 5 Effect of PMPPICY concentration on elongation of HDPE-aspen composites

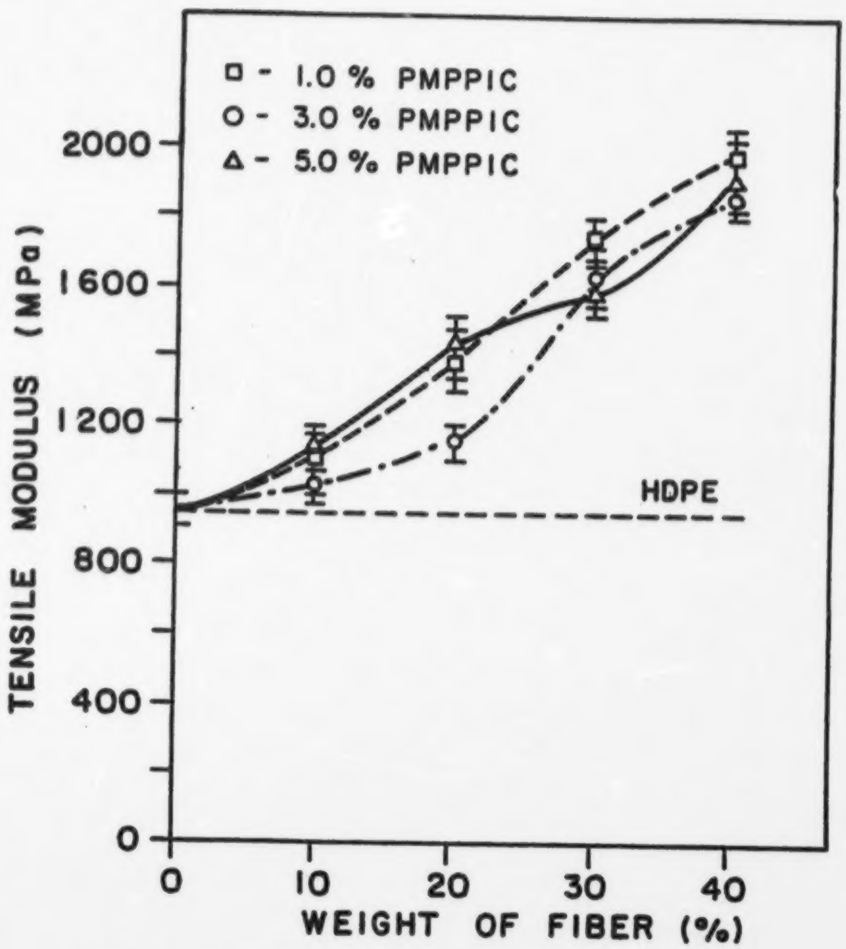

Fig. 6 Effect of PMPPICY concentration on tensile modulus of HDPE-aspen composites

Table 11. Polymethylene (Polyphenyl isocyanate) treated HDPE aspen (CTMP) fiber composites effect of mesh size

Mesh size	Stress (MPa)				Energy (KJx10^{-5})				Elongation (%)				Modulus (MPa)			
Fibers (wt %)	10	20	30	40	10	20	30	40	10	20	30	40	10	20	30	40
20 Mesh	27.1	31.2	30.1	31.8	13.8	17.3	10.7	11.2	5.1	5.1	5.2	3.5	1183	1383	1554	1732
40 Mesh	27.1	29.6	30.5	26.7	14.9	16.0	12.4	8.1	5.1	5.0	4.1	3.0	1180	1234	1622	1795
60 Mesh	25.3	29.4	35.1	33.2	17.0	19.1	19.4	9.2	5.1	5.1	5.2	2.8	1013	1143	1634	1862
HDPE		21.7				15.1				5.1				966		

The isocyanate (PMPPIC) groups can form covalent bonds with cellulose and the other part of the isocyanate can be interlinked by Van der Walls type of bonding with the hydrophobic polymer.

Figs. 3-6 show the effect of PMPPIC concentration on mechanical properties of HDPE-Aspen composites. The stress increased steadily with the addition of fiber, but the variation was marginal at higher concentration levels of PMPPIC (Fig. 3). The elongation and energy decreased at higher fiber loading in the composites (Figs. 4 and 5). However, the modulus increased significantly and reached a maximum at 40.0 percent fiber in the composites (Fig. 6).

The effect of fiber mesh size on tensile properties of the composites is shown in Table 11. It can be observed that there is an improvement in the properties of shorter fiber reinforced composites (mesh size 60). Similar behavior was observed by Kokta et al. [12] for grafted wood fiber thermoplastic composites. The stress and modulus values are superior for mesh size 60 fiber reinforced composites. The stress increased from 21.7 MPa to 33.2 MPa and the modulus increased from 966 MPa to 1862 MPa at 40 percent fiber weight in the composites.

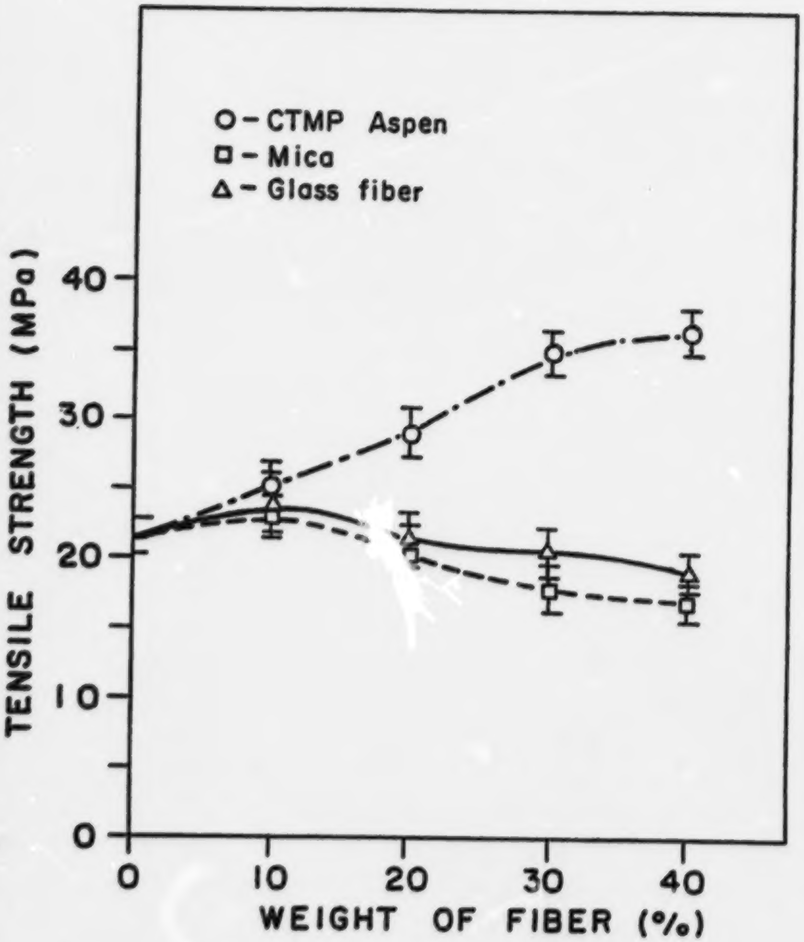

Fig. 7 Effect of different filler reinforcement on tensile strength of HDPE

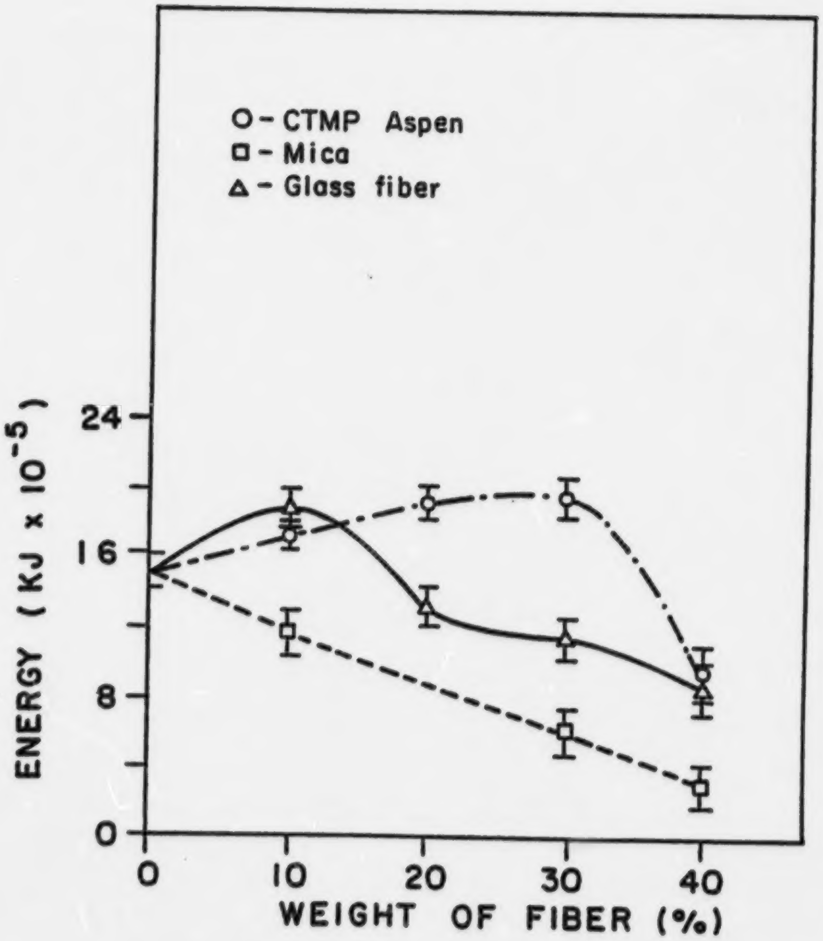

Fig. 8 Effect of different filler reinforcement on energy values of HDPE

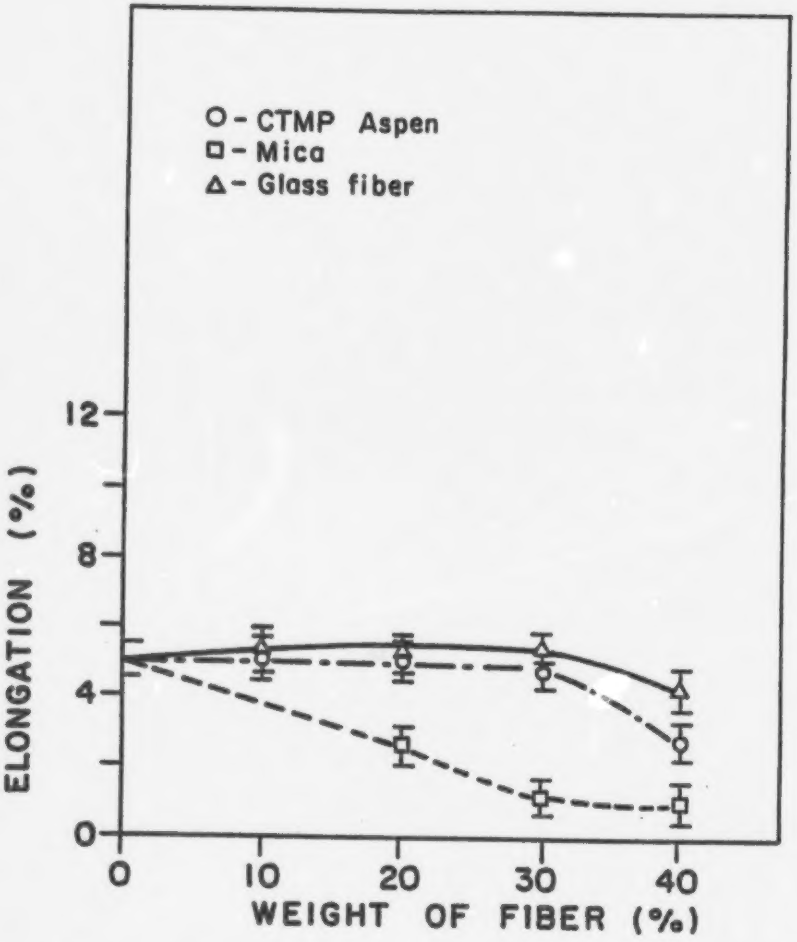

Fig. 9 Effect of different filler reinforcement on elongation of HDPE

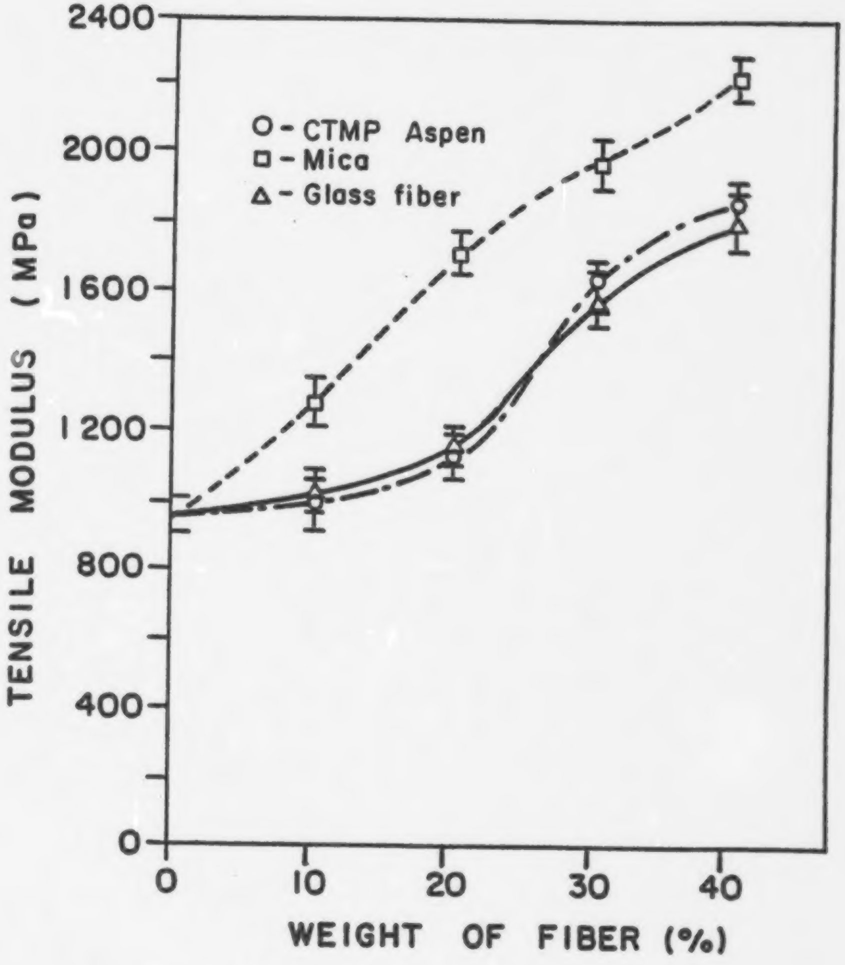

Fig. 10 Effect of different filler reinforcement on tensile modulus of HDPE

The tensile properties of HDPE reinforced with aspen, mica and glass fibers are shown in Figs. 7-10. At higher fiber loading, the stress values are superior in aspen composites compared to that of mica or glass fiber (Fig. 7). The energy increased until 30.0 percent fiber level in HDPE-Aspen composites, but it decreased in other cases (Fig. 8). The retention of elongation was good in aspen and glass fiber composites, however HDPE-mica composites showed a decrease in elongation at higher concentrations of mica (Fig. 9). In the case of modulus, HDPE reinforced with mica showed better values but still aspen composites performed well compared to that of glass fiber (Fig. 10). However, it is also important to note the lower cost ($500/ton) advantage of CTMP wood fibers over the higher cost of mica ($700/ton) and glass fibers ($2 900/ton)[6].

CONCLUSION

The use of isocyanates as bonding agent has significantly enhanced the adhesion at the fiber and matrix interface, which is obvious from the improvement in mechanical properties. The stress and modulus increased more than 60.0 and 90.0 percent respectively in HDPE and LLDPE composites depending on the type of isocyanate treatment. The study also reveals that there is an optimum concentration of isocyanates above which the strength does not increase significantly. The tensile properties of aspen fiber composites compared favorably with mica or glass fiber reinforced composites.

REFERENCES

1. J.E. Theberge and E. Hohn, Polym. Plast. Technol. Eng., 16, 41 (1981).
2. R.T. Woodhams, G. Thomas, D.K. Rodgers, Polymer Eng. Sci., 24, 15, 1166, (1984).
3. G.R. Lightsey, Polym. Sci. Technol., 17, 193 (1981).
4. R.B. Seymour, Popular Plastics, 23, 27 (1978).
5. M.H. Schneider and K.I. Brebner, Wood Sci. Technol., 19, 1, 67 (1985).
6. A.D. Beshay, B.V. Kokta and C. Daneault, Polymer Composites, 6,4, 261 (1985).
7. T. Avella and B. deLhomeux, J. Appl. Polym. Sci. (polymer Symp.) 40, 203 (1984).
8. E. Zavin, Adv. in Chem. Ser. (ACS) No. 207, Chemistry of Solid wood: 349 (1984).
9. W.E. Johns, J. Adhesion 15, 1, 59 (1982).
10. A.J. Michell and D. Willis, Appita, 31, 5 (1978).
11. A.Y. Coran and R. Patel, U.S. pat. 4,323,625 (1982).
12. B.V. Kokta, L. Araneda and C. Daneault, Polym. Eng. Sci.,24, 950 (1984).

STRUCTURE AND PROPERTIES OF OIL EXTENDED STYRENE BUTADIENE BLOCK COPOLYMERS

by

S. Polizzi, N. Stribeck, H.G. Zachmann and R. Bordeianu*
Universität Hamburg
Institut für Technische und Makromolekulare Chemie
Bundesstr. 45, D-2000 Hamburg 13, Federal Republic of Germany

*Ichechim, Bucarest

Presented at the 8th annual NRCC/IMRI symposium "Composites-'87",
November 5 and 6, 1987, Boucherville, Que., Canada

Abstract

The relationships between mechanical properties and structure of rapidly spin cast SBS block copolymers diluted with two different types of mineral oil are discussed.

Small angle X-ray Scattering (SAXS) measurements indicate that both oils are mainly going into the rubbery polybutadiene phase. While during rapid spin casting the paraffinic oil improves the phase separation of polystyrene (PS) and polybutadiene (PB), the opposite is true for the aromatic oil.

The measurements also suggest that the oils cause a preferential swelling of the superstructure along the longitudinal direction of the cylindrical PS domains. From this, it can be concluded that a larger number of interconnecting PB chains is present in the cross direction than in the longitudinal one. With increasing oil content, a further decrease of interconnecting chains in the latter direction may be the reason for the decrease of the tensile modulus. Furthermore, above a critical value of dilution (33 wt.% for paraffinic oil, 50 wt.% for the aromatic one), more and more spherical domains are formed instead of the cylindrical ones. This morphological transition explains the step present in the double logarithmic plot of the large strain tensile modulus as a function of oil dilution.

A. Introduction

Styrene-Butadiene-Styrene (SBS) triblock copolymers are important materials used as thermoplastic rubbers. It is well known that in such systems phase separation takes place. Depending on concentration and preparation conditions, the phase present in a smaller amount forms well ordered lamellae, cylinders or spheres within the matrix of the other phase (1). However, a complete phase separation will only occur under processing conditions in which complete equilibrium can be reached. If this is not the case, for example in technological processes such as injection moulding and spin casting, the phase separation may remain incomplete. Therefore, there exists much interest in studying the structure and the properties of samples obtained under such conditions. Another important problem arises if the SBS block copolymer is extended with mineral oil. This is done in order to reduce the cost of the materials as well as to improve certain mechanical and rheological properties. The question arises of how does the oil influence the structure and the mechanical properties.

In previous publications samples of block copolymers extended with different kinds of oil were prepared and the mechanical properties of these samples as well as the influence of the oil dilution were investigated (2-4). An interesting dependence of the properties on the amount of oil and a difference between the influence of an aromatic oil and that of a paraffinic one were observed.

In order to explain these results, we have performed investigations of the structure of these materials by means of small angle X-ray scattering (SAXS). In the present work we first summarize some of the earlier results on the mechanical properties which are significant for this investigation. We then present some results on the structure obtained by SAXS and discuss the relations between the structure and the mechanical properties.

B. Experimental

Tensile properties were determined on standard dumbbell specimens at a jaw separation speed of 0.5 m/min on a Zwick Mod. 1454 tensile tester. SAXS measurements were carried out using Ni-filtered Cu-k_α-radiation, a Kratky-Compact-Camera and proportional detector with energy discrimination. Absolute intensity was measured using the moving slit method (5). The data were analyzed following a procedure reported elsewhere (6,7), which allows a very precise determination of the fluctuation background. Some measurements were also performed at HASYLAB (Hamburg Synchrotron Radiation Laboratory). Series of X-ray diffraction patterns were collected whilst the specimens were continuously extended.

C. Materials

The polymer investigated is a linear SBS triblock copolymer, the molecular weight, M_n, of the butadiene block being 80,800 g/mole and that of each styrene end-block 21,200 g/mole. The synthesis technique was described earlier (8,9). The polymer

TABLE 1.

Property	Oil P	Oil A
Color	colorless	black
Density at 25 °C [kg/m^3]	866.5	1009.6
Electron density [el/nm^3]	296.	336.
Refractive index	1.4749	1.5785
Viscosity	0.134 (a)	118. (b)
Structural composition (c)		
Aromatic C [wt.-%]	3.5	45.
Naphtenic C [wt.-%]	29.9	21.
Paraffinic C [wt.-%]	66.6	34.

(a) Kinematic, at 37.8 °C (m^2/h); (b) Saybolt, at 100 °C (deg. Saybolt); (c) calculated from refractive index, density and mol. wt.

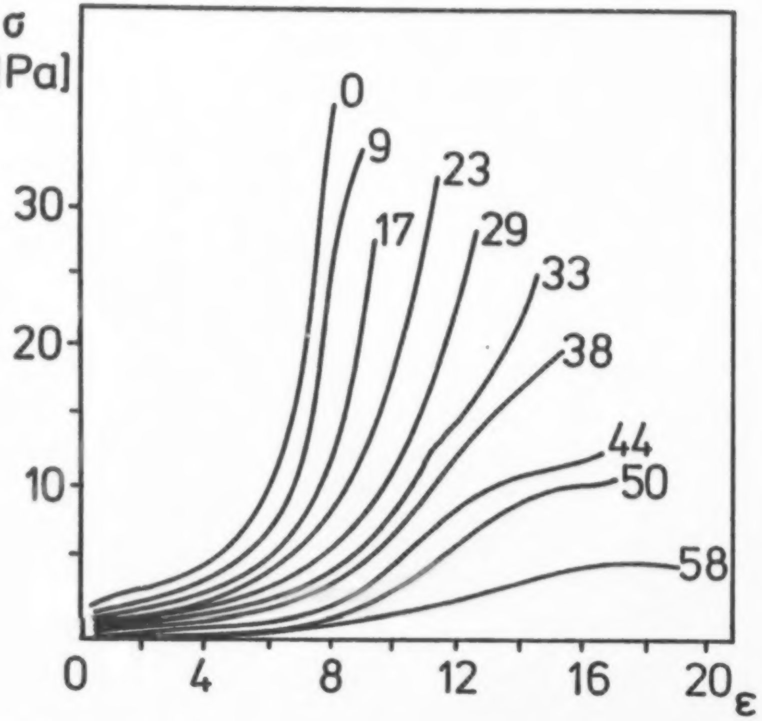

Fig. 1: Stress-strain curves of SBS triblock copolymers diluted with Oil P. Parameter: Oil concentration in wt.-%.

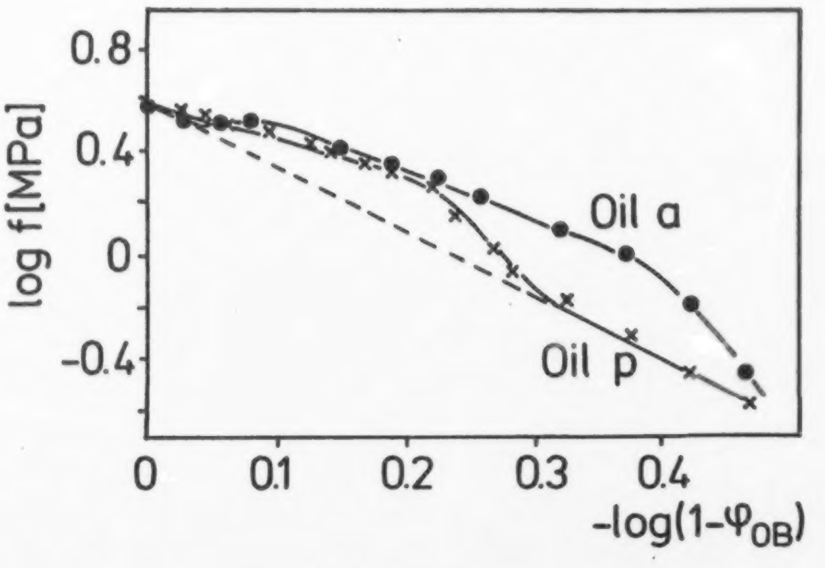

Fig. 2: "Large strain tensile modulus" f at $\lambda = 4$ of the SBS copolymer as a function of the volume fraction φ_{OB} of oil in the PB phase. volume additivity of the oil and the polybutadiene is assumed.

was diluted by two different mineral oils, a paraffinic one called "Oil P" and an aromatic one called "Oil A". Some properties of the two oils are summarized in Table 1.

Since SAXS is caused by variations of the electron density within the sample volume and SBS copolymers can be described by the model of a two-phase system, the electron densities of the extender oils were determined and compared with those of pure polystyrene and polybutadiene. Elementary analysis showed, that more than 98 wt-% of both oils consists of the two elements C and H. Neglecting the rest we computed the C/H-ratio to be 1.90 for the paraffinic and 1.42 for the aromatic oil. This yields electron densities ϱ = 296 el/nm^3 for the paraffinic and 336 el/nm^3 for the aromatic oil, using the mass densities. Compared with the electron densities of the two polymer phases, ϱ of the aromatic oil is close to the electron density of a pure PS sample (339 el/nm^3) and ϱ of the paraffinic oil lies near the electron density of pure PB (301 el/nm^3).

The polymer films were obtained by spin casting from toluene solution containing the necessary amounts of polymer and extender oil. After 4 h the films were dry and could be taken from the heated cylindrical rotating cast mould (2).

D. Mechanical Properties

In Fig. 1 some typical stress-strain curves are reported. They show the following features: already at low strains, yielding and drawing is observed due to disruption of the continuous phase of polystyrene; this is followed by a hardening effect at medium strains caused by lateral impingement of the rigid polystyrene domains; beginning from a certain oil concentration (33 wt.-% for paraffinic oil, 50 wt.-% for aromatic oil) an inflexion in the stress-strain curves at large strains occurs. The higher the oil content, the later the hardening effect will show up.

The chemical composition of the mineral oil has a significant influence on mechanical properties: at constant oil level, the higher the content of aromatic hydrocarbons in oil, the larger is the stress at any given elongation.

In the following, the large strain "tensile modulus" f will be considered. In rubber technology this quantity is a widely used parameter describing the elastic properties of elastomers and is defined as the stress at a fixed elongation (usually $\lambda = 2$, 4 or 6). Since calorimetric measurements (3) suggested that the oil goes mainly into the rubber matrix, the volume fraction of oil in the butadiene phase, φ_{OB}, is used to describe the oil dilution of the polymer.

Fig. 2 shows the modulus f at $\lambda = 4$ as a function of the volume fraction φ_{OB} in a double logarithmic scale. It can be seen that the modulus decreases with increasing dilution, but the dependence is not a linear one: after an initially gentler descent, at higher degrees of dilution a steeper decrease follows. The onset of the transition depends on the chemical composition of the oil (33 wt.-% corresponding to $\varphi_{OB} = 0.43$ for paraffinic oil; 50 wt.-% or $\varphi_{OB} = 0.56$ for aromatic oil). Moreover, for aromatic oil dilution a short plateau is observed at the beginning of the curve.

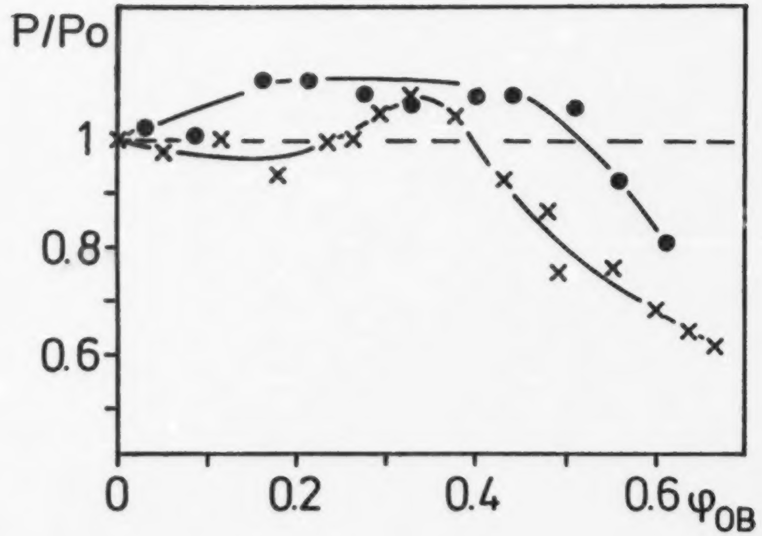

Fig. 3: Variation of the shape factor p/p_0 as a function of oil content φ_{OB} at λ = 4.

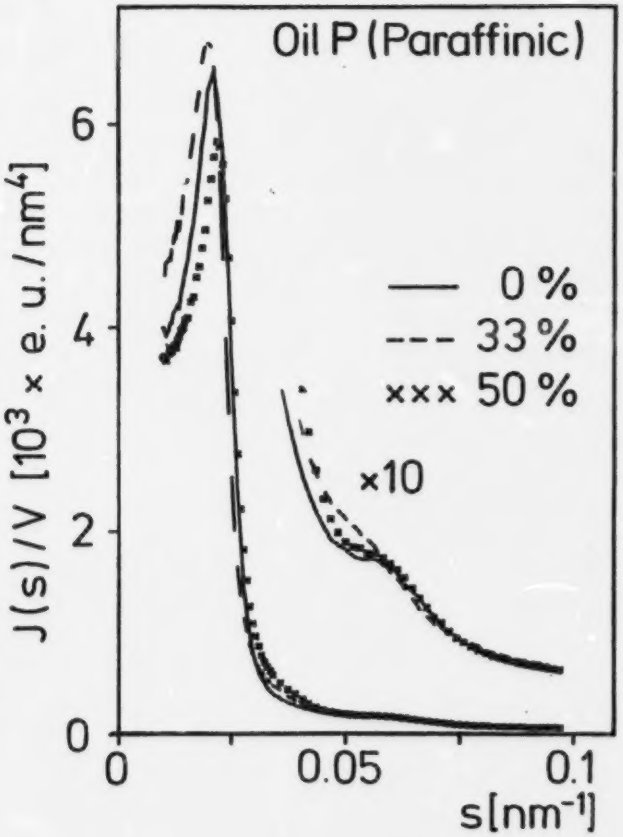

Fig. 4: Absolute SAXS intensities for the SBS sample diluted with different amounts of paraffinic oil. Parameter: weight-% of oil.

An attempt was made (3,4) to interpret the stress-strain data in terms of the known constitutive equations for elastomers (Mooney-Rivlin (10) and Guth-Smallwood (11,12); Holden (13); Leonard (14)). However, no satisfactory results over the whole range of oil dilution were obtained. Since the theories mentioned are restricted to the case of rigid particles of constant shape in an elastic matrix, it seemed obvious that one has to consider changes of the shape of these particles in order to improve the agreement. This was done (3) by multiplying the Mooney-Rivlin equation describing f for unfilled elastomers with a strain amplification factor γ:

$$f = (2C_1 + 2C_2/\lambda)(\lambda - 1/\lambda^2)\cdot\gamma \ . \qquad (1)$$

C_1 and C_2 are two constants. In the case of rigid rodlike domains γ is given by the Guth function:

$$\gamma = E/E_0 = 1 + 0.67\ p\ \varphi_S + 1.62\ p^2\varphi_S{}^2 \qquad (2)$$

with E and E_0 being the Young's moduli of the filled and unfilled elastomer respectively, φ_S the volume fraction of the rigid domains and p a shape factor defined as length/diameter. Although Eq (2) is strictly valid only for rodlike filler particles, the variation of the ratio p/p_0 (p_0 is the shape factor for the undiluted copolymer), can be ascribed to morphological changes of the rigid domains. Fig. 3 shows the ratio p/p_0 as a function of oil content calculated from the data given in (3): with increasing oil content, p/p_0 first remains constant and then decreases. The latter reduction of p/p_0 indicates a transition from elongated domains (lamellae or rods) towards more spherical shapes, taking place at about 33 wt.-% for paraffinic oil and 50 wt.-% for aromatic oil.

E. Structure determination

There already exists some knowledge on the structure which can be considered as a base for the further examinations: As the polybutadiene is the major component in the copolymer, polystyrene will form distinct domains within a polybutadiene matrix. Furthermore, for the composition of the undiluted sample in question, the polystyrene particles are expected to be of cylindrical shape. Due to calorimetric results (3), one can also assume that both the paraffinic and the aromatic oil will mainly go into the polybutadiene phase. However, several important questions still arise:

1. What are shape and dimensions of the domains formed by the styrene blocks under oil dilution?
2. Does the oil completely go into the polybutadiene matrix or does it also enter the polystyrene phase?
3. How complete is the phase separation between styrene and butadiene blocks?
4. Is it possible to prove the morphological changes indicated by mechanical measurements at a critical value of oil content, by means of other, more direct methods?

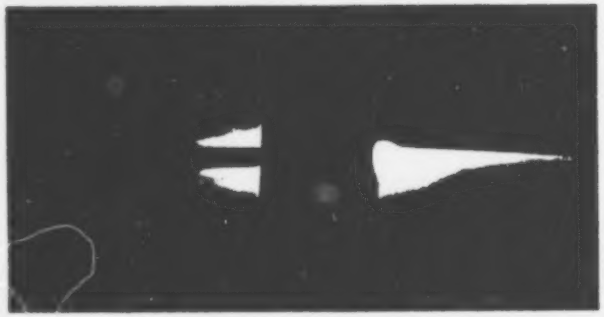

Fig. 5: SAXS layer line pattern of undiluted SBS sample, oriented by stretching to $\lambda = 6$.

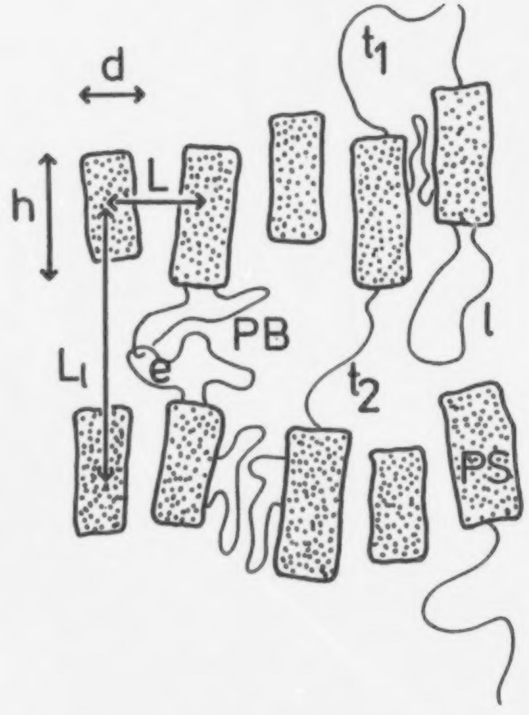

Fig. 6: Structural model of the arrangement of the PS domains in the PB matrix. In order to avoid confusions, only a few PB chains are shown.

1) Shape, dimensions and superstructure of PS domains

An attempt to determine the shape of the domains by electron microscopy (15) was not successful. It turned out that no contrast was obtained by usual staining techniques, probably because the phase separation of styrene and butadiene is not complete (see section c)). Therefore, we tried to get results by SAXS.

Fig. 4 shows the SAXS curves for the pure block copolymer, as well as some curves for samples extended with paraffinic oil. Similar curves were obtained for the case of aromatic oil. The patterns are typical for such triblock copolymers, showing just two relatively broad peaks. If the superstructure formed a completely regular arrangement, it would be possible to distinguish between different morphologies. In this case, due to distortions, this attempt would be questionable. In any case, by means of the Bragg equation, from the position of the first strong maximum it is possible to calculate the most probable interdomain distance, the long period L. With the sample without oil, a value of L = 43 nm is obtained.

Drawing the sample will cause the superstructure to orient, thus allowing more parameters to be determined. Fig. 5 shows one of the SAXS pictures obtained under sample stretching at HASYLAB. In this case, a layer line pattern is obtained: a series of parallel narrow lines perpendicular to the stretching direction, whose intensity envelope gives rise to an ellipsoidal pattern with its longitudinal axis parallel to the lines. In Fig. 6 a structural model is visualized, in which all these results are

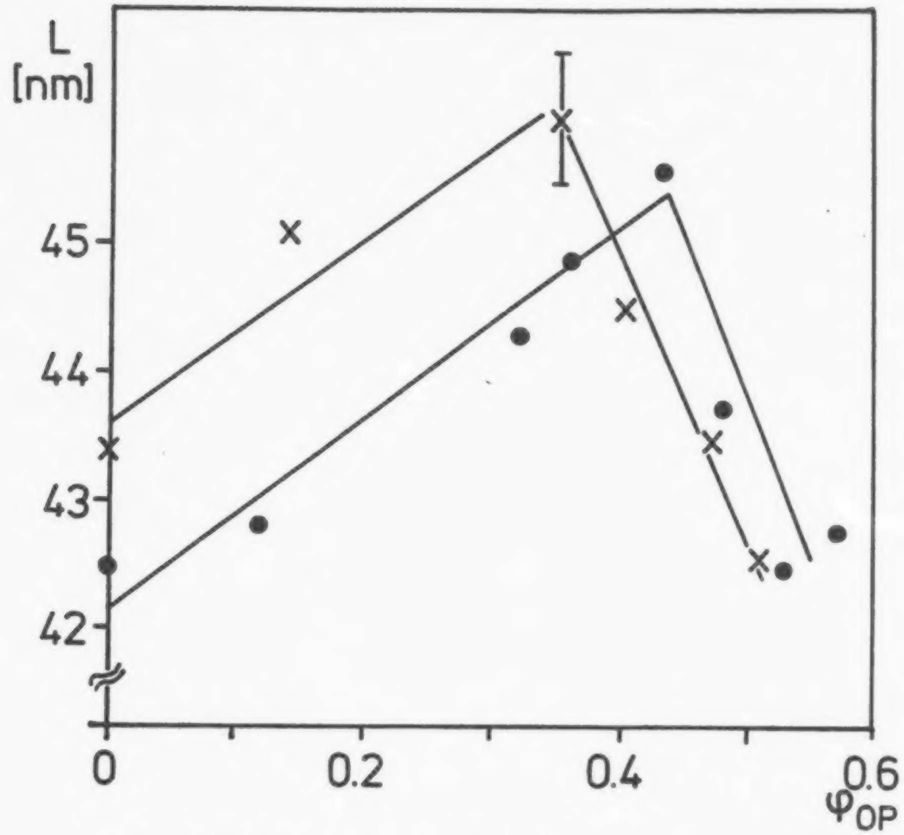

Fig. 7: Long period L as a function of the volume fraction of oil in the polymer. Additivity of the volumes is assumed. (x): paraffinic extender oil; (●): aromatic extender oil

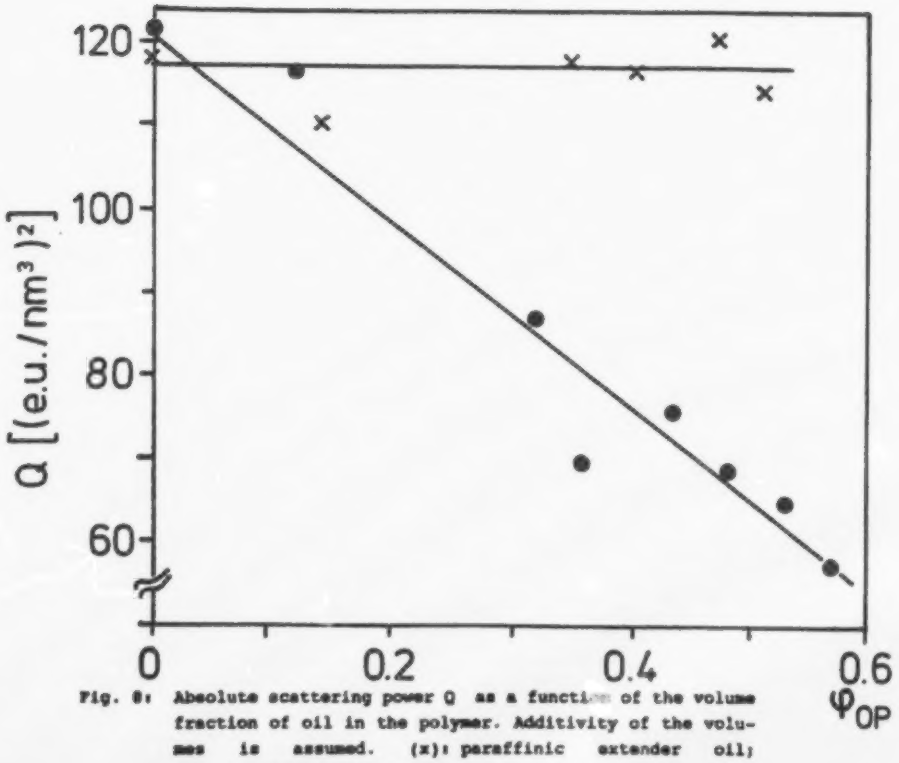

Fig. 8: Absolute scattering power Q as a function of the volume fraction of oil in the polymer. Additivity of the volumes is assumed. (x): paraffinic extender oil; (●): aromatic extender oil

taken into account. It shows polystyrene cylinders of height h and diameter d in a polybutadiene matrix. From the SAXS pattern of the oriented material, a rough approximation for the dimension of the polystyrene particles and the distance L_1 between them can be obtained. This gives cylinders of height h = 66 nm and diameter d = 28 nm at a distance of L_1 = 300 nm in the stretching direction. A more complete analysis of drawing data will be reported elsewhere (16).

If we now describe our unstretched system using the so obtained cylinder dimensions and a hexagonal superlattice, we can even compute the distance L_1. Taking the long period L as the analogous distance in the perpendicular direction and $\varphi_S = 0.31$, we find L_1 = 160 nm for the undiluted sample.

How does the structure change if oil is added? Fig. 7 shows the long period L as a function of the amount of oil for both oils. The slow increase of L with increasing oil dilution is not compatible with an affine swelling of the superstructure. In order to explain the smaller increase of L we have to assume a preferential swelling of the matrix along the longitudinal axis of elongated polystyrene domains. Under the above mentioned assumption of preferential swelling the value of L_1 for a sample diluted with 50 wt.-% of aromatic oil would be increased to 230 nm.

Let us speculate in order to find a possible reason for such an inhomogeneous swelling. The two styrene blocks of each molecule may lie either in the same cylinder or in two different cylinders. In the first case, the PB block forms a loose loop l (see Fig. 6). If, however, the two PS blocks of a molecule are lying in different cylinders, the included PB block must form a tie chain connecting these cylinders. They may connect either two blocks in cross direction, like the chain t_1 in Fig. 6 or two blocks in longitudinal direction, like t_2. By simple entropy considerations on can deduct that tie chains of the type t_1 will occur much more frequently than those of the type t_2: The first ones are part of molecules, which are quite close to the most probable coil conformation, for example the distance in cross direction between two cylinders, L - d, agrees quite well with the average end-to-end distance of a PB block. In contrast, the chains of the type t_2 belong to molecules, which are considerably extended. Due to the large decrease of entropy with extension, the formation of such tie molecules is improbable. In the longitudinal direction, the cylinders are hold together by entanglements between loops (e in Fig. 6) rather than by tie molecules.

The long period L in the cross direction is defined by the principle of maximum entropy of the tie chains t_1. The so defined long period strongly resists to any changes imposed by other influences like addition of oil. On the other hand, the long period in longitudinal direction can be changed much easier, as there are almost no tie chains.

In this model the oil concentration between the cylinders in cross direction may be somewhat lower than between the cylinders in longitudinal direction. This can be explained by the fact, that there arises an additional pressure in the cross direction due to some elongation of the t_1 molecules. In longitudinal direction this pressure is not present.

The decrease of the large strain tensile modulus with increasing oil content may be explained by a decrease of the number of entanglements between the loops (e in Fig. 6).

2) Phase separation in the undiluted polymer

An important quantity is the scattering power Q, defined as the absolute intensity integrated over all angles. For a two-phase system the measured Q can be expressed in terms of the electron densities ϱ_i and the volume fractions φ_i by:

$$Q = (\varrho_2 - \varrho_1)^2 \cdot \varphi_1\varphi_2. \qquad (3)$$

For the pure triblock copolymer φ_1 is the volume fraction of polystyrene, φ_2 that of polybutadiene and ϱ_1 and ϱ_2 are the electron densities of the two materials. Thus $\Delta\varrho = (\varrho_2 - \varrho_1)$ is 38 el/nm^3 and φ_1 is 0.31. From this one obtains Q = 309 el/nm^3. From our experimental data we have obtained a value of 119 ± 2 el/nm^3. From this, by means of Eq. (3), the electron density difference $\Delta\varrho$ = 23.5 el/nm^3 is obtained. Thus $\Delta\varrho$ of undiluted SBS obtained by SAXS, is far below the theoretical value mentioned above.

These data show that the initial SBS-block-copolymer cannot be treated as an undisturbed two phase system, in which both phases behave like pure PS and PB. The phase separation seems to be incomplete. This result is in agreement with electron microscopy observations. As mentioned above, electron microscopy failed to visualize the superstructure in rapidly cast SBS films

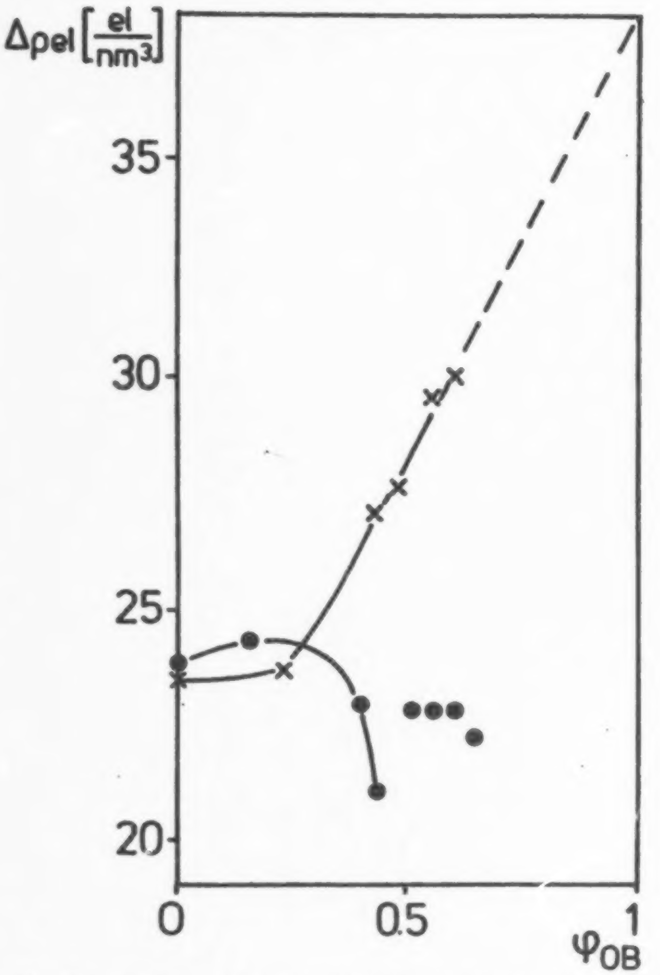

Fig. 9: Electron density difference $\Delta\varrho$ between the two phases of oil diluted SBS copolymers as a function of the volume fraction of oil in the polymer. Additivity of the volumes is assumed. (x): paraffinic extender oil; (●): aromatic extender oil

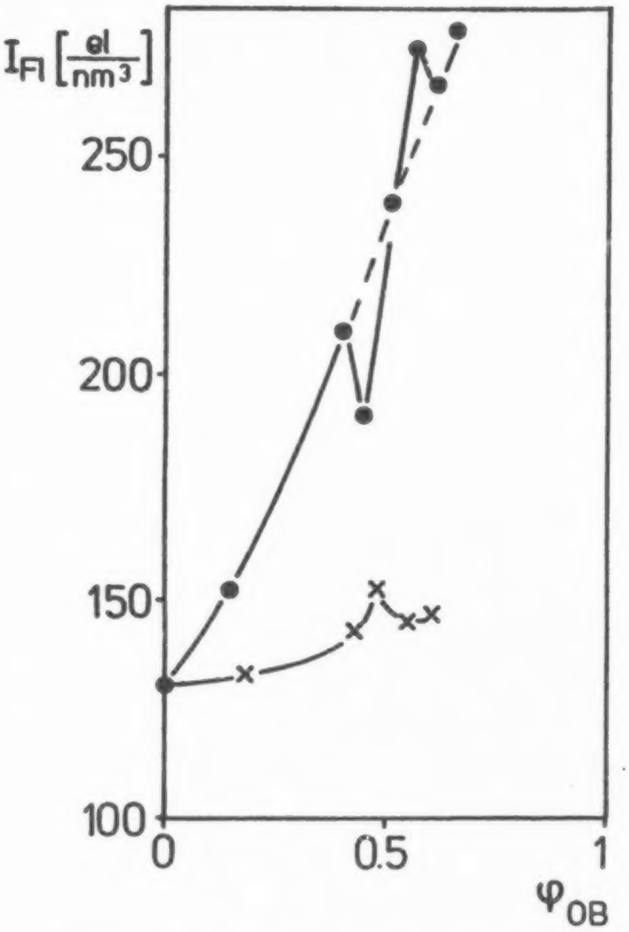

Fig. 10: Absolute electron density fluctuations I_{Fl} of oil diluted SBS copolymers. (x): paraffinic extender oil; (●): aromatic extender oil

like the ones here studied (15). The staining agent seems to couple not only to the PB phase, but also to the PS phase. Therefore, this phase obviously is contaminated by PB.

One can try to estimate which amount of PB is mixed with the PS cylinders and vice versa. If one assumes a pure PB phase and a mixed PS/PB phase, one obtains that 23 vol-% of PB is present in the PS domains. On the other hand, if one has a pure PS phase, one obtains that 16 vol-% of PS is present in the PB domains. For $\Delta\varrho$ this yields values of 22 el/nm^3 in the first and 31 el/nm^3 in the second case.

3) In which phase does the oil go?

The scattering power Q has been also determined for the samples diluted by oil. Fig. 8 shows Q as a function of the volume fraction of oil in the polymer, φ_{OP}. As it can be seen, one obtains a constant value with the paraffinic oil and a linear decrease with the aromatic one. For $\varphi_{OP} = 0$ the value $Q = 119.5$ el/nm^3 mentioned before is obtained.

From Eq. 3 the electron density difference $\Delta\varrho$ was calculated under the assumption that the oil goes into the PB matrix and that the volumes are additive. The results are shown in Fig. 9. One can see, that $\Delta\varrho$ considerably increases with increasing amount of paraffinic oil. With aromatic oil $\Delta\varrho$ first remains constant, then decreases and eventually increases again. As mentioned in section b), the phase separation between PB and PS is incomplete. If we assume to have a pure PS phase in which some PB is present and, further, that the oil only enters the PB phase, we would get a trend indicated by the dashed lines in the figure.

If, moreover, also the PB is assumed to contain some PS, the slope of the line is slightly changed. In a very rough approximation the experimental data follow the theoretical lines, so that it can be concluded that the assumption that the oils only enter the PB phase is correct. However, the deviations from the theoretical behaviour observed are far beyond the experimental error. How can these deviations be explained?

If one extrapolates the experimental results for the paraffinic oil to $\varphi_{OB} = 1$, one obtains a value of $\Delta\varrho = 38$ el/nm^3, which is the theoretical value calculated for pure PS and PB. As the electron density of this oil is close to that of PB, one has to conclude that in this extrapolated situation the phase separation of PS and PB would be complete. Therefore, we can state that an increasing amount of paraffinic oil improves the phase separation between PS and PB domains.

At small concentration no increase of $\Delta\varrho$ is observed. This suggests that for such small concentrations of oil the additivity of volumes is not strictly valid: small amounts of oil can enter some "holes" in the PB matrix.

The aromatic oil leads to a decrease in $\Delta\varrho$. This decrease is, however, by far not so large as it would be expected theoretically. Apparently, the volume of the PB/aromatic oil blend increases more rapidly than the volume additivity would suggest. This can be explained by the incompatibility between the aromatic oil and PB. The later increase of $\Delta\varrho$ from $\varphi_{OB} \approx 0.5$ can be ascribed to a true phase separation of oil and PB.

From the tails of SAXS curves, the fluctuation of the electron density within each phase averaged over both phases, I_{Fl}, can be calculated. This quantity is a measure of the homogeneity within the phases. Fig. 10 reports the values obtained from our data. As it can be seen, with paraffinic oil dilution, I_{Fl} remains almost constant, while it strongly increases under aromatic oil extension. This confirms that the paraffinic oil homogeneously mixes within the rubber phase. On the other hand, the steep increase of I_{Fl} for aromatic oil shows that this oil considerably raises the inhomogeneity when it goes into the PB phase. As aromatic oil mixes in even parts, the fluctuation background has a sudden drop. We assume that a critical concentration has been reached at which a phase separation between oil and PB can occur. During this phase separation, already suggested by the behaviour of $\Delta\varrho$, larger homogeneous oil regions (clusters, droplets) are formed within the PB phase.

An alternative explanation of the abrupt drop of I_{Fl} would be that from this concentration some oil enters the PS phase. SAXS is not able to distinguish between these two assumptions.

4) Morphological changes

The onset of a morphological transition of the PS domains is more or less directly suggested by the trend of different parameters.

A rather sharp decrease of the long period L (Fig. 4) is observed for both oils at a certain critical value of dilution. These critical values (33 wt.-% for paraffinic oil and 50 wt.-%

for aromatic oil) are the same ones at which a change of the shape factor is obtained in the investigation of the mechanical properties.

Also sharp variations in the fluctuation background (Fig. 10) correlate with the points suggested for the morphological transitions.

A more direct indication is obtained by segment length distributions (SLDs), calculated from the experimental SAXS curves (18,19).

F. Conclusions

The study showed, that even for films rapidly cast from solution SAXS was able to detect a two phase system similar to that found with slowly cast SBS films. The main difference between slowly and rapidly cast films seems to be the degree of phase perfection.

Paraffinic oil forms a homogeneous solution with PB and reduces the interactions between the two incompatible polymers by improving the phase separation under the rapid casting process. On the other hand, aromatic oil surely mixes with the PB matrix for low oil content, even if with a high level of inhomogeneity, but for greater oil contents either it gives rise to large clusters in the polybutadiene or even partly diffuses into the PS domains.

For the samples diluted by oil, a structure with a larger distance between elongated PS domains in the direction of their length is suggested. The distance in the transversal direction only slightly varies. Furthermore, the form of the PS domains changes from an elongated to a more spherical one at a certain critical amount of oil content. This morphological transition takes place at an oil content of 33 wt.-% with paraffinic oil, while with aromatic oil it appears only at more than 50 wt.-%.

References

1. A. Noshay and J. E. McGrath, "Block Copolymers", ps. 200,201, Academic Press, New York (1977).
2. E. Ceausescu, R. Bordeianu, P. Ghioca and M. Balanescu, Mat. Plast., 17, 201 (1980)
3. E. Ceausescu, R. Bordeianu, P. Ghioca, I. Cerchez, E. Buzdugan and R. Stancu, Revue Roumaine de Chimie, 28, 299 (1983)
4. E. Ceausescu, R. Bordeianu, P. Ghioca, E. Buzdugan, R. Stancu and I. Cerchez, Pure & Appl. Chem., 56, 319 (1984)
5. H. Stabinger and O. Kratky, Makromol. Chem., 179, 1655 (1978)
6. N. Stribeck and W. Ruland, J. Appl. Cryst., 11, 535 (1978)
7. U. Siemann and W. Ruland, Colloid & Polym. Sci., 260, 999 (1982)
8. P. Dreyfuss, L. J. Fetters and D. R. Hansen, Rubber Chem. Technol., 53, 728 (1980)
9. E. Ceausescu, R. Bordeianu, I. Cerchez, M. Balanescu and P. Ghioca, Revue Roumaine de Chimie, 26, 509 (1981)
10. R.S. Rivlin, in "Rheology", F. R. Eirich ed., Vol. 1, p. 351, Academic Press, New York (1956)
11. H.M. Smallwood, J. Appl. Phys., 15, 758 (1944)
12. E. Guth, "Proc. 2nd Rubber Technol. Conf.", p. 353, London (1948)
13. G. Holden, E.T. Bishop and N.R. Legge, J. Polymer Sci. C, 26, 189, (1969)
14. W.J. Leonard, J. Polymer Sci. Polymer Symp., 54, 237 (1976)
15. We are grateful to Prof. Petermann, Techn. Univ. of Hamburg-Harburg, for carrying out these measurements.
16. S. Polizzi and R. Zietz, in preparation
17. P. Mittelbach and G. Porod, Kolloid-Z. u. Z. Polym., 202, 40 (1965)
18. J. Mering and D. Tchoubar-Vallat, C.R. Acad. Sci. Paris, 264, 1703 (1966)
19. J. Mering and D. Tchoubar-Vallat, J. Appl. Cryst., 1, 153 (1968)
20. S. Polizzi, N. Stribeck, H.G. Zachmann and R. Bordeianu, to be submitted for publication to Polymer